An Experimental Study of Evaporation Waves in a Superheated Liquid

Thesis by

Larry G. Hill

In Partial Fulfillment
of the Requirements for the Degree of
Doctor of Philosophy

California Institute of Technology
Pasadena, California

1991
(Submitted May 23, 1990)

To my parents, Alan and Carol Hill, and to my wife, Andrea

ACKNOWLEDGMENTS

I would like to express my gratitude to my advisor, Professor Bradford Sturtevant, for his motivation and advice throughout the course of our association. My thesis has benefited greatly from his high standards and his approach to fundamental research.

I would also like to thank my peers for their useful input. In particular, David Frost, Ichiro Sugioka, and David Goldstein have offered many suggestions, several of which I have incorporated.

The cheerful and competent assistance of the GALCIT staff is much appreciated. In particular, Jean Anderson, Karen Cheetham, Jeri Chittum, Pat Gladson, Alan Goudey, Harry Hamaguchi, Clarence Hemphill, Jerry Landry, George Lundgren, Howard McDonald, George Willson, Betty Wood, and Phil Wood have all contributed to my research in a tangible way.

I shall be forever grateful to my family for their encouragement, understanding, and support during the course of my studies. I especially wish to thank my parents for providing me with the many resources that have allowed me to pursue my education. I also especially thank my wife, Andrea, for her companionship, patience, and financial support, as well as for her many hours spent helping with proofreading, printing, and drawing figures. She has earned her "Ph.T." degree with highest honors.

This project was supported by the National Science Foundation under research grant #EAR-8512724. I have also received personal support from the ARCS foundation and from Caltech's program in advanced technologies, sponsored by Aerojet General, General Motors, and TRW.

ABSTRACT

Evaporation waves in superheated liquids are studied using a rapid-depressurization facility consisting of a vertical glass test cell situated beneath a large, low-pressure reservoir. The objective of this study is to learn more about the physical mechanisms of explosive boiling (of which an evaporation wave is a specific example), as well as properties of the flow it produces.

The test cell is initially sealed from the reservoir by a foil diaphragm, and is partially filled with a volatile liquid (Refrigerant 12 or 114). An experiment is initiated by rupturing the diaphragm via a pneumatically driven cutter. The instrumentation consists of fast-response pressure measurements, high-speed motion pictures, and spark-illuminated still photographs. The liquid temperature is typically 20°C; the liquid superheat is controlled by setting the reservoir pressure to values between vacuum and 1 atm. The pressures subsequent to depressurization are very much less than the critical pressure, and the initial temperatures are sufficiently low that, although the test liquid is highly superheated, the superheat limit is not approached. Evaporation waves in which bubble nucleation *within* the liquid column is suppressed *entirely* are considered almost exclusively.

When the diaphragm is ruptured, the liquid pressure drops to virtually the reservoir value within a few milliseconds. Provided that the liquid superheat so obtained is sufficiently high, the free surface then erupts in a process known as explosive boiling, which is characterized by violent, fine-scale fragmentation of the superheated liquid and extremely rapid evaporation. The explosive boiling process proceeds as a "wavefront" into the liquid column, producing a high-speed, two-phase flow that travels upward into the low-pressure reservoir, emptying the test cell in a few hundred milliseconds. The speed of the wavefront varies between 0.2 and 0.6 m/s, depending on run conditions; the corresponding two-phase flow varies between about 5 and 35 m/s.

In the highest superheat case for the more volatile liquid (Refrigerant 12), explosive boiling usually initiates by the rapid formation of nucleation sites at random spots on the liquid free

surface and at the glass/free-surface contact line. Boiling spreads to the remaining surface within 160 μs. In the highest superheat case for the less volatile liquid (Refrigerant 114), nucleation begins only at the glass/free-surface contact line. Boiling then spreads radially inward toward the center. In the lower superheated cases for both liquids, nucleation begins at one or more sites on the glass/free-surface contact line, and propagates across the free surface.

At the higher superheats, explosive boiling initiates within a few milliseconds from diaphragm burst, the same time scale as that of liquid depressurization. No distinction is made between the onset of nucleation and that of explosive boiling. However, if the reservoir pressure is raised above a certain approximate value, the onset of explosive boiling is delayed. During the delay period, relatively slow bubbling (initiated at one or more nucleation sites at the glass/free-surface contact line) occurs, and a cluster of bubbles forms in the vicinity of the initial site. The bubble cluster then "explodes," marking the transition to explosive boiling. The delay period increases significantly as the reservoir pressure is raised slightly further. Reservoir pressures corresponding to a delay period of order 100 ms define an approximate *self-start threshold* pressure, above which the transition to explosive boiling does not occur.

Within about 10 ms of initiation, the wave reaches a quasi-steady condition in which the average wave speed, two-phase flow speed, and base and exit pressures are constant. However, the instantaneous propagation rate and the mechanisms that generate the mean flow are observed to be highly nonsteady. The wavefront appears to propagate by heterogeneous bubble nucleation at its leading edge, and any given region of the wavefront tends to propagate in surges associated with new nucleation and/or very fine-scale surface perturbations. Measurements of the instantaneous position of the upstream tip of the wavefront indicate that local velocity fluctuations are the same order as the mean velocity. The leading-edge bubble lifetimes and diameters are statistically distributed; mean values are of order 1 ms and 1 mm, respectively. The leading-edge bubbles are fragmented in violent "bursts" of aerosol. Bursts have a tendency to sweep over the leading-edge bubble layer in a wavelike manner: They are "large-scale structures" associated with the fragmentation of *many* bubbles.

Fragmentation, rapid evaporation, flow acceleration, and pressure drop occur primarily within about 1 cm of the leading edge. Downstream of this region, the average speed and

appearance of the flow are virtually constant. This developed flow is a highly nonuniform, two-phase spray containing streaklike structures. Its liquid phase is composed of drops (with a maximum diameter of about 100 μm), as well as clusters and chains of bubbles (with a diameter of a few hundred microns). A thin liquid layer begins climbing the wall upon wave initiation. Its speed is a few m/s—significantly slower than that of the two-phase flow through the center. Exit pressure measurements indicate that the flow chokes for sufficiently low reservoir pressure; at higher reservoir pressures the flow is unchoked.

The self-start threshold is not a *propagation* threshold, as waves are observed to propagate at somewhat lower superheats if started artificially. This is accomplished in Refrigerant 114 by "jump-starting" the wave, using the more volatile Refrigerant 12. For sufficiently high reservoir pressures, an "absolute" threshold is reached at which the quasi-steady rapid evaporation processes break down.

Possible mechanisms for explosive boiling are discussed in light of the present results. While neither of the two previous schools of thought (interfacial instability hypotheses and the secondary nucleation hypothesis) are alone adequate to explain the observed behavior, there is evidence that both may play a role. It is here proposed that the bursting phenomenon and bubble nucleation at the wavefront leading edge are mutually interactive processes—bursting occurring as the violent breakup of interstitial bubble liquid, and nucleation (and fine-scale perturbations) being caused by burst-generated aerosol striking the leading-edge surface. It is not understood what role interfacial instability may play in the bursting process.

An evaporation wave is analogous to a premixed flame in that both are classified as "weak deflagration" waves in gasdynamic theory. It is shown that using several approximations that are valid for the type of evaporation waves studied, the conservation equations (jump conditions) can be reduced to a single, simple expression in terms of readily measured and inferred properties.

TABLE OF CONTENTS

Chapter	Title	Page
	Copyright	ii
	Dedication	iii
	Acknowledgements	iv
	Abstract	v
	Table of Contents	viii
	List of Figures	xi
	List of Tables	xviii
	List of Symbols	xix
1	INTRODUCTION	1
	1.1 Motivation	2
	1.2 Background	3
	1.3 Previous Evaporation Wave Experiments	12
	1.4 Outline of Present Work	15
2	EXPERIMENTAL METHODS	17
	2.1 Apparatus	17
	2.2 Instrumentation	25
	2.3 Experimental Conditions	34
	2.4 Experimental Procedure	37
3	OVERVIEW OF EXPERIMENTAL OBSERVATIONS	40
	3.1 Start-Up	40
	3.2 Quasi-Steady Propagation	42
4	QUASI-STEADY PROPAGATION	46
	4.1 Upstream Liquid Region	46
	4.2 Wavefront Region	53

	4.3 Developed Two-Phase Flow Region	82
	4.4 Absolute Threshold	91
	4.5 Summary of Average Wave Properties	94
5	START-UP	98
	5.1 Depressurization Process	98
	5.2 Modes of Wave Initiation	104
	5.3 Self-Start Threshold	111
	5.4 Transition to Quasi-Steady Propagation	116
6	DISCUSSION OF WAVEFRONT MECHANISMS	118
	6.1 Generic Mechanisms	118
	6.2 Specific Mechanisms	120
7	JUMP CONDITION MODEL	138
	7.1 Analogy to a Premixed Flame	138
	7.2 Basic Assumptions	139
	7.3 Rankine-Hugoniot Equation	141
	7.4 Treatment by Previous Authors	142
	7.5 An Analytic Solution of the Jump Conditions	143
	7.6 Analytic Expressions for Two-Phase Flow Properties	147
	7.7 Comments on Model Closure	148
8	SUMMARY AND CONCLUSIONS	150
	8.1 Quasi-Steady Propagation	150
	8.2 Start-Up Behavior	153
	8.3 Thresholds	154
	8.4 Mechanisms of Wave Propagation	154
	8.5 Jump Condition Model	155
	8.6 Suggestions for Future Work	155
	APPENDICES	
A	Guide to Video Supplement	157
	A.1 Views	157
	A.2 Program Guide	160

	A.3 Ordering Information	165
B	Base and Exit Pressure Traces for the Six Primary Run Conditions	166
C	Runs with Nucleation in the Upstream Liquid Column	174
	C.1 Generation and Expulsion of a Bubbly Mixture	174
	C.2 Evaporation Wave in a Column of Rising Bubbles	177
	REFERENCES	180

LIST OF FIGURES

Figure	Title	Page
1.1	Schematic representation of an evaporation wave in wave-fixed coordinates.	2
1.2	Relationship between superheat temperature and superheat pressure.	5
1.3	Pressure-temperature diagram for Refrigerant 12, indicating the compressed liquid, superheated liquid, and vapor regions.	7
1.4	Mechanical equilibrium of a gas/vapor bubble in a superheated liquid.	9
1.5	Adiabatic, isobaric evaporation of a superheated liquid.	10
2.1	Schematic of evaporation wave facility.	17
2.2	Photograph of evaporation wave facility.	18
2.3	Photograph of reservoir/test-cell interface, free standing.	19
2.4	Photograph of test cell, reservoir/test-cell interface, and circulation system.	20
2.5	Schematic of evaporation wave facility control system.	22
2.6	Test cells.	23
2.7	Experimental setup for pressure measurements.	26
2.8	Mounting and thermal insulation of exit pressure transducer.	27
2.9	Experimental setup for high-speed motion picture runs.	29
2.10	Photographic configurations for high-speed motion picture experiments.	31
2.11	Experimental setup for still photography runs.	33
2.12	Photographic configurations for still photographs.	35

Figure	Title	Page
3.1	Base and exit pressure traces. Liquid: R12, T_{liq} = 20°C, P_{res} = 0 bar, Run #: MPR 25.	41
3.2	Quasi-steady flow regions. Liquid: R12, T_{liq} = 20°C, P_{res} = 0 bar, Large ruler divisions: cms, t = 25 ms from diaphragm burst, Initial liquid height: 8.0 cms, Test cell #: 2, Run #: SPR 4.	44
4.1a	Evaporation wave in R114 approaching a density-matched, dyed solution of cesium chloride. T_0 = 20°C, P_{res} = 0 bar, Test cell #: 2, Run #: MPR 81.	50
4.1b	Motion of the interface in Figure 4.1a as the wavefront approaches.	50
4.2	Solution of the heat equation for the temperature profile in the upstream liquid.	52
4.3	Side-view still photograph of a typical evaporation wave. Liquid: R12, T_0 = 20°C, P_{res} = 0 bar, x_0 = 8.1 cm, t ≃ 20 ms, Test cell #: 2, Run #: SPR 1.	54
4.4	Side-view still photograph of an evaporation wave at the same run conditions as the previous figure, but with the wavefront highly inclined. Liquid: R12, T_0 = 20°C, P_{res} = 0 bar, x_0 = 7.9 cm, t = 21.1 ms, Test cell #: 2, Run #: SPR 3.	55
4.5	Side and bottom view still photographs of evaporation waves for four different run conditions. T_0 = 20°C, x_0 = 8.0 cm.	57

Figure	Title	Page
4.6	Side-view still photograph of an evaporation wave in a test cell with annular geometry. Gap width: 1.75 mm, Liquid: R12, T_0 = 20°C, P_{res} = 0 bar, x_0 = 8.1 cm, t = 31.9 ms, Test cell #: 2, Run #: SPR 29.	59
4.7	(a) Spherical bubble growing in a uniformly superheated liquid, (b) Floating bubble growing in a semi-infinite superheated liquid, (c) Isolated perturbation at the surface of a semi-infinite superheated liquid.	61
4.8	Evolution of the global wavefront shape. Liquid: R12, T_0 = 20°C, P_{res} = 0 bar, Test cell #: 1, Run #: MPR 76.	64
4.9a	Instantaneous position of the upstream tip of the wavefront leading edge. Liquid: R12, T_0 = 20°C, P_{res} = 0 bar, Run #: MPR 25.	69
4.9b	Instantaneous velocity of the upstream tip of the wavefront leading edge, obtained from the above $x-t$ diagram.	69
4.10a	Instantaneous position of the upstream tip of the wavefront leading edge. Liquid: R12, T_0 = 20°C, P_{res} = 1 bar, Run #: MPR 31.	70
4.10b	Instantaneous velocity of the upstream tip of the wavefront leading edge, obtained from the above $x-t$ diagram.	70
4.11	Sequence of high-speed motion pictures illustrating two surges in wavefront velocity by the growth of smooth bubbles. Liquid: R12, T_0 = 20°C, P_{res} = 1 bar, Divisions: mms, Test cell #: 2, Run #: MPR 31.	71

Figure	Title	Page
4.12	Sequence of high-speed motion pictures illustrating a surge in wavefront velocity by the growth of a "rough" bubble. Liquid: R12, T_0 = 20°C, P_{res} = 1 bar, Divisions: mms, Test cell #: 2, Run #: MPR 31.	72
4.13	Growth rates of three selected leading-edge bubble samples compared to the classical theory of a bubble growing in an infinite superheated liquid. Liquid: R12, T_0 = 20°C, P_{res} = 0 bar, Run #: MPR 25.	75
4.14	Dimensionless growth rates of selected leading-edge bubble samples for the six different run conditions, compared to the classical theory for a bubble growing in an infinite superheated liquid.	77
4.15	Lifetimes of 100 selected leading-edge bubble samples. Liquid: R12, T_0 = 20°C, P_{res} = 0 bar, Run #: MPR 25.	78
4.16	An approximate, partial wave-speed model in terms of leading-edge bubbles.	80
4.17	Developed two-phase flow region. Liquid: R12, T_0 = 20°C, P_{res} = 0 bar, x_0 = 10.0 cm, Test cell #: 1, Run #'s: MPR 76, SPR 22.	83
4.18	Developed two-phase flow region. Liquid: R12, T_0 = 20°C, P_{res} = 1 bar, x_0 = 10.0 cm, Test cell #: 1, Run #'s: MPR 78, SPR 24.	84
4.19	Developed two-phase flow region. Liquid: R114, T_0 = 20°C, P_{res} = 0 bar, x_0 = 10.0 cm, Test cell #: 1, Run #'s: MPR 77, SPR 25.	85

Figure	Title	Page
4.20	$x-t$ diagram showing the three fronts and four axial-position/time regions. Liquid: R12, T_0 = 20°C, P_{res} = 0 bar, Test cell #: 1, Run #: MPR 76.	89
4.21	Relaxation length for evaporation of liquid droplets.	91
4.22	"Jump-start" run using R12 over R114. T_{l0} = 20°C, P_{res} = 1/2 bar, Test cell #: 2, Run #: MPR 72.	92
4.23	Sequence of photographs showing wave breakdown at the absolute threshold. Liquid: R114, T_0 = 20°C, P_{res} = 1/2 bar, Test cell #: 2, Run #: MPR 72.	93
4.24	Inferring two-phase flow speed from base and exit pressure traces when the flow is choked. Liquid: R12, T_0 = 20°C, P_{res} = 0 bar, Run #: MPR 25.	95
5.1	$P-t$ and $x-t$ diagrams for evaporation wave start-up. Liquid: R12, T_0 = 20°C, P_{res} = 0 bar, Run #: MPR 25.	99
5.2	Fog formation in R12 vapor upon depressurization and prior to initiation of explosive boiling. T_0 = 20°C, P_{res} = 0 bar, Run #: MPR 25.	103
5.3	Mode 1 start-up. Liquid: R12, T_0 = 20°C, P_{res} = 0 bar, Test cell #: 2.	105
5.4	Mode 2 start-up. Liquid: R114, T_0 = 20°C, P_{res} = 0 bar, Test cell #: 2.	106
5.5	Mode 3 start-up. Liquid: R114, T_0 = 20°C, P_{res} = 1 bar, Test cell #: 2.	107

Figure	Title	Page
5.6	Mode 3 start-up in highest superheat case (cf. Figure 5.5). Liquid: R12, T_0 = 20°C, P_{res} = 0 bar, t = 3.75 ms, Run #: SPR 37.	109
5.7	Delay in transition to explosive boiling, for R12 as a function of reservoir pressure. T_0 = 20°C.	112
5.8	Base and exit pressure traces for a run near the self-start threshold, with a substantial delay time. Liquid: R114, T_0 = 20°C, P_{res} = 1/3 bar, Run #: MPR 57.	113
5.9	Sequence of top oblique view high-speed motion pictures, illustrating near-threshold start-up behavior. Liquid: R114, T_0 = 20°C, P_{res} = 1/3 bar, Run #: MPR 66.	114
6.1	Generic "evaporation/fragmentation interaction."	119
6.2	Mesler's Secondary Nucleation Hypothesis in the context of free-surface boiling (from Mesler, 1988).	121
6.3	The Landau Instability Hypothesis, applied to an evaporating interface by Shepherd and Sturtevant (1982) and by Frost and Sturtevant (1986).	132
6.4	Suggested interaction between the leading-edge bubble layer and bursting.	137
7.1	Schematic representation of an evaporation wave.	140
7.2	Generic Hugoniot curve for an evaporation wave.	141
7.3	Ideal jump condition relation compared with experiments.	147
A.1	The four motion picture views and their appearance in the video.	159
B.1	Liquid: R12, T_0 = 20°C, P_{res} = 0 bar. Comments: choked exit during quasi-steady propagation phase.	167
B.2	Liquid: R12, T_0 = 20°C, P_{res} = 1/2 bar. Comments: unchoked exit during quasi-steady propagation phase.	168
B.3	Liquid: R12, T_0 = 20°C, P_{res} = 1 bar. Comments: unchoked exit during quasi-steady propagation phase; near self-start threshold; transition to explosive boiling occurs at about 25 ms.	169

Figure	Title	Page
B.4	Liquid: R12, T_0 = 20°C, P_{res} = 1 bar. Comments: near self-start threshold; transition to explosive boiling does not occur (cf. Figure B.3).	170
B.5	Liquid: R114, T_0 = 20°C, P_{res} = 0 bar. Comments: choked exit during quasi-steady propagation phase.	171
B.6	Liquid: R114, T_0 = 20°C, P_{res} = 1/3 bar. Comments: unchoked exit during quasi-steady propagation phase; near self-start threshold; transition to explosive boiling occurs at about 350 ms.	172
B.7	Liquid: R114, T_0 = 20°C, P_{res} = 1/2 bar. Comments: near absolute threshold (jump-started with R12); exit is unchoked during R114 quasi-steady propagation phase; wave shuts off at 140 ms with liquid remaining.	173
C.1	Sequence of motion pictures showing a typical run in which nucleation occurs within the liquid column. Liquid: R12, T_0 = 20°C, P_{res} = 1.5 bar, Test cell #: 2, Run #: MPR 29.	175
C.2	Base and exit pressure traces corresponding to the run shown in the previous figure. Liquid: R12, T_0 = 20°C, P_{res} = 1.5 bar, Run #: MPR 29.	176
C.3	Sequence of motion pictures showing an evaporation wave propagating into a column of rising bubbles. Liquid: R12, T_0 = 21.6°C, $P_{res} \simeq 1$ bar, Test cell #: 2, Run #: MPR 11.	178
C.4	Base pressure trace corresponding to run shown in the previous figure. Liquid: R12, T_0 = 20°C, $P_{res} \simeq 1$ bar, Run #: MPR 11.	179

LIST OF TABLES

Table	Title	Page
2.1	Specifications for pressure measurements	26
2.2	Physical Properties of Refrigerants 12 and 114	36
2.3	Run Conditions and Views	37
4.1	Summary of Measured and Inferred Average Wave Properties	96
5.1	Summary of Start-Up Modes	110

LIST OF SYMBOLS

Symbol	Description	Reference
a	Sound speed	
c_p	Specific heat at constant pressure	
d	Diameter	
g	Acceleration due to gravity	
h	Specific enthalpy	
k	Thermal conductivity	
$\dot{m}$	Mass flux per unit area	
s	Specific entropy	
t	Time	
$\overline{t}_b$	Average bubble lifetime	
$\overline{t}_n$	Average time between nucleation events at a local region of the wavefront leading edge	
v	Specific volume	
x	Axial position	
y	Lateral position	
Bo	Bond number	Equation 4.7
Fr	Froude number	Equation 6.1
I	Propagation intermittency of a local region of the wavefront leading edge	Equation 4.14
Ja	Jakob number	Equation 1.10
$\hat{Ja}$	Modified Jakob number	Equation 7.5b
K	Isothermal compressibility	Equation 1.7
L	Latent heat of evaporation	

Symbol	Description	Reference
P	Pressure	
P'	Pressure fluctuation	
Pe	Peclet number	Equation 4.16
R	Radius	
$\bar{R}_{bmax}$	Average maximum bubble size	
T	Temperature	
V	Velocity	
We	Weber number	Equation 6.1
α	Volume fraction of vapor	
β	"Jump condition" number	Equation 7.5a
γ	Ratio of vapor specific heats	
δ	Thermal boundary layer thickness	
ζ	Dimensionless wave amplitude	Equation 7.5c
η	Leading-edge bubble-growth efficiency compared to classical theory	
κ	Thermal diffusivity	
ν	Nucleation frequency	
ρ	Density	
σ	Surface tension coefficient	
χ	Mass fraction of vapor	
Δh	Superheat enthalpy	Equation 1.3
ΔP	Superheat pressure	Equation 1.2
ΔP_w	Wave amplitude	Equation 7.5a
ΔT	Superheat temperature	Equation 1.1

Chapter 1

Introduction

It is well known that highly superheated liquids (i.e, liquids that are hotter than the boiling temperature at their pressure) can release their stored thermal energy through rapid, and often violent, evaporation. The evaporation rate depends in part on energy considerations, i.e., the thermal energy per unit mass available to produce evaporation compared to that which is required. In addition, the evaporation rate depends in a crucial way on the surface-area of evaporating liquid/vapor interfaces. Other factors being equal, the evaporation rate is proportional to the interfacial surface area. The latter factor is what makes rapid evaporation (also called flash evaporation or explosive boiling) an interesting and complex phenomenon. Under the proper conditions, surface area production by fragmentation of liquid into small droplets can increase the evaporation rate and mass flux by orders of magnitude.

In some experiments, explosive boiling has been observed to proceed as a "front" propagating into the superheated liquid, producing a high-speed, two-phase spray flow behind it. This general behavior has been observed in both pure and bubbly liquids. The front satisfies the general definition of a wave used by Whitham (1974)—"a recognizable signal that is transferred from one part of the medium to another with a recognizable velocity of propagation"—and has been called an *evaporation wave* by several authors.

Figure 1.1 shows a schematic illustration of an evaporation wave in a coordinate system fixed with the wavefront. The inflowing liquid shown in the schematic is pure, but, as mentioned above, it could in general be bubbly. As liquid evaporates through the wavefront, the density decreases. Mass conservation dictates that the velocity must increase, and momentum conservation requires that as the flow accelerates through the wavefront, the pressure must decrease. In this sense an evaporation wave is somewhat analogous to an expansion wave in a single-phase fluid; however, it is most analogous to a flame in a combustible mixture, since stored *thermal* energy in the inflowing liquid provides energy for *evaporation* in the former, just as stored *chemical* energy provides energy for *combustion* in the latter. Unlike either example, evaporation waves involve a change of phase. In the primary example to be presented in this study, the inflowing liquid is 50°C above its boiling point, and enters the wavefront at 0.6 m/s.

The fluid is fragmented and accelerated by explosive boiling (indicated schematically by the darkest region downstream of the wavefront leading edge) to produce a two-phase spray, which exits the wavefront region at 35 m/s.

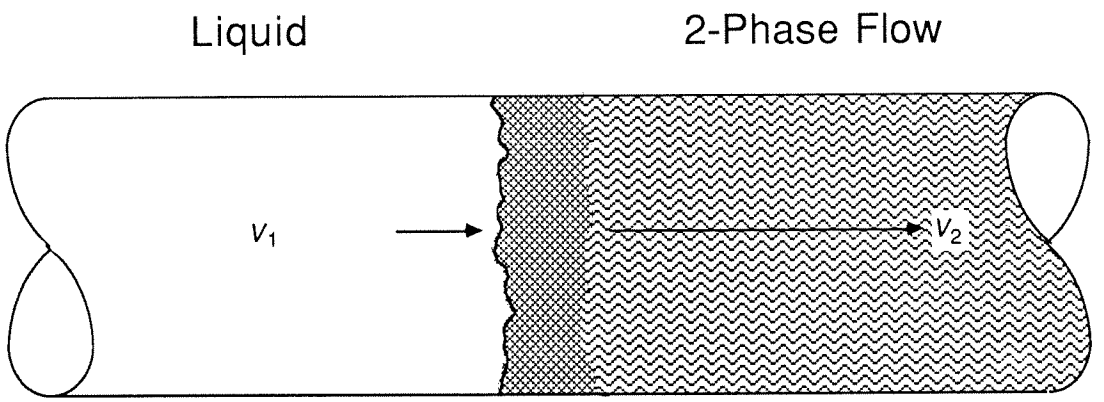

Figure 1.1: Schematic representation of an evaporation wave in wave-fixed coordinates.

1.1. Motivation.

Rapid evaporation can be hazardous in both nature and industry. For example, when a volatile liquid is accidentally spilled into a hotter liquid or (vice versa), the volatile liquid will explode if heated sufficiently. Many such *vapor explosions* have occurred in industry; an extensive review of incidents is given by Reid (1983). A second, potentially hazardous situation exists when a hot volatile liquid is contained under its vapor pressure, as is water in nuclear power-plant cooling lines. If a pipe ruptures—the so-called loss-of-coolant accident or "LOCA"—the pressure drops, superheating the water. Rapid evaporation then expels the water violently through the break (e.g., Winters and Merte, 1979). An analogous situation in nature is an explosive volcanic eruption. A recent example was the 1980 eruption of Mt. St. Helens, where a reservoir of magma was contained under pressure by the overlying rock. The pressure of the magma destabilized one side of the mountain and caused it to slide, thereby releasing the magma pressure and superheating it. The resulting explosion was estimated by Decker and Decker (1981) to have been the energy equivalent of 400 megatons of TNT.

Rapid evaporation can also be useful if it is controlled. The applications in which it is used typically involve aerosol production. The *flashing injector* is a fuel injection nozzle that superheats the incoming fuel to achieve finer atomization through evaporation (Solomon *et al.*, 1982). *Spray drying* is a technique used to produce powdered foods from liquid foods (e.g., milk), in which the liquid is heated and sprayed through a nozzle into low pressure. The volatile component is thereby evaporated, leaving solid particles (Marshall, 1954). *Spray cooling* is a technique in which a hot object is cooled by the evaporation of a sprayed coolant. The space shuttle employs a spray-cooling system called a *flash evaporator* for temperature control, since radiative cooling from the bay doors is insufficient (Nason *et al.*, 1983).

Despite ample motivation, many of the basic mechanisms of rapid evaporation remain poorly understood. A primary reason, aside from the fact that the problem is complex, is that rapid evaporation is difficult to control for effective study. Moreover, flow visualization is difficult because the processes are extremely rapid and fine scale, and the two-phase, light-scattering flows generated scatter visible light. Besides being a unique phenomenon in itself, the evaporation wave provides a controlled means to study fundamental rapid evaporation processes. The primary objective of this study, therefore, is to use this somewhat "ideal" flow to isolate and identify fundamental explosive boiling processes that may occur in flows of more practical interest.

1.2. Background.

1.2.1. *Superheated Liquids.* A liquid whose temperature exceeds the boiling point at its pressure is said to be superheated, supersaturated, or metastable. Put another way, a superheated liquid is at a temperature and pressure for which the substance would normally be in the vapor phase. A liquid's superheat is expressed by how far its thermodynamic state has transgressed the saturation boundary in terms of a chosen thermodynamic variable. The superheat is most often expressed as the temperature by which the liquid exceeds the saturation temperature at the same pressure:

$$\Delta T \equiv T_l - T_{l,s}(P_l) \tag{1.1}$$

where the subscript l denotes liquid, and the subscript s denotes a saturation value. Sometimes the superheat is more naturally expressed as the difference between the pressure of an equilibrium liquid and that of the superheated liquid at the same temperature:

$$\Delta P \equiv P_{l,s}(T_l) - P_l \tag{1.2}$$

For evaporation waves, the most useful expression of superheat is the enthalpy by which the liquid exceeds that of a saturated liquid at the same pressure:

$$\Delta h \equiv h_l - h_{l,s}(P_l) \tag{1.3}$$

The significance of this measure of superheat is that it is a measure of the thermal energy available to produce evaporation.

The various measures of superheat can be related. For example, ΔT can be expressed in terms of ΔP through a Taylor series expansion for the vapor pressure curve, as shown in Figure 1.2.

$$\Delta P = \left[\frac{L}{T_s v_{lv}}\right] \Delta T + O(\Delta T^2) + \cdots \tag{1.4}$$

where the Clapeyron relation is used to express the slope of the vapor pressure curve in terms of the temperature, the latent heat of evaporation L, and the difference between the specific volume of the saturated vapor and liquid v_{lv}. Similarly, to the extent that the specific heat of the liquid at constant pressure c_p is constant, the superheat enthalpy can be related to the superheat temperature by:

$$\Delta h = c_p \Delta T \tag{1.5}$$

It is usually most convenient to use each definition of superheat as it arises; this strategy is used in the present study.

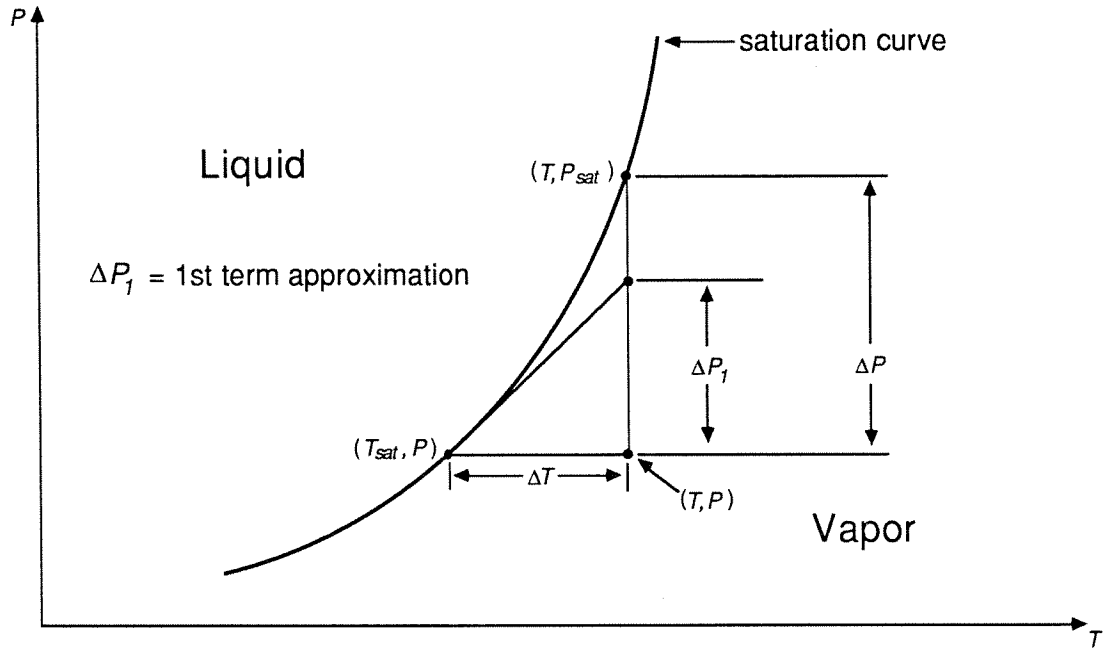

Figure 1.2: Relationship between superheat temperature and superheat pressure.

The physical basis for superheating is that molecules in the liquid phase attract one another, and work is required to overcome that attraction to form a vapor phase. In a pure liquid with no free surfaces, the mechanism for vapor formation involves random density fluctuations, which occur constantly on a molecular scale. A local density deficit of sufficient magnitude is essentially a change in phase, i.e., a microscopic vapor bubble or "embryo." Work is required for such an embryo to grow, because a surface force—which on a macroscopic scale becomes *surface tension*—arises that opposes growth. In a compressed or saturated liquid, there is no driving mechanism to provide work to overcome the surface force, so vapor embryos collapse. A driving mechanism does exist if the liquid is superheated, which can be appreciated by treating the vapor embryo using classical continuum concepts.

A classical vapor bubble can exist in mechanical equilibrium only if the squeeze of surface tension is exactly balanced by the pressure excess inside the bubble, which occurs at the *critical radius*:

$$R_{cr} = \frac{2\sigma}{\Delta P} \tag{1.6}$$

where σ is the surface-tension coefficient. The vapor pressure within the bubble is the saturation value corresponding to the liquid temperature, so the excess pressure ΔP within the bubble is the superheat pressure given by Equation 1.2. The equilibrium is unstable: A vapor bubble smaller than the critical radius will collapse, and one larger than the critical radius will grow indefinitely. Thus, a statistically generated vapor embryo must exceed the critical radius in order to grow. The force that drives the growth is excess internal pressure that arises because the liquid is superheated.

The question of how many vapor bubbles (if any) will exceed the critical radius is a probabilistic one, which is addressed by the fluctuation theory of statistical mechanics. A useful result from this theory (Landau and Lifshitz, 1969) gives the mean-square density fluctuation in a volume of liquid V in terms of mean thermodynamic quantities:

$$\frac{\overline{(\Delta\rho)^2}}{\rho^2} = \left[\frac{kT}{V^2}\right] K \; ; \; K \equiv -\rho\left[\frac{\partial P}{\partial v}\right]_T^{-1} \tag{1.7}$$

where k is Boltzmann's constant and K is the isothermal compressibility.

The important result of Equation 1.7 is that the density fluctuations become large when the isothermal compressibility becomes large. Equations of state predict that there is a locus of states for which the isothermal compressibility (and by Equation 1.7, the mean-square density fluctuation) becomes infinite. This condition, called the *spinodal curve*, represents a theoretical limit beyond which the liquid spontaneously separates into two phases. The experimentally observed *superheat limit* actually lies very close to this condition (Reid, 1976). The growth of statistical density fluctuations is referred to as *homogeneous nucleation.*

The locus of possible superheated liquid states—which lie between the saturation curve and the spinodal—can be readily calculated, given an equation of state for the substance. Figure 1.3 shows the superheated liquid region for Refrigerant 12 (the primary liquid used in this study) on a pressure-temperature diagram. The temperature and pressure in this figure are normalized by

their critical values. The vapor pressure and spinodal curves are calculated using the Redlich-Kwong equation, which is a fairly simple equation of state. Note that the minimum superheat limit temperature is about $0.9\,T_{cr}$. The initial liquid state (T_0, P_0) used in the present experiments is indicated on the diagram. The initial reduced temperature is 0.76 (20°C). Superheating is achieved by depressurization, which occurs at almost constant temperature. The final reduced pressure is very low: about 0.02. Clearly, the superheat limit is not approached in this case, nor is it for the other liquid used in this study, namely, Refrigerant 114. Hence, homogeneous nucleation is not observed.

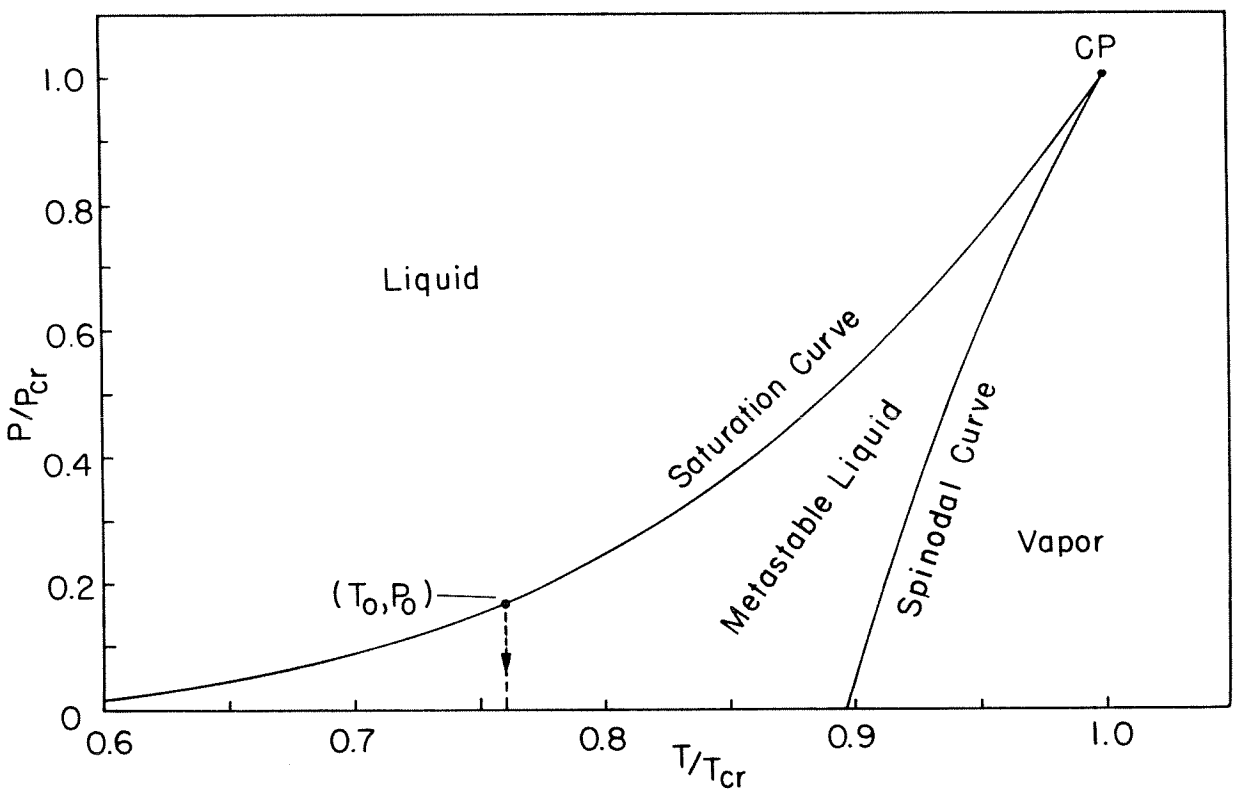

Figure 1.3: Pressure-temperature diagram for Refrigerant 12, indicating the compressed liquid, superheated liquid, and vapor regions.

The above discussion of a pure liquid does not account for the fact that real liquids almost always contain some dissolved gas and/or small gas bubbles, and that container walls have scratches and other defects that harbor small nuclei. Consequently, in most cases a liquid will nucleate well below the superheat limit. Nucleation of this type is referred to as *heterogeneous*.

The heterogeneous nucleation process is illustrated in Figure 1.4, by considering a bubble containing vapor and a noncondensable gas. Unlike the pure vapor bubble, the gas/vapor bubble is stable over a *range* of sizes. Let R_0 be the radius of the bubble in a saturated liquid,[1] and consider the effect of superheating the liquid by isothermal depressurization (consistent with the technique of the present experiments). Figure 1.4 is a nondimensional form of the family of curves obtained by Daily and Johnson (1956). It indicates that as the liquid is superheated, the bubble will grow to a larger equilibrium size; however, there is a critical radius, corresponding to a critical superheat pressure, for which the bubble will grow indefinitely without any additional superheat:[2]

$$\frac{R_{cr}}{R_0} = \sqrt{3} \tag{1.8a}$$

$$\frac{R_0 \Delta P_{cr}}{2\sigma} = \frac{2}{3\sqrt{3}} \tag{1.8b}$$

There are additional issues, such as the solubility of the noncondensable gas component in the liquid, which are not considered in the above analysis. The reader is referred to Knapp *et al.* (1970) for a more complete discussion of heterogeneous nucleation.

The present study is primarily concerned with evaporation waves in which nucleation within the liquid column is suppressed *entirely*. By the above analysis, for the highest superheat pressure during wave propagation (ΔP = 4.7 bar), the radius R_0 of the largest gas bubble in the initially saturated liquid must be less than 15 nm in order to achieve this goal.[3] Maintaining high superheats therefore requires special techniques, which are outlined in Chapter 2. A detailed treatise on superheated liquids is given by Skripov (1974).

---

1. The mass of noncondensable gas in the bubble is accounted for in R_0.
2. Note that in Equation 1.8b, ΔP_{cr} refers to the superheat pressure corresponding to the critical bubble radius, whereas, in Figure 1.3, P_{cr} refers to the thermodynamic critical pressure of the fluid.
3. That is, bubble nuclei having an initial radius larger than R_0 = 15 nm will grow to macroscopic sizes when the superheat pressure is ΔP_{cr} = 4.7 bar.

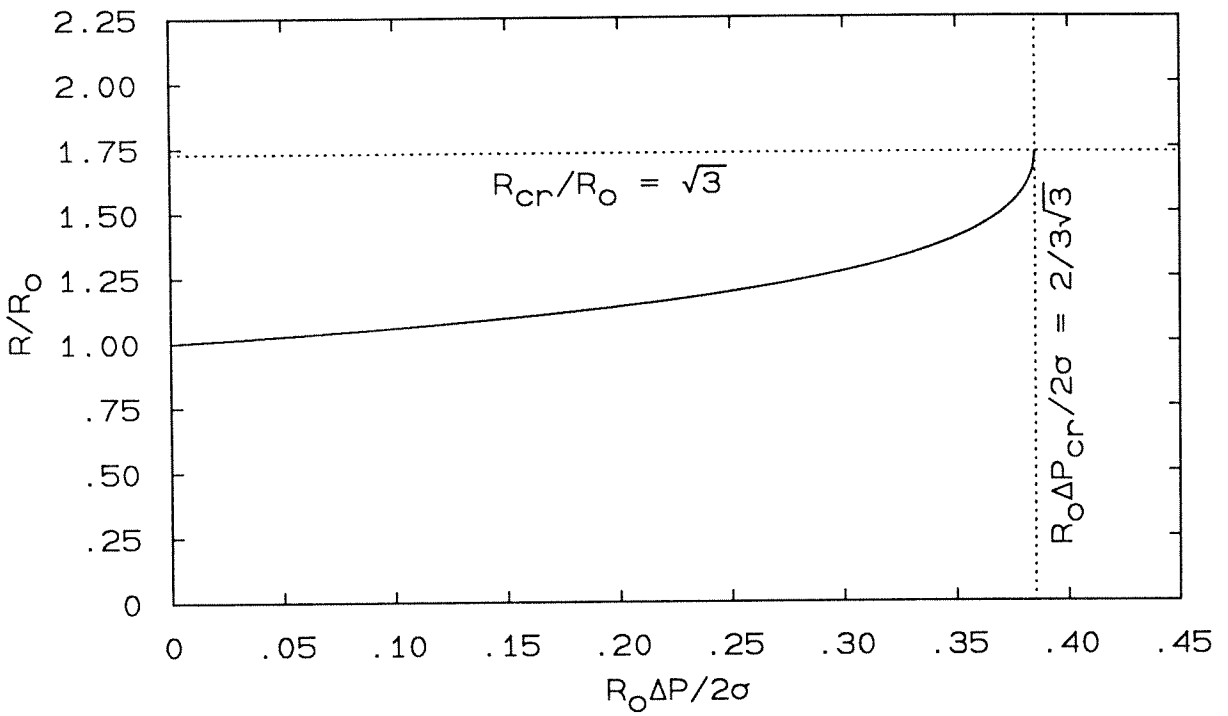

Figure 1.4: Mechanical equilibrium of a gas/vapor bubble in a superheated liquid.

1.2.2. *Adiabatic Evaporation.* When a pot of water boils on a stove, the sources of nucleation are sites on the bottom (heated) surface of the pan. The abundance of evaporating bubbles prevents significant build-up of thermal energy in the form of superheat, because the energy is absorbed as "latent heat" in producing the phase change. In the absence of nuclei, or when nuclei occur infrequently, a liquid can be heated above its boiling point. In doing so, thermal energy is then *stored.* If the stored energy becomes sufficiently great, evaporation is usually explosive when it is finally released. Two familiar examples are the popping of water droplets in hot cooking oil and wet wood in a fire. This type of evaporation is *adiabatic* in the sense that heat transfer from the surroundings is negligible during the brief time in which rapid evaporation occurs.

When a liquid is superheated by depressurization (as in the present study), its enthalpy is nearly conserved, and its boiling point is lowered. The advantages of superheating by depressurization are that the liquid can be superheated with a combination of uniformity and speed not achievable by heating. Figure 1.5 presents an example that demonstrates the energy considerations for the adiabatic evaporation of a liquid superheated by depressurization. A volatile liquid is maintained in a compressed state (0) by two weights. One of the weights is

then removed, depressurizing the liquid isentropically to a superheated state (1), whereupon, the liquid evaporates isobarically to achieve a new equilibrium (2).[4] The energy equation dictates that enthalpy is conserved between states (1) and (2).

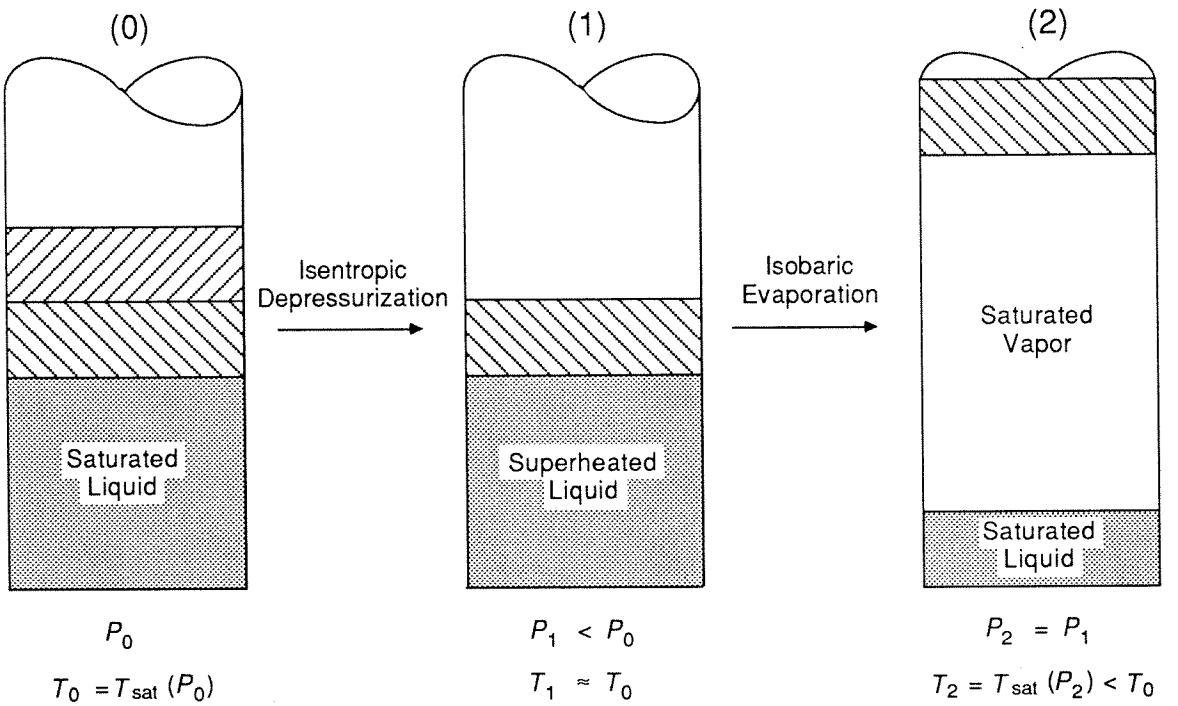

Figure 1.5: Adiabatic, isobaric evaporation of a superheated liquid.

The fraction of liquid χ_2 that evaporates (i.e., the final mass fraction of vapor) is obtained by equating the enthalpy of states (1) and (2):

$$h_{l1} = (1 - \chi_2)h_{l2} + \chi_2 h_{v2} \tag{1.9}$$

Rearranging Equation 1.9 and using the conditions $h_{l2} = h_{l1,s}$ and $h_{v2} = h_{v1,s}$ (where s refers to saturation conditions at $P_1 = P_2$) gives:

4. No assumptions are made about the mechanisms or rates of evaporation; it is only assumed that the pressure is maintained constant.

$$\chi_2 = \frac{\Delta h_{l1}}{L_1} \equiv Ja_1; \quad \Delta h_{l1} \equiv h_{l1} - h_{l1,s}; \quad L_1 \equiv h_{v1,s} - h_{l1,s} \tag{1.10}$$

Thus χ_2 can be expressed in terms of properties of the superheated liquid in state (1). Specifically, it is the ratio of the superheat enthalpy defined in Equation 1.3 (i.e., the specific enthalpy of liquid *available* for evaporation) to the latent heat (the specific enthalpy of liquid *required* for evaporation). This ratio—called the *Jakob number*—is the key parameter in adiabatic evaporation problems. The Jakob number is typically less than one, indicating that only a portion of the liquid can evaporate. This is the case in the present experiments. Jakob numbers greater than unity can, however, be achieved for liquids of sufficiently high molecular weight (Shepherd *et al.*, 1989). In such cases complete evaporation is possible.

In the above example, it is assumed that sufficient time passes for equilibrium to be established. The question of the *rate* at which state (1) proceeds toward state (2) is generally quite complicated: It depends not only on the Jakob number, but also on the regime of evaporation or boiling that occurs. It is, however, straightforward and illustrative to consider the growth rate of a single vapor bubble in a uniform superheated liquid. Bubble growth in a uniform infinite superheated liquid proceeds in three stages (Prosperetti and Plesset, 1978). The first stage occurs as the bubble exceeds its critical radius and begins to grow; here, the primary restrictive force is due to surface tension. As growth continues, the bubble enters the second stage, in which the inertia of the surrounding liquid accounts for the primary restrictive force. In the third and final stage, the growth rate is controlled by the balance between heat flux from the superheated liquid to the evaporating surface, and the latent heat absorbed at the surface in producing phase change. In many evaporation problems the third stage is of primary interest. The mass flux per unit area and the radius as a function of time for this limit (Prosperetti and Plesset, 1978) are:

$$\dot{m} = \left[\frac{3}{\pi}\right]^{1/2} Ja_1 \rho_{l1,s} \left[\frac{\kappa_{l1}}{t}\right]^{1/2} \tag{1.12a}$$

$$R = \left[\frac{12}{\pi}\right]^{1/2} Ja_1 \left[\frac{\rho_{l1,s}}{\rho_{v1,s}}\right] \sqrt{\kappa_{l1} t} \tag{1.12b}$$

The proportionality to the Jakob number is expected since it characterizes the net driving energy for evaporation. The liquid/vapor density ratio controls the degree to which liquid is displaced by the evaporated vapor phase, and therefore appears in the expression for the bubble radius. Since the increase in the mixture specific-volume due to vapor production is the driving mechanism in all evaporation-induced flows, the liquid/vapor density ratio is an important parameter in general.

In the case of classical thermal bubble growth, the evaporation rate is limited by conductive heat transfer through a thermal boundary layer. The decrease in the mass flux per unit area with time reflects the thickening of this layer. In situations where many nucleation sites exist in a volume of volatile liquid (or alternatively on its container walls), the overall evaporation rate immediately following rapid depressurization can be quite high, even though heat transfer is primarily conductive. This is often the case in "blowdown" experiments used to model loss-of-coolant accidents (e.g., Winters and Merte, 1979; Terner, 1962).

As the fluid in the above example starts to move in response to the increase in specific volume, the situation becomes complicated in detail. (For example, convective heat transfer becomes important.) Still, there is little that is *conceptually* mysterious about such a flow. There are, however, situations in which simple intuition fails: Sometimes violent, fine-scale fragmentation of liquid into droplets occurs, and the surface area and evaporation rates are thereby decreased dramatically. The range of conditions under which this type of behavior occurs is not known, nor have the physical mechanisms been resolved. It has, however, been documented that fragmentation often proceeds through a superheated liquid as an evaporation wave. All such instances known to the author are now reviewed.

1.3. Previous Evaporation Wave Experiments.

Evaporation waves were first proposed by Bennett *et al.* (1964) to explain anomalies in the current and resistance histories of exploding wires. The wave speeds inferred from electrical measurements were of order 100 m/s. Bennett suggested that the appropriate wave speed was the equilibrium, two-phase sound speed calculated at the liquid phase boundary, which gave satisfactory agreement with experimental estimates. Bennett (1965) later proposed that evaporation waves should occur in substances besides liquid metals, which subsequent studies of superheated liquids have confirmed. These divide naturally into two categories: waves with bubbly upstream liquid, and waves with pure upstream liquid.

1.3.1. *Waves with Bubbly Upstream Liquid.* The first direct observation of an evaporation wave known to the author was made by Friz (1965). Friz conducted studies with distilled degassed water and untreated water at temperatures between 105 and 125 °C. His apparatus was a vertical glass test tube, initially sealed by a plastic diaphragm. The test cell was pressurized to 3.5 atm with a foreign gas prior to heating. The experiment was initiated by rupturing the diaphragm, which exposed the liquid column to the 1 atm ambient pressure. High-speed motion pictures showed many bubbles throughout the entire length of the liquid column "immediately" after the arrival of the initial (acoustic) expansion wave. An "acceleration front" several centimeters thick then propagated into the bubbly liquid at a nearly constant average speed, which ranged from 1→2 m/s for the conditions tried. This wavefront fragmented the bubbly mixture into an aerosol. Friz estimated the wave speed using jump conditions and assuming equilibrium upstream and downstream states. The calculated results were within 50% of the measured values. Results similar to those of Friz were reported briefly by Le Gonidec *et al.* (1967).

Thompson *et al.* (1987) conducted experiments in a similar apparatus, but used a highly retrograde fluorocarbon[5] (C_6F_{14}) at near-critical temperatures. The liquid was initially in equilibrium under its own vapor pressure at temperatures between 140 and 178 °C (the latter value is the critical temperature). The liquid was rapidly depressurized by rupturing a diaphragm that initially sealed the test cell from an overlying evacuated reservoir. Evaporation waves were observed at temperatures above an approximate threshold value of 140 °C. For initial temperatures sufficiently close to the critical temperature, the first acoustic expansion wave initiated homogeneous nucleation, which in turn limited its amplitude. High-speed movies and pressure measurements showed that a relatively slow evaporation wave (4→27 m/s, depending on the initial temperature) then propagated into the nucleating liquid at an essentially constant velocity, producing a two-phase flow downstream. At lower temperatures the

5. A *retrograde* fluid is one for which an equilibrium mixture tends to evaporate upon adiabatic expansion. Conversely, a *normal* fluid is one for which an equilibrium mixture tends to condense upon adiabatic expansion. Retrograde liquids are characterized by high heat capacities. For a detailed discussion of the properties of retrograde liquids, the reader is referred to Thompson *et al.* (1986).

evaporation wave initiated after one or more reflections of the acoustic wave. Thompson *et al.* computed the jump condition between the superheated upstream state (whose properties were assumed to be that of a pure liquid) and the downstream state (which was assumed to be an equilibrium mixture). This analysis suggested that the Chapman-Jouguet condition (sonic outflow in the reference frame of the wave) that arises in the theory of gasdynamic discontinuities (e.g., Hayes, 1958) is valid for evaporation waves.

1.3.2. *Waves with Pure Upstream Liquid.* Evaporation waves with pure upstream superheated liquid states were first observed by Grolmes and Fauske (1970, 1974) in an apparatus similar to those used in the above experiments; however, steps were taken to prevent *any* nucleation from occurring within the liquid column. Three liquids—Refrigerant 11, methyl alcohol, and (degassed) water—were tried. Evaporation waves were observed in all the liquids when the superheat exceeded a threshold value that depended on the liquid and the test-cell diameter. Below the threshold, the free surface remained quiescent, and receded at a rate several orders of magnitude slower. High-speed motion pictures showed that the waves proceeded at a constant average velocity, which ranged between 0.32 and 0.48 m/s for the liquids and conditions used.

Similar behavior was observed on a small scale by Shepherd and Sturtevant (1982) and by Frost and Sturtevant (1986). In those experiments, a *bubble column* was used to heat millimeter-scale hydrocarbon droplets to the superheat limit, whereupon, a single vapor bubble nucleated near the droplet boundary. Evaporation then propagated across the drop. For lower superheats the evaporating surface remained smooth and the evaporation was relatively slow—basically consistent with classical bubble-growth theory. For higher superheats the surface appeared rough and generated a jet of aerosol, and evaporation was explosive. Estimates of wave speed, though approximate, gave values of order 10 m/s. Shepherd considered several interfacial instabilities that could lead to the observed behavior, and suggested the *Landau instability* (in which the mass flux of the departing vapor causes distortion of the evaporating interface) as a likely mechanism for explosive boiling at the superheat limit.

Experiments similar to those of Grolmes and Fauske were performed by Das *et al.* (1987) using both distilled water and tap water. Their reported wave speeds range from about 0.2→4.5 m/s. Das *et al.*'s wave speeds for tap water agree basically with Grolmes and Fauske's data for water at the same superheat temperature. Curiously, Das *et al.*'s wave speeds for distilled water

are significantly greater for the same superheat. Their interpretation was that impurities in the tap water impeded evaporation. The qualitative behavior reported was rather different from that of Grolmes and Fauske. The "boiling front" seen by Das *et al.* was not associated with liquid fragmentation, but was a rather poorly defined transition zone between pure liquid upstream and bubbly liquid downstream. Das *et al.* suggested that the means of propagation was convection of bubbles upstream by eddies.

1.3.3. *Summary.* Evaporation waves have been observed in a variety of liquids. So far, water is the only liquid in which waves with both pure and bubbly upstream liquids have been reported. Experiments have indicated that evaporation waves travel at constant average velocity and are not dispersive. The measured wave speeds have generally been of order 1 m/s—much less than the acoustic speed in the upstream state. With the exception of Das *et al.* (1987), the wavefront is observed to be a region in which fragmentation occurs, and the downstream flow is a two-phase spray.[6] For any given liquid and temperature, there appears to be a threshold of superheat below which waves do not occur.

1.4. Outline of Present Work.

The present work is an experimental study of evaporation waves with pure upstream liquid states. Its primary purpose is to learn about the mechanisms of the explosive boiling process and the properties of the flow it produces. To this end, there is a strong emphasis on flow visualization. The test liquid is superheated by rapid depressurization in a facility similar to those used by previous experimenters. This facility and the experimental methods used are discussed in Chapter 2.

An overview of the general behavior is presented in Chapter 3. A detailed presentation of experimental observations follows in Chapter 4 (which describes the fully developed or "quasi-steady" regime) and in Chapter 5 (which describes start-up behavior). Observations of flows with bubble nucleation within the liquid column are discussed in Appendix C. The majority of

6. Complete evaporation is expected for liquids of sufficient molecular weight, for the proper initial and downstream conditions (Shepherd *et al.*, 1989).

the experimental observations discussed in Chapters 4 and 5 are obtained from high-speed motion pictures. Several of the best motion pictures have been assembled into an 18-minute video program, which is intended to supplement this thesis. Appendix A is a guide to the video program, and provides ordering information.

Chapter 6 presents a discussion of the qualitative physical mechanisms of wave propagation and flow generation on the basis of the observations presented in Chapters 4 and 5 and Appendix C. Chapter 7 takes an opposite approach to Chapter 6, treating the flow from a generic, global viewpoint: Jump conditions are applied to arrive at approximate, analytic expressions for average wave properties.

Chapter 2

Experimental Methods

2.1. Apparatus.

The experimental facility is shown schematically in Figure 2.1, and pictorially in Figure 2.2. It consists of a vertically oriented Pyrex glass test cell mounted beneath a large, low-pressure reservoir. The test cell is sealed by an aluminum foil diaphragm, which is ruptured by pneumatically driven knife blades to initiate the experiment. The primary test cell used, shown in Figure 2.1, is a section of glass pipe surrounded by a liquid-filled jacket with flat windows. The liquid jacket serves two purposes: to provide temperature control (by circulating the jacket liquid through a heat exchanger), and to cancel the cylindrical lens effect of the test liquid (by choosing a jacket liquid with refractive index similar to that of the test liquid).

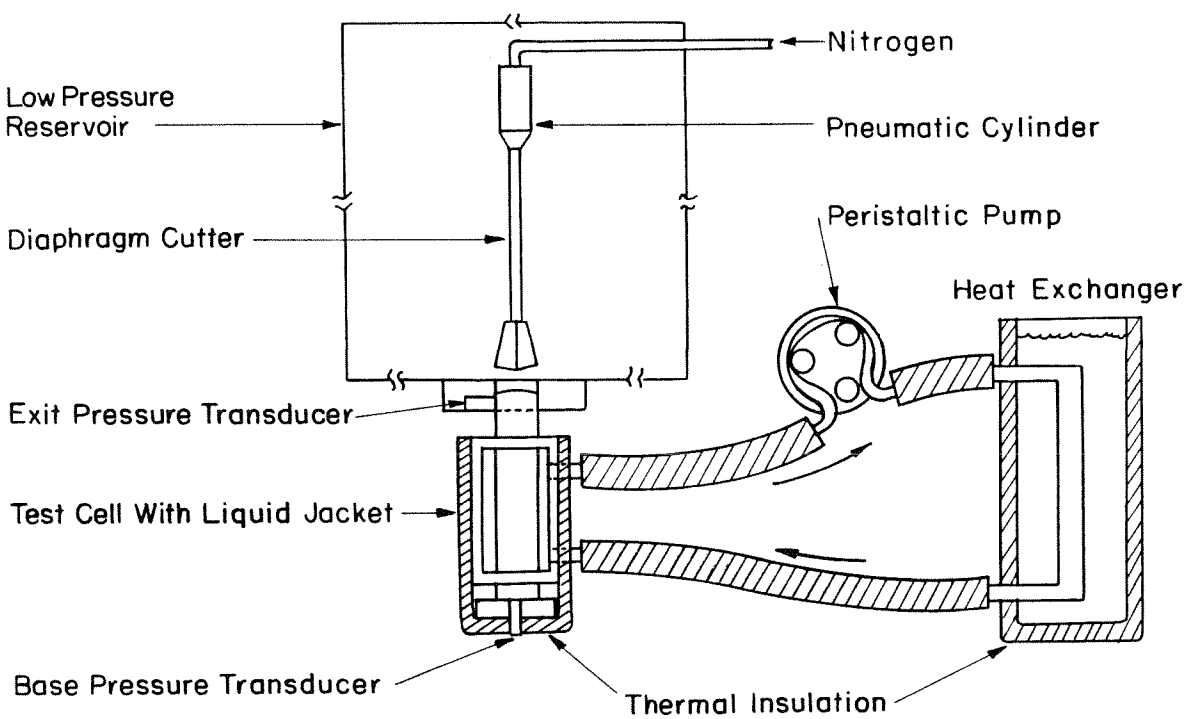

Figure 2.1: Schematic of evaporation wave facility.

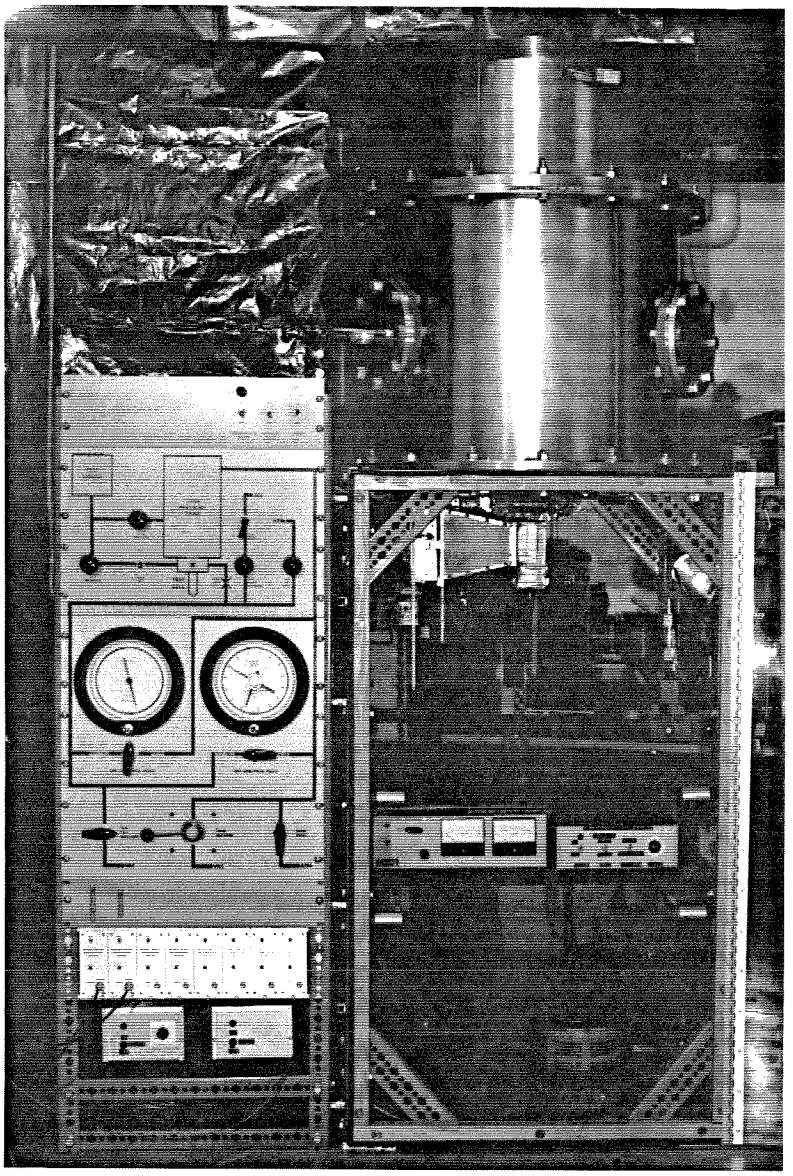

Figure 2.2: Photograph of evaporation wave facility.

2.1.1. *Basic Facility.* The basic facility consists of the large, low-pressure reservoir into which the test liquid is expelled, the *reservoir/test-cell interface* assembly, which fastens beneath it, and the control system located on an adjacent panel. The facility is surrounded by a black plastic "tent" by which it may be darkened for photography.

The low-pressure reservoir is composed of two cylindrical sections; each is constructed of 1/8-inch-thick rolled stainless steel with 3/4-inch-thick stainless steel flanges. The end plates are 3/4-inch-thick aluminum. The reservoir is 2 feet in diameter and 3 feet in length, with a

volume of 9.4 cubic feet. It is supported 4 feet off the floor by a slotted-angle structure, a height that puts the test cell at eye level when the operator is seated. The reservoir may be set at any pressure between vacuum and 4 bar absolute by air or another gas.

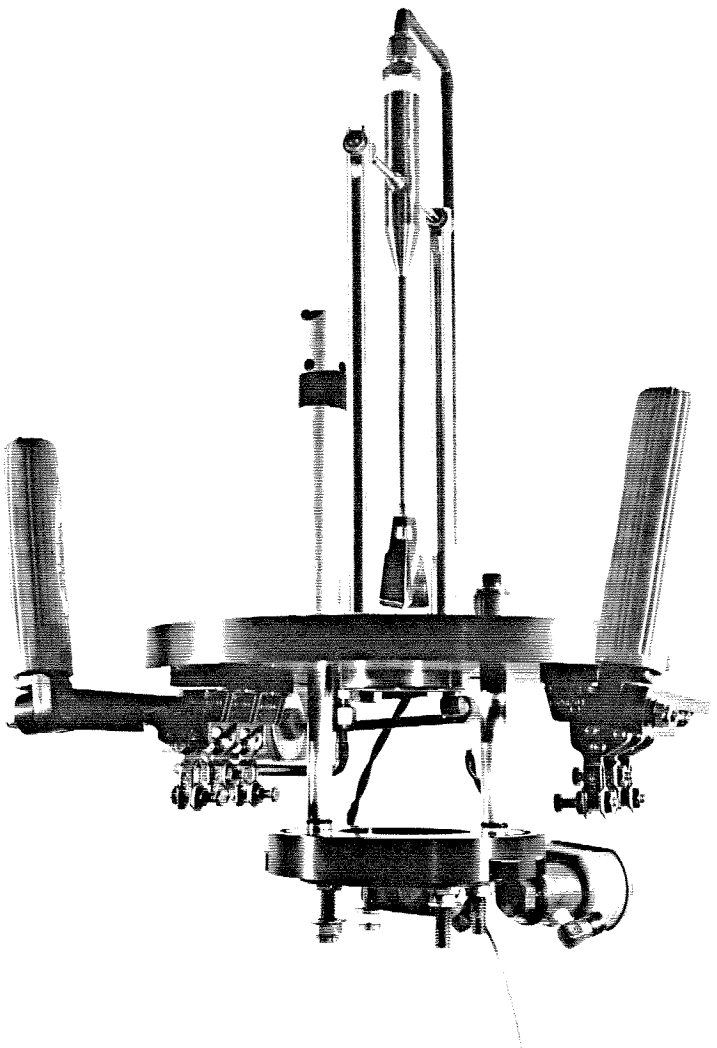

Figure 2.3: Photograph of reservoir/test-cell interface, free standing.

The reservoir/test-cell interface is pictured in Figure 2.3 (free standing) and in Figure 2.4 (mounted with test cell attached). Its main body is the 10-inch-diameter, 3/4-inch-thick aluminum *reservoir adaptor plate*, which bolts and seals to the bottom of the low-pressure reservoir. The diaphragm is sealed by O-rings between the reservoir adaptor plate and the

smaller 5-1/4-inch-diameter *test-cell adaptor plate* below it. The two plates are joined via two sliding stainless steel shafts, which allow the test-cell adaptor plate to drop down for diaphragm insertion. Two sets of clamps attached to the bottom of the reservoir adaptor plate force the plates together to seal the diaphragm. The test cell bolts to the bottom of the test-cell adaptor plate and is sealed to it by a rubber gasket.

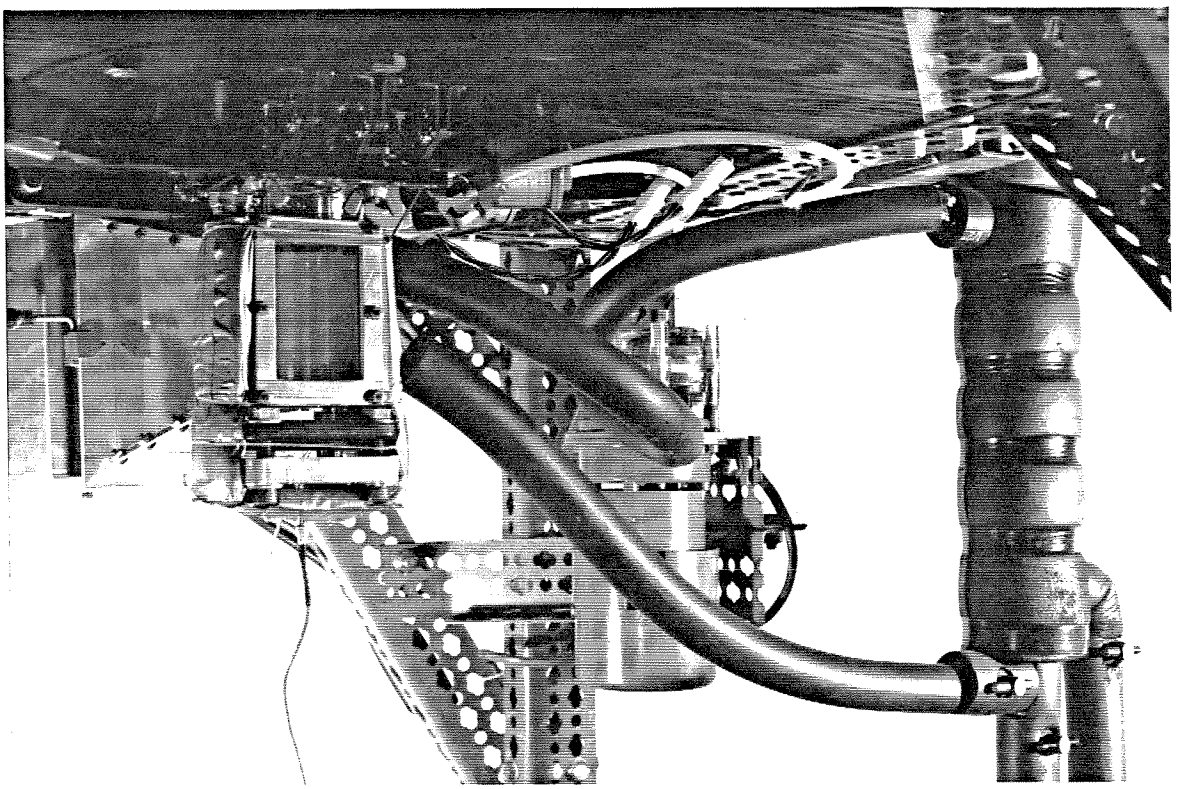

Figure 2.4: Photograph of test cell, reservoir/test-cell interface, and circulation system.

The diaphragm cutter is mounted on the top (i.e., reservoir) side of the reservoir adaptor plate, as shown in Figure 2.1 and Figure 2.3. It consists of crossed knife blades mounted on a stainless steel rod. This "spear" is driven into the diaphragm by a pneumatic cylinder, which delivers 50 lbs of force for 100 msec through a stroke of 1-1/4 inch. The pneumatic cylinder is energized with 150 psi nitrogen through a 3-way solenoid valve. A return spring resets the cutter when the cylinder is de-energized. The knife blade assembly is pointed in the center so that the diaphragm breaks from the inside out, but the taper angle is kept sufficiently small (5°)

so that the rupture time is not limited by the speed of knife-blade penetration.

The diaphragm material is 1100-O soft aluminum; thicknesses between 2 and 4 mil are used depending on the initial pressure difference between test cell and reservoir. A diaphragm of given thickness works dependably over a finite range of pressure differences. The upper limit of the operating range is determined by spontaneous rupture; the lower limit is due to the fact that the diaphragm stiffness decreases as the pressure difference is decreased. For a sufficiently small pressure difference, the diaphragm "caves in" rather than cuts. The delay between activation of the diaphragm cutter solenoid valve and the initiation of diaphragm rupture is about 30 ms; the rupture process is accomplished in about 1 msec.

The controls and plumbing for the facility are shown schematically in Figure 2.5. The test cell is accessed by two lines that enter through the test-cell adaptor plate: the *test fluid fill line*, which connects to the test fluid supply reservoir, and the *general access line*, which connects to the rest of the control system. Both lines are sealed at the test-cell adaptor plate by a solenoid valve, which prevents pressurized fluid from spraying into the test cell during an experiment. The fluid-fill solenoid valve is normally closed, except when filling. The general-access solenoid valve is normally open to allow the pressure to be monitored, but closes for 2 seconds (which exceeds the longest run time) upon activation of the diaphragm-cutter solenoid valve. The test cell and low-pressure reservoir may be evacuated or vented to atmosphere independently, but they share the two Heise 6-inch, Bourdon-tube pressure gauges (accurate to 0.1% full scale), which are selected by one or the other unit via three-way ball valves. One gauge covers the range 0 to 15 psia, the other 0 to 300 psia.

2.1.2. *Test Cells.* As mentioned in Section 1.2.1, care is required to prevent heterogeneous nucleation within the liquid column. In particular, the test-cell walls must be made very smooth. Glass has been found to be an excellent material for this purpose (Reid, 1976). It is also a good choice for this experiment because it is transparent and chemically inert. Two test cells are used, both of which are constructed from 1-inch inner-diameter Pyrex "conical-system" glass tubing. This trade name refers to the fact that the tube ends are conically flared to fit accompanying flanges. The nominal wall thickness is 5/32-inch; the factory rated pressure is 100 psig. This pressure rating is quite conservative and allows for severe temperature shock.

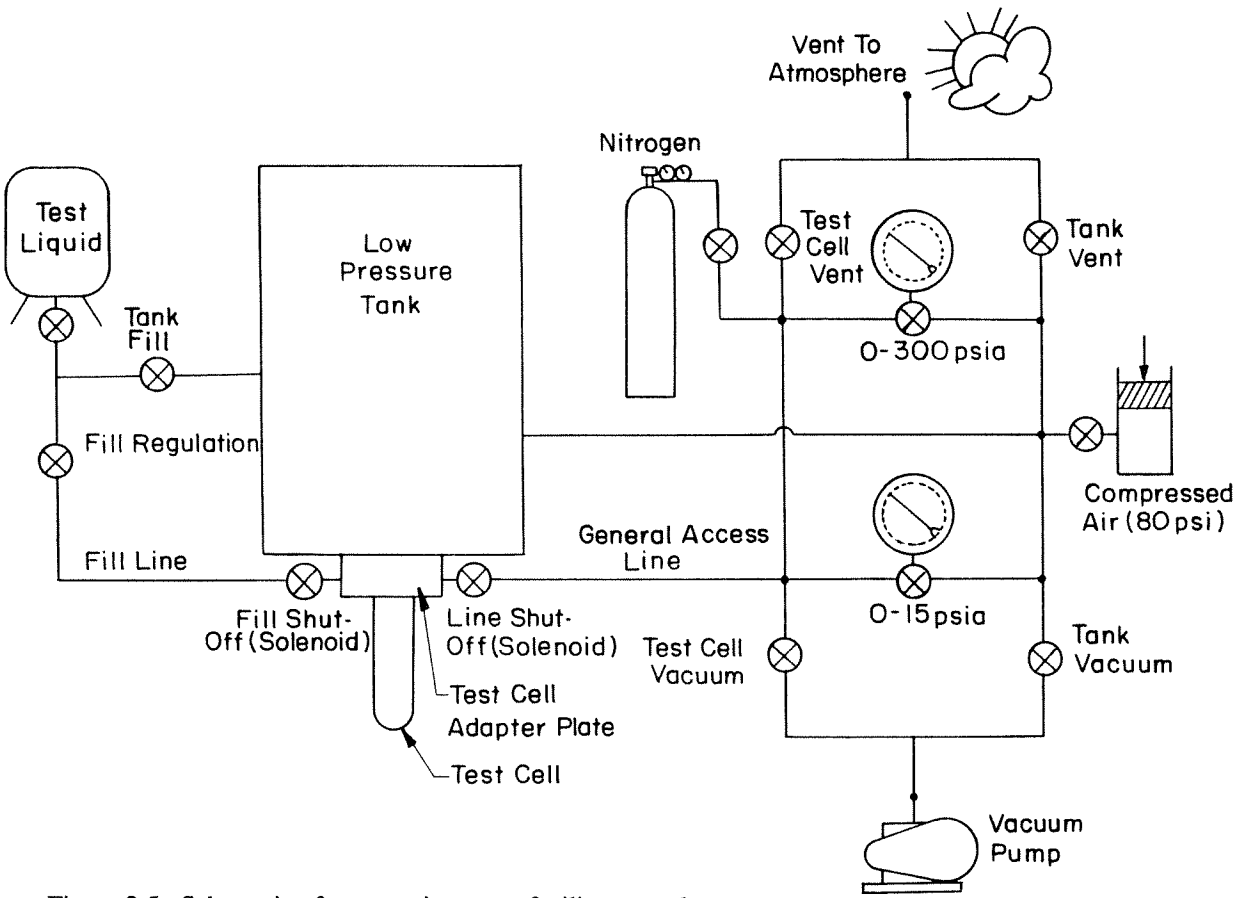

Figure 2.5: Schematic of evaporation wave facility control system.

Both test cells were hydro-tested to 200 psig.

The two test cells are shown in Figure 2.6. Test cell (1) is a 10-inch long "test tube." This configuration is best for nucleation suppression since only smooth glass walls contact the liquid column; however, it has two disadvantages. First, the pressure cannot be measured within the liquid, and second, the cylinder of liquid and curvature of the walls cause optical distortion of the interior features. A second test cell was designed to overcome these difficulties.

Test cell (2) is a 6-inch section of Pyrex pipe surrounded by a liquid-filled jacket having windows on two sides, through which the test cell is lighted and photographed. The liquid jacket removes the optical distortion caused by the cylindrical lens of the liquid column, and controls the test liquid temperature by circulating the jacket liquid through a heat exchanger.

Optical distortion was minimized by choosing a jacket liquid with similar refractive index as the test liquid. The refractive index of the refrigerant test liquids is 1.29. The jacket liquid is methyl alcohol with refractive index 1.33. This method does not eliminate distortion that is due

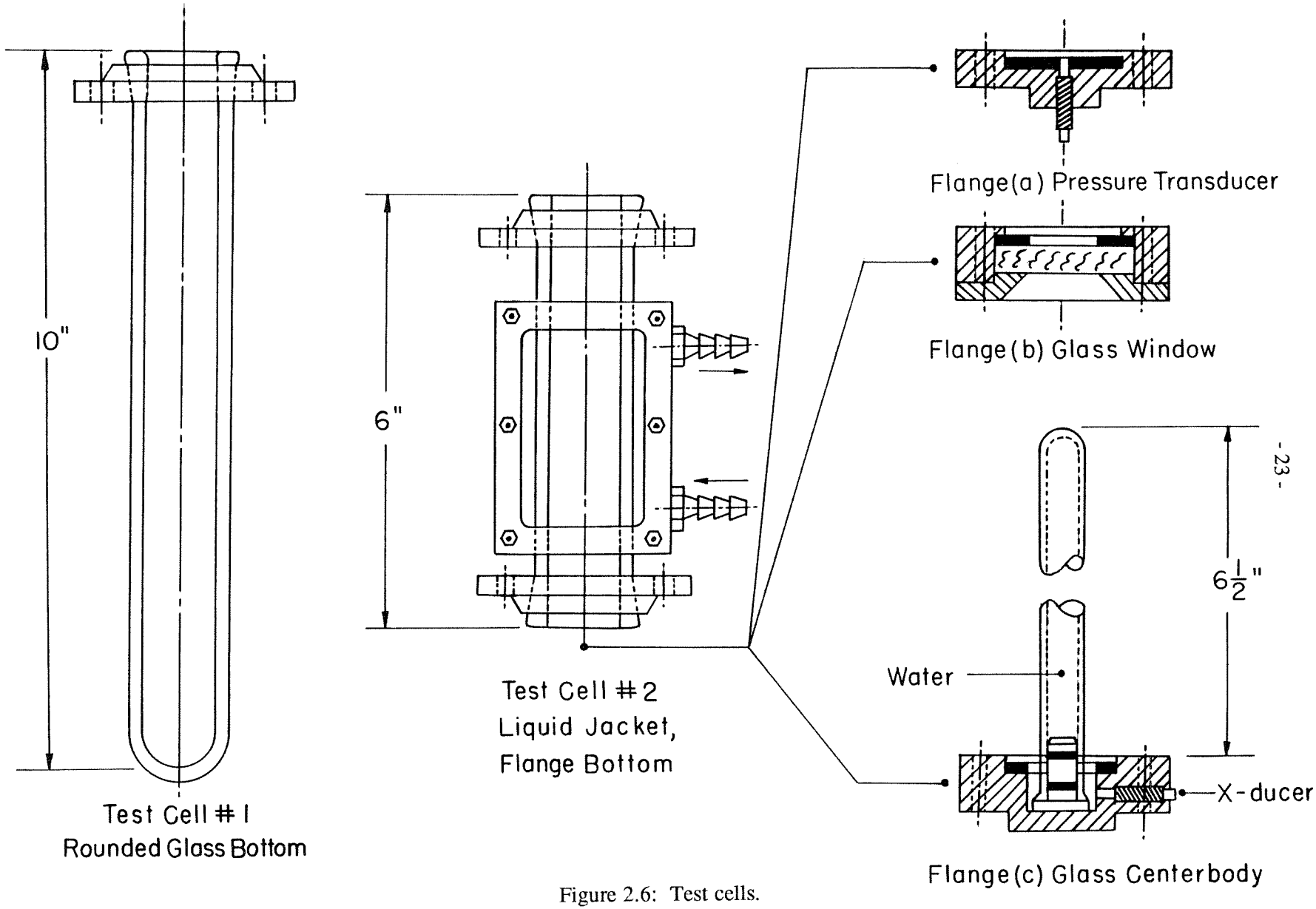

Figure 2.6: Test cells.

to the curvature of the glass walls because the refractive index of Pyrex (1.47) is different from that of the two liquids; however, the latter distortion is slight and significantly less than it is with air inside and out. Although the liquid jacket solution is optimized for viewing wavefront features seen through the test liquid, features in the two-phase flow region do not appear to be greatly affected.

The bottom of test cell (2) is sealed by one of three aluminum flanges via a neoprene rubber gasket. Flange (a) contains a pressure transducer; flange (b) contains an optical window for bottom views; flange (c) holds one of four glass centerbodies used to create annular flow configurations, and also contains a pressure transducer. The centerbodies are water-filled Pyrex test tubes sealed on the open end by an aluminum mandrel with two O-rings. The mandrel screws onto flange (c). The refractive index of the water (1.33) is close to that of the test liquids so that the lighting remains uniform. The centerbodies run the entire length of the test cell. The gap widths are 1.75, 2.75, 3.75, and 4.75 mm. Each of the three flanges has to be isolated from the superheated test liquid to prevent nucleation from joints and rough surfaces. This procedure is described in Section 2.4.1.

2.1.3. *Temperature-Control System.* In all runs reported in the body of this thesis, the temperature is set to 20°C.[1] When test cell (1) is used, the liquid temperature is set by immersing the test tube in a Dewar flask filled with water at 20° C. The flask is removed just prior to the run. The temperature-control system for test cell (2) is shown in Figures 2.1 and 2.4. In this case, the liquid temperature is controlled by circulating the jacket liquid (methyl alcohol) through the heat exchanger. The heat exchanger temperature is in turn maintained via a 20°C water bath. The circulating pump is a Cole-Parmer model 7017 peristaltic pump. The heat exchanger, test cell, and connecting Tygon hoses are insulated with Armaflex thermal insulation.

---

1. In preliminary runs, one of which is discussed in Appendix C, the temperature is the ambient value.

The liquid temperature is inferred from the vapor pressure. Since the latter is determined by the temperature at the liquid free surface, the test cell must be heated slowly to ensure that the temperature at the surface is the same as that of the entire liquid column. A temperature survey was made using an Omega Engineering RTD probe to check the temperature uniformity in the test cell. The probe was inserted through a Cajon "Ultra Torr" fitting in flange (c), which allowed it to be moved axially. It was found that the temperature in the jacketed region is uniform to 0.2°C.

2.2. Instrumentation.

2.2.1. *Pressure Measurement.* The experimental setup for high-speed pressure measurements is shown in Figure 2.7. The pressure is measured at the base and exit of the test cell using PCB model 113A26 piezoelectric transducers, chosen for their fast time response and compatibility with liquids. The transducer outputs are amplified by H-Tech Laboratories Model RCVR/XMTR-01 amplifiers.[2] The amplified pressure signals are recorded on a Nicolet 4094B digital oscilloscope, which is triggered by the expansion wave initiated by diaphragm burst. The properties of the transducers, amplifiers, and oscilloscope are listed in Table 2.1.

Piezoelectric transducers are *dynamic*, meaning that their response to a step change in pressure decays to zero. The rate of decay is approximately exponential, and is characterized by the *discharge time constant.* For the transducers used in this study, the nominal discharge time constant is about 25 sec. Piezoelectric transducers are also *pyroelectric*, meaning that their pressure sensitivity changes with temperature. In the present experiments, the temperature at the test-cell exit drops by as much as 75°C (assuming that the flow is an equilibrium mixture). Consequently, the pyroelectric effect causes extreme errors unless the exit transducer is thermally shielded.

---

2. These units are low-noise, transducer amplifiers designed primarily for applications in which the transducer is remote from the measuring site. The author is indebted to Dr. Bruce Hartenbaum for his generous loan of this equipment.

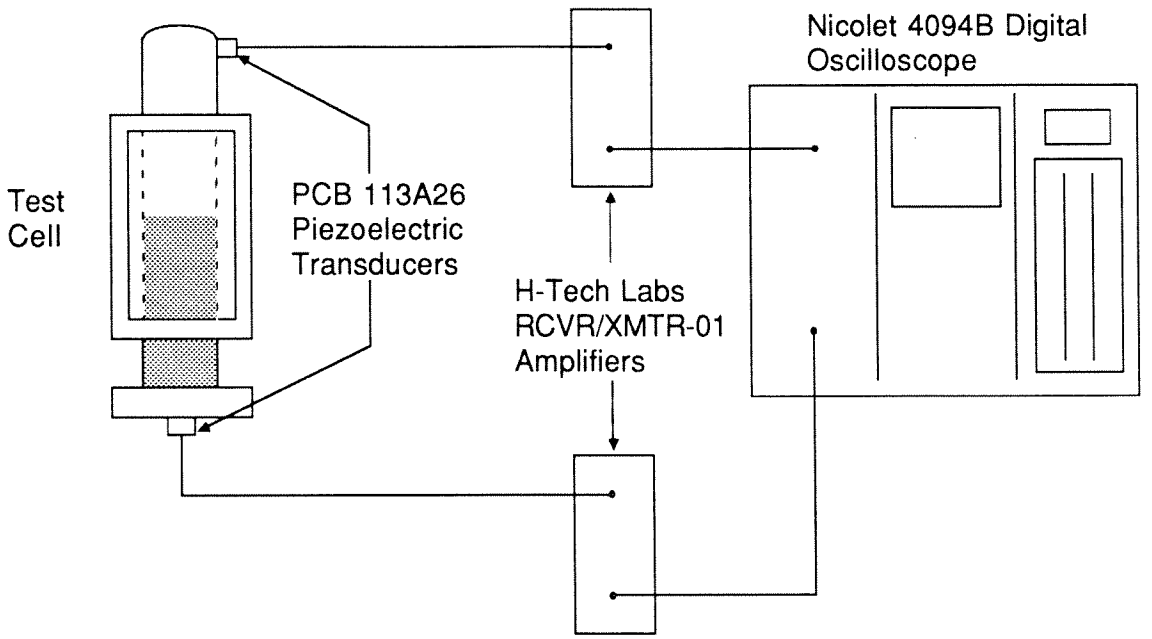

Figure 2.7: Experimental setup for pressure measurements.

Table 2.1. Specifications for Pressure Measurements

Property	Unit	Transducer	Amplifier	Oscilloscope
Manufacturer	n/a	PCB	H-Tech Labs	Nicolet
Model	n/a	113A26	RCVR/XMTR-01	4094B
Linearity	% F.S.	1	1	0.1
Bandwidth	kHz	250	143	400
Signal to Noise Ratio	dB	72	60	72
Time Constant	sec	25	100	D.C. coupled

To insulate the exit transducer, a 1/8-inch-thick plug of neoprene rubber is cemented to the face of the transducer with RTV silicone rubber. The exit transducer is mounted in the test-cell adaptor plate, with the rubber plug flush with the wall of the test cell (Figure 2.8). A Teflon collar was added in later runs to thermally insulate the region of the test-cell adaptor plate in which the transducer is mounted. Nitrogen depressurization tests were performed to compare the properties of the bare and insulated transducer. The change in dynamic response was observed to be negligible at the frequencies of interest. Thermal shielding is much less important for the base transducer because it experiences no cooling until the end of the run. The pressure transducers were calibrated for each run using the well-defined initial (test cell vapor) and final (reservoir) pressures.

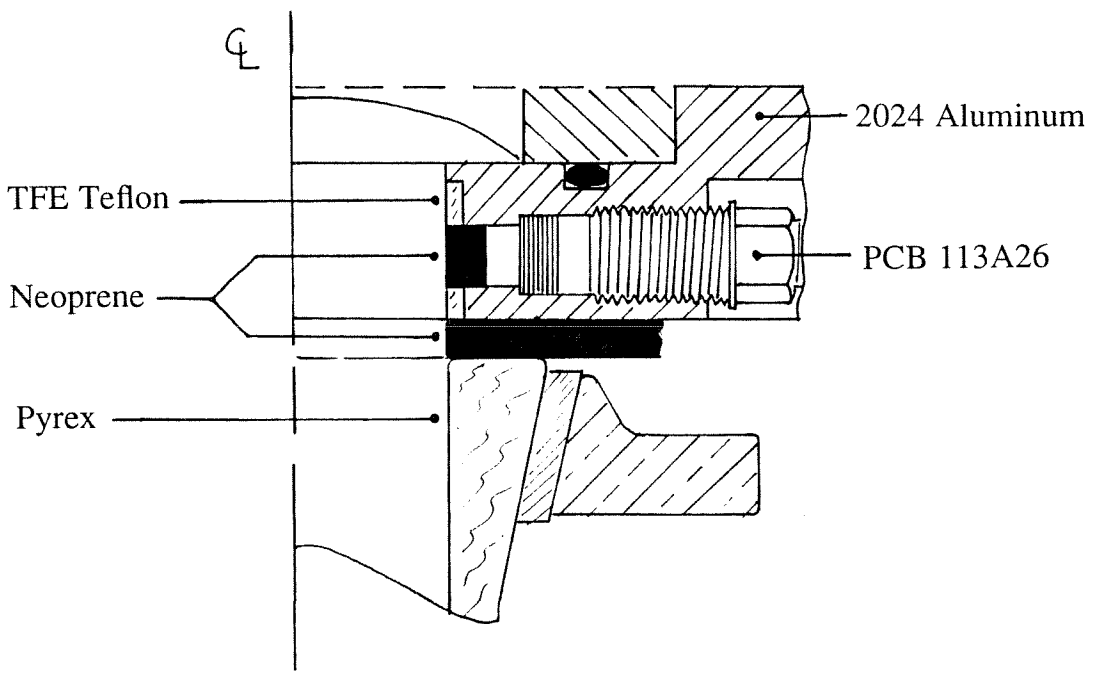

Figure 2.8: Mounting and thermal insulation of exit pressure transducer.

2.2.2. *High-Speed Motion Pictures.* The experimental set-up for high-speed motion picture experiments is shown schematically in Figure 2.9. The motion pictures are taken with a Hycam II high-speed 16mm camera, manufactured by Redlake Corporation. This camera has an "event trigger" relay that closes when the film has been accelerated to the set framing rate. This switch is used to trigger the diaphragm-cutter solenoid valve. The motion pictures are related to the

pressure traces through a circuit that marks the edge of the film using the camera's *auxiliary timing light* when the oscilloscope triggers. Figure 2.9 indicates the sequence of events. The photoflood lamp is turned on first, followed by the camera when the lamp has reached full intensity (about 1 second). The camera initiates the experiment after a preset length of film has elapsed.

The Hycam II is a high-speed, *rotating prism camera*, in which the images are translated with the moving film by a multifaceted rotating prism. The Hycam can achieve a framing rate of 11,000 fr/sec with a 400-foot film roll, but the entire roll is used in accelerating to this speed. The Hycam regulates the framing rate if the desired value is attained before the end of the film; however, precise values of the framing rate are determined from *timing light* marks on the edge of the film. In this experiment, 100-foot film rolls and framing rates between 4000 and 6000 fr/sec are used. The framing rate for a particular experiment is dictated by the run time; for example, a set framing rate of 6000 fr/sec is achieved with about 200 msec and 30 ft of film remaining. The exposure time is the reciprocal of the framing rate divided by 2.5. For a framing rate of 6000 fr/sec, the exposure time is 67 μsec.

Kodak 7222 negative film (ASA 200) is used almost exclusively. Typically, the side views are processed normally and the other views are pushed two stops. Kodak 7302 print stock is used for all views except the bottom, in which case Kodak 7362 high contrast stock is used to compensate for the inherently flat subject matter. The resolving power of 7222 film is 100 lines/mm at a contrast ratio of 1000:1. This value, together with an image magnification of 0.15 (side view) dictate that the maximum spatial resolution in the object plane (neglecting limitations in the optical system) is of order 100 μm.

The primary illumination for high-speed motion pictures is a single 1000-watt type-FCM photoflood lamp, in a Berkey Colortran model 104-051 fixture. The light intensity is increased a factor of 2.5 by boosting the lamp voltage to 160 V. Since this procedure decreases the lamp life significantly, a power-booster/timer box was constructed so that the lamp could be used at the highest possible voltage. The properties of photoflood lamps operating at voltages above and below their rated value are given by Thomas (1973).

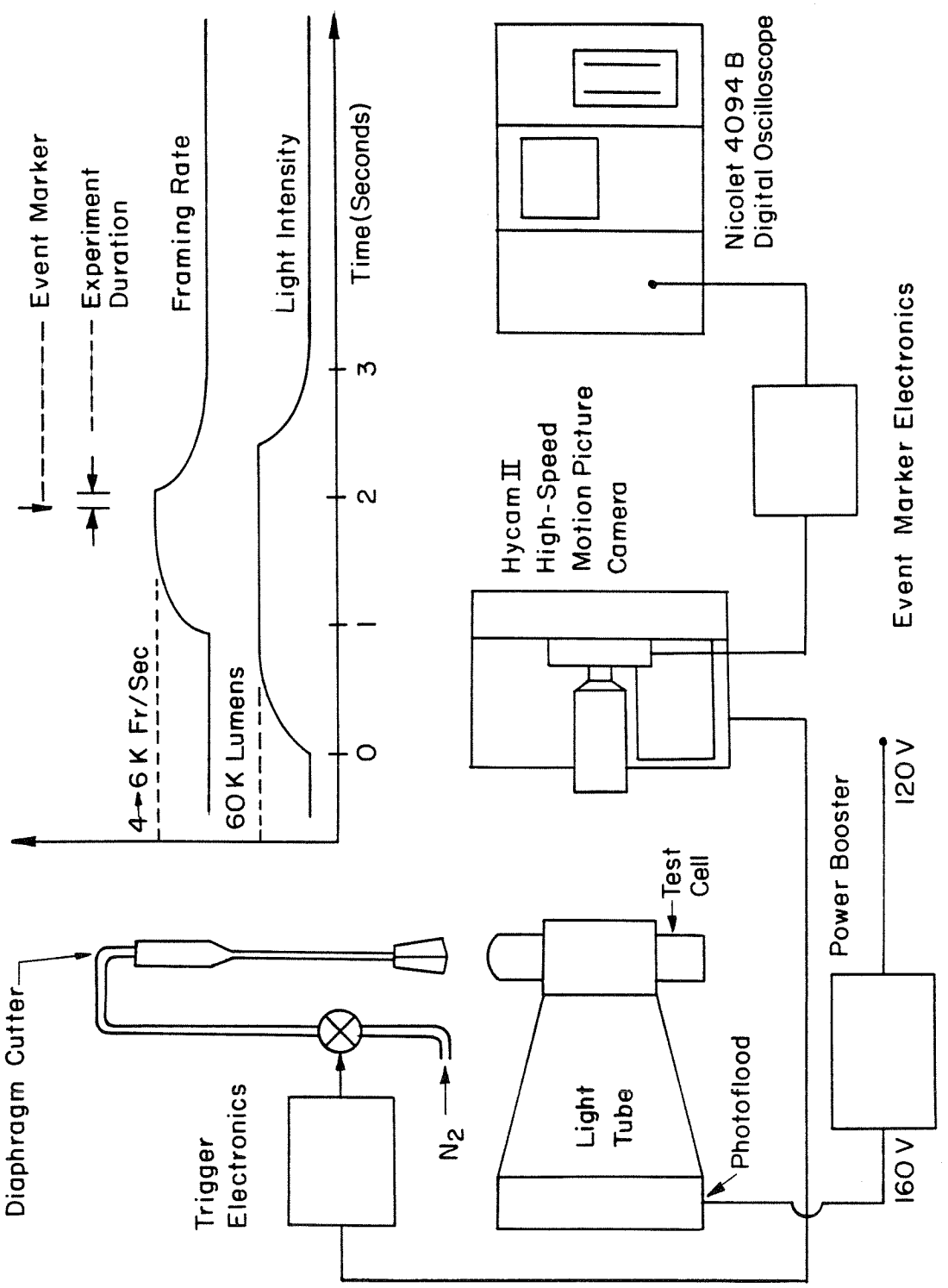

Figure 2.9: Experimental setup for high-speed motion picture runs.

The test cell is lit from behind. The light is concentrated on it by an approximately 86% reflecting polished aluminum light tube that fits to the rear window frame of the liquid jacket of test cell (2). The light tube is fitted with an infrared filter to decrease heat absorption in the liquid. Light is diffused as it enters the test cell by using a ground-glass rear window for the test-cell liquid jacket.

Four different views are used for high-speed motion pictures: side, oblique bottom (looking up at a 45° angle), oblique top (looking down at a 45° angle), and bottom. The photographic configuration of each view is shown in Figure 2.10. In all views the camera is mounted sideways in order to align the long side of the frame with the test cell axis. Mirrors are used for the oblique and bottom views rather than tilting the camera. For side and oblique views a single photoflood was used to back-light the test cell. The top oblique views required a special lighting configuration to avoid total internal reflection from the liquid surface. In this view, the test cell is immersed in a bath of water, which has a light-diffusing bottom. The photoflood shines through the bottom of the bath at a 45° angle. In the bottom views, a second photoflood is used to light the test cell from the front side of the liquid jacket. Additionally, an Ealing model 27-1031 100-watt mercury arc lamp is used to light the test cell from the bottom. The light from the arc lamp is collimated and split into two beams (to obtain more symmetrical lighting), which then enter the test cell through the bottom window at about 5° on either side of the optical axis. This angle is sufficient so that the Fresnel reflection of the beam from the glass window does not enter the camera.

The side views are taken at f-number 5.6 using a Tamron macro zoom lens (f = 28-80 mm). The other views are taken at f-number 11 using an Olympus Telephoto zoom lens (f = 85-250 mm).

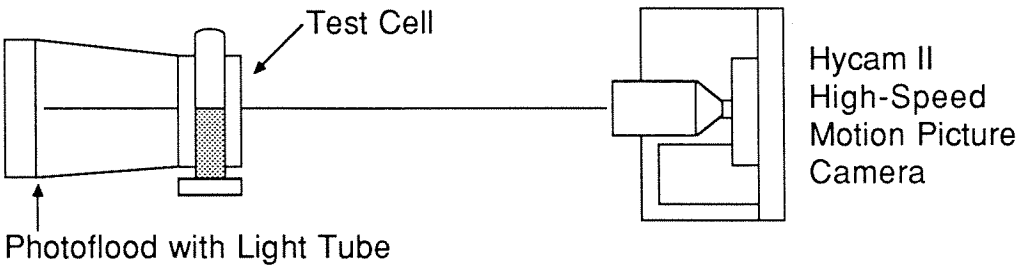

a) Side View

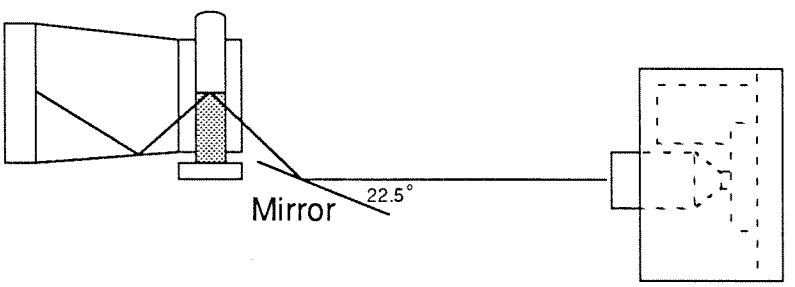

b) Oblique bottom view (45°)

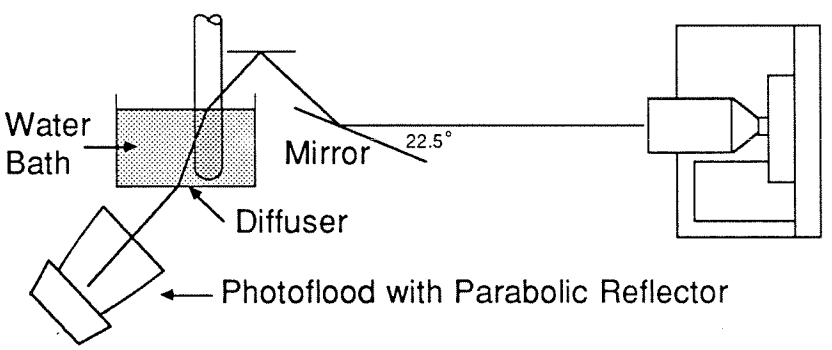

c) Oblique top view (45°)

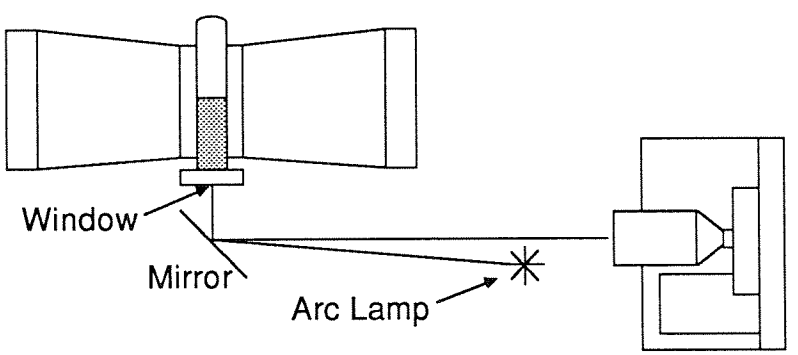

d) Bottom view

Figure 2.10: Photographic configurations for high-speed motion picture experiments.

2.2.3. *Still Photography.* The nominal setup for still photography is illustrated schematically in Figure 2.11. Side and bottom views are taken simultaneously using two Nikon FE2 35mm cameras. Two spark flash units are used to light the flow: one from the back and one from the bottom. An Intel 8085 microprocessor with a three-channel Intel 8254 "programmable interval timer chip" was used to control the experiment. A 1 mW HeNe laser shines through the test cell at an angle mutually orthogonal to the two optical axes and falls upon a photodiode on the opposite side. When the evaporation wavefront passes through the laser beam, the light is scattered, and the intensity measured by the photodiode is greatly attenuated. This information allows the flash units to be triggered when the wavefront is in precisely the desired location. This method is particularly valuable in capturing the start-up behavior, which, because of delay variations from run to run, requires a direct method of sensing the onset of explosive boiling.

The sequence of events in a still photograph experiment is as follows: With the apparatus darkened, the microprocessor is manually triggered. The motor drives are activated and the camera shutters are opened for 1/2 sec. (The motor drives must be given a head start because they are relatively slow.) After a delay of 1/4 sec from the original trigger, the microprocessor sends a signal to energize the diaphragm-cutter solenoid valve, which initiates the experiment. The laser beam is "broken" when the wave passes through it, causing a drop in photodiode voltage. When the photodiode voltage falls below a specifiable threshold, a trigger circuit sends a pulse to the microprocessor. Following a specifiable delay, the microprocessor simultaneously triggers both flash units. The flash trigger pulse is recorded on the oscilloscope along with the exit pressure trace.

The spark flash units and power supplies are a previous Caltech design incorporating 10kV, 0.1μf annular capacitors. The flash unit used for the side view is a line source. This unit can be filled with a chosen gas to control the spark characteristics. In the present experiments, an atmospheric pressure mixture of 90% argon and 10% air (by mass) is used at a voltage of 10kV. The spark unit used for the bottom view is a point source; it is air-filled and is operated at 7.5 kV. The spark durations are of order 1 μsec.

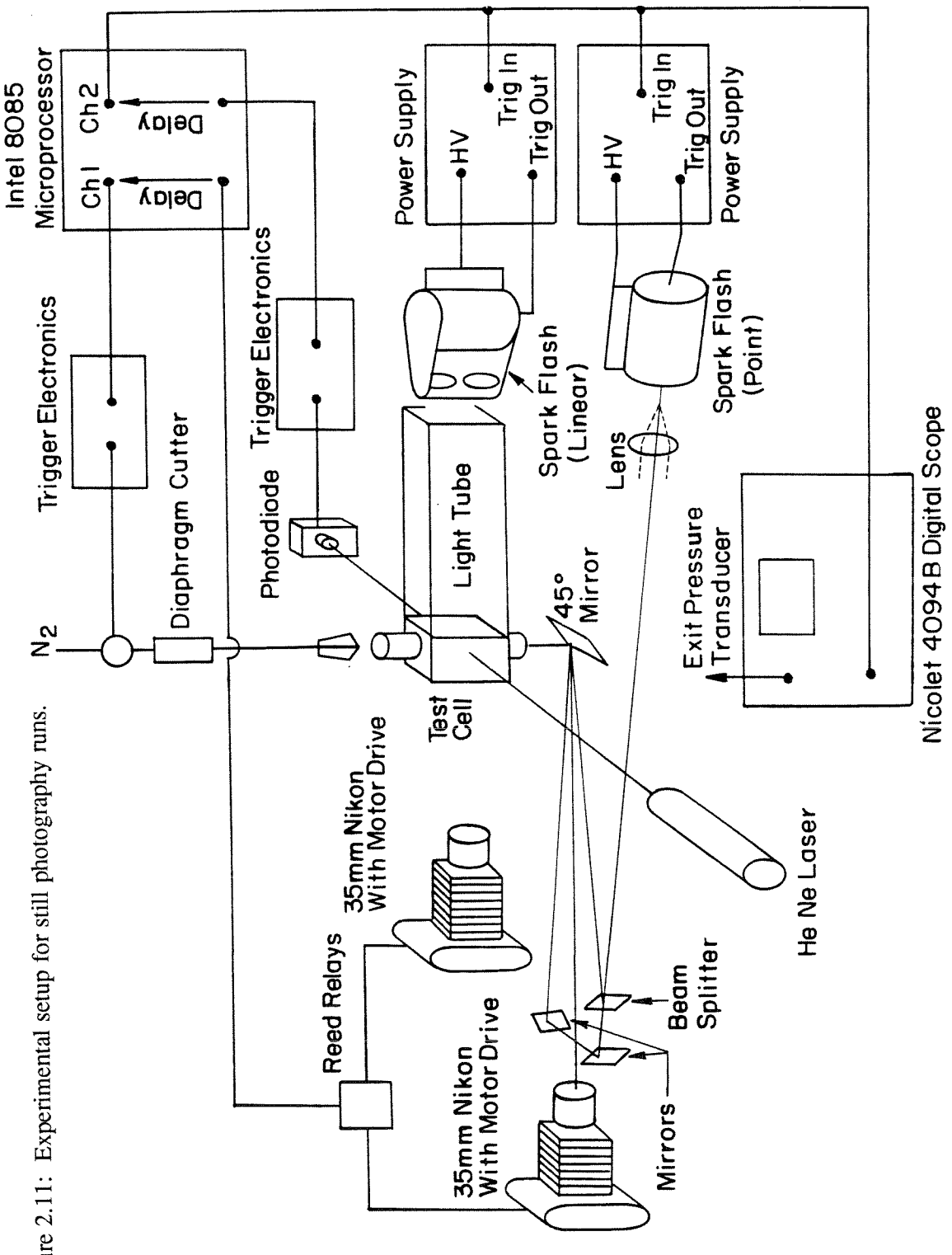

Figure 2.11: Experimental setup for still photography runs.

The side view spark unit is coupled to the test cell via a light tube, which collects and diffuses the light. As in the motion picture views, the light is further diffused by using ground glass as the rear window of the test-cell liquid jacket. The bottom view spark unit is collimated, split into two beams, and brought into the test cell through the bottom window at an angle of about 5 degrees on either side of the optical axis, in a manner very similar to the arc lamp in motion picture runs.

The film used for still photographs is Kodak Tmax (ASA's 400 and 3200). The resolving power of Tmax 400 is 125 lines/mm at a contrast ratio of 1000:1. The magnification used is 0.53 (side view), which limits the spatial resolution to order 10 microns in the object plane. The side and oblique views are taken using a Nikon 105 mm micro lens; the bottom view is taken using a Nikon 135 mm lens with 2x teleconverter. The side views are shot at f/32; the other views are shot at f/22.

Three configurations are used for still photograph experiments, as shown in Figure 2.12. The first, which is used for observing wave propagation in the quasi-steady regime, employs side and bottom views taken simultaneously. The second configuration involves a side view of the two-phase flow only, using test cell (1). Photographing the two-phase flow only is desirable because the optimum exposure for it is much greater—about 4 f-stops—than for the complete flow. The third configuration, which is used for observing start-up behavior, employs 45° oblique bottom and bottom views taken simultaneously.

2.3. Experimental Conditions.

2.3.1. *Test Liquids.* The liquids used in this experiment are Refrigerants 12 and 114 (R12 and R114). Refrigerants in general are chosen for several reasons: They are sufficiently volatile to produce rapid evaporation with little or no heating; they are nonflammable, nontoxic, inexpensive, and are resistant to heterogeneous nucleation (Grolmes and Fauske, 1974). R12 and R114 in particular are chosen for their convenient vapor pressures, which at 20°C are 5.69 and 1.83 bar, respectively. Most of the physical properties of the two liquids are quite similar; however, they differ qualitatively in one respect: R12 is a *normal* liquid, while R114 is *retrograde* (cf. footnote, Section 1.3.1). The properties of R12 and R114 are listed in Table 2.2.

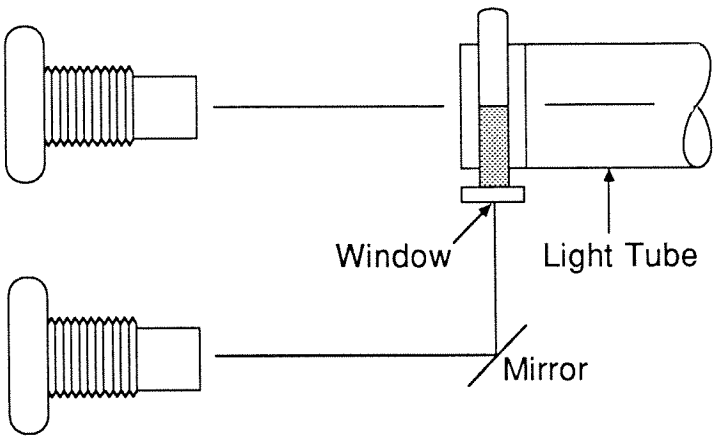

a) Quasi-steady propagation: wavefront region.

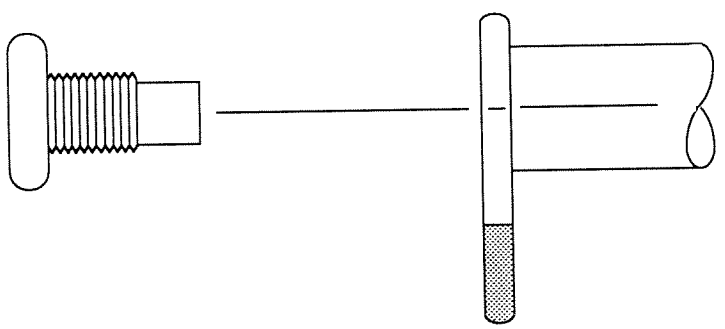

b) Quasi-steady propagation: two-phase region.

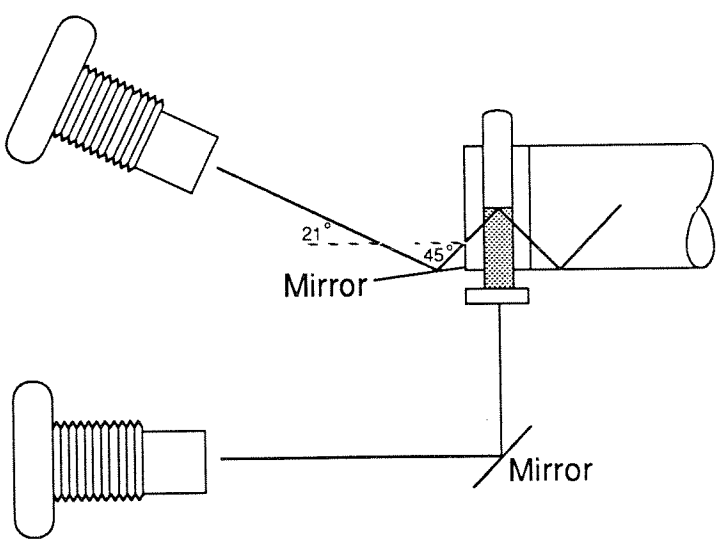

c) Start-up phase.

Figure 2.12: Photographic configurations for still photographs.

Table 2.2. Physical Properties of Refrigerants 12 and 114

Property	Unit	Refrigerant 12	Refrigerant 114
Chemical Formula	n/a	CCl_2F_2	$C_2Cl_2F_4$
Chemical Name	n/a	Dichlorodifluoro-methane	1,2-Dichlorotetra-fluoroethane
Molecular Weight[a]	None	120.914	170.922
$C_v(T_{cr})/11.2R$ (>1 = retrograde) [a,b]	None	0.789	1.472
Boiling Point @ 1 atm[a]	K	243.38	276.93
Vapor Pressure @ 25 C[a]	Bar	6.514	2.146
Critical Pressure[a]	Bar	41.159	32.675
Critical Temperature[a]	K	385.17	418.86
Critical Density[a]	kg/m^3	588.08	581.79
Latent Heat of Vaporization @ 25 C[a]	kJ/kg	138.04	128.38
Specific Heat Liquid @ 25 C[c]	J/kg-K	971	1020
Thermal Diffusivity @ 25 C[c]	$m^2/s \times 10^8$	5.51	4.35
Surface Tension @ 25 C[c]	$N/m \times 10^3$	9	12
Refractive Index of Liquid[c]	None	1.287	1.288

a) From Reynolds (1979)
b) For a discussion of this parameter see Thompson *et al.* (1986).
c) From DuPont Product Information Sheet G-1

2.3.2. *Summary of Run Conditions and Views.* The parameters varied in this study are the test liquid, tank pressure, and container geometry/cross-sectional area. The initial temperature is normally 20°C. Three pressures are studied for each liquid. For both liquids, the lowest pressure is essentially vacuum (actually, $P_{res} < 0.01$ bar). For both liquids, the highest pressure corresponds to an experimentally determined threshold value, which is discussed in the following chapters. The run conditions and views are summarized in Table 2.3. In each figure in the following chapters, the run number is given for reference purposes. The abbreviation "MPR" denotes "motion picture run"; likewise, "SPR" denotes "still picture run."

Table 2.3. Run Conditions and Views

Run Classifications	Views and Reservoir Pressures					
	Refrigerant 12; P_0 = 5.69 bar			Refrigerant 114; P_0 = 1.83 bar		
	0	1/2	1	0	1/3	1/2
Motion Picture Runs	S, OB, AS	S, OB, B	S, OB, B	S, OB, OT, B	S, OB, OT, B	S, B
Still Picture Runs (Wavefront Region during Quasi-Steady Propagation)	S, B, AS	—	S, B	S, B	—	S, B
Still Picture Runs (Two-Phase Flow Region during Quasi-Steady Propagation)	S	—	S	S	—	S
Still Picture Runs (Liquid Free-Surface during Start-Up Phase)	OB, B	—	OB, B	OB, B	—	—
Views: S=Side, AS=Annular Side, B=Bottom, OB=Oblique Bottom (45°), OT=Oblique Top (45°)						

2.4. Experimental Procedure.

2.4.1. *Nucleation Suppression.* The preferred method of isolating the bottom flange from the superheated test liquid would be to use a nonvolatile "buffer" liquid, which is both denser than, and immiscible with, the overlying test liquid. No liquid satisfying these criteria was found for the refrigerant test liquids; however, two adequate buffer materials were found: gelatin and Refrigerant 113.

The primary motivation for using gelatin is that it is water-based. Refrigerants, being hydrophobic, are not absorbed by it. It is also easy to remove, unlike other candidates such as pourable polyurethane. The hot liquid gelatin/water mixture is pipetted into the test cell one drop at a time—taking care not to introduce bubbles—and allowed to cure. Each gelatin layer is used for only one run.

The motivation for using R113 to suppress nucleation is that it is heavier and less volatile than the test refrigerants. Although R113 is miscible with R12 and R114, the diffusion layer

grows only about 1 centimeter in the test preparation time (convective mixing is avoided because of stable stratification). The boiling point of R113 is above room temperature, so it may be poured directly into the test cell before the latter is attached to the apparatus. The test cell is then filled with the test liquid in the manner to be described in the following section.

Each of the two above methods of nucleation suppression has its advantages. Using R113 is considerably easier and is superior in suppressing nucleation. However, the wave shutoff characteristics (i.e., when the test liquid runs out) are better defined when gelatin is used, because with R113 there is a diffusion layer. As will be discussed in Section 4.5.2, the shutoff condition is useful in inferring flow properties from the pressure traces. The nucleation resistance provided by gelatin is observed to be time-dependent—it is actually more effective in suppressing nucleation at *higher* superheats, because they are associated with shorter run times.

2.4.2. *Filling and Heating the Test Cell.* In preliminary runs, R12 was drained from the supply bottle into the test cell as liquid by hydrostatic pressure. The test liquid so obtained contained visible impurities, primarily small metallic particles. Although these did not tend to cause nucleation (they were evidently well "wetted"), it was not clear in what way they might affect the physics of the problem. For this reason, in subsequent runs the test fluid vapor is distilled directly within the test cell.

When test cell (1) is used, the test liquid is filled by surrounding the test tube with a Dewar flask filled with ice water, and by exposing the test cell to the test fluid vapor in the supply reservoir. When test cell (2) is used the procedure is the same, except that the test cell liquid jacket is used to cool the test cell. This is accomplished by filling the heat exchanger bath (Figures 2.1 and 2.4) with ice water, and running the circulation pump, while exposing the test cell to the test fluid vapor.

After the test liquid is filled to the desired level, it is sealed from the supply tank and heated to 20°C. When test cell (1) is used, the test cell is heated by surrounding the test tube with a Dewar flask filled with water at 20°C. When test cell (2) is used, the heat-exchanger bath (Figure 2.1) is filled with water at 20°C and the circulation pump is run. In both cases, the water bath must be replenished since it is cooled by heat transfer.

2.4.3. *Outline of Nominal Run Procedure.*

1. **Clean and assemble test cell**: Test cell is swabbed with methyl alcohol, rinsed with filtered, distilled water, and blown dry with an "aero duster" (which is R12 vapor). The bottom flange is attached (test cell (2) only) and the top is covered to keep out dust.

2. **Apply nucleation suppression material to test cell**: Gelatin or R113 is applied in a manner discussed in Section 2.4.1 (test cell (2) only).

3. **Fill circulation fluid**: The test cell is connected to the circulation system; the latter is filled with methyl alcohol (test cell (2) only).

4. **Install and evacuate test cell**: The diaphragm is inserted and clamped; the test cell is attached to the test-cell adaptor plate; the test cell is evacuated.

5. **Fill test fluid**: The test cell is filled by distilling the liquid directly within it, in the manner discussed in Section 2.4.2.

6. **Set low pressure reservoir to desired pressure**: The tank is evacuated to rid it of residual refrigerant from the preceding run, then filled with air to the desired pressure.

7. **Raise test liquid to desired temperature**: The test liquid is heated to 20°C in the manner described in Section 2.4.2.

8. **Initiate Experiment**: The experiment is initiated in the manner discussed in Section 2.2.2 or 2.2.3, depending on whether motion or still pictures are taken.

Chapter 3

Overview of Experimental Observations

This chapter outlines the general behavior of the evaporation waves observed in this study, a detailed description of which is presented in the next two chapters. As discussed in Section 2.3.1, the test liquids are Refrigerants 12 and 114 (R12 and R114). The liquid temperature is 20°C, and the superheat is varied by changing the tank pressure. To simplify the discussion, a representative example will be considered primarily, namely, R12 exhausting into 0 bar reservoir pressure. The other conditions are qualitatively similar in most respects.

3.1. Start-Up.

After the experiment is prepared in the manner discussed in Chapter 2, the run is initiated by rupturing the diaphragm seal between the test cell and the low-pressure reservoir. The diaphragm opens fully in about 1 ms, during which time an expansion wave is launched into the vapor above the test liquid. When this wave reaches the liquid, it is partially transmitted, thereby superheating the liquid, and is partially reflected. The subsequent wave motions are complicated because of further reflections from the tube bottom, the liquid surface, and the tube exit. However, the details of the depressurization processes are relatively unimportant because the liquid is rapidly depressurized (within a few milliseconds) virtually to the reservoir pressure *before* explosive boiling begins. This can be seen in Figure 3.1, which shows pressure traces for R12 into 0 bar reservoir pressure: Both the base and the exit pressures drop from 5.69 bar to essentially 0 bar before rapid evaporation raises them to a higher value, which is maintained for the duration of the run.

After the liquid pressure has fallen essentially to the reservoir value, but (for most run conditions) before the residual acoustic waves have died out, bubbles nucleate at the free surface. The pattern or "mode" of initiation depends on the liquid and the reservoir pressure. In the highest superheat case for R12 (the more volatile of the two liquids), explosive boiling usually initiates by the rapid formation of nucleation sites at random spots on the liquid free surface and at the glass/free-surface contact line. Nucleation spreads to the remaining surface

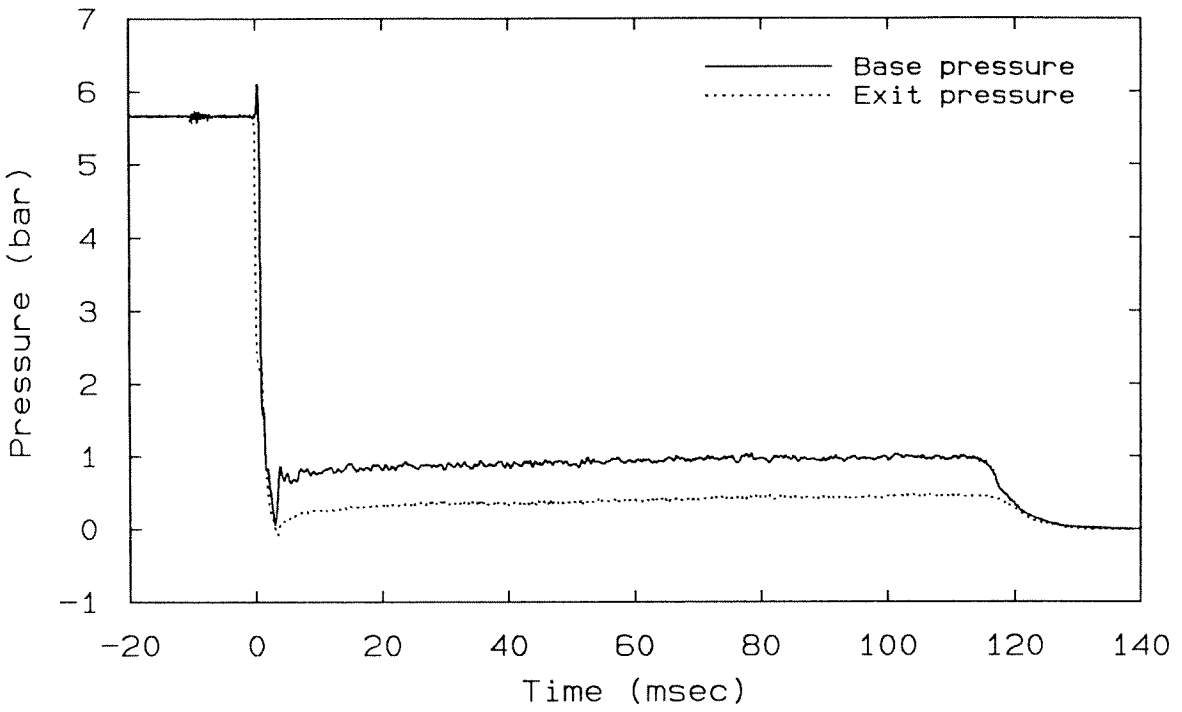

Figure 3.1: Base and exit pressure traces. Liquid: R12, T_{liq} = 20°C, P_{res} = 0 bar, Run #: MPR 25.

within one motion picture frame (160 μs). In the highest superheat case for R114 (the less volatile of the two liquids), nucleation begins only at the glass/free-surface contact line, and spreads radially inward toward the center. In the lower superheated cases for both liquids, nucleation begins at one or more sites on the glass/free-surface contact line, and propagates across the free surface.

For both R12 and R114, in the higher superheat (lower reservoir pressure) cases, no distinction is apparent between the onset of nucleation and explosive boiling. The characteristics of explosive boiling—fine-scale aerosol ejected upward and the rapid propagation of the wavefront into the liquid—are observed virtually immediately. For both R12 and R114, in the lower superheat (higher reservoir pressure) cases, a dramatic distinction between "quiescent boiling" and explosive boiling arises. In those cases, nucleation initiates only at one or at a few spots at the glass/free-surface contact line, and bubbling continues benignly in the immediate vicinity of the initial nucleation sites until a small bubble cluster is formed. Explosive boiling is established when, after bubbling has been occurring for periods as long as a

few hundred milliseconds, the bubble cluster "explodes" within a few hundred microseconds. At this time boiling rapidly spreads to the entire surface and the wave begins to propagate.

For both R12 and R114, the delay to explosive boiling transition increases markedly as the reservoir pressure is raised slightly above the value for which it is first observed. If the pressure is raised slightly higher still, transition never occurs. This phenomenon was discovered by Grolmes and Fauske (1974). Herein it will be referred to as the *self-start threshold.* Although it is statistical in nature—depending on random features such as the smoothness and cleanliness of the tube wall at the glass/free-surface contact line—the self-start threshold is nevertheless fairly well defined because of its high sensitivity to reservoir pressure. The details of the start-up phase and the self-start threshold are presented in Chapter 5.

3.2. Quasi-Steady Propagation.

For the first several milliseconds after explosive boiling is established, the appearance and speed of the wavefront are changing; however, within about 10 ms, the *average* appearance of the wavefront becomes constant. The wave speed, two-phase flow speed, base pressure, and exit pressure achieve constant values when averaged over times greater than about 10 ms. Accordingly, this regime will be referred to as *quasi-steady propagation.* However, on millisecond time scales, the propagation of the wavefront and the mechanisms that drive it are observed to be highly nonsteady.

Nonsteady wavefront mechanisms are suggested by the base pressure trace in Figure 3.1. In the quasi-steady regime the average base pressure is very well defined, but exhibits fluctuations whose RMS value is about 3% of the mean pressure. (Fluctuations in the exit pressure are greatly attenuated—they are less than or of order the noise level.) The nonsteady features seen in the high-speed movies are significantly more dramatic and complex than can be inferred from the pressure measurements. To appreciate this fact the reader is referred to the video program, which is discussed in Appendix A. A general description of the features seen in the high-speed movies will now be presented with the aid of still photographs.

Figure 3.2 shows simultaneous side-view and bottom-view still photographs for the example condition, R12 exhausting into 0 bar. The photographs were taken at 25 ms after diaphragm

burst, which is well into the quasi-steady regime. The free surface was initially at the 8.0 cm mark. Since the side view is back-lit, the upstream liquid region appears light and the highly light-scattering, two-phase flow above it appears dark. The wave propagates downward at a speed of 0.63 m/s, and the two-phase flow travels upward at 35 m/s.

The flow can be divided into three basic regions, as indicated in Figure 3.2. The *upstream liquid region* is uniformly superheated and essentially stagnant. The *wavefront* is a region several millimeters thick within which liquid fragmentation, rapid evaporation, and flow acceleration take place. The wavefront is composed of two subregions. The upstream edge is composed of bubble-structures of distributed sizes, a typical diameter being about 1 millimeter. The formation of bubbles at this *leading-edge bubble layer* is an intermediate step between pure liquid and aerosol. Fine fragmentation of the liquid occurs through violent disintegration of the leading-edge bubbles. It is observed that aerosol is not created by the breakup of individual bubbles, but rather by larger-scale explosively expanding *bursts* of aerosol, each of which involves the disintegration of many bubbles. The *fragmentation/acceleration region*, which extends several millimeters downstream of the leading-edge bubble layer, is basically the ensemble of individual bursts. Downstream of the fragmentation/acceleration region, the two-phase flow travels at a nearly constant speed, indicating that the evaporation rate is relatively small. Accordingly, this region will be referred to as the *developed flow region.*

Any given region of the wavefront (say, of order 10 mm^2 area) appears to propagate fairly independently of neighboring regions. Individual regions all propagate at the same average rate but at different instantaneous rates: portions of the wavefront tend to surge ahead at relatively high velocity and then remain relatively quiescent. Consequently, the leading edge of the wavefront is globally convoluted. Overall, the wavefront tends to propagate normal to itself, and highly inclined regions tend to run into the test cell wall. For this reason the distance between the upstream-most and downstream-most tip of the wavefront leading edge is limited to about one tube diameter.

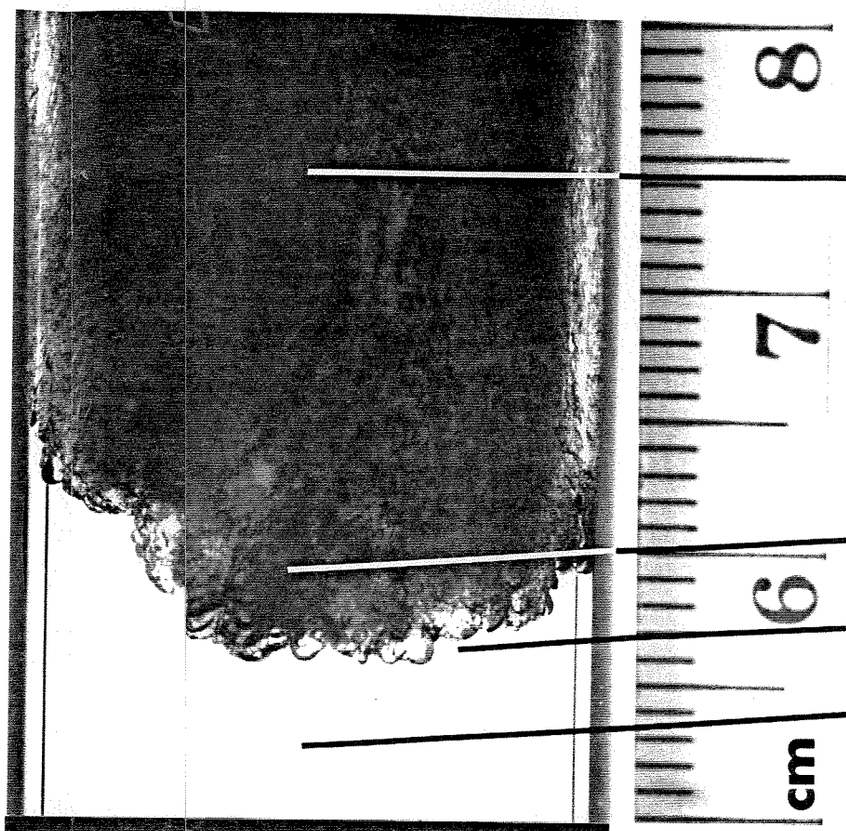

Side View

Developed two-phase flow region

Fragmentation/acceleration region

Leading edge bubble layer

Upstream liquid region

Bottom View

Leading edge bubble layer

Figure 3.2: Simultaneous still photograph of the quasi-steady flow regions. Liquid: R12, T_{liq} = 20°C, P_{res} = 0 bar, Large ruler divisionms, t = 25 ms from diaphragm burst, Initial liquid height: 8.0 cms, Test cell #: 2, Run #: SPI

Conditions near the self-start threshold produce waves that appear quite vigorous, once initiated. Therefore, experiments were conducted to determine if waves could propagate for superheats less than that of the self-start threshold if started artificially, a procedure that will be referred to as "jump starting." R12 is placed above the denser, less volatile R114 under conditions for which R12 self-starts but R114 does not. The purpose of this procedure is to determine whether the wave will continue to propagate into the R114. It is found that R114 can be jump-started over a modest range of reservoir pressures: The self-start threshold for R114 at 20°C is about 1/3 bar, and waves can be successfully jump-started for reservoir pressures up to 1/2 bar. The latter pressure is an *absolute threshold* that reflects the wave's ability to maintain rather than to start itself. In particular, the absolute threshold is associated with the breakdown of the bursting process. At reservoir pressures between the two thresholds, waves can also be initiated by other forms of external perturbation. In fact, most of the R114 runs exhausting into 1/3 bar were initiated by a small bit of diaphragm material falling to the liquid surface. The details of quasi-steady propagation, including breakdown at the absolute threshold, are discussed in Chapter 4.

Chapter 4

Quasi-Steady Propagation

In this chapter the experimental observations regarding the quasi-steady propagation regime, which was introduced in Chapter 3, are discussed in detail. The three primary regions—the upstream liquid region, the wavefront region, and the developed two-phase flow region—are each discussed separately, using selected examples from the six run conditions listed in Section 2.3.2. (The condition R12, P_{res} = 0 is chosen as the primary representative example.) The observations at the *absolute threshold of superheat*—at which the quasi-steady propagation mechanisms break down—is then presented. Finally, the measured and inferred average wave properties for the six run conditions are summarized, and the trends are discussed.

4.1. Upstream Liquid Region.

The questions concerning the upstream liquid region during quasi-steady propagation are: 1) What thermodynamic state is reached by depressurization of the initially saturated liquid? 2) What motions are induced in the upstream liquid by the approaching wavefront? 3) How is the upstream liquid state affected by heat absorption at the wavefront?

4.1.1. *Upstream Liquid State.* Depressurization of the liquid column is accomplished through a series of isentropic pressure waves. The upstream liquid state (1) during quasi-steady propagation therefore lies on the metastable isentrope passing through the initial state (0). Calculation of this isentrope requires an equation of state for the fluid that is valid in the liquid region (Thompson *et al.*, 1987); state (1) is then fixed by specifying the upstream pressure P_1. As will be seen in Chapter 7, the upstream liquid density and enthalpy ρ_{l1} and h_{l1} are the most important upstream quantities. In the present experiments these properties can be inferred without calculating the metastable isentrope, as is now demonstrated.

Superheated liquids can generally be considered incompressible provided that the superheat limit is not approached. (As illustrated in Figure 1.3, this condition is satisfied in the present experiments.) The isothermal compressibility of saturated R12 at 20 °C, is about 5.4×10^{-4}

bar^{-1} (Brelvi and O'Connell, 1972). Assuming that depressurization is virtually isothermal, and that the compressibility remains constant, the corresponding density decrease is estimated to be of order 0.1%. This value is consistent with the fact that no rise of the free surface is detectable in the high-speed movies upon liquid depressurization.

The drop in liquid enthalpy can be calculated using the identity:

$$Tds = dh - \frac{dP}{\rho} \tag{4.1}$$

where s and h are the specific entropy and enthalpy, respectively. Making use of the fact that the liquid entropy and density are virtually unchanged by depressurization, the decrease in enthalpy becomes:

$$h_{l1} - h_{l0} = \frac{P_1 - P_0}{\rho_{l0}} \tag{4.2}$$

The maximum fractional decrease in liquid enthalpy occurs when the liquid is fully depressurized (i.e., $P_1 = 0$) and depends only on initial conditions:

$$\left.\frac{h_{l1} - h_{l0}}{h_{l0}}\right]_{P_1=0} = \frac{-P_0}{\rho_{l0} h_{l0}} \tag{4.3}$$

For R12 and R114 under the initial conditions of the present experiments, the maximum possible decrease in liquid enthalpy given by Equation 4.3 is 0.51% and 0.15%, respectively. The corresponding decrease in liquid temperature is also negligible.

In Figure 3.1 it was shown that the liquid pressure, and hence the superheat, fluctuate about a well-defined mean value. The above properties of state (1) are therefore time-averaged values. It is straightforward to show that the RMS fluctuation in liquid pressure, P_1, is equal to the RMS fluctuation in the superheat pressure based on the upstream pressure, ΔP_1. In the present experiments the temporal fluctuation in superheat is negligible compared to the mean value: For the example of R12 into 0 bar, it is about 0.5%. The normalized fluctuation in the superheat temperature ΔT_1 and the superheat enthalpy Δh_{l1} are the same order of magnitude as

the normalized fluctuation in the superheat pressure. Likewise, the RMS fluctuations in the exit pressure are negligible compared to the mean value.

4.1.2. *Upstream Liquid Motion.* As mentioned in Section 3.2, the instantaneous propagation of the wavefront is quite nonsteady. Since the instantaneous propagation of the wavefront is nonsteady (Section 3.2), some amount of convection in the upstream liquid is expected in order for the latter to adjust to changes in the wavefront shape. In particular, Das et al. (1987) concluded that convection played a causative role in the evaporation waves he observed. (Section 1.3.2). The extent of convective motions is now estimated experimentally, to determine whether they may affect wavefront propagation in the present experiments.

Since the upstream liquid is featureless, convection within it cannot be detected directly. Moreover, particulate flow markers cannot be used since they would cause nucleation. An alternative approach is used, namely, to observe the motion of a dyed interface as the wavefront approaches it. Ideally, one would like to place a column of clear test liquid above a dyed column of the same liquid. In practice, diffusion and thermally-induced convection during the filling process render such an interface too diffuse to be useful. The most successful alternative tried is to form an interface between the test liquid and a different (dyed) immiscible liquid of the same density. No suitable pure liquid was found to match the density of the refrigerant test liquids; however, the desired density is achieved using a solution of a heavy salt: cesium chloride (*CsCl*). The dyed saltwater is poured in the test cell first; the test liquid is then added in the usual manner.

Unlike the "ideal" case (in which the interface is formed between clear and dyed test liquid), the immiscible liquid pairs have an interfacial tension. When two such liquids are "stacked" in a tube, the shape of the interface depends both on the *contact angle* at the wall, and the ratio of gravitational to surface tension forces, characterized by the *Bond number*:

$$Bo \equiv \frac{\Delta\rho\, g\, R_{tc}^{\,2}}{\sigma} \tag{4.4}$$

where $\Delta\rho$ is the density difference between the liquid pairs, g is the acceleration of gravity, R_{tc} is the test-cell radius, and σ is the coefficient of surface tension between the liquid pairs. The

present (density-matched) case is equivalent to the zero gravity case and the capillary case ($R_{tc} \rightarrow 0$), as all three have a zero Bond number. In the zero Bond number limit, the interface is a section of a sphere whose radius of curvature (normalized by the tube radius) is uniquely determined by the contact angle. For the present liquid pairs, the contact angle is about 55°, and the interface is substantially curved.

Figure 4.1 shows the result of a test using R114 (specific gravity 1.456) at 20 °C and 0 bar reservoir pressure. Figure 4.1a identifies the features of interest. The wavefront is approaching the *CsCl* solution, which is dyed and appears dark. The obvious boundary between the liquid pairs (which is approximately flat and level) is the contact line where the spherical meniscus between the liquid pairs meets the wall. The outline of the meniscus is the barely visible circular arc below it. Figure 4.1b is a sequence of high-speed motion picture frames, at 5 ms intervals, showing the movement of the interface as the wavefront approaches. The first photograph in the sequence (which is taken as t = 0) corresponds to the observation of the first disturbances at the meniscus, which are small amplitude capillary waves that initiate when the wavefront is about 4 mm from the meniscus/glass contact line. Similar capillary waves are seen upon initial depressurization, suggesting that they are sensitive indicators of interfacial disturbances. From the speed and wavelength of the capillary ripples, the interfacial tension is estimated to be about 1/6th that of R114 liquid and its vapor, at the same temperature.

In subsequent frames, the capillary ripples become more noticeable and the meniscus is pushed down slightly on the left side by the approaching upstream tip of the wavefront. Since the liquid volume below the meniscus is conserved, the right side of the meniscus is simultaneously pushed upward. The movement of the meniscus ahead of the wavefront upstream tip just before the latter reaches it (final photograph) is about 1 mm relative to its initial position, at which point the meniscus has moved about 3 mm upward on the right side. The ratio of the above height shifts is consistent with the change in global shape of the wavefront leading edge during the same time interval. No motion that would be expected to influence the rate or dynamics of rapid evaporation at the wavefront is detectable; any such motion is evidently restricted to the immediate vicinity of the wavefront leading edge.

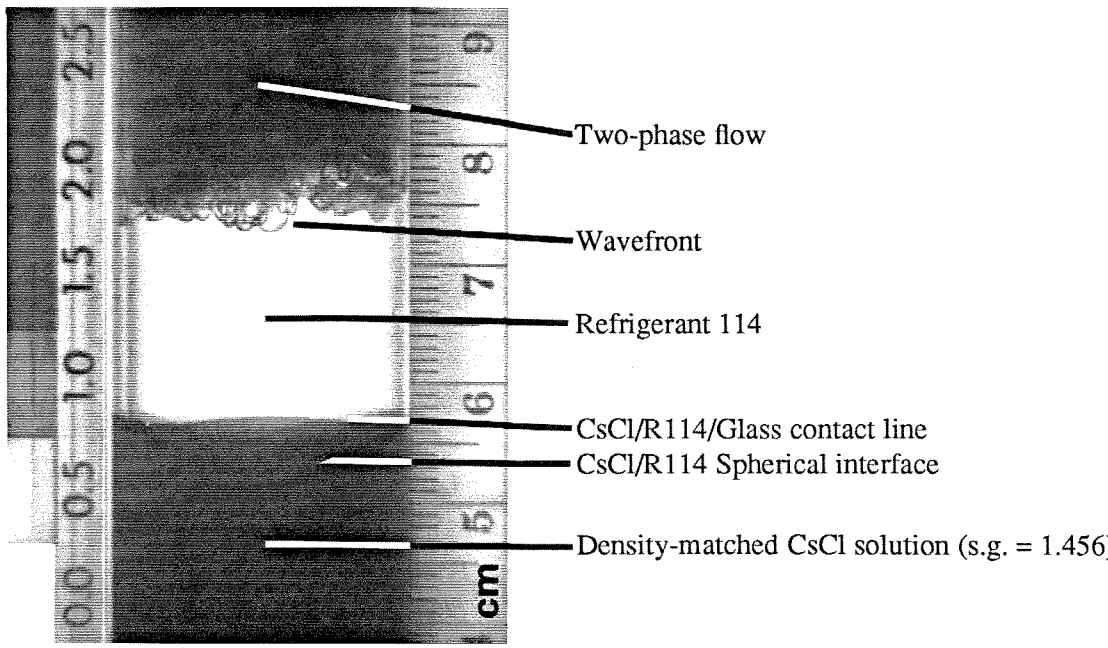

Figure 4.1a: Evaporation wave in R114 approaching a density-matched, dyed solution of cesium chloride. $T_0 = 20°C$, $P_{res} = 0$ bar, Test cell #: 2, Run #: MPR 81.

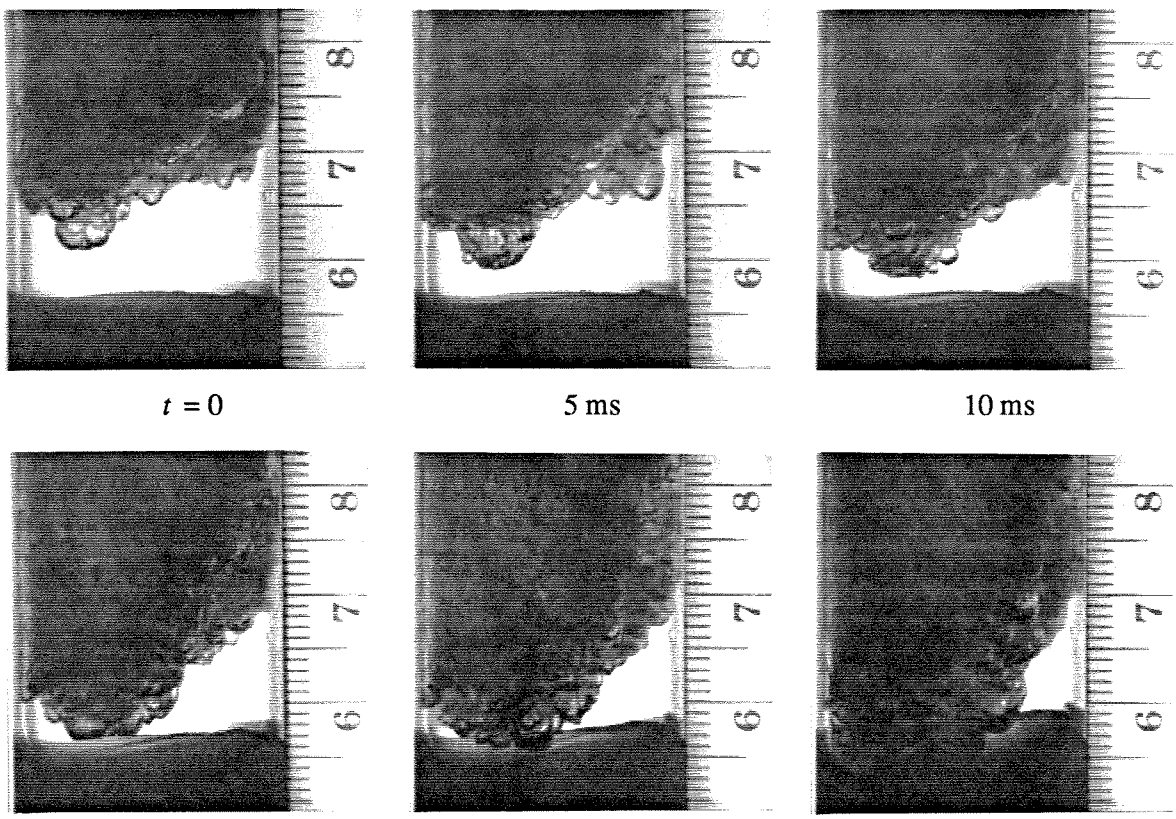

Figure 4.1b: Motion of the interface of Figure 4.1a as the wavefront approaches.

4.1.3. *Cooling of the Liquid Column.* Evaporation at the wavefront leading edge cools a layer of liquid ahead of it. It can be inferred from the quasi-steady nature of wave propagation that the average thickness of the thermal boundary layer is constant in time—for if it increased with time, the heat flux to the wavefront would decrease with time, causing the evaporation rate and wave speed also to decrease. Physically, the thermal boundary layer is maintained at a constant average value because cold liquid is stripped away as the wavefront propagates. (cf. the example of the thermally-limited bubble in Section 1.2.2.)

In the previous section it was concluded that at upstream distances more than a few millimeters from the wavefront leading edge, convection in the upstream liquid is negligible. This suggests that the heat equation may be used to solve for the time-averaged temperature profile in the upstream liquid. One way to solve the heat equation in this case (cf. Frost, 1985) is to consider the wavefront as a discrete heat sink moving through the stagnant liquid at the average wave speed. To apply this model, the heat generation term in the heat equation is made a delta function (with negative sign, signifying heat absorption). The solution in the frame of the wavefront is:

$$\frac{T(x) - T_w}{T_1 - T_w} = 1 - e^{-(\frac{V_w}{\kappa_{l0}})x} \tag{4.5}$$

where the subscript 1 denotes values taken far upstream, w denotes values at the wavefront leading edge, κ_{l0} is the thermal diffusivity of the upstream liquid, V_w is the wave speed, and x is the upstream distance measured with respect to the wavefront. Equation 4.5 is illustrated in Figure 4.2.

The characteristic temperature of the wavefront leading edge, T_w, is unknown; it lies somewhere between T_1 and $T_s(P_1)$. To determine it would require that the strength of the heat sink in the model problem be known, which depends on the complex processes of evaporation and fragmentation. The characteristic thermal boundary-layer thickness can be defined independently of T_w. Specifically, let the thermal boundary-layer thickness, δ_{avg}, be defined as the distance ahead of the wavefront leading edge at which the temperature rises to within 1/e of T_1, based on the temperature difference $T_1 - T_w$ (see Figure 4.2). Then:

$$\delta_{avg} = \frac{\kappa_{l0}}{V_w} \tag{4.6}$$

where the subscript *avg* expresses the fact that δ is a time-averaged value. Equation 4.6 is identical to the early classical result for a laminar flame (Mallard and LeChatelier, 1883). Inserting measured values of wave speeds into Equation 4.6 gives thicknesses of order 0.1 μm. In light of the discussion of Section 4.1.2, the thermal boundary layer is contained within the region in which convective motion due to wavefront nonsteadiness is expected to occur. Therefore, the assumption that heat transfer within it is purely conductive cannot be justified ex post facto. Nevertheless, the estimated value of δ_{avg} is so much smaller (about four orders of magnitude) than the characteristic scales of the wavefront leading edge, that any reasonable degree of error will not change the result that the thermal boundary layer thickness is extremely thin. An estimate of the instantaneous thermal boundary-layer thickness can be obtained from the growth of individual bubbles. This is done in Section 4.2.2.4.

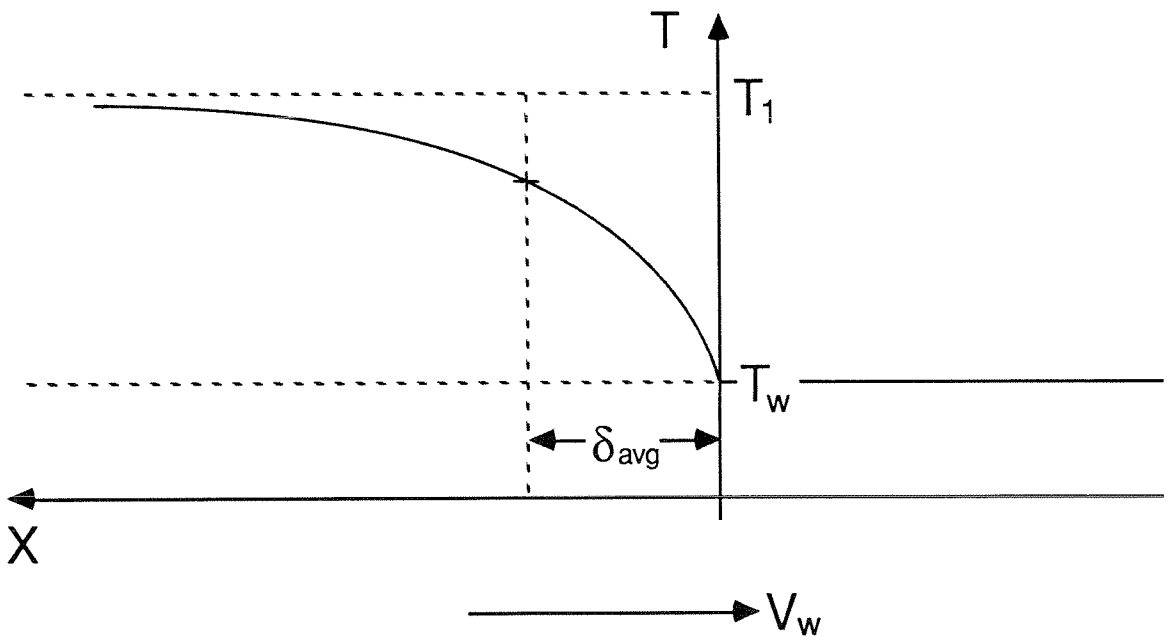

Figure 4.2: Solution of the heat equation for the temperature profile in the upstream liquid.

4.2. Wavefront Region.

The behavior in the wavefront region will be divided into two major categories: structure and dynamics. Observations of wavefront structure are drawn primarily from still photographs (a representative sample of which are presented in this section) since they offer greater resolution. Observations of wavefront dynamics are drawn from high-speed movies (a representative sample of which are presented in the video supplement, Appendix A), and to some extent from pressure measurements.

4.2.1. *Structure.*

4.2.1.1 Features of the Still Photographs. Figures 4.3 and 4.4 show side-view photographs of two evaporation waves in R12 and 0 bar reservoir pressure. In these figures, $t = 0$ is taken as the time corresponding to the sharp drop in exit pressure upon diaphragm burst (see Figure 3.1). This convention will be used throughout unless otherwise noted. The leading edge of the wavefront is composed of a layer of bubble-like structures of various diameters, up to a few millimeters: Some structures are smooth and relatively large, while others are so fine that they appear rough. The issue of whether these structures are predominantly closed bubbles or open-ended will be discussed in the following section. The term "bubble structure" will be used generically when neither scenario is intended.

On a scale large compared to the diameter of a typical bubble structure but small compared to the diameter of the test cell, the wavefront appears convoluted. As a consequence, it usually appears much thicker than it actually is. This is particularly true of the example shown in Figure 4.4, for which the wavefront is highly inclined. In this photograph, the radial component of the vector normal to the "plane" of the wavefront and pointing in the direction of its propagation, is perpendicular to the paper and points outward. Thus, the upstream tip of the leading edge is in the background, and the downstream edge of the surface is in the foreground. From the projected height of the leading-edge bubble layer, the wavefront is inferred to be inclined at about 45°.

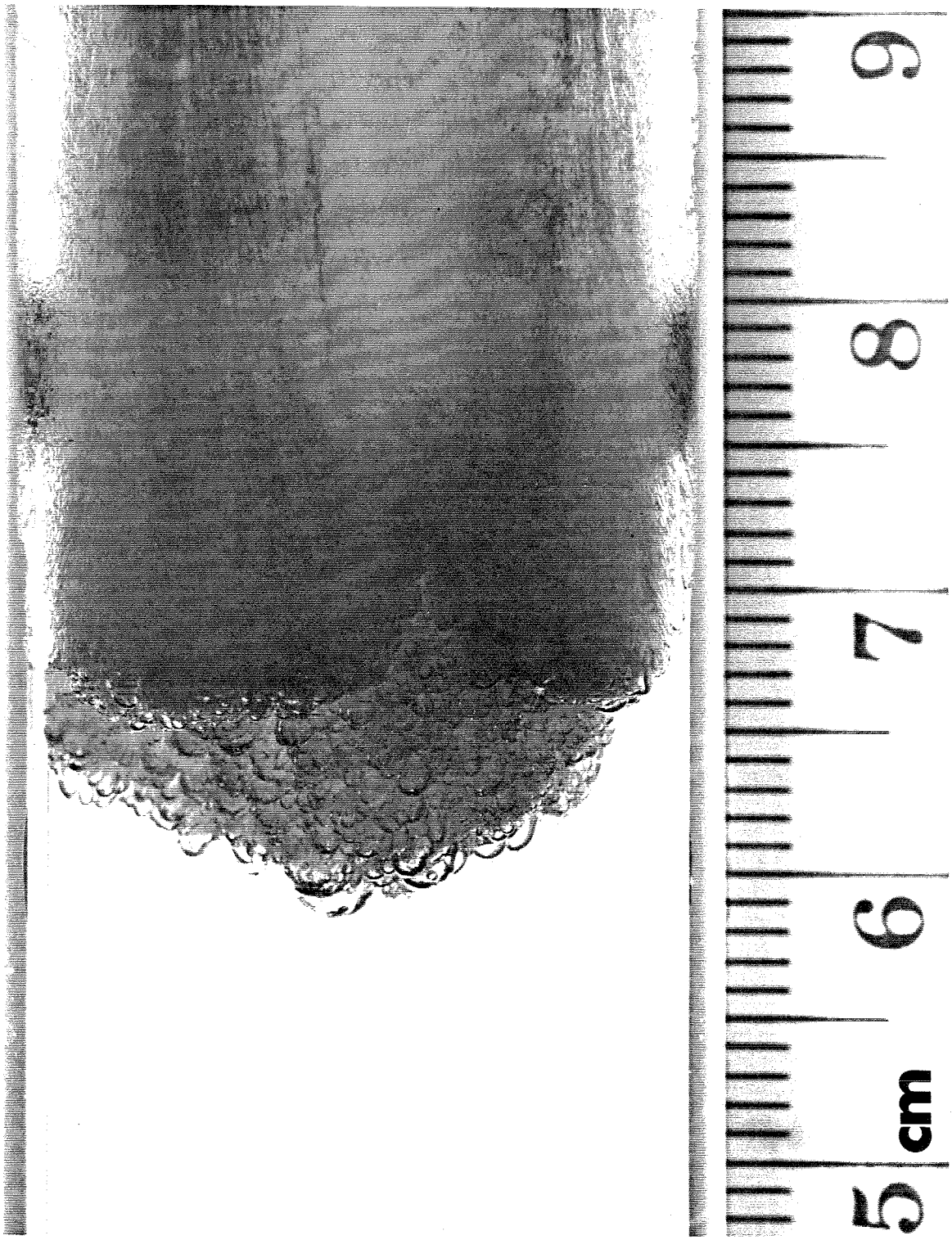

Figure 4.3: Side-view still photograph of a typical evaporation wave. Liquid: R12, T_0 = 20°C, P_{res} = 0 bar, x_0 = 8.1 cm, t ≈ 20 ms, Test cell #: 2, Run #: SPR 1.

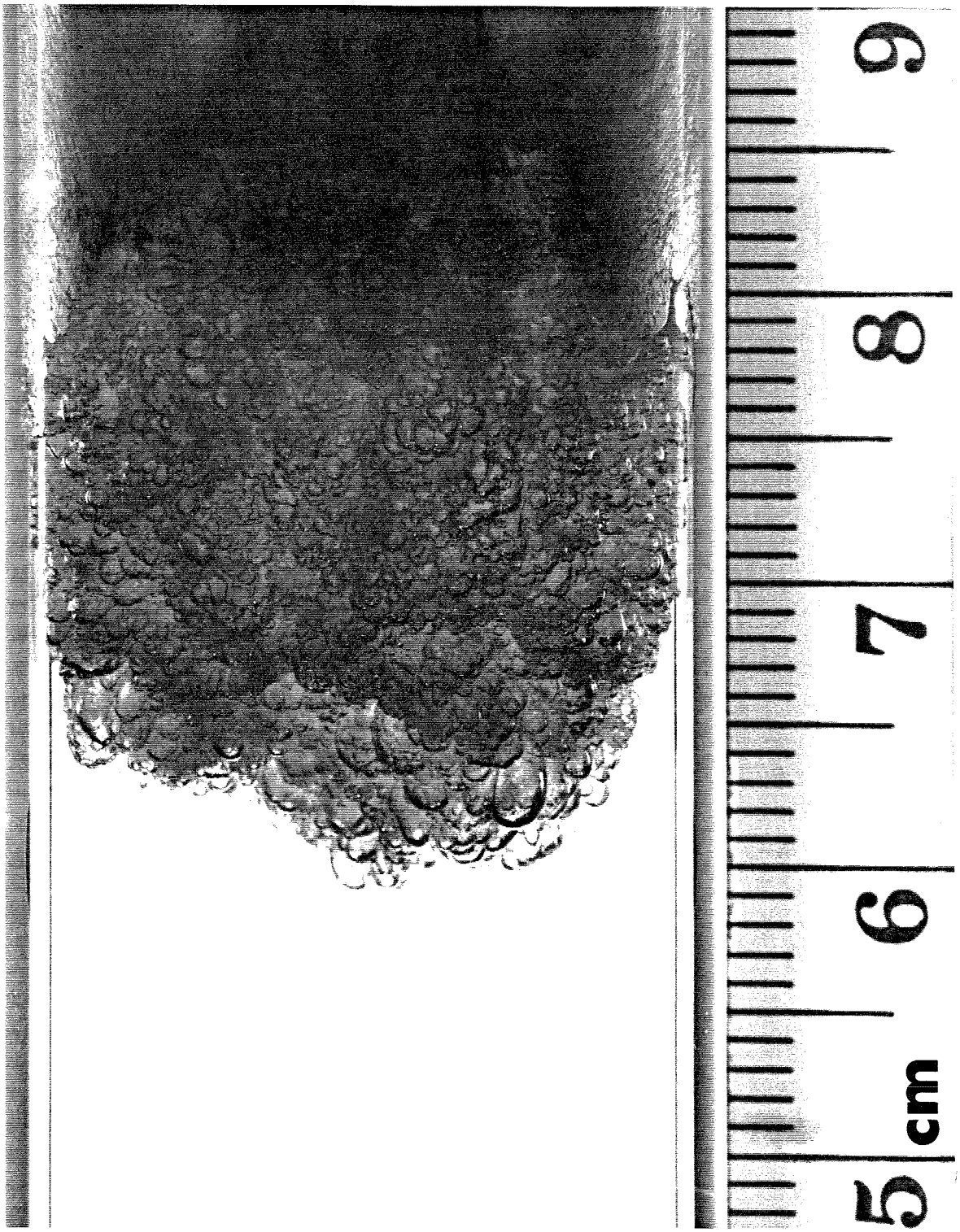

Figure 4.4: Side-view still photograph of an evaporation wave at the same run conditions as the previous figure, but with the wavefront highly inclined. Liquid: R12, T_0 = 20°C, P_{res} = 0 bar, x_0 = 7.9 cm, t = 21.1 ms, Test cell #: 2, Run #: SPR 3.

When the orientation is such that the local normal surface vector is in the plane of the paper, it becomes apparent that the true thickness of the leading edge bubble layer is only a few millimeters. This is the case in the foreground of Figure 4.3 (which is the region, located at the 6.5 cm mark, from which the two-phase flow can be seen to emanate.) The flow is very dark just downstream of the leading edge, indicating that substantial fragmentation occurs there. The dynamics of fragmentation are discussed in Section 4.2.2.2; the structure of the downstream two-phase flow is the subject of Section 4.3.1.

Figure 4.5 shows simultaneous side and bottom view still photographs for four of the six run conditions: R12, P_{res} = 0 bar, 1 bar; R114, P_{res} = 0 bar, 1/2 bar. (The average wave properties for each of the six run conditions are summarized in Table 4.1, Section 4.5.3.) The photos are arranged in order of decreasing wave speed and upstream superheat enthalpy. Overall, each of the conditions appear remarkably similar, even though there is a factor of three difference in wave speed between the leftmost and rightmost wave. For example, the distance Δx_w between the upstream-most and downstream-most tips of the projected leading edge contours is approximately the same in each case. In fact, the global shape of the leading edge varies about as much between runs at the same conditions (and even during the same run) as it does in these four runs at different conditions. From the bottom views it is clear that in all cases the average appearance of the leading edge bubble-structures is uniform over the cross-section of the test cell. Thus, the walls play no causative role in quasi-steady propagation (cf., start-up behavior, Section 5.2).

The most noticeable difference between the different run conditions is that, as the superheat and wave speed decrease, the characteristic size of the leading-edge bubble-structures tends to increase. In the leftmost photo (R12 into 0 bar), the diameter of largest structures is about 2 mm, and there are many structures whose diameter is 100 μm or smaller. In the rightmost photo (R114 into 1/2 bar), the largest structures are only moderately larger than in the above case, but a higher percentage of structures are large—there are few structures that are 100 μm in diameter or less.

Side View

Bottom View

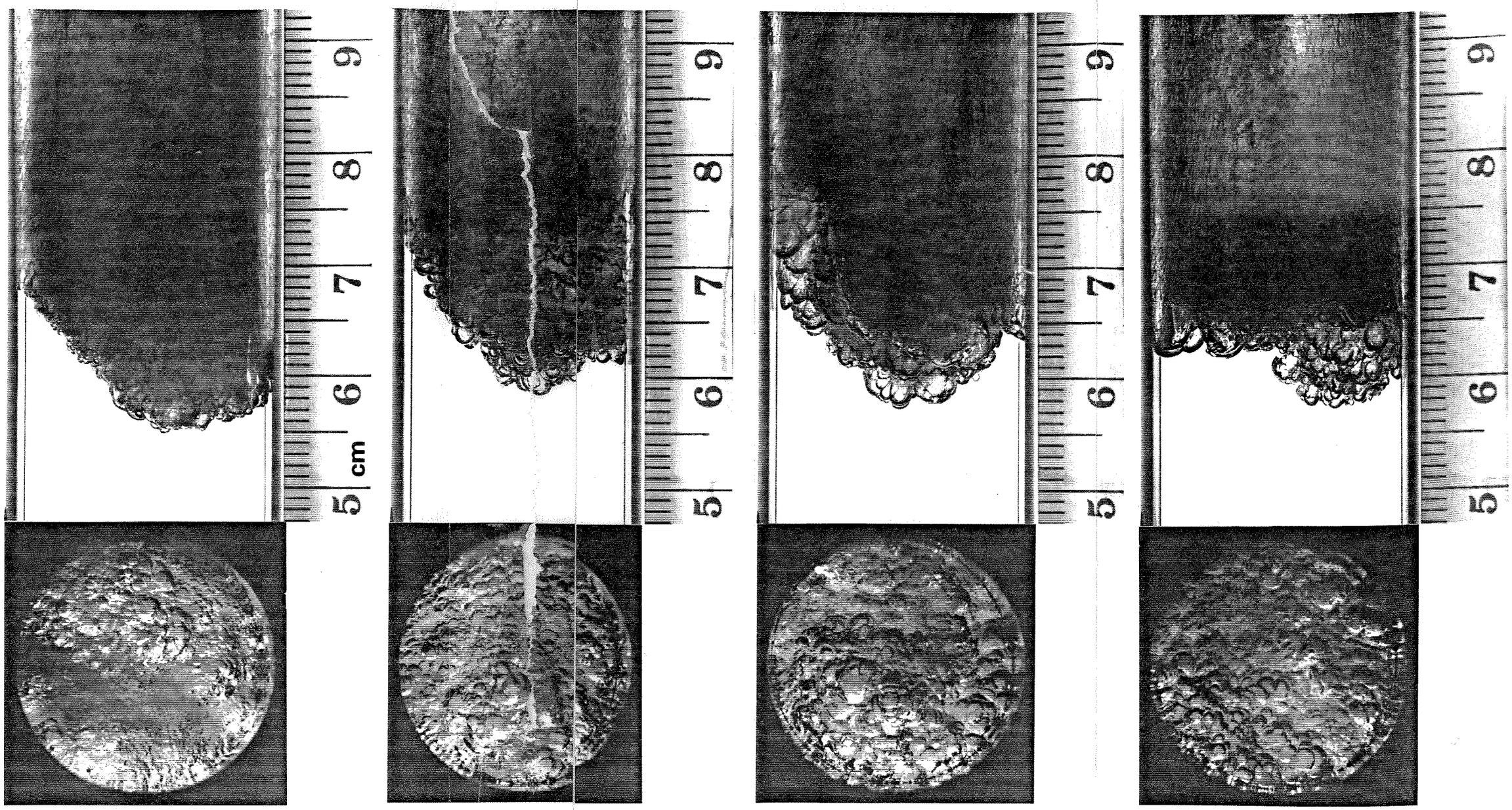

Liquid:	R12	R12	R114	R114
P_{res} (bar):	0	1	0	1/2
V_w (m/s):	0.63	0.36	0.32	0.21
ΔT_1 (°C):	50.9	48.8	36.2	31.9
Run #:	SPR 08	SPR 1	SPR 13	SPR 16

Figure 4.5: Simultaneous side and bottom view still photographs of evaporation ves for four different run conditions. T_0 = 20°C, x_0 = 8.0 cm.

In general, it is not possible to match fine-scale features in simultaneous side and bottom views; however, it is generally possible to deduce the global wavefront shape. Most of the light is from the rear of the test cell, so that in the bottom views the overall terrain is suggested by the highlight and shadow patterns. Individual views can often give a mistaken impression of features, which can be appreciated by examining the rightmost photo of Figure 4.5 (R114, P_{res} = 1/2 bar). The bottom view shows no particular structure of interest at the right-hand side of the test cell, while the side view clearly shows that there is a large structure protruding ahead on the right-hand side of the test cell.

Because the test cell diameter is much greater than the scales at which the flow is generated, many independent events are superimposed in the photographs. This fact makes interpretation of events more difficult, and greatly attenuates the transmitted light. Ideally, one would like to observe a cross-section of the flow; however, such a feat would be nearly impossible in the present experiments because of the severe light scattering. A useful compromise is to thin the flow down to a thickness only slightly larger than the largest scale that is important in generating the flow. This was accomplished by installing transparent centerbodies in the existing test cell to produce an annular geometry. The centerbodies are Pyrex tubes filled with degassed, distilled water (Section 2.1.2). Four different diameters were tried, and a gap width of about 2 mm was found to provide a good trade-off between flow clarity and unwanted wall effects. Because the test-cell radius is about 7 times the gap width, this geometry is approximately like a two-dimensional channel. Both high-speed motion pictures and still photographs were obtained for R12, P_{res} = 0 bar.

Although no fundamentally different behavior is seen in the annular runs than is seen in the circular cross-section runs, they have proved useful for clarifying certain features. Figure 4.6 shows a still photograph of an annular run with a 1.75 mm gap. Because of the annular geometry, the global shape of the leading edge assumes a "crown-like" appearance. The two-phase flow near the center of the photograph is much more transparent to light than is the flow at the left and right edges, where its thickness in the direction of the optical axis is greater.

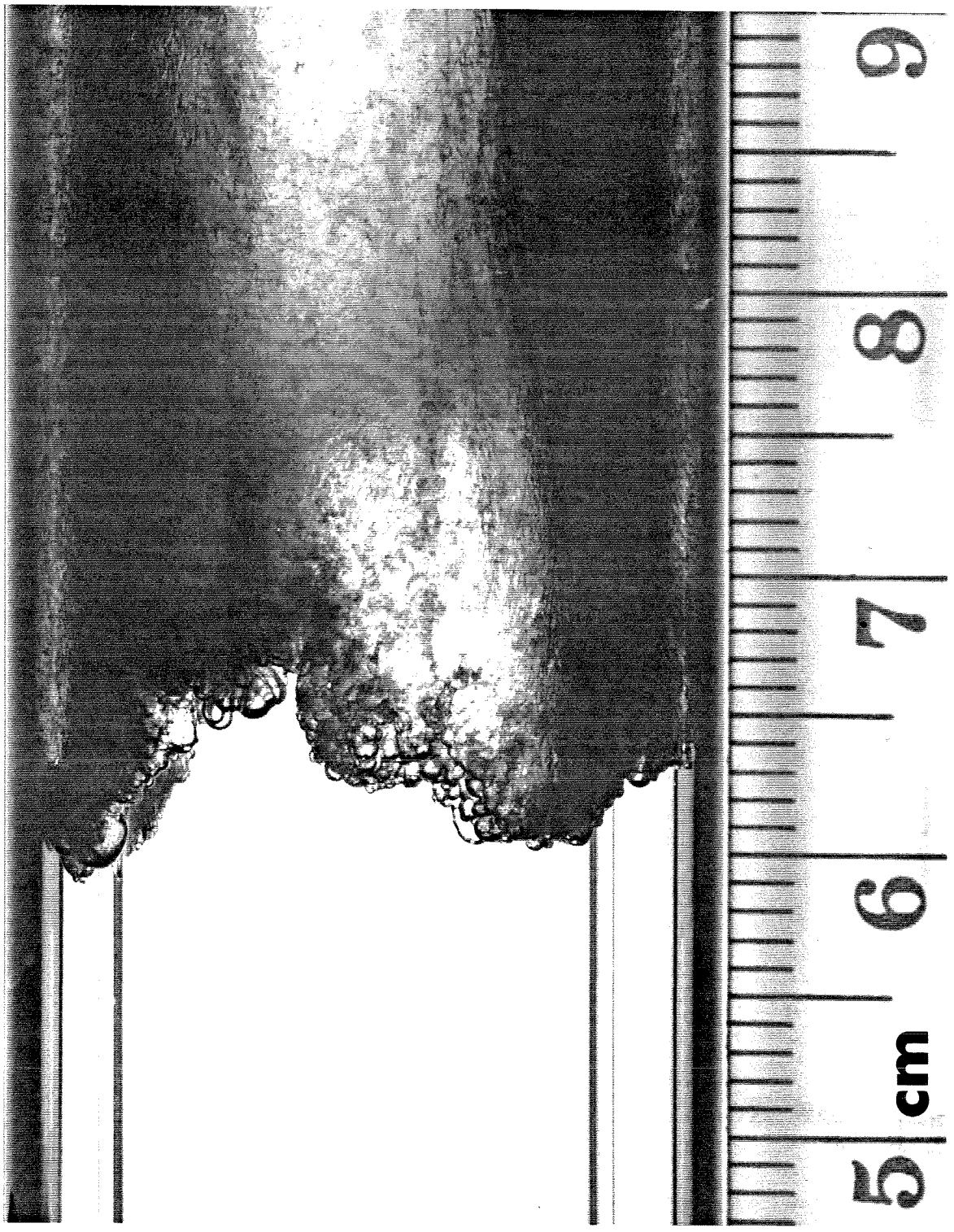

Figure 4.6: Side-view still photograph of an evaporation wave in a test cell with annular geometry. Gap width: 1.75 mm, Liquid: R12, T_0 = 20°C, P_{res} = 0 bar, x_0 = 8.1 cm, t = 31.9 ms, Test cell #: 2, Run #: SPR 29.

Moreover, the flow near the centerline of the photograph is much more transparent compared to the leading-edge bubble layer than the corresponding flow in runs with circular geometry (e.g., Figures 4.3 and 4.4). This is because in runs with circular geometry, the leading-edge contour (which is the projection of the leading edge surface on the film plane) by definition protrudes ahead of the other portions of the leading-edge surface. Thus, the bubble structures that compose the leading-edge contour receive virtually full illumination. However, slightly downstream of the leading edge light-scattering flow fills the entire tube, so the image is much darker. In contrast, the annular configuration provides a realistic picture of the relative amount of light scattering caused by the leading edge versus the downstream regions.

Other features are also enhanced or clarified in the annular views. For example, the apparent thickness of the wavefront reflects its true thickness, except for in the gap regions near the edges. Also, the spatial variation in flow generation is accentuated in the annular views. In Figure 4.6 it is seen that at the instant at which the photograph is taken, there are regions (i.e., to the left of the centerline of the photograph) in which substantial aerosol is being produced, as well as regions (i.e., to the right of the centerline) in which very little aerosol is being produced. (Note that such behavior is not clear from the circular cross-section still photos, e.g., Figure 4.3.) As will be discussed in Section 4.2.2.2, the temporal unsteadiness of flow generation observed in the high-speed movies is accentuated by the annular configuration.

4.2.1.2 Leading Edge Bubble-Structures. This section considers the question of whether or not the leading-edge structures are closed bubbles or open-ended perturbations. The difficulty in interpretation arises in part because the downstream portions are obscured by light-scattering two-phase flow. The issue is an important one because, as will be discussed in Chapter 6, previous authors have suggested alternative theories that involve both types of wavefront structures.

Figure 4.7a illustrates a spherical evaporating bubble that is completely surrounded by liquid. The cross-hatching indicates a thermal boundary layer. The behavior of such a bubble has been widely studied, and its dynamics are expressed by the Rayleigh-Plesset equation (Section 1.2.2). This type of bubble is not observed in the present experiments, provided that nucleation in the upstream liquid is successfully suppressed (cf. Appendix C).

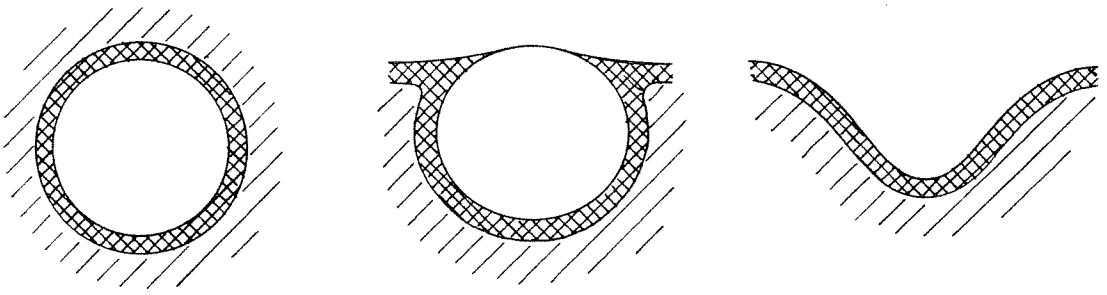

a) b) c)

Figure 4.7: (a) Spherical bubble growing in a uniformly superheated liquid, (b) Floating bubble growing in a semi-infinite superheated liquid, (c) Isolated perturbation at the surface of a semi-infinite superheated liquid.

Figure 4.7b illustrates an evaporating bubble on a free surface, or "floating bubble." Again, the cross-hatching indicates a thermal boundary layer. Non-evaporating floating bubbles are familiar from everyday experience. Such bubbles are partially submerged in the liquid, and are sealed on top by a film cap. The range of possible shapes of such a (non-evaporating) bubble at a free surface were calculated by Toba (1959). The only parameter in the static problem is the Bond number (which characterizes the ratio of gravitational to surface tension forces) based on the bubble radius and the difference between liquid and vapor densities (cf. Equation 4.4):

$$Bo \equiv \frac{(\rho_l - \rho_v)\, g\, R^2}{\sigma} \tag{4.7}$$

For Bond numbers less than or of order 0.1, floating bubbles are almost spherical and are constrained almost entirely below the liquid surface, as is the case in the drawing of Figure 4.7b. The surface area of the film cap is small compared to that of the submerged portion. As the Bond number (and, for given liquid properties, the bubble radius) increases, a bubble becomes more oblate in shape, rises farther above the level of the free surface, and develops a larger film cap. A bubble with a Bond number of order one is roughly half submerged in the liquid. For sufficiently low evaporation rates, the shape of an evaporating floating bubble would be expected to conform to that predicted by the static theory. For higher evaporation rates the shape would evidently be affected. Although growing floating bubbles can occur in boiling whenever the liquid bulk is superheated (e.g., Balaji and Mesler, 1990), the effect of growth rate on floating bubble shape has not previously been an issue. No experiments or

calculations of this effect are known to the author.

Figure 4.7c shows an isolated perturbation on an evaporating liquid surface, the shape of which is roughly compatible with the observed shape of an individual leading-edge structure. Unlike the bubbles of Figure 4.7a and 4.7b, such a perturbation cannot persist in the absence of evaporation, because surface tension and gravitational forces act to flatten it. *Distributed* perturbations have been clearly observed in the bubble column experiments of Frost and Sturtevant (1986), at thermodynamic conditions near the superheat limit. These disturbances covered a surface large compared to their characteristic wavelength, and had an appearance much like that of an orange peel. Such behavior has not been observed in the present experiments; rather, each bubble structure grows from an individual point. The question that remains is, therefore, whether in the present experiments there is any reason to expect that evaporation-induced forces might give rise to isolated, transient, structures similar to that of Figure 4.7c.

Given the observations of the still photographs in the previous section, there appear to be two likely scenarios for the leading edge structure. In the first, the leading edge would be composed of a "sheet" of bubbles, each of which would have a structure similar to the bubble in Figure 4.7b. The structure of the leading edge would resemble a two-dimensional foam; however, unlike a foam the situation would be very dynamic: at any instant many bubbles would be forming, growing, and breaking.[1] The Bond number corresponding to the maximum characteristic bubble radius during the quasi-steady propagation phase of the present experiments is of order 0.1. Thus, but for the unknown effect of the evaporation rate, the bubble shapes would be expected to be almost spherical. The film cap area is estimated to be less than about 10% of the total surface area.[2] Besides having a film cap on its free-surface side, a film would separate each bubble from its neighbors as well. The thickness of the film is a poorly defined parameter, and is time-changing due to drainage and bubble growth. However,

---

1. Theories of foams (e.g., Kitchener and Cooper, 1959) are not particularly relevant to the present situation, as they are mainly concerned with relatively slow gravity-induced viscous drainage, gas diffusion through bubble walls, the stabilizing effect of surfactants on liquid films, etc.
2. Estimated from Toba (1959).

comparison to seawater bubbles suggests that the film would probably be less than or of order 1 μm thick (MacIntyre, 1972). The lifetime of such a bubble would be defined as the interval of time between nucleation and the rupture of one of its walls. Following rupture of a wall, the bubble would momentarily remain a perturbation, somewhat like that shown in Figure 4.7c. It is observed that new bubbles continuously appear while old ones disappear; hence, at any given instant the leading edge would be composed of both closed bubbles and open perturbations.

Many structures do look strikingly like bubbles: Complete circular outlines are often seen, and the structures maintain a self-similar shape as they grow. If the leading-edge structures are in fact bubbles, a specific source of nucleation is required (Section 1.2.1). Such "nucleation events" are not resolved in the photographs. However, isolated bubble structures can often be seen growing on the face of a previous structure in such a way that a specific nucleation event is implied.

An alternative scenario is that the leading edge is composed of many rounded, roughly hemispherical structures, which resemble bubbles on the upstream side but have no film caps on the downstream side. From the appearance of the boundaries between structures, it is inferred that the liquid between adjacent perturbations would tend to be drawn to rather sharp peaks.

4.2.2. *Dynamics of Propagation.*

4.2.2.1 Evolution of the Leading Edge Global Shape. In this section, the fine structure of the leading-edge will be ignored, and the variation in wavefront shape over regions large compared to individual bubble structures will be considered. The evolution of wavefront shape is illustrated in Figure 4.8 for R12 and P_{res} = 0 bar. Test cell #1 (the 10-inch test tube) is used in order to observe wave propagation over several test-cell diameters. Contours of the wavefront leading edge (i.e., two-dimensional projections of the wavefront surface) are drawn at 10 ms intervals. Here, the origin of time corresponds to the initiation of explosive boiling on the free surface. The shape of the wavefront constantly changes as it propagates; however, the contours are approximately evenly spaced, indicating that the average wave speed is constant.

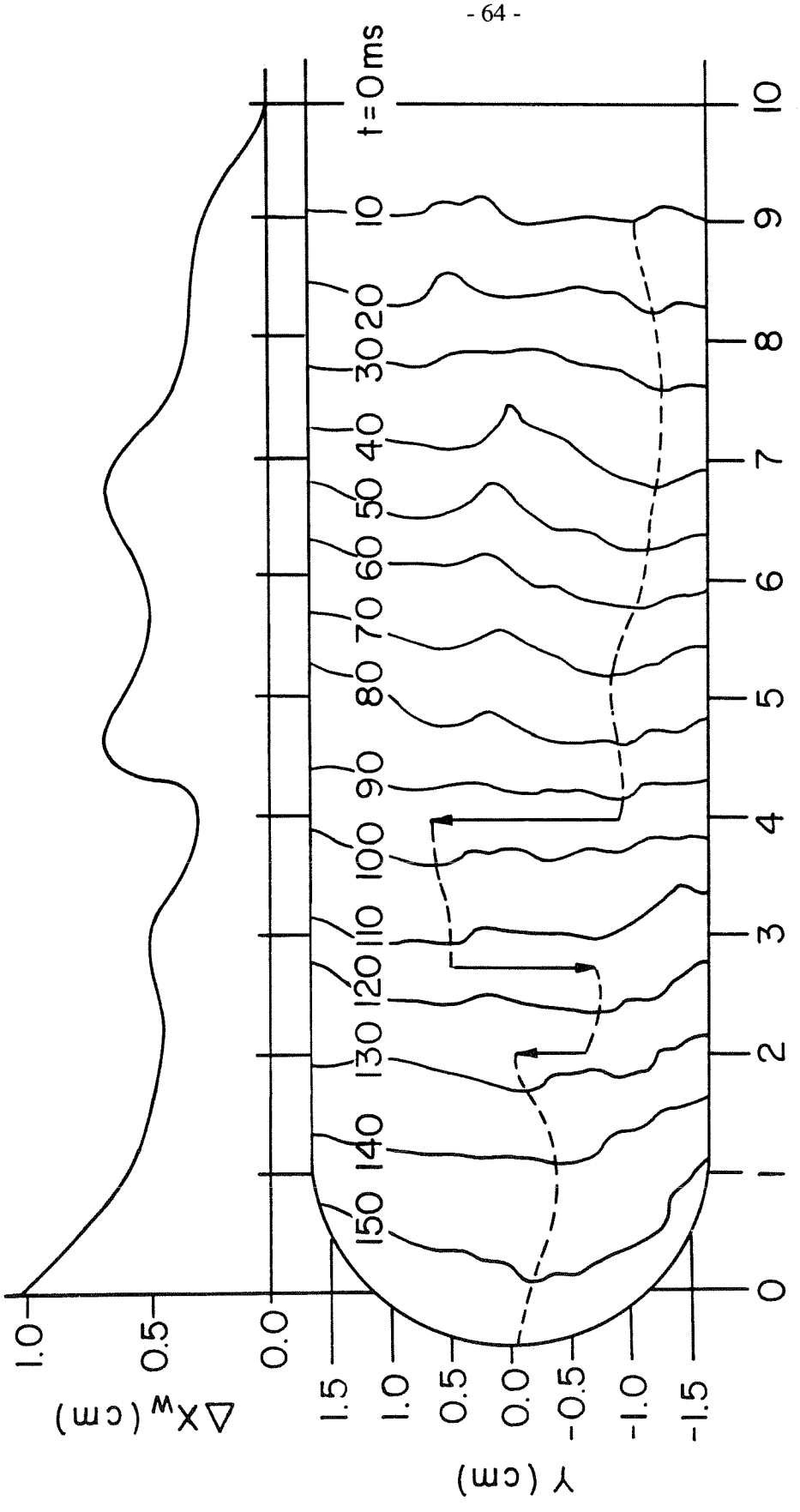

Figure 4.8: Evolution of the global wavefront shape. Liquid: R12, T_0 = 20°C, P_{res} = 0 bar, Test cell #: 1, Run #: MPR 76.

The lateral position of the upstream tip of the wavefront is indicated by the dotted line. The average speed at which the upstream tip moves laterally is much slower than the average speed at which it propagates axially. Occasionally, a remote region of the wavefront overtakes the current upstream tip; these rapid jumps in upstream tip position are indicated by arrows. The characteristic propagation distance between jumps is of order one test-cell diameter. A smoothed plot of the distance between the upstream and downstream tips of the projected contours, Δx_w, is also shown in the figure.

High-speed motion pictures indicate that the propagation of any given wavefront region is statistical in nature. Any two remote regions of the wavefront that are sufficiently removed from one another, while evidently obeying the same statistics, appear to propagate virtually independently. To the extent that such a picture is accurate, the axial position of two arbitrary regions (say, "A" and "B") relative to each other would appear to be analogous to the classical "persistence of bad luck" problem in statistics (Feller, 1966). This problem addresses the following question: what is the probability that the leading point "A" will be overtaken by the trailing point "B," and what is the expected time at which this event occurs? The answer is that point "B" is certain to overtake point "A," but the expected time at which it occurs is infinite. Thus, it is expected that the upstream tip of the wavefront should maintain its lead over relatively long distances, and that it should be overtaken by other regions occasionally.

Viewed globally, the wavefront tends to propagate normal to itself, and oblique regions therefore have a component of lateral motion. Regions of the wavefront that trail too far behind the leading edge are necessarily associated with regions of high obliqueness, and tend to be eliminated as those oblique regions run into the wall. Observations show that the relevant length scale for this process is the test-cell diameter d_{tc}; hence, the maximum value of $\Delta x_w / d_{tc}$ is at most of order one. For a sufficiently large test-cell diameter, Δx_w would evidently be limited by the stabilizing effect of gravity.[3]

---

3. Global stability would also be affected by an axial temperature gradient within the liquid column. A decreasing temperature would be stabilizing; an increasing temperature would be destabilizing.

4.2.2.2 Fragmentation Processes. High-speed motion pictures reveal that fragmentation of liquid into droplets occurs through a complex, spatially nonuniform and temporally nonsteady process. Specifically, fragmentation occurs in localized "bursts" rather than continuously over the surface. Bursts are rapidly expanding regions composed of relatively dense aerosol, which appear as dark clouds because they scatter light more efficiently than their surroundings. Bursts are observed in the region immediately downstream of the leading edge, and range from a few millimeters up to about one centimeter in extent. Their rates of expansion are of order 10 m/s, and their duration tends to be several hundred microseconds. The motion of a burst's geometric center typically has a component parallel to the wavefront surface (i.e., transverse to the direction of wavefront propagation) as well as normal to it (i.e., in the downstream direction). The translation rate of bursts is approximately the same as their expansion rate. Translation is especially apparent in the bottom views, in which bursts tend to sweep randomly over the wavefront in a wavelike fashion.[4]

At any given time, the ensemble of bursts over the entire wavefront surface comprises the *fragmentation/acceleration region*, the thickness of which is between several millimeters and about 1 centimeter, reflecting the scale of individual bursts. The momentum equation dictates that, because most of the flow acceleration occurs in this region, most of the pressure drop must occur there also. For a given liquid, individual bursts are more distinct in runs with lower superheat: under those conditions each is more extensive, but they are less frequent. Conversely, for a given liquid, bursting becomes less distinct as the superheat is increased. This is particularly true in the side views in which, for the two conditions of highest superheat (R12, P_{res} = 0, 1/2 bar), it appears that many bursts are simultaneously superimposed (cf. annular side views, Section 4.2.1.1).

The instantaneous base pressure is basically consistent with what would be expected from visual observations. The average value is constant, but the instantaneous value fluctuates due to the nonsteady fashion in which the thrust is generated (Section 4.1.1). The characteristic base

4. In the annular views, the boundary conditions restrict burst propagation to the circumferential direction.

pressure fluctuation is of order 0.1 bar peak-to-peak, and the RMS base pressure fluctuation is of order 0.01 bar. Referring again to Figure 3.1 (R12, P_{res} = 0 bar), the frequency components are mostly in the range of a few hundred Hertz, with negligible energy above a few thousand Hertz. The behavior of the other run conditions is similar (Appendix B). The visual bursting frequency, obtained by observation of the larger bursts from bottom-view high-speed motion pictures, is in basic agreement with the frequency spectrum obtained from pressure measurements.

Since bursts appear very dark, much of the liquid within them must already be finely fragmented. Hence, their rapid expansion is likely due to the large surface area, and hence evaporation rate, of this constituent liquid. The question still remains as to how the initial fragmentation occurs that leads to the subsequent rapid expansion. Unfortunately, this process is not resolved in the high-speed movies or in the still photographs. Because bursts are located just downstream of the leading edge, much of their constituent liquid must be supplied by interstitial liquid between bubble structures. The scale of bursts is such that each shatters the liquid associated with many (tens or hundreds) of leading edge structures. However, whether or not interstitial liquid plays an active or passive role is uncertain. In particular, *interfacial instability* hypotheses have been suggested (e.g., Shepherd and Sturtevant, 1982) that would not necessarily attach particular significance to shattering of interstitial liquid. Such speculation regarding specific fragmentation mechanisms is deferred until Chapter 6, since observations discussed in the following chapter are also relevant.

4.2.2.3 Instantaneous Propagation of the Leading Edge. In Chapter 3 it was mentioned that, although the average wave speed is constant, the instantaneous speed of any given region is very nonsteady. This fact is now illustrated by considering the axial motion of a representative point on the wavefront leading-edge surface, namely the upstream-most tip.

Figures 4.9a and 4.10a show $x-t$ diagrams for R12, P_{res} = 0 bar and R12, P_{res} = 1 bar, respectively. These diagrams are constructed by counting the number of frames required for the leading edge to propagate a specified increment of axial distance, namely 0.25 mm. Measurements are made using a motion analyzer projector equipped with a digital frame counter. By comparing the two $x-t$ diagrams, one can see that after a start-up period the average slope is constant. (During the start-up period the wave speed is faster than the average wave speed in the 0 bar case, and the opposite is true in the 1 bar case. This behavior is

discussed in Section 5.4.) The important time scale for nonsteadiness in wavefront propagation is the characteristic lifetime of a bubble structure, which is of order 1 ms in the present experiments. The characteristic time over which the wave speed must be averaged to obtain a relatively stationary value is of order 10 ms, and the total run times are of order 100 ms.

The nonsteady features of propagation are more easily visualized by differentiating the $x-t$ diagram to obtain a $v-t$ diagram (Figures 4.9b and 4.10b). This is done using a second-order central difference method. For the sampling method used (which was chosen for convenience), the criterion for good *velocity* resolution is that the average number of frames between successive samples be large. In the present experiments this number is between 2.5 and 5, and the resolution of velocity peaks is rather limited. That the peaks appear "clipped" is related to this fact. Nevertheless, the important qualitative features are demonstrated.

The first important observation is that the velocity fluctuations are large: of order the mean value. Occasionally, the instantaneous velocity can even be negative (Figure 4.10b). This behavior is in contrast to the instantaneous base pressure, for which the fluctuations are small compared to the mean (Appendix B). Note, however, that the instantaneous pressure is "spatially averaged" in the sense that the transducer simultaneously feels pressure disturbances from all portions of the wavefront. The second important observation is that wavefront propagation becomes increasingly intermittent as (for a given liquid and initial temperature) the reservoir pressure is raised. The decrease in average speed is not due to the fact that the *peak* speed is less; rather, the minimum speed is less and the wavefront is moving fast for a smaller fraction of the time. Thus, the question arises as to what causes the velocity surges, and what happens between them. The $v-t$ diagrams are a useful tool in answering this question because they isolate a very limited region of the wavefront, and suggest precisely when to look for interesting behavior in that region. Two causes of velocity surges are identified in this manner.

The first cause of velocity surges is the formation of one or more bubble structures near the observation point, i.e., the upstream tip of the wavefront leading edge. In this case the wave speed reflects the growth rate of that structure. Figure 4.11 shows a sequence of high-speed motion pictures taken from the same experiment as Figure 4.10 (R12, P_{res} = 1 bar). The bubble structure of interest lies on the far right side of the leading edge and is identified by an arrow in the first photograph. In frame 386 a new bubble structure appears on the face of the existing one. This structure grows for about 4.5 ms until, in frame 408, the cycle repeats itself.

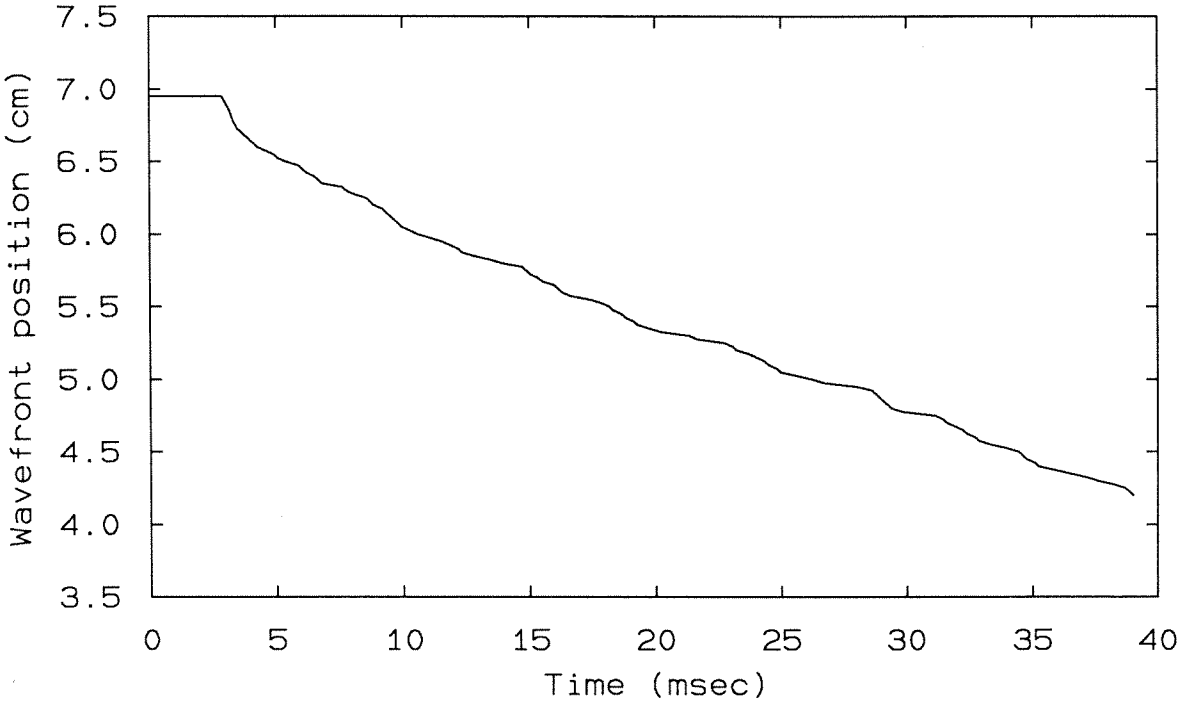

Figure 4.9a: Instantaneous position of the upstream tip of the wavefront leading edge. Liquid: R12, T_0 = 20°C, P_{res} = 0 bar, Run #: MPR 25.

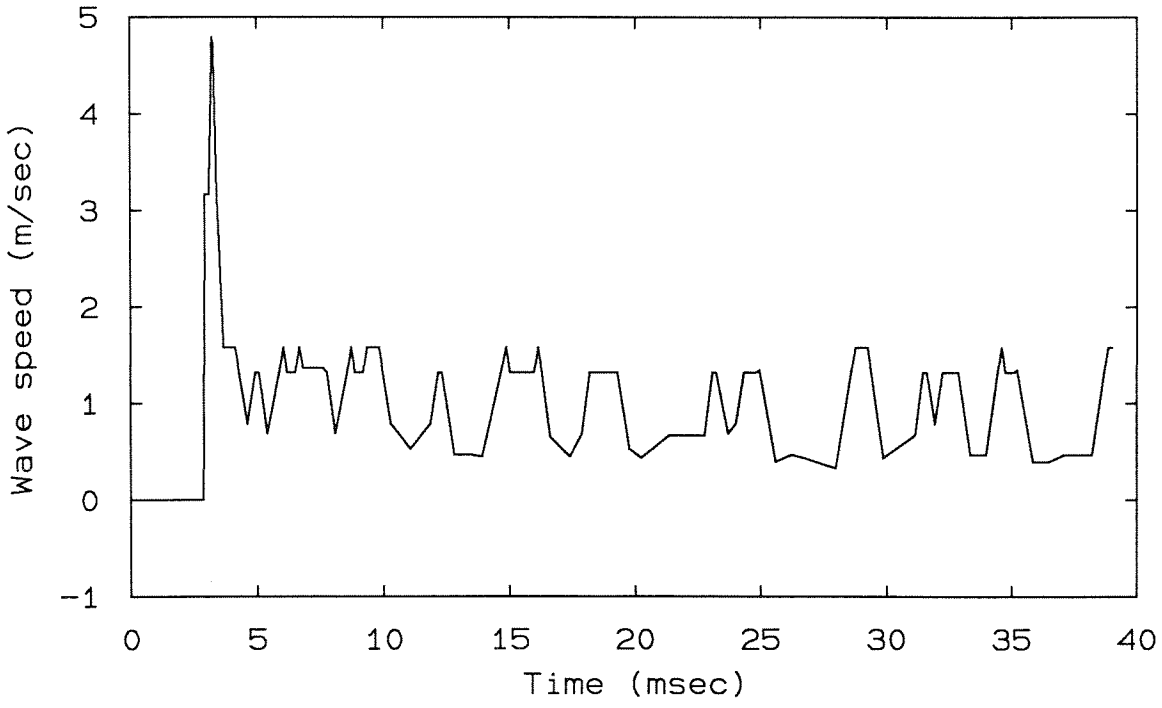

Figure 4.9b: Instantaneous velocity of the upstream tip of the wavefront leading edge, obtained from the above $x-t$ diagram.

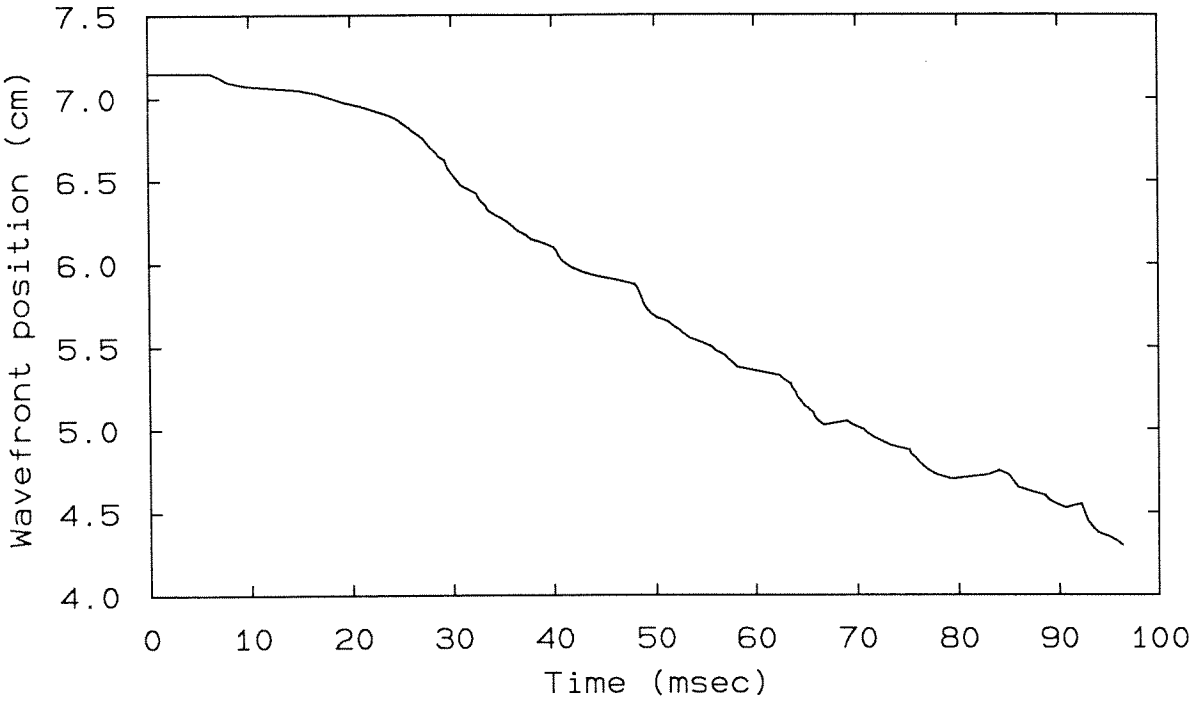

Figure 4.10a: Instantaneous position of the upstream tip of the wavefront leading edge. Liquid: R12, T_0 = 20°C, P_{res} = 1 bar, Run #: MPR 31.

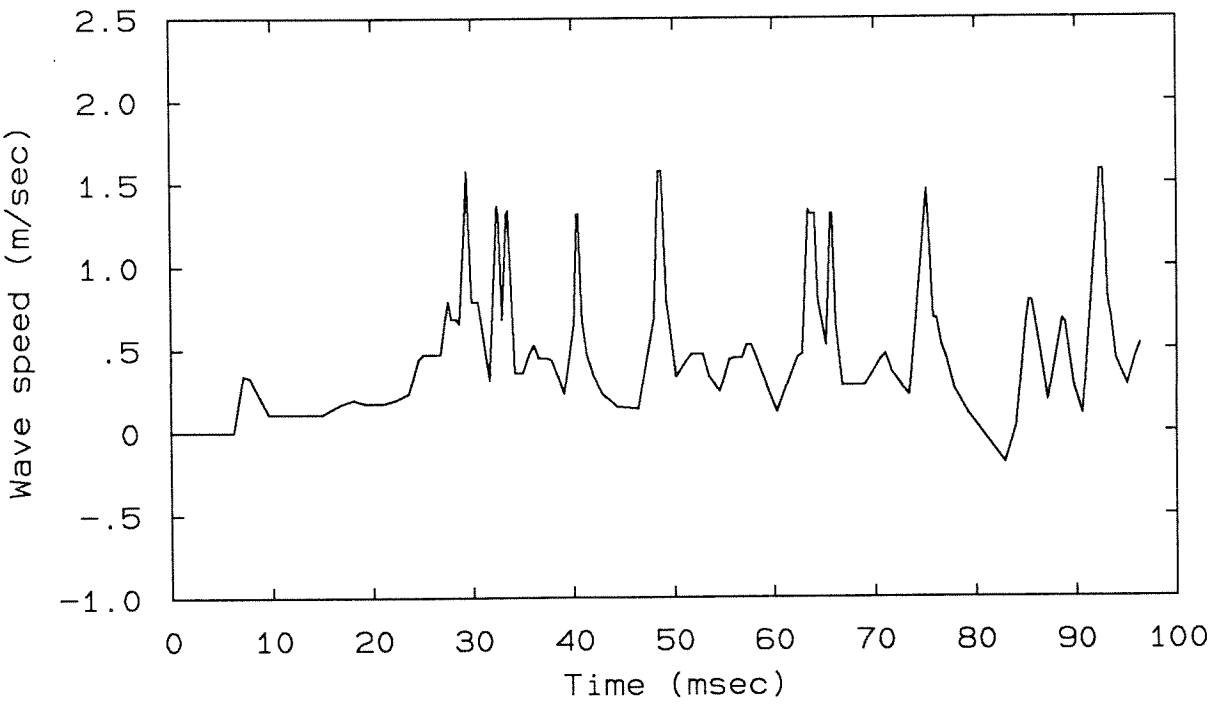

Figure 4.10b: Instantaneous velocity of the upstream tip of the wavefront leading edge, obtained from the above $x-t$ diagram.

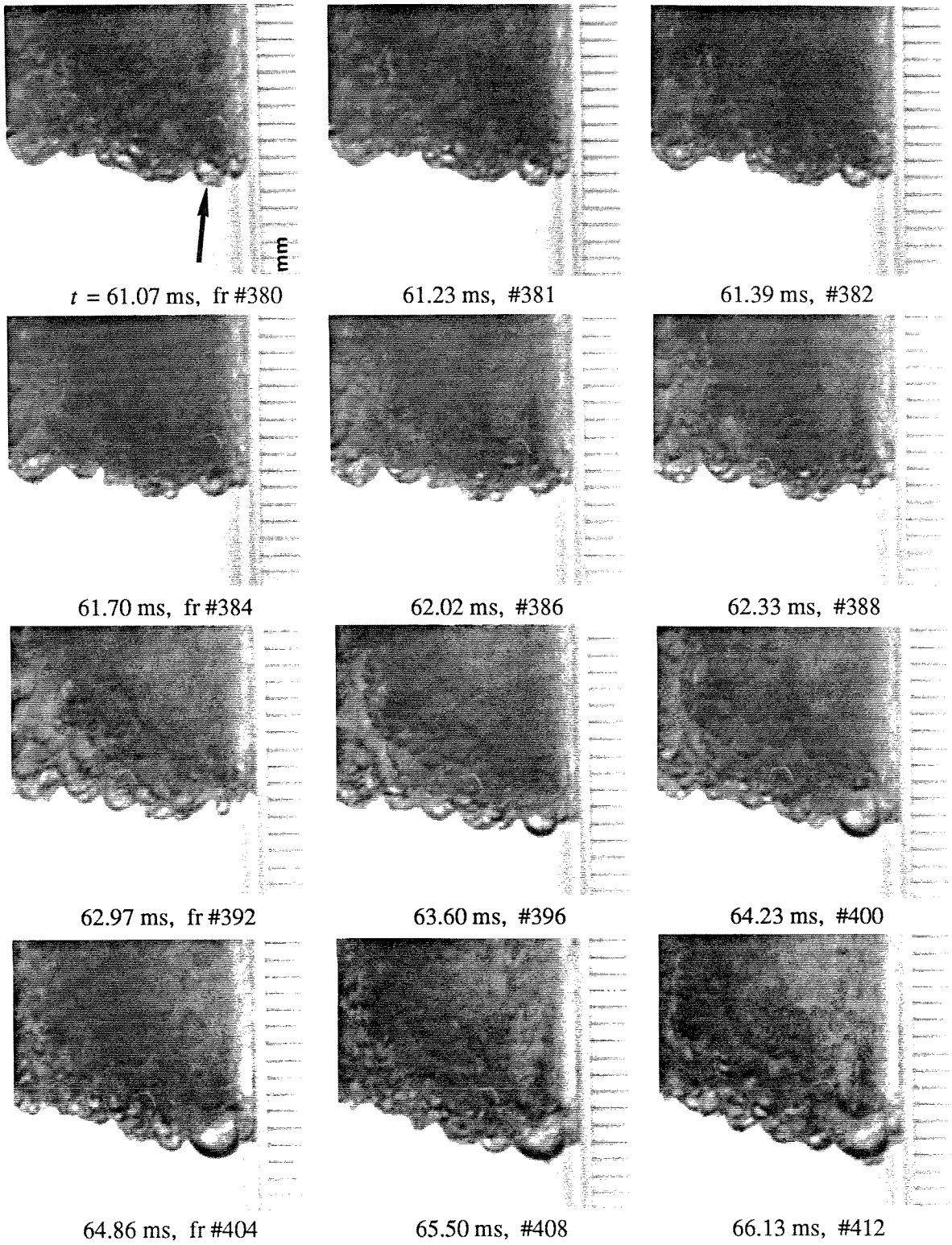

Figure 4.11: Sequence of high-speed motion pictures illustrating two surges in wavefront velocity by the growth of smooth bubbles. Liquid: R12, T_0 = 20°C, P_{res} = 1 bar, Divisions: mms, Test cell #: 2, Run #: MPR 31.

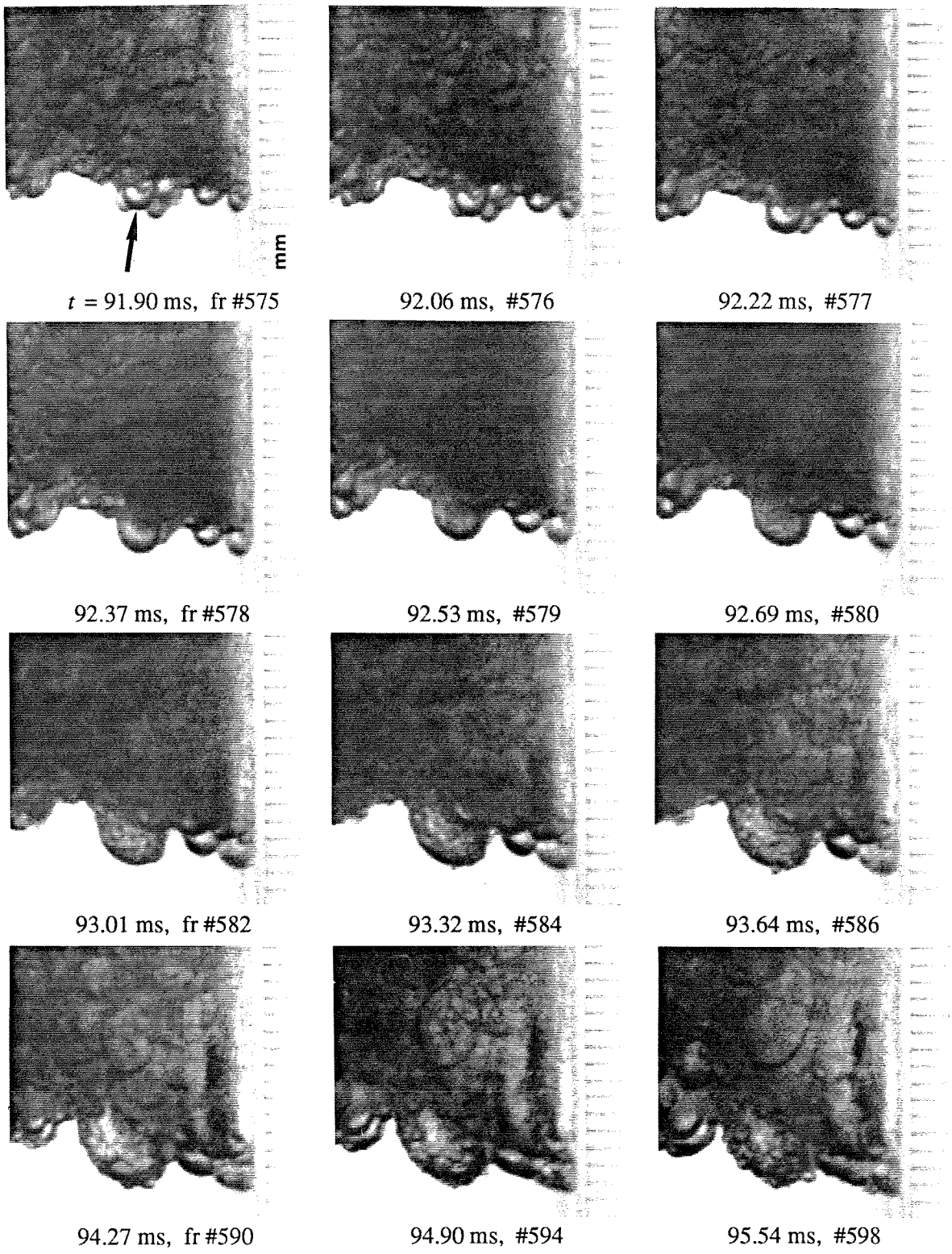

Figure 4.12: Sequence of high-speed motion pictures illustrating a surge in wavefront velocity by the growth of a "rough" bubble. Liquid: R12, T_0 = 20°C, P_{res} = 1 bar, Divisions: mms, Test cell #: 2, Run #: MPR 31.

The second cause of velocity surges is illustrated in Figure 4.12, which shows a sequence of high-speed motion pictures taken from the same run as Figure 4.11. In frame 575, a bubble structure (denoted by the arrow) has grown to a diameter of about 2 mm. Meanwhile, a burst (which can be identified as being relatively dark compared to the surrounding aerosol) starts on an adjacent region of the leading edge. Because of the inclination of the wavefront, the burst appears above and to the right of the structure in question. In subsequent frames, the bubble structure grows, and the burst spreads to the left across the leading edge. In frame 578, it appears that aerosol from the burst (which appears dark) may be in the process of spraying into the upper right portion of the structure. In the following two frames, the structure appears dark and rough. The time at which roughness is first observed (i.e., frame 579) corresponds to a velocity peak on the $v-t$ diagram. The rough, fine-scale perturbations grow so that, after a few hundred microseconds they appear smooth (frame 582). By frame 598, the new structures, discrete and round in appearance, can be clearly seen on the face of the original bubble structure.

The fact that the bursts seems to precede the roughening can be taken to suggest that the latter is caused by aerosol splattering the surface of the structure. Because the thermal boundary layer is thin (Section 4.1.3), it would appear likely that the surge in velocity in this case is due, in part, to the sudden fine-scale perturbation of the interface, which evidently both enhances the interfacial area and brings hotter liquid to the surface. This observation suggests the possible relevance of *evaporative interfacial instability* hypotheses, which will be considered in Chapter 6. As in other cases, it cannot be proven whether the bubble structure of interest was initially a closed floating bubble or an open perturbation prior to the influx of aerosol in frame 578. If it is in fact a floating bubble, then the blast of aerosol would rupture its film cap prior to splattering the free surface. Thus, in either case, the structure is an open perturbation by frame 578.

By frame 598 the new structures look very much like bubbles at a free surface (Figure 4.7b). If this is the case, the source of nucleation would appear to be small droplets—too small to detect individually—striking the leading edge. As will be discussed in Chapter 6, droplets striking a liquid free-surface have in some cases been shown to cause vapor entrainment, and hence bubble nucleation. In the present experiments, nucleation of bubbles by liquid droplets is observed in certain runs with bubbly upstream liquid (Appendix C).[5] These observations

suggest that a previous idea regarding boiling at a free surface, called the *secondary nucleation* hypothesis (Mesler, 1988), may be relevant in the present experiments (Chapter 6).

4.2.2.4 Growth Rates of Leading-Edge Bubble Structures. Figure 4.13 shows growth rates of three selected leading-edge bubble-structure samples for R12 and 0 bar reservoir pressure. Motivated by the classical theory for a spherical bubble in an infinite superheated liquid (Figure 4.7a), the radius is plotted as a function of the *square root* of time. Although no leading edge bubble structures are completely immersed in liquid, it is suggested that they should nevertheless approximately follow the classical theory if in fact they are floating bubbles (Figure 4.7b). The reason is because at the observed Bond numbers, floating bubbles are constrained almost completely beneath the free-surface, and the areas of their film caps are small compared to the total surface area (Section 4.2.1.2).

For sufficiently large classical bubbles in a superheated liquid, the simple analysis for thermal bubble growth (Equations 1.12) is adequate. By comparing the inertial and thermal terms in the Rayleigh-Plesset equation, the size at which thermal effects begin to dominate can be estimated (Brennen, 1973):

$$R_{th} = O\left[Ja_1^{\frac{3}{2}} \left(\frac{c_p T_{1,s}}{L_1} \right)^{\frac{1}{2}} \left(\frac{\rho_{l1,s}}{\rho_{v1,s}} \right)^{\frac{5}{2}} \frac{\kappa_{l0}}{\sqrt{L_1}} \right] \tag{4.8}$$

For the conditions of the present experiments, R_{th} is of order 10 microns, which is about the limit of resolution of the still photographs. The thermally-limited solution is therefore adequate.

The solid line is the theoretical prediction, the "+" symbols are the data points, and the dotted lines connect the data points for each sample. The samples are taken from side view motion pictures, and the bubble diameter d_b is taken as the maximum width. The samples are

5. Appendix C discusses situations in which nucleation (accidentally) occurs at the test cell wall below the level of the initial free surface.

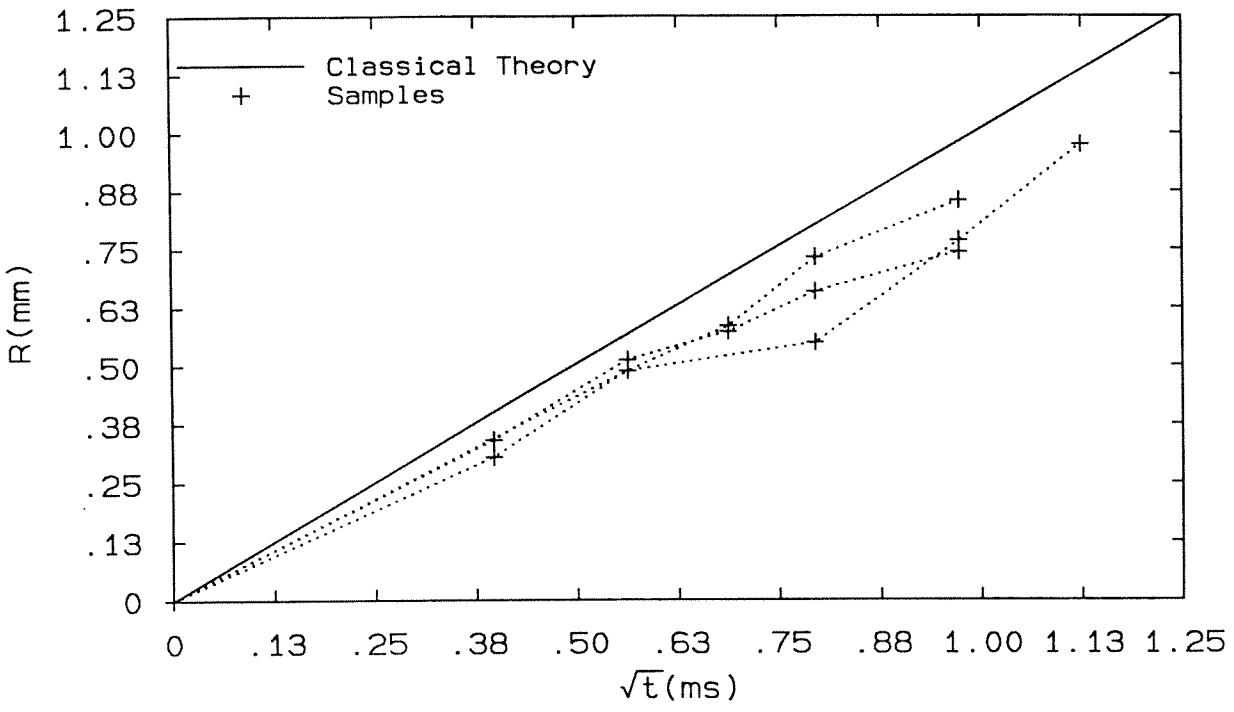

Figure 4.13: Growth rates of three selected leading-edge bubble samples compared to the classical theory for a bubble growing in an infinite superheated liquid. Liquid: R12, T_0 = 20°C, P_{res} = 0 bar, Run #: MPR 25.

not chosen at random, as there are some restrictions as to what constitutes a useful sample. The bubbles must be visible from the time of nucleation (to define the time origin), they must have sufficiently long lifetimes so that several data points can be obtained, and they must be clearly visible (i.e., not obscured by neighboring bubbles) during their lifetimes. The biggest error associated with bubble-growth measurements is that there is one frame ambiguity as to when the bubble first appears. The time origin is assigned to the frame preceding the first appearance of a bubble.

To within experimental error, the growth rate of bubble samples has the $\sqrt{t}$ time dependence as does classical thermal bubble-growth theory, but the growth rate is slightly slower—in this case 87% of that predicted by the classical expression. The other five run conditions show qualitatively the same behavior. This result is qualitatively consistent with the floating bubble structure of Figure 4.7b, because the film side of the bubble contributes less heat flux, and therefore less mass flux, than the upstream side that is immersed in the superheated liquid.

Define the parameter η to be the efficiency of leading-edge bubble growth compared to ideal theory, in which case the expression for leading-edge bubble growth is:[6]

$$R = \eta\left[\frac{12}{\pi}\right]^{1/2} Ja_1 \frac{\rho_{l1,s}}{\rho_{v1,s}}\sqrt{\kappa_{l0}t} \; ; \quad Ja_1 \equiv \frac{\Delta h_1}{L_1} \; , \quad \Delta h_1 = h_{l0} - h_{l1,s} \tag{4.9}$$

One can modify the classical expression for thermal boundary-layer thickness using the efficiency η, to obtain:

$$\frac{\delta_{ns}}{R} = 0.35\left[\frac{1}{\eta Ja_1}\right]\left[\frac{\rho_{v1,s}}{\rho_{l1,s}}\right] \tag{4.10}$$

where the subscript *ns* denotes "nonsteady". The constant 0.35 has been chosen to be consistent with the definition of δ_{avg} (Equation 4.6). For the example of R12 and 0 bar reservoir pressure, δ_{ns} is 3 μm for a 1 mm diameter bubble, which is about an order of magnitude greater than the estimate for δ_{avg}. The disparity between these two values is perhaps due to a very heterogeneous temperature field near the wavefront leading edge.

The growth efficiency η would be most useful if it were the same for all run conditions. To test whether this is so, Equation 1.12b is rearranged in dimensionless form:

$$R\left[\frac{\pi}{12\,\kappa_{l0}\,t}\right]^{1/2} = Ja_1\left[\frac{\rho_{l1,s}}{\rho_{v1,s}}\right] \tag{4.11}$$

so that all six run conditions can be plotted on the same diagram. The left-hand side of Equation 4.11 is an expression of the growth rate of a bubble, which is ideally equal to what will be referred to as the *modified Jakob number*, namely, the Jakob number defined in Equation 1.10 multiplied by the saturated liquid-vapor density ratio.[7]

---

6. Since the liquid thermal diffusivity varies as the 1/3 power of the liquid density, and the liquid density doesn't change significantly, the initial value of the diffusivity is used.
7. In the literature, this grouping is often referred to simply as the Jakob number.

The ideal dimensionless growth rate parameter (left-hand side of Equation 4.11) and the measured growth rate parameters for each of the six run conditions are plotted in Figure 4.14. The solid line is Equation 4.11. For each of the six run conditions there is a unique value of the modified Jakob number that is inferred from initial and saturated conditions, and the experimental data therefore scatter on vertical lines. For each run condition, the amount of scatter in the individual samples ("+" signs) is an indication of how well the dimensional data fall on a single $\sqrt{t}$ curve. The average value of the measured growth parameter is also shown: The circles are the three R12 runs; the triangles are the three R114 runs. For each liquid the superheat increases from left to right; however, note that the R114 points have a higher modified Jakob number than the R12 points even though they have lower superheat. If the bubble-growth efficiency η were universal, the average growth parameter would fall on a common line for all six run conditions. The four lowest modified Jakob numbers do approximately fall on a common line; however, the highest two do not. Hence, η must generally be specified for each run condition. The reason for the discrepancy in the cases with the highest two modified Jakob numbers is not understood.

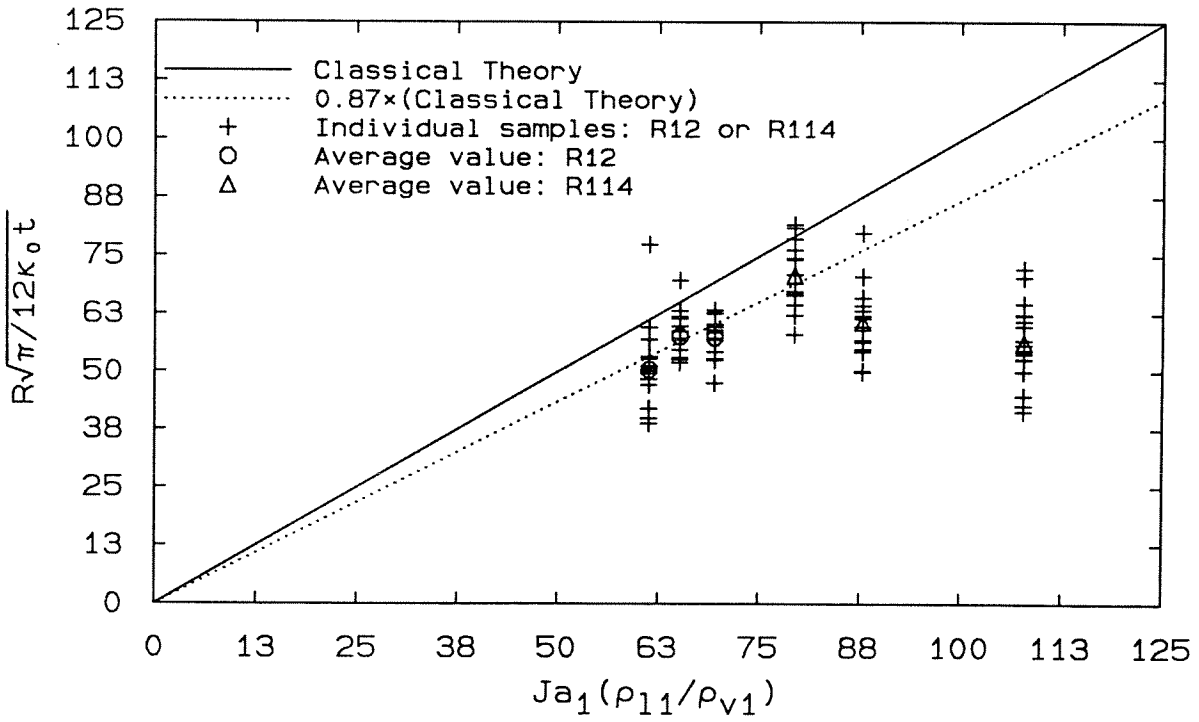

Figure 4.14: Dimensionless growth rates of selected leading-edge bubble samples for the six different run conditions, compared to the classical theory for a bubble growing in an infinite superheated liquid.

4.2.2.5 Lifetimes of Leading-Edge Bubble Structures. The lifetime of a bubble structure is defined as the length of time that it can be recognized as a distinct entity. The average lifetime is of order 1 ms for all six run conditions. Figure 4.15 is a histogram of 100 bubble lifetimes for the condition R12, P_{res} = 0 bar. The samples were taken from the bottom view, and were chosen according to the same restrictions as were the bubble-growth rates (Section 4.2.2.4). The reason for using the bottom view is that there are many more samples to choose from. Figure 4.15 shows that the lifetimes of bubbles are statistically distributed. Thus, there is not a single "critical" time or size at which bubbles disappear. In this case the most probable lifetime is about 1 ms, but a few bubbles last about five times this value. The bubbles with smaller lifetimes are likely to be under-represented, as they are harder to see because of the limited resolution of the film. The distribution of the corresponding maximum bubble diameters is qualitatively similar to the lifetime distribution.

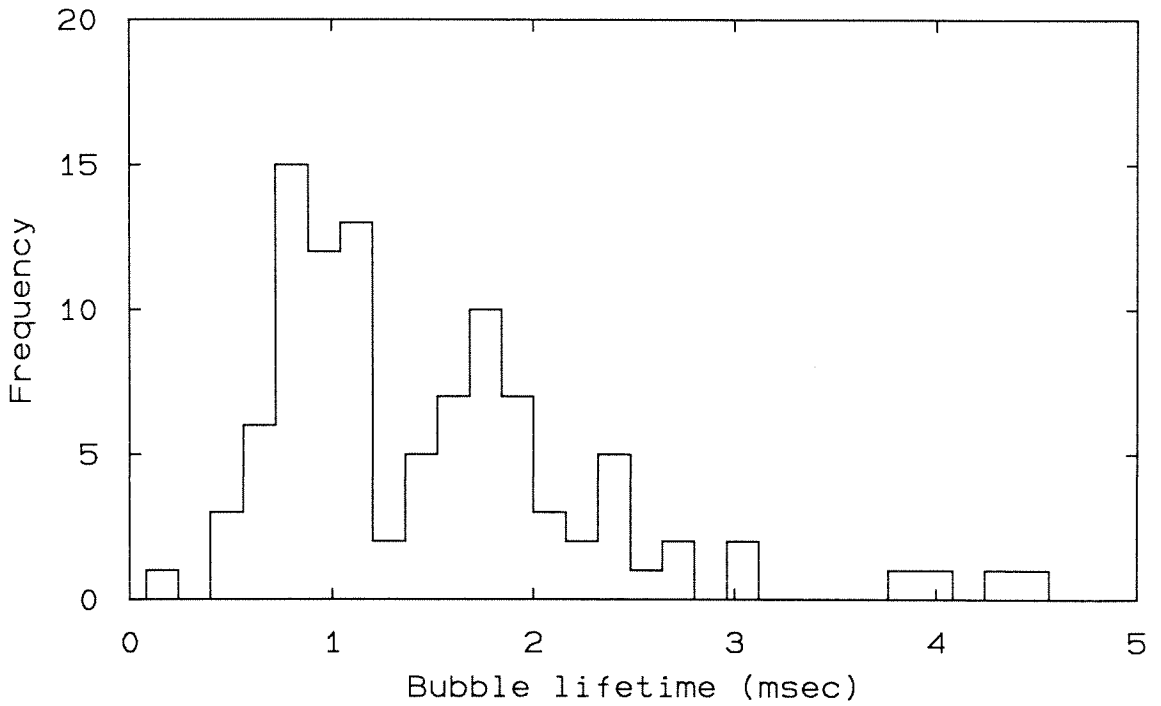

Figure 4.15: Lifetimes of 100 selected leading-edge bubble samples. Liquid: R12, T_0 = 20°C, P_{res} = 0 bar, Run #: MPR 25.

Observations regarding bubble disappearance vary between the bottom and side views. In the bottom views, many bubbles appear to be destroyed by bursts sweeping laterally through the leading-edge bubble layer. This is particularly evident in the runs with lower superheats (for each liquid), because in those cases the leading-edge bubbles tend to be larger (Section 4.2.1.2) and the bursts tend to be larger and less numerous (Section 4.2.2.2). In the side views, each bubble grows to a maximum size (which varies from bubble to bubble) and, in the absence of external influences, begins to recede and soon disappears behind a closer portion of the wavefront. This behavior is basically consistent with a floating bubble structure (Figure 4.7b), in that transition from growth to recession would occur upon rupture of its film cap.

4.2.2.6 Average Nucleation Rate. A rough estimate of the average nucleation rate[8] can be made using the observation that, because the wavefront processes are quasi-steady, the average number density of leading edge bubble-structures, n_a, per unit area of wavefront is constant. The characteristic time for replenishment of bubbles is the average bubble lifetime, $\overline{t}_b$, so the nucleation rate, ν_a, per unit area of wavefront is:

$$\nu_a = O\left[\frac{n_a}{\overline{t}_b}\right] \tag{4.12}$$

For the condition R12, P_{res} = 0 bar, ν_a is estimated to be of order 10^6 $s^{-1}cm^{-2}$. In cases with the lowest superheat, the nucleation rate is perhaps an order of magnitude lower.

4.2.2.7 Partial Model for Wavefront Propagation. In this section, an approximate expression for wave speed is obtained by considering the growth rate of individual bubbles, the characteristic bubble lifetime, and the intermittent nature of wavefront propagation. To keep the analysis simple, the statistical nature of the nucleation and bubble lifetimes is suppressed by considering an ensemble average over many events. The first assumption is that for each region of the leading edge there are two relevant time scales: the characteristic bubble lifetime,

8. In this section the term "nucleation" is used describe the birth of leading-edge structures whether or not they are in fact closed bubbles.

denoted by $\bar{t}_b$, and the characteristic time between nucleation events for that region, denoted by $\bar{t}_n$.

Next, the floating bubble structure of Figure 4.7b and the growth rate of Equation 4.9 is assumed. Let the bubble grow for a time equal to the characteristic lifetime $\bar{t}_b$, at which time it is assumed that no advancement occurs until the nucleation of the next bubble in that region at time $\bar{t}_n$. Clearly this is an idealistic picture, but it includes what is believed to be the essence of several important observed features.

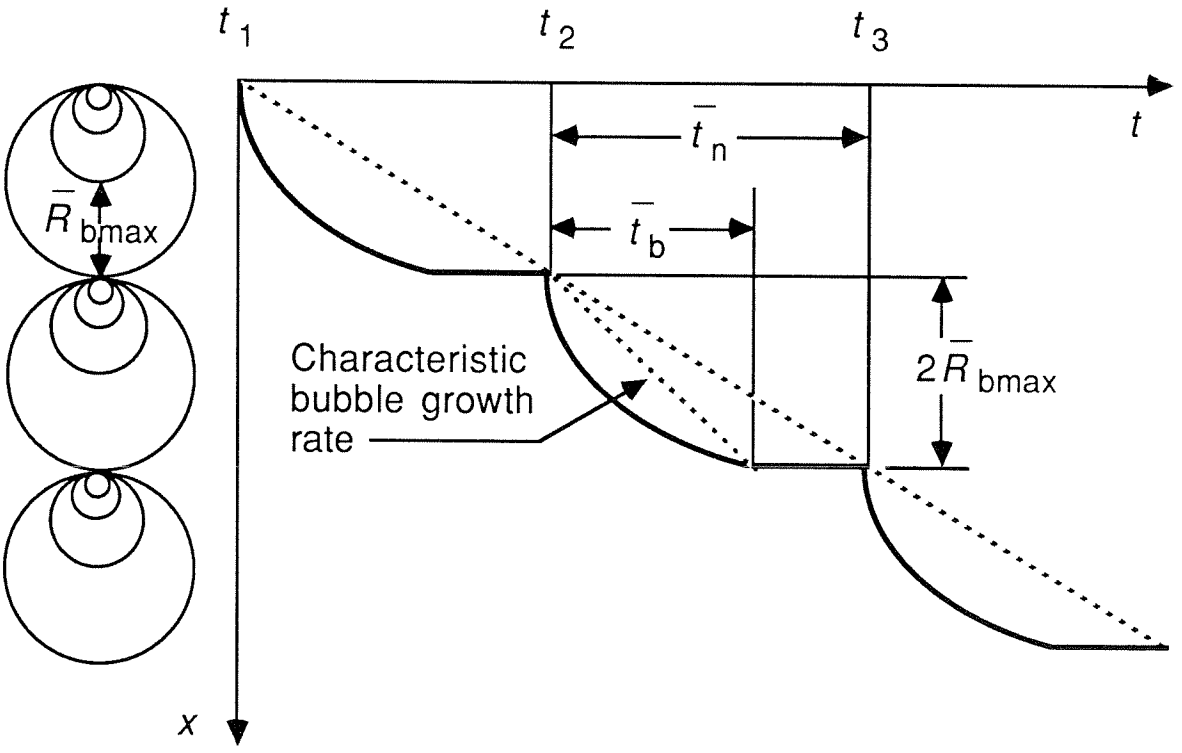

Figure 4.16: An approximate, partial wave-speed model in terms of leading-edge bubbles.

The average speed of the wavefront in Figure 4.16 is the slope of the dashed line:

$$V_w = \frac{2\bar{R}_{bmax}}{\bar{t}_n} \tag{4.13}$$

where $\bar{R}_{bmax}$ is the characteristic maximum size of a bubble, which is related to the characteristic lifetime through Equation 4.9. The two characteristic times, $\bar{t}_b$ and $\bar{t}_n$, can be

combined in a convenient way that separates the effects of bubble-growth rate and intermittent nucleation. In this model, the intermittency of propagation is defined as:

$$I \equiv \frac{\overline{t}_b}{\overline{t}_n} \; ; \; 0 < I < 1 \tag{4.14}$$

Inserting this definition of intermittency and the expression for the bubble growth rate (Equation 4.9) into Equation 4.13 yields:

$$V_w = \left[I \right] \left[\left(\frac{24}{\pi} \right) \eta Ja_1 \left(\frac{\rho_{l1,s}}{\rho_{v1,s}} \right) \left(\frac{\kappa_{l0}}{\overline{t}_b} \right)^{1/2} \right] \tag{4.15}$$

Equation 4.15 states that the wave speed depends on the product of two factors, the first representing the intermittency of nucleation and the second representing the characteristic growth rate of individual bubbles during their lifetime, $\overline{t}_b$ (the slope of the dotted line in Figure 4.16). It also suggests that the wave speed is proportional to the square root of the thermal diffusivity, which is a second result that parallels classical laminar flame theory (cf., Equation 4.6). The variables in Equation 4.15 can be estimated to provide a comparison to experiments. For R12 and 0 bar reservoir pressure, η = 0.87 (Figure 4.14) and $\overline{t}_b$ = 1.46 ms (Figure 4.15). The intermittency can be estimated from Figure 4.9b; it is about 0.5 ± 0.1. Inserting these values into Equation 4.15 gives a value of 0.5 ± 0.1 m/s, compared to the experimental value of 0.63 m/s. It should be stressed that Equation 4.15 is not a "solution" to the evaporation wave problem because most of the physical complexity is buried within the three measured quantities: I, η, and $\overline{t}_b$.

4.3. Developed Two-Phase Flow Region.

Downstream of the wavefront region, the average speed and appearance of the two-phase flow are nearly constant; hence, this region is referred to as the *developed flow region.* The issues regarding the developed flow region discussed in this section are the global and fine structure of the flow, and the relaxation length over which thermodynamic equilibrium is achieved. The average flow properties are discussed in Section 4.5.

4.3.1. *Flow Structure.* Figures 4.17 → 4.19 show photographs of the two-phase flow region for three of the six run conditions. The left photo in each figure is a print taken from a high-speed movie, which shows the development of the flow over several test-cell diameters. The right photo in each figure is a close-up still photograph, taken from a different (nominally identical) run at approximately the same time. In each case the initial liquid level was 10.0 cm.

It is apparent from both the movies and the still photos that the two-phase flow is spatially nonuniform; however, the flow structure appears somewhat different in the two cases because of the difference in exposure time. For the example of R12 and P_{res} = 0 bar, the flow speed is 35 m/s. The exposure time of the high-speed movies is 63 μs in this case, which corresponds to an axial blur of about 2 mm in the flow region. The exposure time of the still photographs is approximately 1 μs, which corresponds to an axial blur of about 35 μm. Hence, the movies show blurred flow features, whereas the still photographs are essentially "stop action."

In the high-speed motion pictures, the flow appears streaky, similar to the impulsively started gas-particle flows observed by Anilkumar (1989). The streaks are regions with a relatively high number density of scattering centers. A grey scale in the high-speed photographs indicates that the dark streaks attenuate the light by about a factor of 100, the lightest areas by about a factor of 10. There may be several reasons for the observed global nonuniformities in the present flows. Anilkumar (1989) has shown that uniformly dispersed flow patterns can be inherently unstable. However, in the present experiments the flow is spatially and temporally nonuniform from the source, since it is generated by the bursting process in the wavefront region (Section 4.2.2.2). In addition, there is a coupling between the two-phase flow pattern and the global shape of the wavefront leading edge.

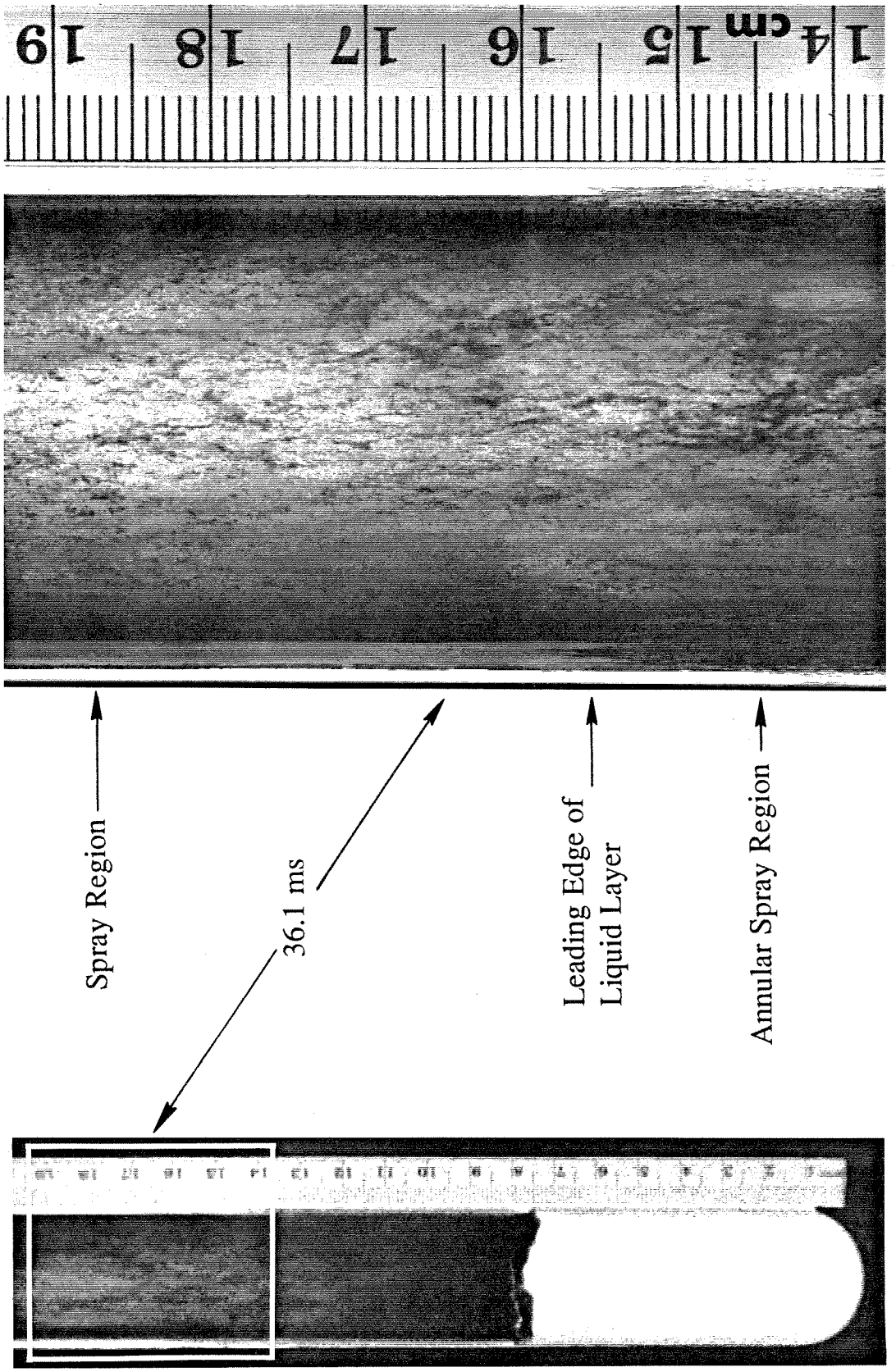

Figure 4.17: Developed two-phase flow region. Liquid: R12, T_0 = 20°C, P_{res} = 0 bar, x_0 = 10.0 cm, Test cell #: 1, Run #'s: MPR 76, SPR 22.

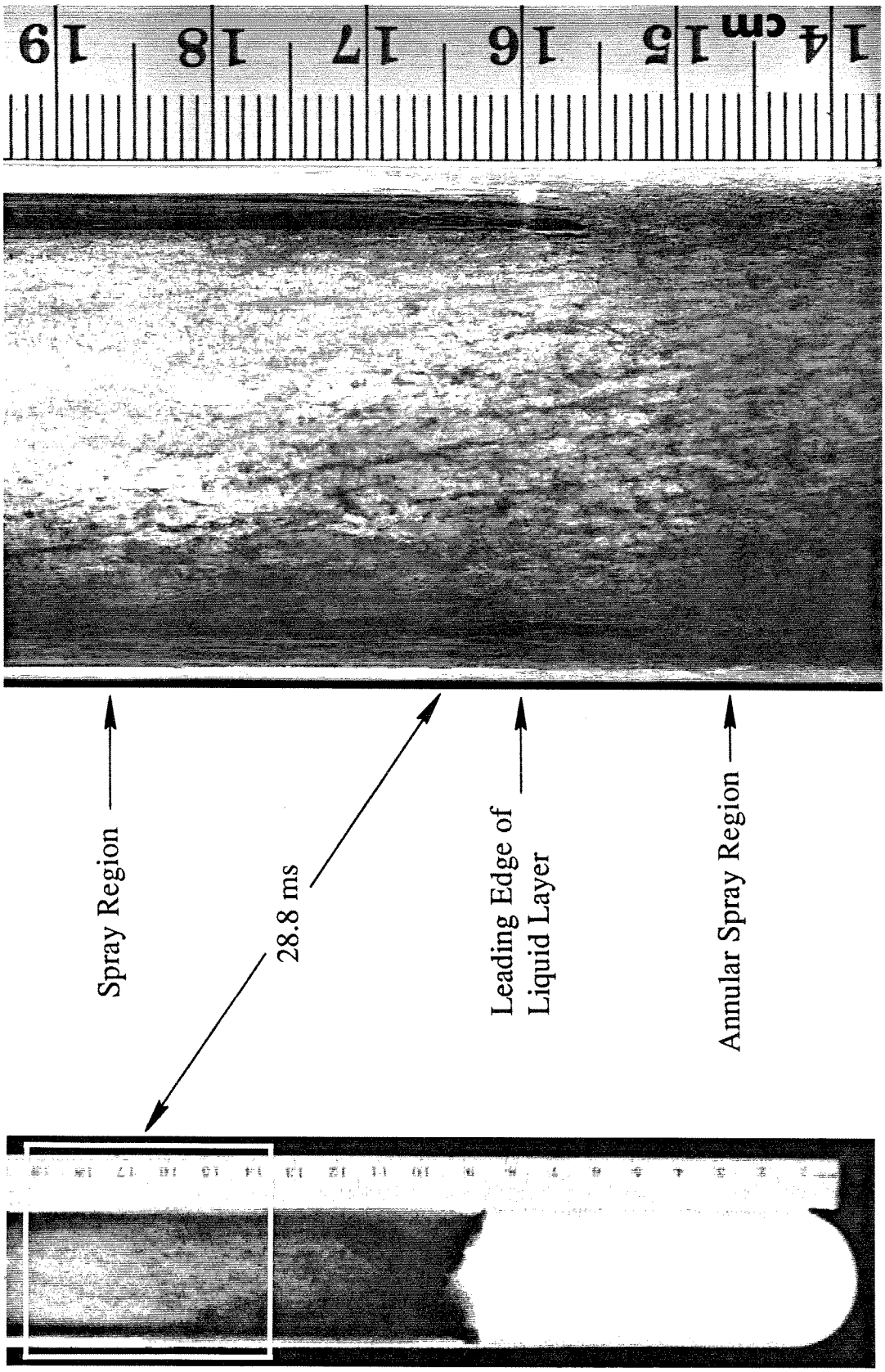

Figure 4.18: Developed two-phase flow region. Liquid: R12, T_0 = 20°C, P_{res} = 1 bar, x_0 = 10.0 cm, Test cell #: 1, Run #'s: MPR 78, SPR 24.

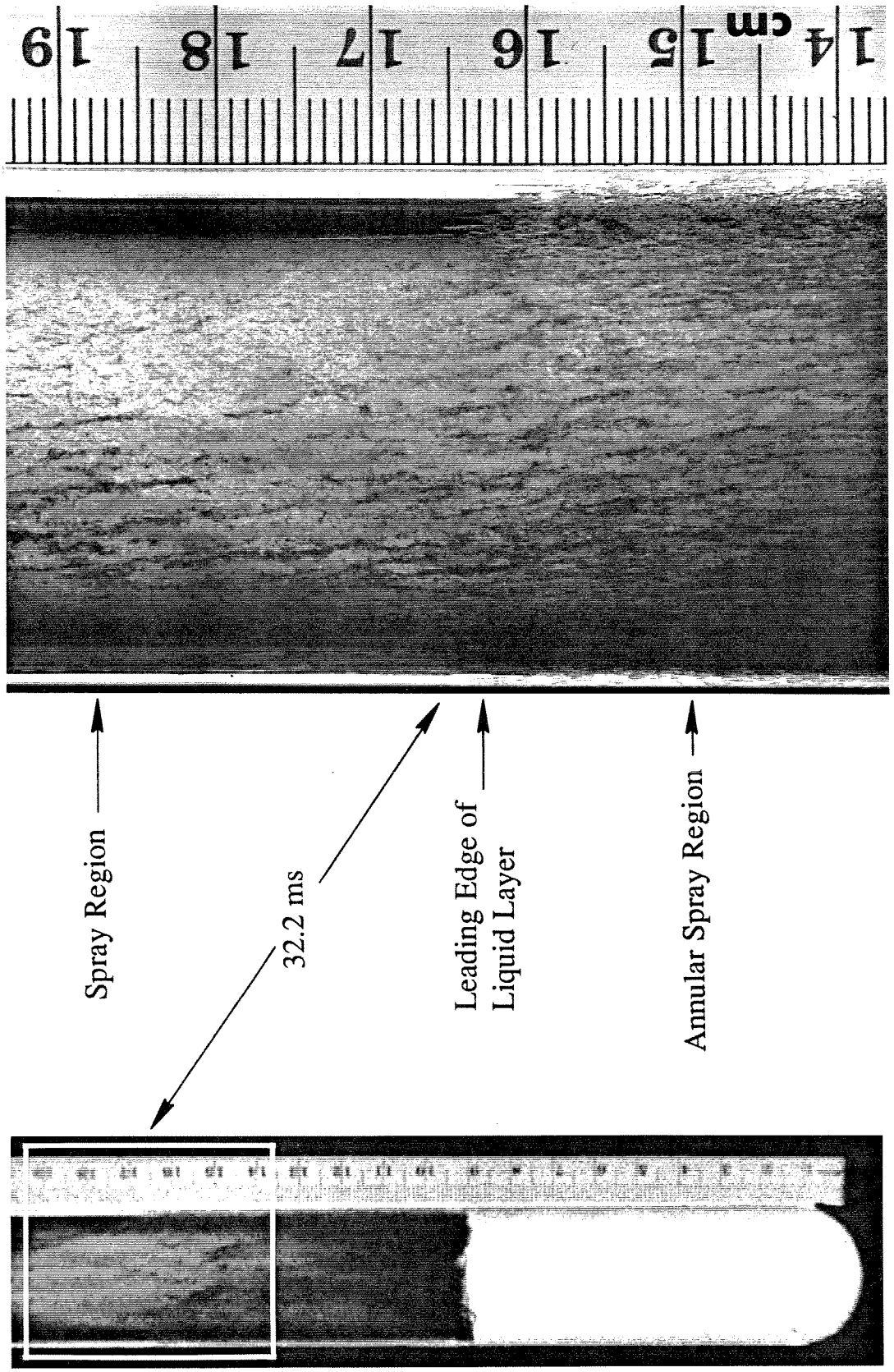

Figure 4.19: Developed two-phase flow region. Liquid: R114, T_0 = 20°C, P_{res} = 0 bar, x_0 = 10.0 cm, Test cell #: 1, Run #'s: MPR 77, SPR 25.

The flow tends to emanate from the wavefront in a direction approximately normal to the direction of the local wavefront leading edge, and consequently tends to concentrate in regions where the wavefront is concave up, and thin in the regions where the wavefront is convex up. Figure 4.3 shows a good example of this behavior. Farther downstream (several test-cell diameters), the flow often concentrates on one side of the test cell, leaving the flow on the opposite much thinner.

Because of the shorter exposure time, the flow appears more "splotchy" than "streaky" in the still photographs. Upon close inspection of the dark splotches in the original prints of Figures 4.17 → 4.19, it is seen that in many cases they appear to be clusters and chains of small bubbles, rather than denser clouds of aerosol as would be expected. Admittedly, it is difficult to distinguish small drops from bubbles in still photographs; however, for one experimental condition in particular (namely R12, P_{res} = 1 bar) the flow is slow enough and the bubbles large enough, that the latter can be seen to rupture within the flow. In the still photographs, bubbles can be inferred whenever two spherical objects in question are observed to touch, as appears to be the case with the clusters and chains mentioned above. This is because drops, upon touching, immediately merge due to surface tension.

The maximum bubble diameter tends to decrease as the superheat (and flow speeds) increase; this behavior is expected because smaller bubbles are more stable than larger bubbles because of the greater influence of surface tension. The largest flow bubbles observed in the highest superheat cases for each liquid are a few hundred microns in diameter; whereas, the largest bubbles observed in the lowest superheat cases for each liquid (Figures 4.17 and 4.19) are of order 1000 μm in diameter. High-speed movies indicate that the order 1000 μm diameter bubbles tend to be on the wall. That bubbles this large survive for any amount of time can probably be attributed to the fact that the speed of the inner flow in the lowest superheat cases is significantly less than in the higher superheat cases (Table 4.1, Section 4.5.3).

The origin of bubbles in the flow is not resolved in the photographs. One possibility is that they are the smaller, more stable leading-edge bubbles that survive fragmentation. The question then arises as to how such bubbles would be extracted from the leading-edge region without rupturing, since it is unclear how this would occur in the case of a floating bubble (Figure 4.7b). It would appear that only leading-edge bubbles that become completely surrounded by other bubbles have the potential of escaping from the wavefront intact, as such bubbles could be freed

by the break-up of interstitial liquid. It is also possible that flow bubbles are created by a different mechanism, perhaps related to bursting.

Much of the liquid phase (though the fraction is unknown) appears to be in the form of an aerosol. This component of the flow appears lighter and more uniform (but often "mottled") than the splotchy structures described above. The maximum scale of this dispersed liquid appears to be about 100 μm. There may well be many smaller droplets, but they are not detectable in the present experiments because of limited photographic resolution.

A notable feature of the left-hand prints of Figures 4.17 → 4.19 (which are taken from high-speed movies) is that the flow clears significantly downstream of the fragmentation/acceleration region. Some of the clearing may be attributable to the lateral consolidation of the dispersed liquid phase into streamers, as mentioned above. Other regions would thereby be left comparatively void of spray and hence more transparent to light. Some clearing of the flow is also expected to be associated with axial acceleration, most of which occurs within the first centimeter or so of the wavefront leading edge. As a mass of fluid expands, the average distance between droplets increases while, to a reasonable approximation, the droplet size remains the same.[9] If one adopts an average picture of the flow at each cross-section and assumes that the number of scattering centers is conserved, the one-dimensional continuity equation dictates that the number density of scattering centers decreases in inverse proportion to the flow velocity.

Two characteristic flow speeds are detectable in the high-speed movies. The first is associated with the high-speed (order 10 m/s) flow through the center, as has been described above. The second is associated with a much slower (order 1 m/s) liquid layer on the test-cell wall, which is pulled up by shear stress caused by the high-speed inner flow. In the two-phase flow literature such flows are classified as "annular sprays" (Wallis, 1969). One might expect

9. The droplet size decreases somewhat as a result of evaporation, but because the density of the liquid is very much larger than that of the vapor, the effect is small. In fact, for the example of R12, P_{res} = 0 bar, energy considerations dictate that the maximum possible diameter decrease of a droplet as it convects downstream is 30%. This condition occurs when the droplet has reached the saturation temperature.

that the liquid layer would form uniformly on all portions of the wall simultaneously soon after the two-phase flow is established, but this is not the case. Instead, liquid initially attaches to the wall only in the vicinity of the free surface. A front of liquid then climbs up the tube, ahead of which the wall is virtually liquid-free, and behind which it is coated with a rough liquid layer that appears to be about 100 μm thick. The features of the liquid layer in Figures 4.17 → 4.19 are subtle. It is primarily visible at the edges of the photographs; away from the edges its presence can be inferred by the slight optical distortion that it imposes on the interior flow. The pictures in Figures 4.17 → 4.19 are timed such that the liquid layer takes up about the bottom third of the still photographs. The leading edge of the liquid layer is seen to have a jagged structure, with long protruding "fingers." The liquid layer is more noticeable in the high-speed movies because of its motion, especially in the oblique views.

Figure 4.20 is an $x-t$ diagram showing the three "fronts" visible in the high-speed movies, for the case of R12 and 0 bar reservoir pressure. When explosive boiling initiates (1) a two-phase front travels up the tube at 45 m/s, (2) the leading edge of the liquid layer climbs the wall at 1.5 m/s, and (3) the wavefront propagates into the liquid at 0.64 m/s. Thus, the flow can be divided into two subregions, the *spray region* (no liquid layer) and the *annular spray region* (with liquid layer).

Since in the early stages the test-cell wall is much hotter than the liquid cooled by evaporation, it appears likely that it is the *Liedenfrost* effect that prevents liquid from attaching to the wall at early times. The attachment of the liquid layer near the initial free surface upon explosive boiling initiation may in part be caused by increased heat transfer due to lateral motion of bursts. It may also be caused by the boundary condition at the wavefront leading edge, namely, that cold liquid in the region of the leading edge is necessarily in contact with the wall. As the layer is pulled up the wall, some of the liquid near its leading edge evidently evaporates, thereby cooling the new territory gained.

In the high-speed movies it is clear which features are on the wall and which are in the center, because of the significant difference in speeds. In the still photographs, almost all features can be ascribed to the central flow before the arrival of the liquid layer; however, a judgement must be made by comparison to the high-speed movies in regions where the liquid layer is present. On the basis of such a comparison, it appears that in the two highest superheat cases for each liquid, most of the observable features are in the central high-speed flow. As

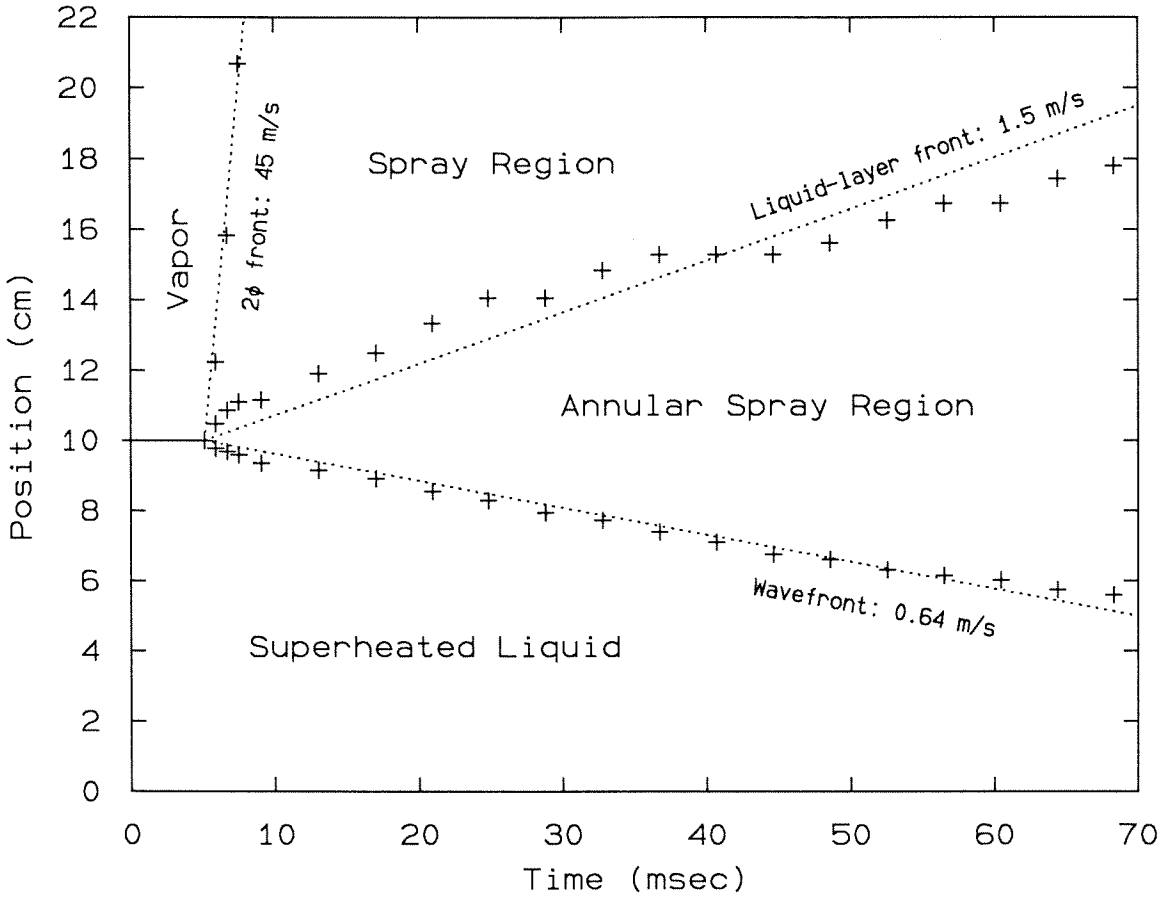

Figure 4.20: $x-t$ diagram showing the three fronts and four axial-position/time regions. Liquid: R12, T_0 = 20°C, P_{res} = 0 bar, Test cell #: 1, Run #: MPR 76.

mentioned above, high-speed movies indicate that the larger (order 1000 μm diameter) bubbles that appear in the lowest superheat cases for each liquid tend to be on the wall.

4.3.2. *Relaxation Length for Evaporation.* The relaxation length for evaporation is defined as the distance downstream of the wavefront at which the flow can be considered to have reached a saturation condition, by some chosen criterion. Since flow models generally assume that the flow has reached thermodynamic equilibrium, the relaxation length is of practical interest. The preferred method of judging the extent to which equilibrium is achieved would be to measure the local temperature and pressure at a desired axial station, and to compare the measured pressure with the vapor pressure corresponding to the measured temperature. However, the flow temperature was not measured in this study, and an approximate estimate is therefore made on the basis of visual observations.

Consider a liquid droplet generated at the wavefront, of diameter d_d. The droplet partially evaporates as it is carried downstream at the two-phase flow velocity V_2. As noted in the previous section, the decrease in droplet diameter is modest because of the large difference in liquid and vapor densities. Assume that heat transfer within the drop is primarily conductive, and that cooling proceeds toward the center of the drop via a thermal layer whose thickness is of order $\sqrt{\kappa_{l0} t}$, where κ_{l0} is the thermal diffusivity and t is the time relative to drop formation. Let the relaxation time be defined as the time at which the thermal boundary layer reaches the center of the drop, and the relaxation length be defined as the distance that the drop has convected relative to the test cell in the relaxation time.

To determine the extent to which equilibrium is achieved in the present experiments, the relaxation length is equated with the length of the test cell, and the drop diameter is determined for which the equilibrium criterion is satisfied at the test-cell exit. The result is:

$$\frac{d_d}{l_{tc}} = 2\left[\frac{\kappa_{l0}}{V_2 l_{tc}}\right]^{1/2} = 2\,Pe^{-1/2} \tag{4.16}$$

where d_d is the drop diameter and l_{tc} is the test-cell length. The dimensionless group inside the radical is the inverse of a Peclet number Pe and is abbreviated as such.

Figure 4.21 is a map of equilibrium conditions for the present experiments. Each run is associated with a single value of Pe. The maximum and minimum values of Pe for the six run conditions are shown in the figure as vertical lines, and lines of constant droplet diameter are horizontal. Equation 4.16 is shown as the solid line, below which the flow is in equilibrium by that criterion. For all run conditions, the droplet diameter that just reaches equilibrium at the exit is between 10 and 100 μm. The cases with lower superheat are closer to equilibrium for a given droplet size because the flow is slower. However, the difference between the extreme cases is rather modest. In light of the discussion of the fine-scale properties of the flow (Section 4.3.1), the strongest statement that can be made is that for all the run conditions, the test-cell length is the right order of magnitude to expect equilibrium to be achieved at the test-cell exit; however, equilibrium is not likely to be achieved within the wavefront region.

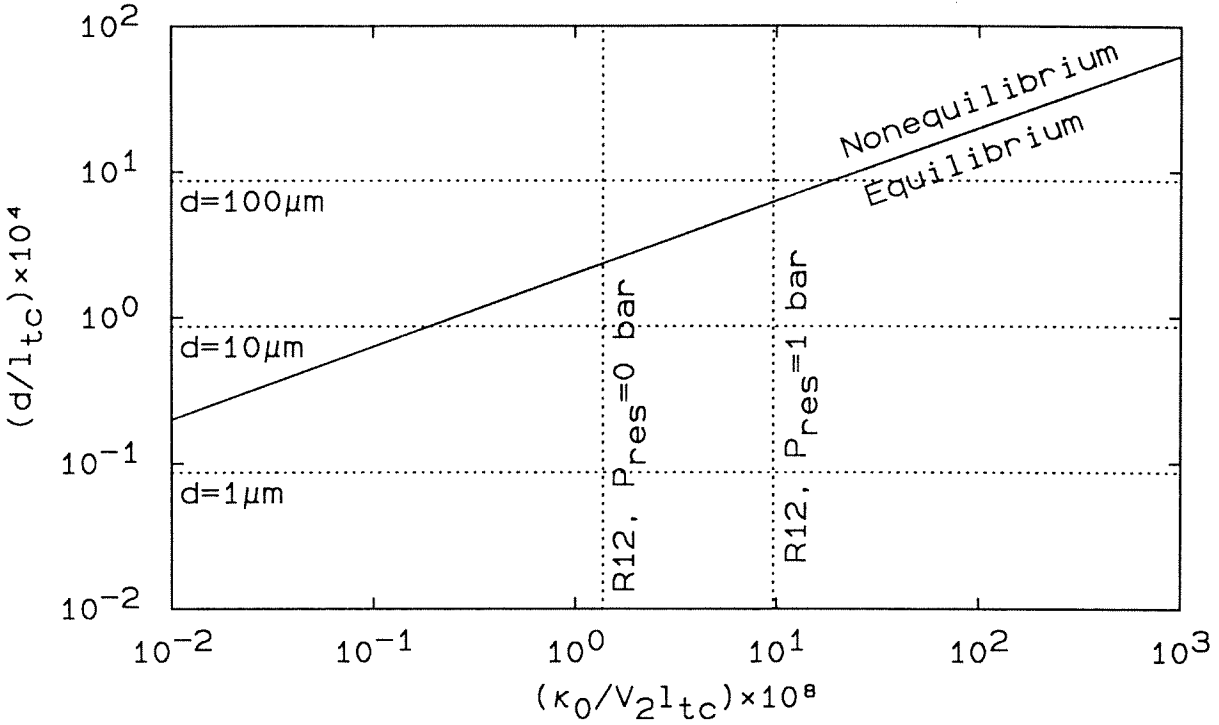

Figure 4.21: Relaxation lengths for evaporation of liquid droplets.

4.4. Absolute Threshold.

For both liquids at the given temperature (i.e., 20°C), there is a threshold reservoir pressure above which the wave will not start. This condition is referred to as the self-start threshold (to be discussed in Section 5.3). Near the self-start threshold, the wave is observed to have difficulty starting, as is evident by increasingly long delays in the initiation of explosive boiling as the threshold reservoir pressure is approached. Nevertheless, waves appear vigorous, once initiated. This observation suggests that waves might propagate at lower superheats if started artificially. The ultimate test of whether a wave is able to propagate at a given condition is somehow to start the quasi-steady explosive boiling process, and to determine whether that process is able to sustain itself.

It is found that over a modest range of pressures above the self-start threshold value, waves in R114 can be started artificially by the following "jump-start" procedure. The test cell is filled part-way with dyed R114, then is filled further with R12. The R12 and R114 are miscible; however, R114 is denser, so the liquids are stably stratified. Mixing is thereby confined to a

layer that is a few millimeters thick. R12 is significantly more volatile than R114: At 20°C, the vapor pressure of R12 is about three times that of R114. Hence, waves can be started in R12 at pressures for which the R114 cannot. The object is to see under what conditions the wave established in R12 is able to continue propagating in the R114.

The reservoir pressure corresponding to the self-start threshold for R114 at 20 °C is found by trial and error to be 1/3 bar. Likewise it is found, using the jump-starting technique, that quasi-steady waves in R114 at 20°C can be sustained at reservoir pressures up to 1/2 bar. The latter condition represents the *absolute threshold* for wave propagation. The wave speed in R114 just above the absolute threshold is 0.21 m/s, the slowest yet observed.

Figure 4.22 shows a photograph taken from a high-speed movie of a run at the absolute threshold. The R114 is filled to the 6.3 cm mark, and the R12 was initially filled to the 9.5 cm mark. The diffusion layer between the two liquids is about 4 mm thick. The R114 is dyed and appears slightly darker than the R12. The wavefront is in the R12, approaching the R114.

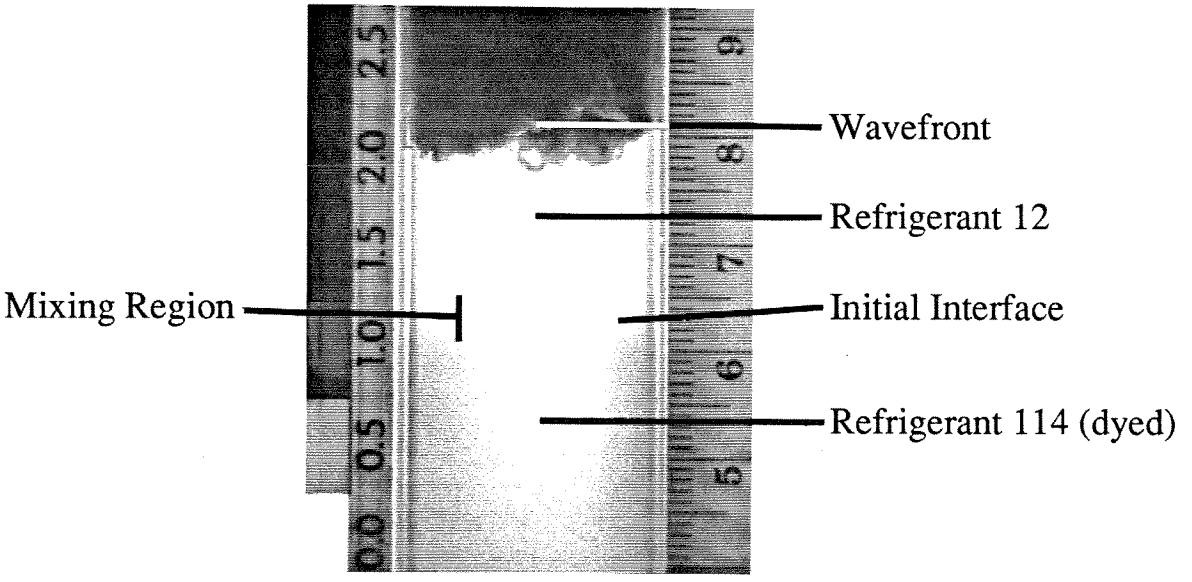

Figure 4.22: "Jump-start" run using R12 over R114. T_{l0} = 20°C, P_{res} = 1/2 bar, Test cell #: 2, Run #: MPR 72.

As the absolute threshold is approached, bursting becomes increasingly sporadic, and the absolute threshold is coincident with the complete breakdown of the bursting process. This is illustrated in Figure 4.23, which shows a sequence of photographs taken from high-speed motion pictures, later in the same run that is shown in Figure 4.22. At the time of the first

photograph (which is assigned time t = 0), the wave has propagated in the R114 for 2.0 cm. The last burst is in progress in the first photograph. This event marks the end of explosive boiling and wave propagation. In subsequent frames "quiescent" boiling occurs, but there is no advancement of the leading edge. Bubbling persists for several hundred milliseconds, and since in this regime there is no mechanism for efficient fragmentation of bubbles, they grow large to form a "froth." Eventually, the remaining liquid becomes sufficiently cold that all bubbling ceases. The base pressure at the absolute threshold (see Figure B.7, Appendix B) reflects the sporadic nature of the bursting prior to complete wave breakdown: Between bursts, the base pressure is the reservoir value; during a burst, the pressure pulsates slightly above the reservoir value. The run illustrated in Figures 4.22 and 4.23 was very fortuitous, in that it is the only case in which the wave is observed to stop in mid-run. The absolute threshold is sufficiently sensitive so that in the other cases tried, the wave typically either consumed all or none of the R114.

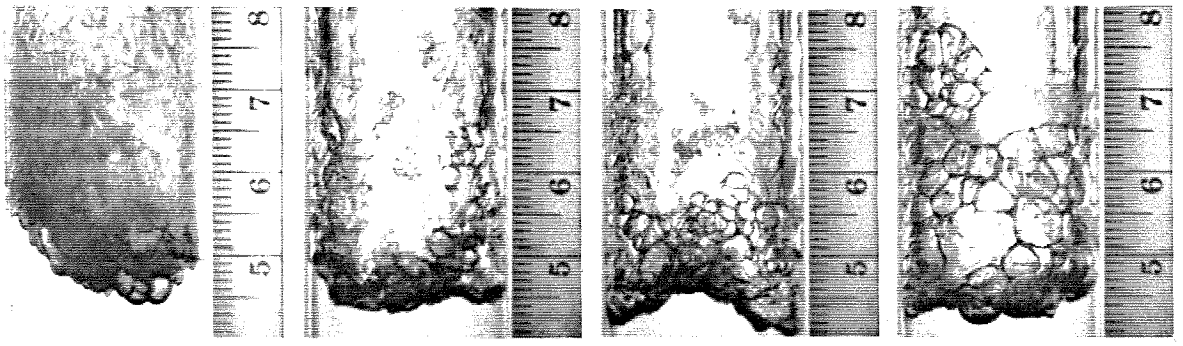

Figure 4.23: Sequence of photographs showing wave breakdown at the absolute threshold. Liquid: R114, T_0 = 20°C, P_{res} = 1/2 bar, Test cell #: 2, Run #: MPR 72.

The significance of the observations at the absolute threshold is that one cannot achieve an arbitrarily weak evaporation wave, as would be permissible from mass, momentum, and energy considerations alone (c.f. Chapter 7). The basic reason is clear from the above discussion; namely, the physical processes that drive explosive boiling occur only if the liquid is sufficiently superheated, and not at all below the critical superheat.

4.5. Summary of Average Wave Properties.

In this section, the measured average wave properties, together with those properties that can be directly inferred from them, are presented for the six run conditions. The methods of measurement and calculation are discussed first; presentation and discussion of the results follow.

4.5.1. *Measured Properties.* The directly measured properties are the initial pressure, the base and exit pressures during the run, the wave speed, and the two-phase flow speed. Mean base and exit pressures are obtained by averaging the instantaneous pressures over the duration of the quasi-steady propagation phase. In Section 2.2.1 it was mentioned that response of piezoelectric transducers decays with time, and in the present experiments this decay is a few percent.[10] Therefore, in computing the average pressures during a run, a linear correction is made that uses nitrogen calibration runs as a basis for comparison.

The average wave speed is obtained from high-speed movies by taking the average slope of the $x-t$ diagram of the wavefront leading edge (e.g., Figure 4.9a) during the quasi-steady propagation phase. The average two-phase flow speed is obtained from high-speed movies by observing the motion of large-scale structures. The accuracy of this technique is limited by the temporal resolution of high-speed movies (Section 4.3.1). The assumption is also made that the speed of the large-scale structures is representative of the average flow speed.

4.5.2. *Inferred Properties.* For the runs in which the exit is choked, the two-phase flow speed can be inferred from the base and exit pressure traces as follows. It first is assumed that the speed and properties of the mixture are uniform over the length of the test cell when the wavefront reaches the bottom, and that the flow at this time is representative of other times during quasi-steady propagation. These assumptions appear to be valid on the basis of visual observations. When the wavefront reaches the bottom of the test cell, a reflected expansion wave travels back up the tube to the test-cell exit, and is detected at both the base and exit

10. The decay at early times is greater than would be expected based on the discharge time constant, due to a departure from the ideal (exponential) behavior.

transducers. The head of this wave travels at the sound speed with respect to the mixture, which in turn travels at the sound speed with respect to the test cell because the exit is choked. Hence the head of the expansion wave travels at twice the sound speed with respect to the test cell. The flow speed can therefore be determined by the time of flight Δt_{tc} between the base and exit transducers, which is indicated in Figure 4.24 for the example of R12, P_{res} = 0 bar.

The superheats ΔT_1, Δh_{l1}, and the Jakob number, Ja_1, are determined from the measured pressures and saturation data based on those pressures. The mixture density, ρ_2, and the mass flux, $\dot{m}$, make use of the one-dimensional mass conservation. Additional quantities, such as the mass and volume fractions of vapor, can be calculated if a more restrictive model is adopted. This is done in Chapter 7.

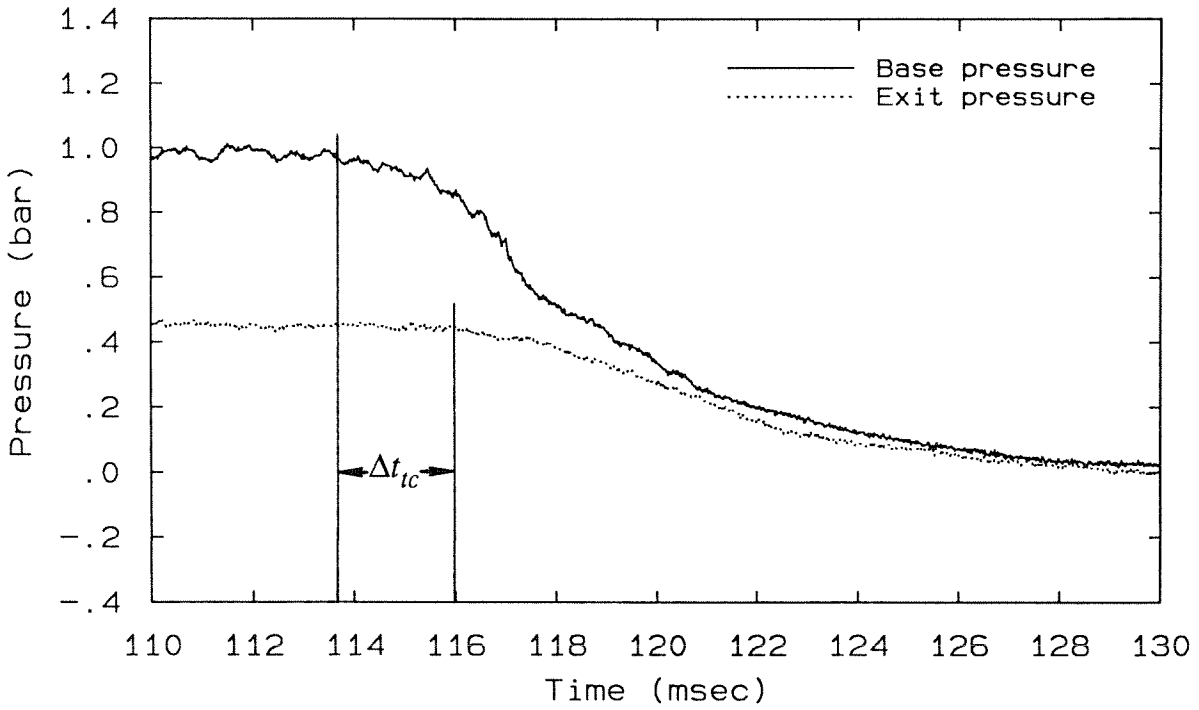

Figure 4.24: Inferring two-phase flow speed from base and exit pressure traces when the flow is choked. Liquid: R12, T_0 = 20°C, P_{res} = 0 bar, Run #: MPR 25.

4.5.3. *Discussion of Average Wave Properties.* The measured and inferred wave properties for the six run conditions are listed in Table 4.1. Recall that in all cases the temperature is 20°C. For both liquids the lowest pressure is 0 bar (actually, P_{res} < 0.01 bar). The highest

reservoir pressure for R12 (1 bar) and the intermediate reservoir pressure for R114 (1/3 bar) correspond to the self-start threshold (the details of which are discussed in the following chapter). For R114, the highest pressure (1/2 bar) corresponds to the absolute threshold. For both liquids, only the runs corresponding to an evacuated reservoir are choked.

Table 4.1. Summary of Measured and Inferred Average Wave Properties

Property	Symbol	Unit	Refrigerant 12			Refrigerant 114		
Initial Test Cell Pressure	P_0	bar	5.69			1.83		
Reservoir Pressure	P_{res}	bar	0	1/2	1[a]	0	1/3[a]	1/2[b]
Motion Picture Run Number	MPR	—	25	26	31	55	57	72
Exit: Choked/Unchoked	—	—	c	u	u	c	u	u
Measured Properties								
Superheat Pressure[c]	ΔP_1	bar	4.72	4.68	4.63	1.38	1.33	1.29
Base Pressure	P_1	bar	0.97	1.01	1.06	0.45	0.50	0.54
Exit Pressure	P_2	bar	0.46	0.51	1.01	0.23	0.33	0.51
Wave Amplitude $(P_1 - P_2)$	ΔP_w	bar	0.51	0.50	0.05	0.22	0.17	0.03
Wave Speed[d]	$V_w = V_1$	m/s	0.63	0.57	0.36	0.32	0.27	0.21
Two-Phase Flow Speed[d]	V_2	m/s	35	35	5	25	15	5
Inferred Properties								
Superheat Temperature[c]	ΔT_1	°C	50.9	49.8	48.8	36.2	33.5	31.9
Superheat Enthalpy[c]	Δh_{l1}	kJ/kg	46.7	45.8	44.9	34.5	32.1	30.6
Two-Phase Flow Speed[e]	V_2	m/s	31	—	—	26	—	—
Mass Flux $(\rho_{l0} V_w)$	$\dot{m}$	kg s^{-1} m^{-2}	837	758	478	471	397	309
Mixture Density $(\dot{m}/V_2)$	—	kg/m^3	25	20	95	20	25	60
Upstream Jakob Number	Ja_1	—	0.28	0.28	0.27	0.24	0.23	0.22

[a]: Near self-start threshold.
[b]: Near absolute threshold.
[c]: Based on upstream liquid pressure; saturated properties from Reynolds (1979)
[d]: From high-speed movies.
[e]: From pressure traces. (Obtainable in choked cases only.)

The trends are the same for both liquids as the reservoir pressure is raised, so the following discussion applies to both. The base pressure increases only slightly as the reservoir pressure is increased, so that the liquid superheat and Jakob number decrease only slightly. The wave amplitude, the wave speed, the flow speed, and the mass flux all decrease as the reservoir pressure is increased. At the highest reservoir pressure for each liquid the wave amplitude becomes quite small—the same magnitude as the fluctuations in base pressure. The flow speed is more sensitive to the reservoir pressure than is the wave speed, which means that the estimated average mixture density tends to increase as the reservoir pressure is increased.

Perhaps the most surprising result in Table 4.1 is the degree to which the base pressure is insensitive to the reservoir pressure. One would expect that the 40% decrease in wave speed and the 90% decrease in wave amplitude (from the lowest reservoir pressure R12 case to the highest) would be associated with a significant change in the energetics of the upstream superheated liquid. However, the corresponding decrease in Jakob number is less than 4%.

Previous authors have speculated as to the downstream boundary condition for the two-phase flow. Friz (1965) thought the flow to be choked in his experiments because that assumption fit his model better. Based on visual observations of the downstream plume, Grolmes and Fauske (1974) thought that some of their runs were choked while others were unchoked. Based on the theory of exothermic gasdynamic discontinuities (to be discussed in Chapter 7), Thompson *et al.* (1987) and Frost (1987) assumed that the flow was sonic in the reference frame of the wavefront (the so-called Chapman-Jouguet (Ch-J) condition). In the present experiments, a choked condition is associated with an exit pressure that is higher than the reservoir pressure, $P_2 > P_{res}$. Recall that this is the case for the two run conditions in which the reservoir is evacuated (R12, $P_{res} = 0$; R114, $P_{res} = 0$). The other runs with higher reservoir pressures are unchoked. In the present experiments, a choked condition is essentially the same as the Ch-J condition because the two-phase flow speed is of order 100 times the wave speed. That is, a sonic condition in the wave frame (Ch-J condition) and the lab frame (choked condition) are essentially the same. It follows that the Ch-J condition is evidently not satisfied in the unchoked cases.

Chapter 5

Start-Up

In this chapter the experimental observations regarding the start-up regime, which was introduced in Chapter 3, are discussed in detail. The features of the initial depressurization process are examined first, followed by a description of the three observed modes of wave initiation. The behavior at the *self-start threshold* is then discussed. Finally, the observations regarding the transition to quasi-steady propagation are presented.

5.1. Depressurization Process.

The initial depressurization process is illustrated in Figure 5.1 using the example R12, P_{res} = 0 bar. Base and exit pressure traces are shown, along with an $x-t$ diagram that identifies the leading edges of the observed acoustic waves and "phase-change fronts." The former are deduced from pressure traces; the latter are deduced from high-speed movies. In this figure time is relative to the oscilloscope trigger, which almost coincides with the initial drop in the exit pressure. Most features of this example are representative of all six run conditions; important deviations will be noted.

As the diaphragm is ruptured, an expansion wave is launched into the vapor overlying the liquid column. The amplitude of this wave is limited by choking at the exit, as is indicated by the plateau in the exit pressure at 2.25 bar. The initial temporal width of the wave is set by the diaphragm rupture time. From the bottom view high-speed movies it is seen that the time for *complete* rupture is 1.4 ± 0.2 ms, depending on the pressure difference and diaphragm thickness used. However, the pressure traces indicate that the *effective* opening time is less: If one defines the temporal width of the initial expansion wave as the time at which the pressure drops to 1/e of the plateau pressure, then the temporal width is about 0.25 ms for this example. At a sound speed of 150 m/s, this value corresponds to a spatial thickness of about 3.8 cm: about one fourth the length of the test cell.

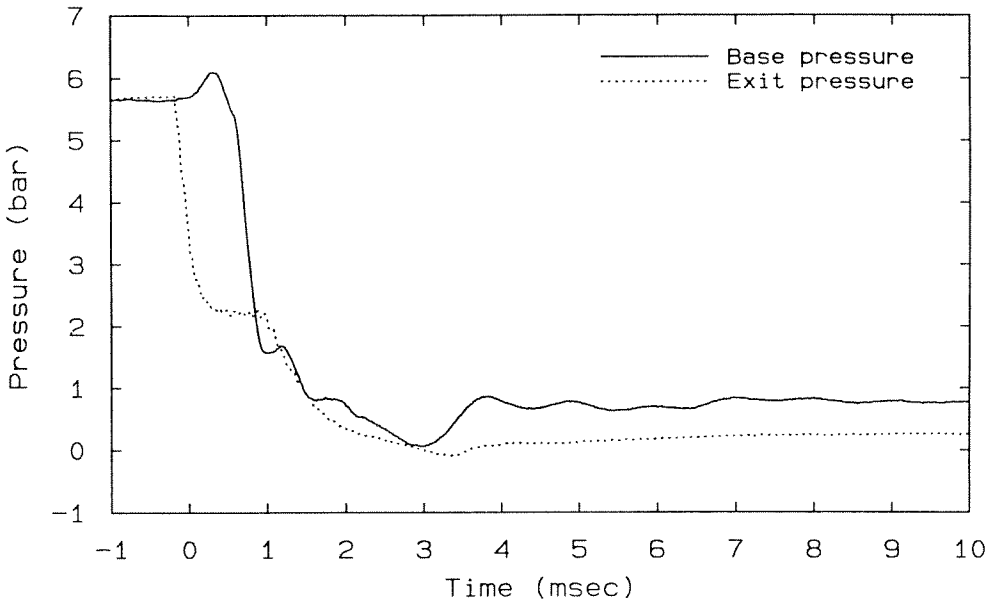

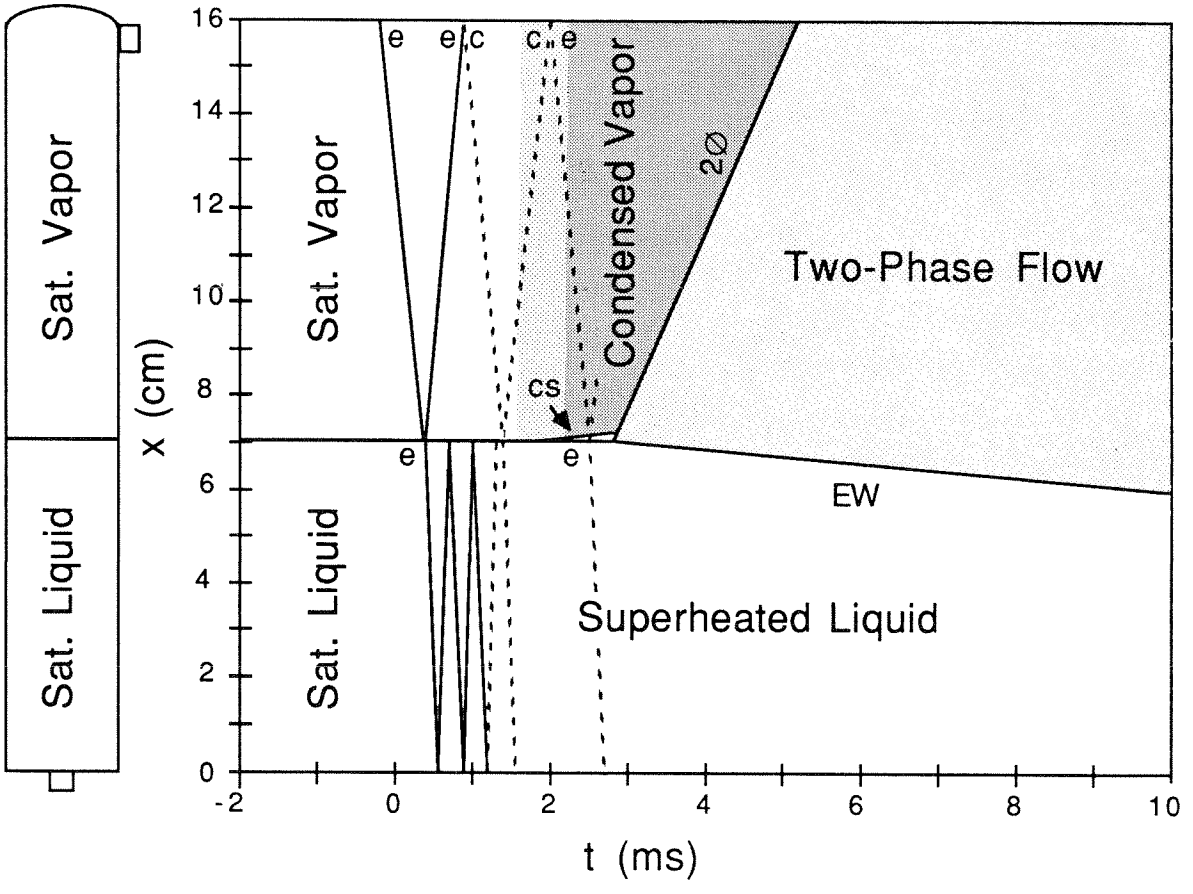

Figure 5.1: $P-t$ and $x-t$ diagrams for evaporation wave start-up. Liquid: R12, T_0 = 20°C, P_{res} = 0 bar, Run #: MPR 25.

Given the fact that the depressurization process is isentropic, and assuming that the vapor behaves like an ideal gas, the exit properties at any time during depressurization can be expressed in terms of the measured pressure:

$$\frac{\rho_{v0} - \rho_{ve}}{\rho_{v0}} = 1 - \left[\frac{P_{ve}}{P_0}\right]^{\frac{1}{\gamma}} \tag{5.1a}$$

$$\frac{T_{ve}}{T_0} = \left[\frac{a_{ve}}{a_{v0}}\right]^2 = \left[\frac{P_{ve}}{P_0}\right]^{\frac{\gamma-1}{\gamma}} \tag{5.1b}$$

where a denotes the sound speed, γ is the ratio of specific heats, and the subscript e denotes the test-cell exit. If the fractional change in density (the left hand side of Equation 5.1a) is very much less than one, then the "acoustic approximation" holds. For the initial expansion wave the fractional density decrease is about 0.56, so the initial large amplitude waves in the vapor are not acoustic. When the head of the initial expansion wave reaches the liquid surface, it is partially transmitted and partially reflected. The acoustic impedance of the liquid is 130 times that of the vapor; hence, so far as waves in the vapor are concerned, the tube ends at the liquid free surface. The head of the reflected wave returns to the test-cell exit at about 1 ms after the initial drop in exit pressure.

The transmitted expansion wave travels into the liquid at about 500 m/s.[1] Since the liquid is virtually incompressible, the acoustic approximation holds for this and all subsequent waves. The 0.25 ms temporal width of the incident wave translates to a spatial width of 12.5 cm at the liquid sound speed. This length is almost twice that of the liquid column; hence, the acoustic waves in the liquid are quite indistinct. Nevertheless, reverberations, though "smeared out," can be detected in the liquid pressure trace during depressurization. The ratio of the acoustic impedance of the end flange to the liquid is 26.7; thus, the flange behaves essentially like a closed end for early times (i.e., less than the round trip time of acoustic waves in the flange) as

1. This value of sound speed is the measured value of Winters and Merte (1977) for R12 at 26.7°C.

well as for late times (i.e., very much greater than the round trip acoustic time).

Referring to the $x-t$ diagram of Figure 5.1, expansion waves are denoted by "e" and compression waves are denoted by "c." The solid lines in the diagram represent those waves that can be directly detected from the pressure traces (pressure waves) or the high speed movies (phase change waves). The dashed lines are inferred.

One unexpected aspect of depressurization is the compression precursor felt by the base transducer prior to the arrival of the initial expansion wave (Figure 5.1). (There is also a small compression precursor in the exit trace, caused by the downward deformation of the diaphragm just prior to rupture; however, the precursor measured at the base transducer is an order of magnitude larger.) An analogous *negative* precursor preceding shock waves in liquid R11 was noted by Tepper (1983), who suggested interaction with the tube walls as a likely explanation. This would seem to be a likely possibility in the present case as well. The physical cause of a compressive precursor in this case would evidently be the slight contraction of the tube as the initial expansion wave propagates into the vapor region. The disturbance in the glass could propagate ahead of the expansion wave in the vapor and, on these time scales, squeeze the liquid. Suitable magnification of the Figure 5.1 pressure traces show that a small signal arrives at the base transducer about 30 μs after the sharp initial drop in exit pressure, which is consistent with the expected delay time due to the sound speed in the glass (which is about 5650 m/s). The temporal width of the precursor is approximately the same as that of the initial expansion wave, which would be expected in this scenario. If indeed the elasticity of the tube wall affects the liquid pressure, the question arises as to whether the liquid sound speed is significantly affected. The desired modification of the sound speed is found in the literature on the "waterhammer" effect (e.g., Streeter and Wylie, 1981). In the present example the estimated decrease in sound speed is only about 2%.

As no rise in the liquid level is detectable upon depressurization, the first visual sign of depressurization is fog formation within the vapor column. The fog forms because R12 is a "normal" fluid, which upon adiabatic depressurization becomes supersaturated (see footnote, Section 1.3.1).[2] In the present experiments, depressurization is severe and homogeneous

nucleation of liquid droplets occurs, which grow to form a fog. (The fog does not form upon depressurization of R114 because it is a "retrograde" fluid.) As illustrated in the $x-t$ diagram of Figure 5.1, the fog begins to form at about 1.7 ms, after about two reverberations have occurred in the vapor.[3] The cloud develops over the length of the test cell in a *spatially uniform* manner, over about a half millisecond interval. When the initial expansion wave reaches the free surface, the latter begins to evaporate (quiescently at this early time). This newly generated vapor is in quasi-equilibrium, and hence does not condense into a fog. A *contact surface*, labeled "CS" in the $x-t$ diagram, is formed between the evaporated "dry" vapor and the preexisting vapor that has condensed. The contact surface rises about 1.5 mm before explosive boiling begins.

The formation of the fog and the contact surface are shown in Figure 5.2. In the side view the fog appears dark because it scatters light away from the camera; in the bottom view, the fog appears light because it scatters light toward the camera. A mottled structure can be seen in the bottom view upon formation of the fog. This is believed to be associated with the contact surface. As will be seen in the following section, waves and boiling on the liquid free surface have a much different appearance.

Explosive boiling initiates at 2.8 ms, at which time both the base and exit pressures are close to their minimum values. At this time the evaporation wave (labelled "EW" on the $x-t$ diagram) begins to propagate into the liquid, and the two-phase front (labelled "2ϕ" on the $x-t$ diagram) travels up the tube (cf. Section 4.3.1). The delay time between the arrival of the first expansion wave at the free surface and the onset of explosive boiling is about 2.3 ms, sufficient for about 8 acoustic reverberations in the liquid column. Since the exit is choked following the initial expansion wave, the first information regarding the reservoir pressure evidently reaches the free surface upon the arrival of the second (compression) wave from the exit at about 1.5 ms. That the free surface senses the reservoir pressure *before* the onset of explosive boiling

---

2. The theory of supersaturated vapor is similar to that of superheated liquids. See, e.g., Wegener (1969).
3. The shading on the $x-t$ diagram reflects the approximate appearance of the corresponding regions in the photographs.

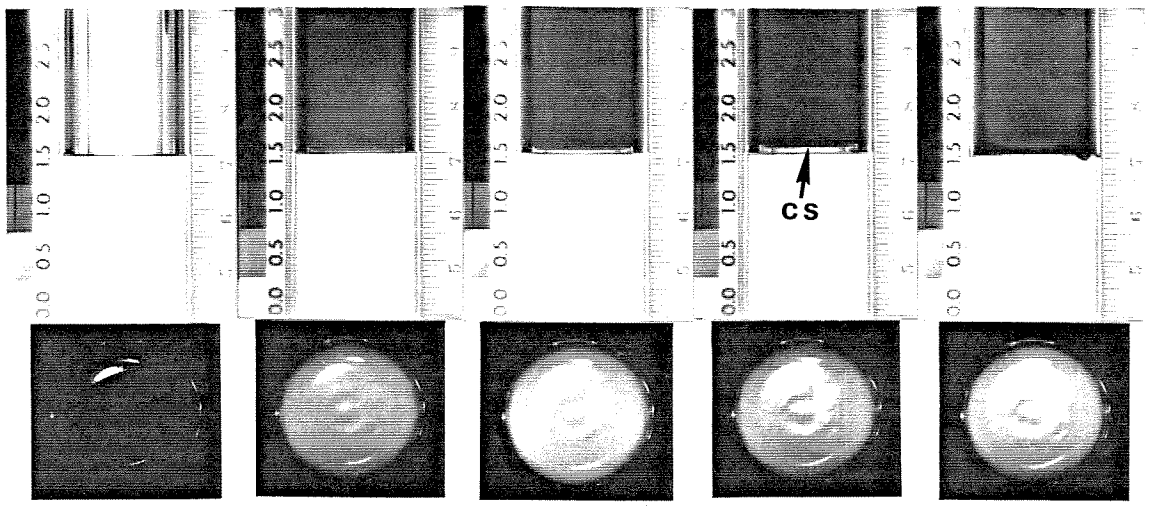

Figure 5.2: Fog formation in R12 vapor upon depressurization and prior to initiation of explosive boiling. $T_0 = 20°C$, $P_{res} = 0$ bar, Run #: MPR 25.

agrees with the fact that visual observations of start-up (to be discussed in Section 5.2) depend on the reservoir pressure as well as on the initial conditions. It is unclear whether the arrival of the (inferred) second expansion wave at the free surface plays a causative role in the nearly coincident onset of explosive boiling.

The rise in base pressure that is essentially coincident with the onset of explosive boiling is also observed for near-threshold conditions (to be discussed in Section 5.3), in which explosive boiling does not initiate, or is substantially delayed. This feature is therefore caused largely by acoustic waves and not, as would otherwise be inferred, primarily by the thrust of rapid evaporation. However, without rapid evaporation the base pressure continues to reverberate; whereas, in the presence of rapid evaporation the quasi-steady base pressure is established within several milliseconds (Figure 5.1). Within about 10 ms of diaphragm rupture, the flow appears to have lost all memory of the start-up process. Since this time is short compared to the approximately 100 ms overall run time, the start-up and quasi-steady regimes are completely decoupled.

5.2. Modes of Wave Initiation.

In contrast to the quasi-steady regime, there are significant qualitative differences in start-up behavior depending on the test liquid and reservoir pressure. Specifically, three modes of wave initiation are observed, representative examples of which are shown in Figures 5.3 → 5.5. The sequence of pictures on the left side of the figures are prints taken from oblique bottom view high-speed movies; the pictures on the right are simultaneous bottom view and oblique bottom view still photographs taken during a different but nominally identical run. The arrow indicates where the still photographs fall relative to the motion picture sequence.

In Mode 1, nucleation initiates at random sites on the liquid free surface and at the glass/free-surface contact line (Figure 5.3). Explosive boiling spreads to the remaining surface in less than one motion picture frame (158 μs). On close inspection of the bottom view still photograph, it is seen that bubbles larger than a few hundred microns in diameter are rough in appearance, that is, they are composed of smaller scales which are poorly resolved in the photographs. Bubbles that have reached a size of order 1 mm appear to be composed of smaller, smooth bubbles of approximately uniform size. The growth of these bubble clusters can be seen in the motion picture sequence. Mode 1 behavior is observed only at the highest superheat case, namely R12 and P_{res} = 0 bar.

In Mode 2, nucleation begins at many sites on the glass/free-surface contact line (Figure 5.4). Boiling then spreads radially inward toward the center, for this example, at 10 m/s. In Mode 2, bubbles do not readily develop smaller scales within them, and the "clustering" observed in Mode 1 does not occur. Mode 2 is observed consistently for the highest superheated R114 case, P_{res} = 0 bar.

In Mode 3, nucleation begins at one or more sites on the glass/free-surface contact line (Figure 5.5), and spreads across the surface, for this example at 1 m/s. Mode 3 is observed consistently for the conditions: R12, P_{res} = 1 bar, and R12, P_{res} = 1/2 bar. The other authors that have observed evaporation wave start-up (Frost, 1985; Grolmes and Fauske, 1974) have reported what is referred to here as Mode 3 start-up. That is, explosive boiling has propagated asymmetrically across the free surface.

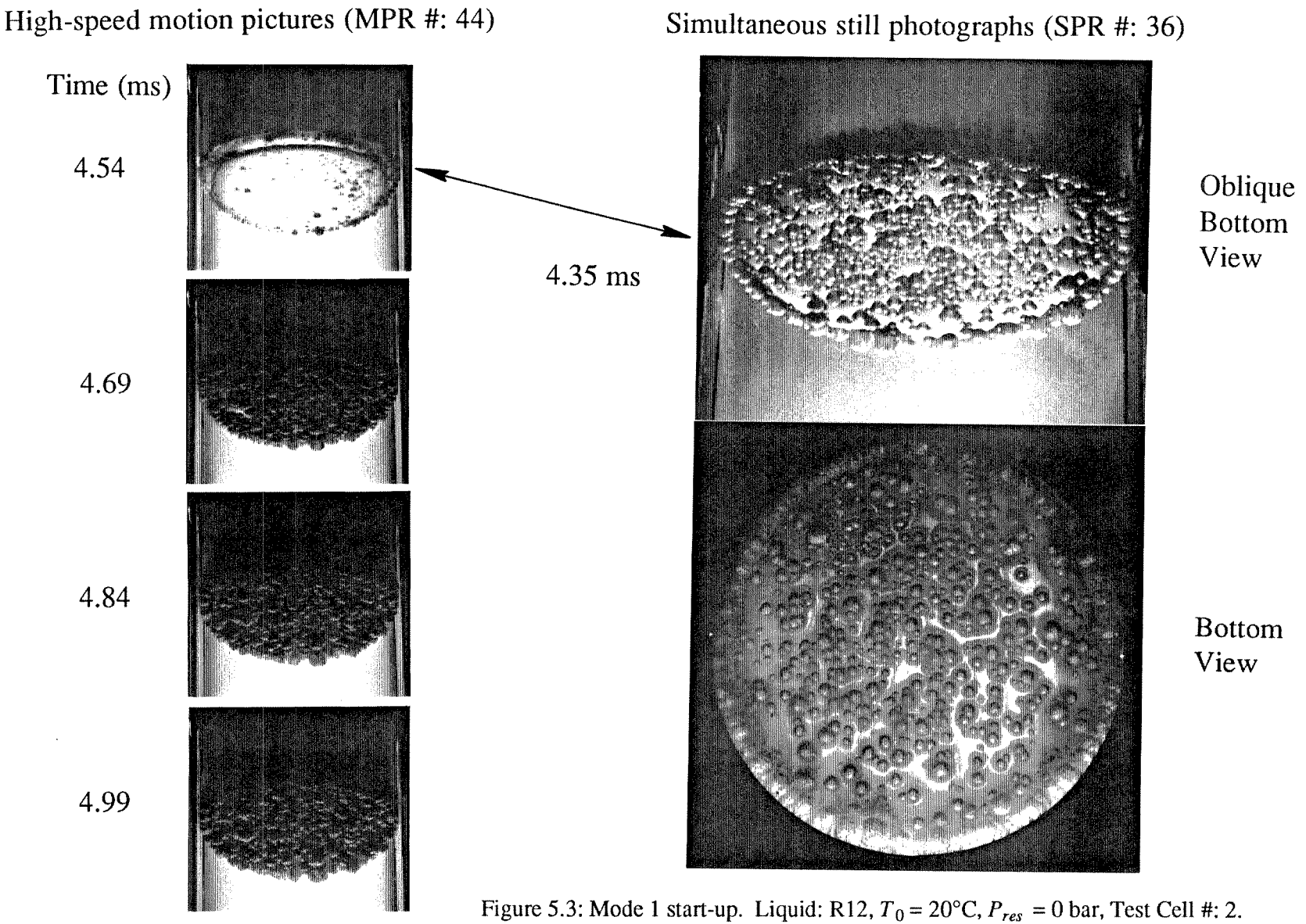

Figure 5.3: Mode 1 start-up. Liquid: R12, T_0 = 20°C, P_{res} = 0 bar, Test Cell #: 2.

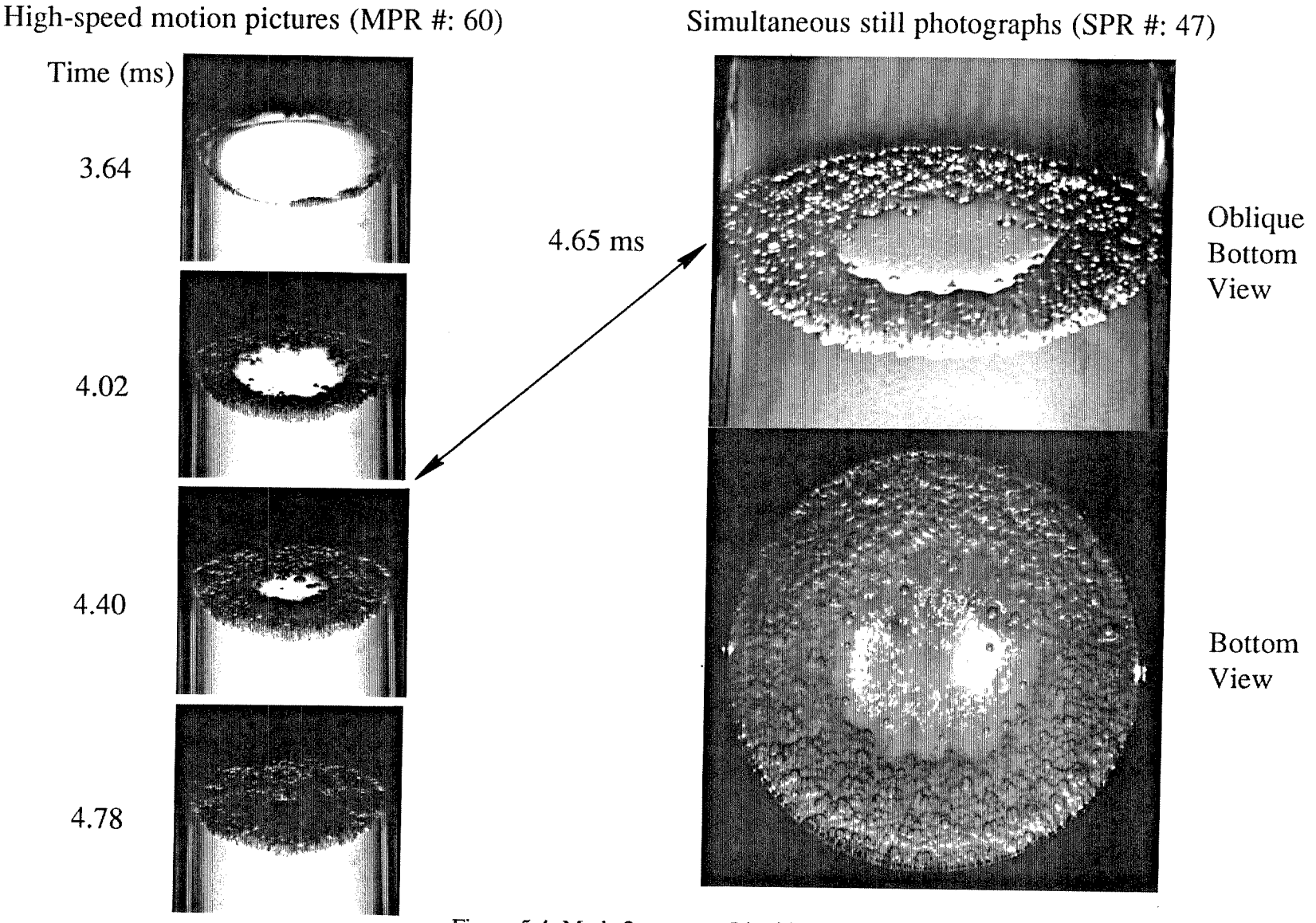

Figure 5.4: Mode 2 start-up. Liquid: R114, T_0 = 20°C, P_{res} = 0 bar, Test Cell #: 2.

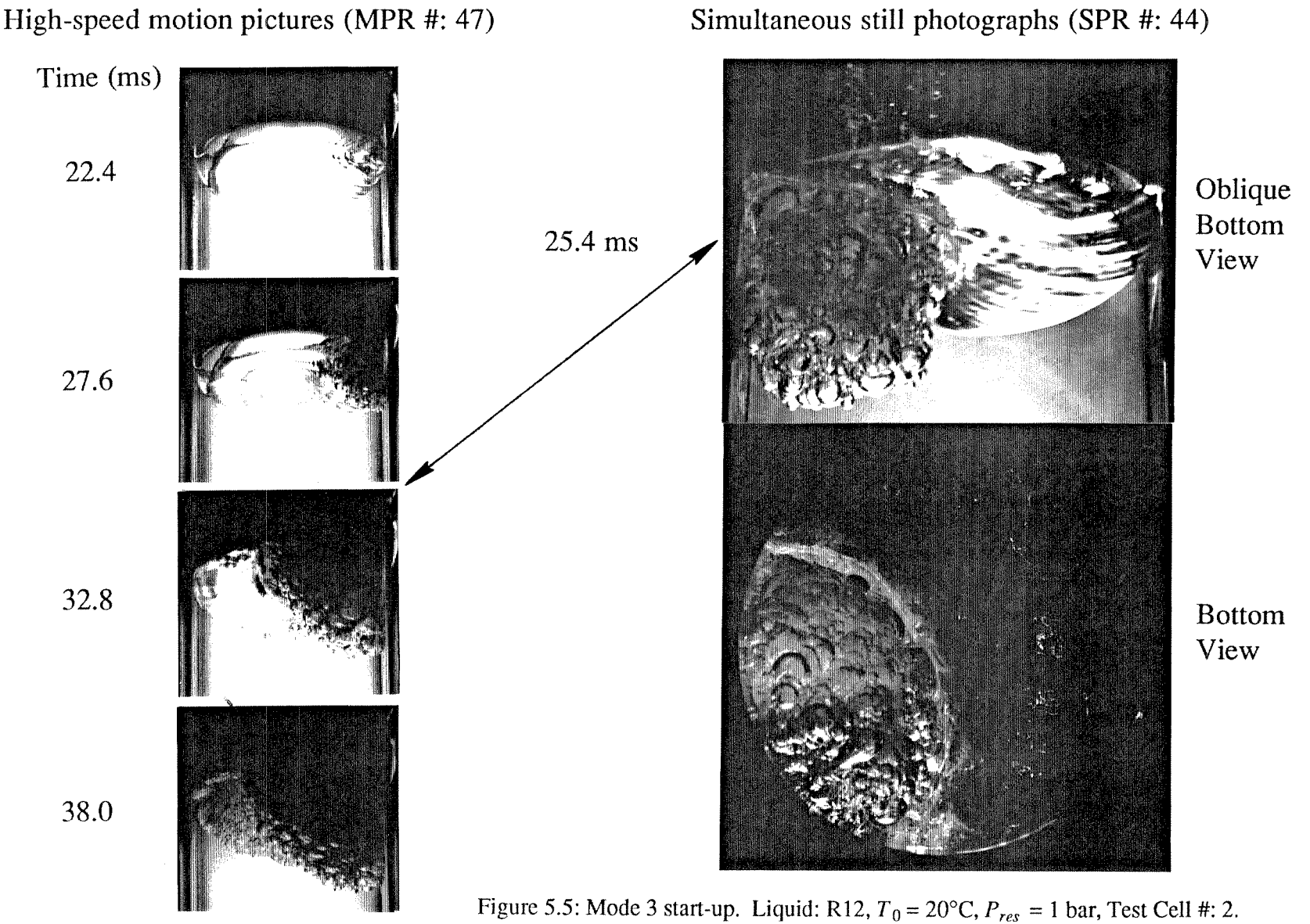

Figure 5.5: Mode 3 start-up. Liquid: R12, T_0 = 20°C, P_{res} = 1 bar, Test Cell #: 2.

The observed start-up mode is generally consistent from run to run, given nominally identical initial conditions (Liquid, T_0, P_{res}, and x_0). The exception is the condition R12, P_{res} = 0 bar. In this case, Mode 3 start-up is sometimes observed rather than Mode 1, as is illustrated in Figure 5.6. As is the case for Mode 2, the rate at which boiling spreads across the free surface for this condition is significantly greater than the rate at which it propagates into the liquid (cf. Figure 5.5). Sometimes what appears to be a "mixed" 1 and 3 mode occurs (e.g., Run #: MPR 39, video supplement). For the condition R12, P_{res} = 1/2 bar, Mode 3 is observed consistently, with a single exception in which Mode 2 occurs (Run #: MPR 74, video supplement). In the exceptional case, the initial liquid height is 9.5 cm—2.5 cm higher than the nominal initial height. The observed modes are summarized in Table 5.1. Note that the condition R114, P_{res} = 1/2 bar is artificially started (Section 4.4) and therefore does not appear in the table. Some suggestions as to the causes of the three modes are offered in Chapter 6.

Oblique Bottom View

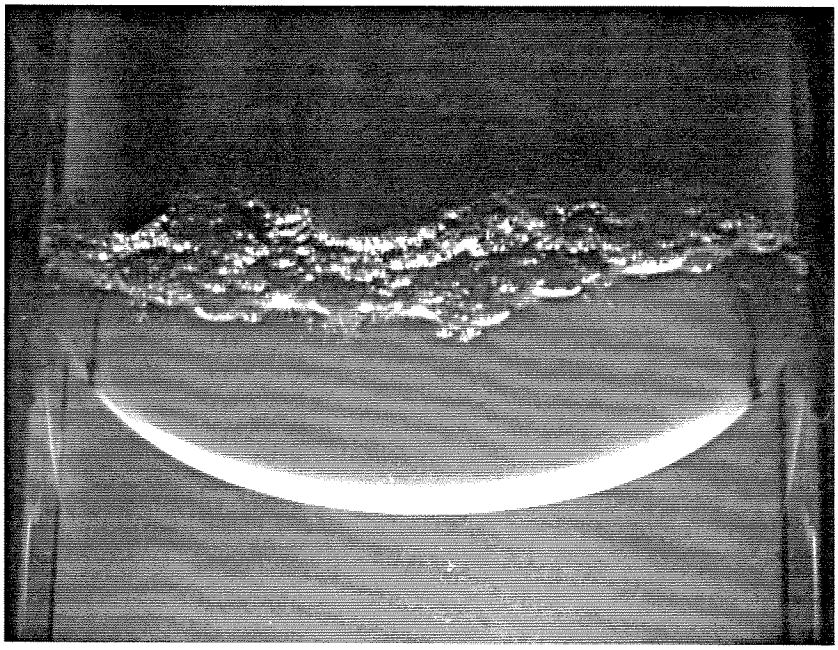

Bottom View

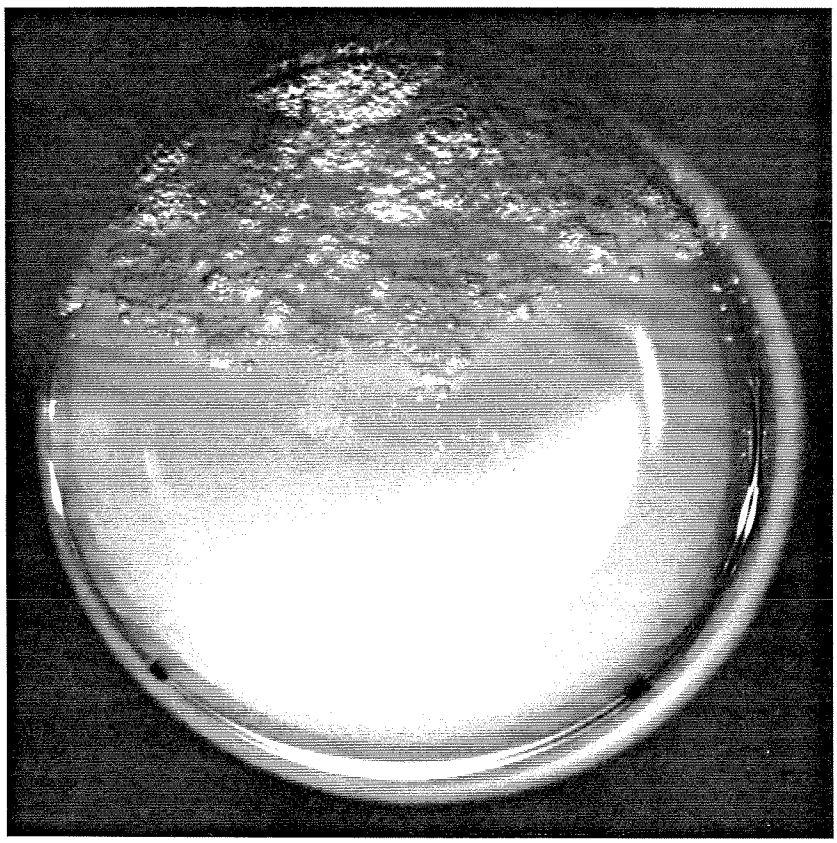

Figure 5.6: Mode 3 start-up in highest superheat case (cf. Figure 5.5). Liquid: R12, T_0 = 20°C, P_{res} = 0 bar, t = 3.75 ms, Run #: SPR 37.

Table 5.1. Summary of Start-Up Modes

Property	Unit	Refrigerant 12			Refrigerant 114	
Initial Test Cell Pressure	bar	5.69			1.83	
Reservoir Pressure	bar	0	1/2	1[a]	0	1/3[a]
Superheat Pressure based on Reservoir Pressure	bar	5.69	5.18	4.67	1.83	1.49
Jakob Number based on Reservoir Pressure[b]	—	0.45[c]	0.34	0.28	0.53[c]	0.28
Observed Mode #	—	1, 3	2[d], 3	3	2	3[e]

[a]: Near self-start threshold.

[b]: $Ja_{res} \equiv \dfrac{h_l(P_0) - h_l(P_{res})}{L(P_{res})}$; saturated properties from Reynolds (1979).

[c]: Reservoir pressure taken to be 0.01 bar.

[d]: $x_0 = 9.5$ cm.

[e]: This condition is usually initiated by a bit of falling diaphragm. The behavior is essentially that of Mode 3.

5.3. Self-Start Threshold.

Grolmes and Fauske (1974) discovered that evaporation waves in pure liquids start spontaneously only under conditions of sufficient superheat. Specifically, they noted that below a certain superheat, "flashing is intermittent and unsustained." As the superheat was decreased further, only quiescent evaporation occurred. Grolmes and Fauske observed that the threshold condition was diameter dependent: The larger the test-cell diameter, the lower the superheat required to achieve sustained flashing. In the present experiments, it is likewise observed that evaporation waves start spontaneously only for conditions of sufficient superheat. Several new observations concerning the start-up mechanisms at the self-start threshold are now presented.

For both R12 and R114, there is no distinction between the onset of nucleation and the onset of explosive boiling for the lower reservoir pressures. That is, the characteristics of explosive boiling, namely rapid propagation of the boiling front into the upstream liquid and vigorous ejection of two-phase flow upward, are present virtually immediately. As the reservoir pressure is raised above a certain approximate value, a distinction arises between explosive boiling and a comparatively quiescent regime of boiling: The onset of nucleation is delayed only slightly; however, boiling does not rapidly spread across the surface as occurs at the lower pressures. Instead, bubbles grow and break benignly in the vicinity of the initial nucleation site(s). (Recall that at the higher reservoir pressures, start-up is observed to proceed by Mode 3 for both liquids, so there is typically one, or at most a few, initial nucleation sites on the glass/free-surface contact line.) During the "quiescent" stage, boiling does not propagate into the liquid column, nor is two-phase flow ejected. At some point, after quiescent boiling has been occurring for tens of milliseconds, a dramatic transition occurs in which the boiling process rapidly escalates into the explosive regime. If the tank pressure is raised slightly higher, the delay to transition increases markedly, to times as great as a few hundred milliseconds. If the reservoir pressure is increased slightly higher still, the wave will not start. The superheat temperature of the liquid at the self-start threshold is significant: 48.8°C and 31.9°C for R12 and R114, respectively (Table 4.1, Section 4.5.3).

An example of a pressure trace from a run with a long delay (R114, P_{res} = 1/3 bar) is given in Figure 5.7. On this time scale, depressurization to the reservoir pressure is virtually instantaneous, although acoustic reverberations are seen for 50 ms. (Recall that when explosive boiling is not delayed these reverberations are damped almost immediately.) Between 50 and

350 ms there is no wave motion (acoustic or otherwise) in the liquid. Transition to explosive boiling occurs at 350 ms, and the base pressure jumps to the value associated with quasi-steady propagation. At 550 ms the wave reaches the bottom of the container and the base pressure falls to the reservoir value again.

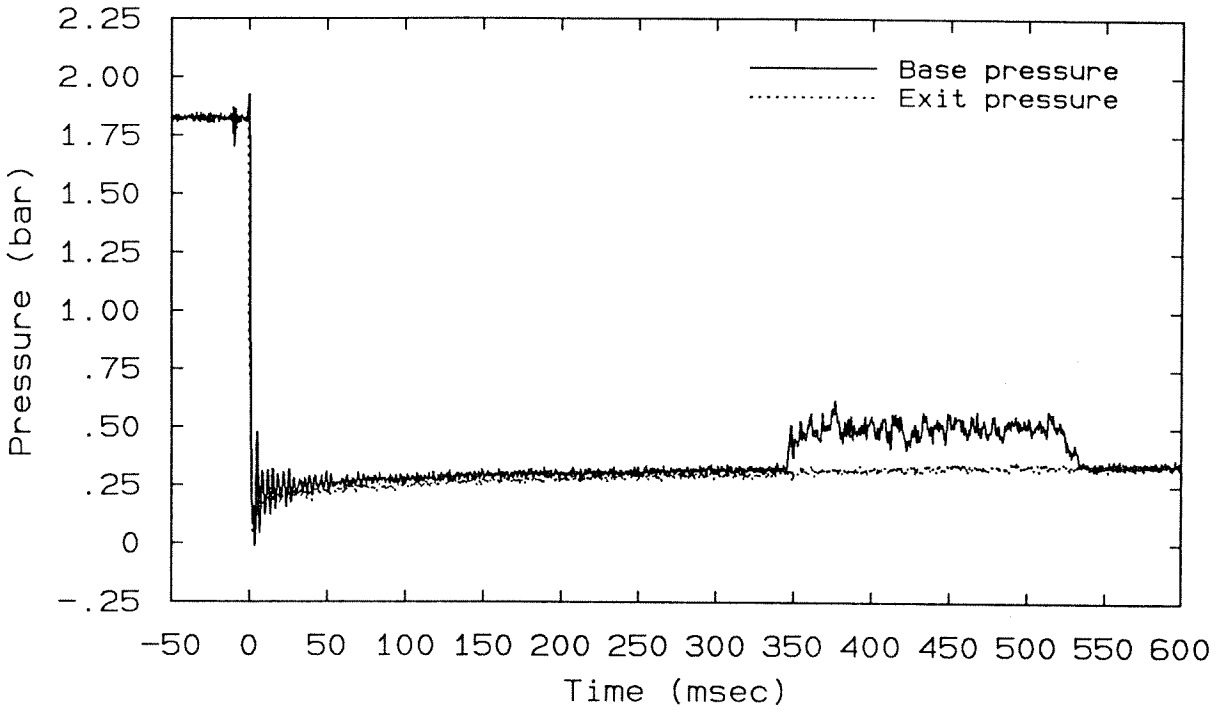

Figure 5.7: Base and exit pressure traces for a run near the self-start threshold, with a substantial delay time. Liquid: R114, $T_0 = 20°C$, P_{res} = 1/3 bar, Run #: MPR 57.

The reservoir pressure corresponding to the self-start threshold condition at 20°C is found by trial and error for both liquids. The delay times measured in this process are shown in Figure 5.8 for R12 start-up. The delay indicated is the time between the initial drop in exit pressure upon diaphragm burst and the start of transition to explosive boiling. The self-start threshold is found to be probabilistic in nature. As the reservoir pressure is increased, the minimum delay times remain the same order of magnitude, but the average delay time increases. Thus, one could define the self-start threshold pressure as the value for which the probability is 50% that the wave will start in a finite time. For R12 at 20°C, that value is approximately 1 bar. The delay time is sufficiently sensitive to reservoir pressure that the uncertainty in the threshold pressure is only a few hundredths of a bar. The physical reason

why there is an upper limit to the observed delay times is that the liquid in the region of the free surface becomes progressively colder as it continues to evaporate. There is therefore a competition between this quenching effect, and the near-threshold start-up mechanisms that will now be discussed.

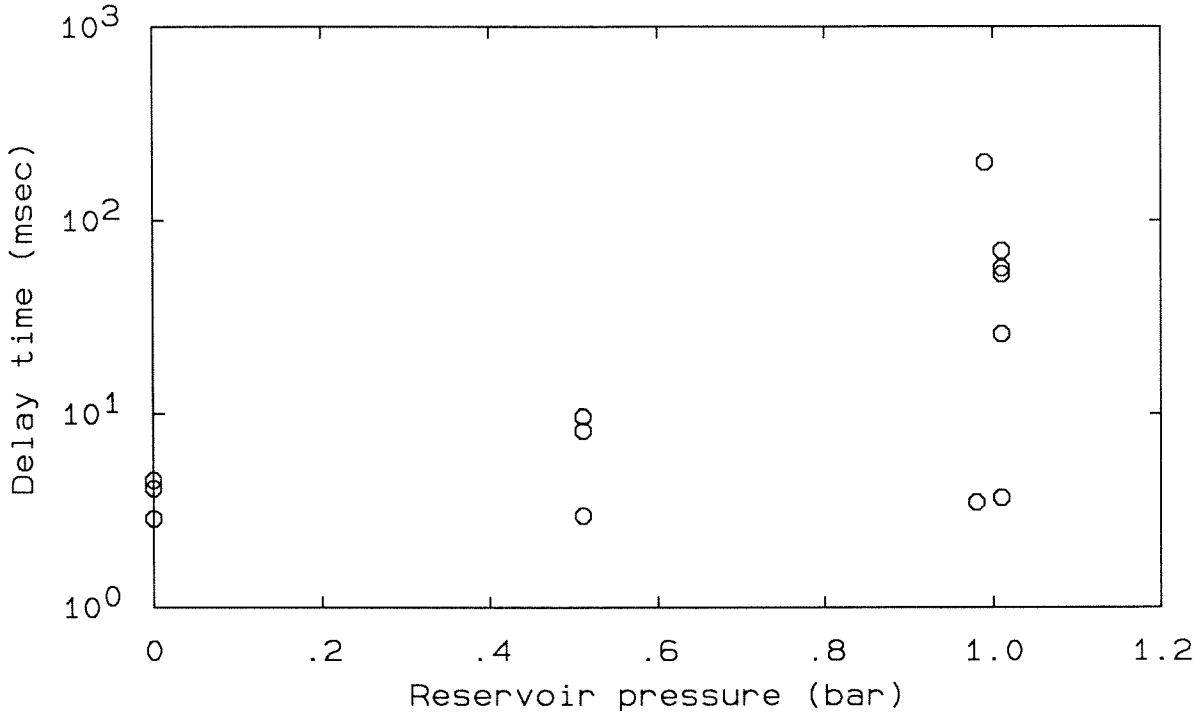

Figure 5.8: Delay in transition to explosive boiling for R12 as a function of reservoir pressure. $T_0 = 20°C$.

The condition of Figure 5.5 (R12, P_{res} = 1 bar) that served as an example of Mode 3 start-up is also an example of near-threshold start-up. In the motion picture sequence of that figure, the first nucleation site appears at about 3 ms. Transition to explosive boiling is delayed until about 20.8 ms, which corresponds to the first photo in the sequence. Figure 5.9 shows another example of near-threshold start-up (R114, P_{res} = 1/3 bar) from the oblique top perspective. (Recall that the oblique top view is useful only in the R114 cases, since in the R12 experiments, fog formation obscures the free surface before boiling initiates.) The first photo corresponds to the beginning of transition to explosive boiling, which in this case occurs at about 6.30 ms. At this time nucleation has initiated at three spots on the glass/free-surface contact line. The site in

the foreground appears to be a single bubble; the other two are clusters of small bubbles. Explosive boiling initiates when one of the clusters explodes, violently ejecting a fine cloud of aerosol.

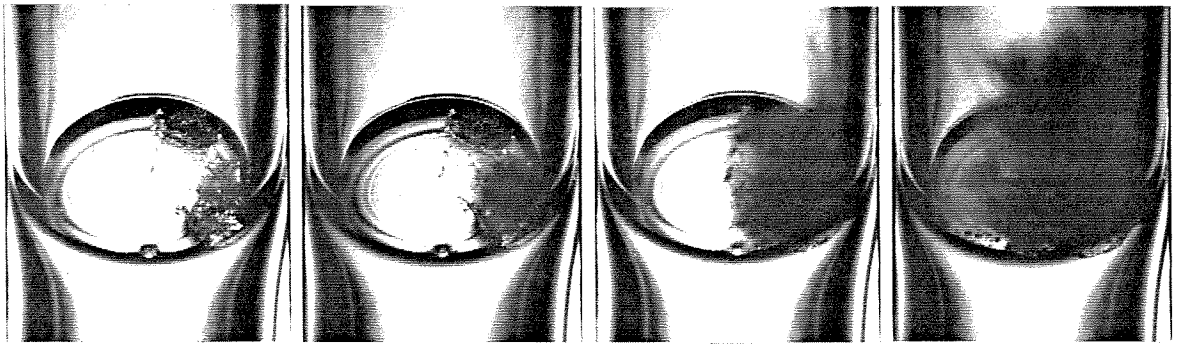

Figure 5.9: Sequence of top oblique view high-speed motion pictures, illustrating near-threshold start-up behavior. Liquid: R114, $T_0 = 20°C$, P_{res} = 1/3 bar, Run #: MPR 66.

The above observations suggest that the self-start threshold is sensitive to the cleanliness and surface quality of the test cell, inasmuch as these factors affect the number of nucleation sites that become active at the glass/free-surface contact line. The more initial nucleation sites, the higher the probability that one of them will lead to the initiation of explosive boiling within a given time. This provides a possible explanation for Grolmes and Fauske's observation that the threshold superheat depends inversely on the test-cell diameter. All other factors being equal, the expected number of active nucleation sites at a given time (any one of which could lead to transition) is proportional to the circumference of the tube. The ultimate limit of the self-start threshold is the absolute threshold discussed in Section 4.4, since a wave cannot start if it cannot continue to propagate. The absolute threshold is expected to be independent of the test-cell diameter, provided that the diameter is sufficiently large so as not to interfere with the naturally occurring flow scales. The disparity between the two thresholds would be expected to become greater as the test walls are made cleaner and smoother.

Nucleation at the walls is not necessary if there are alternative sources. One such source is observed for R114, P_{res} = 1/3 when test cell #2 is used. In this case, conditions are such that little or no nucleation occurs at the glass/free-surface contact line. It appears that without an alternative source of nucleation, explosive boiling would normally not initiate. However, the diaphragm cutter generates small fragments of aluminum which, for this run condition, are not blown out of the test cell by the initial rush of departing vapor. Given sufficient time, some

fragments fall to the free surface. Often, the fragments that strike the free surface are observed to produce a "crater," which gives way to capillary waves.[4] However, surface perturbations and capillary waves do not contribute to explosive boiling transition.

Sometimes it appears that a floating bubble is created when the diaphragm bit strikes, and sometimes bubbles are observed to nucleate on the diaphragm bit as it becomes submerged in the liquid. In either case, transition to explosive boiling typically proceeds along the lines described in connection with Figure 5.9. That is, a small cluster of bubbles is generated, which subsequently explodes. In one case (Run # MPR 57, video supplement), a free-surface bubble that nucleates from a diaphragm bit grows to a particularly large size. The film cap grows to be about one centimeter in length before breaking, at which time the free surface has been quiescently evaporating for 350 ms. As the receding film strikes the free surface, it appears that additional bubbles nucleate. The transition to explosive boiling takes place within 1.5 ms of the estimated time of film impact.

Below the self-start threshold the free surface remains quiescent. On the time scale of the high-speed movies (a few hundred milliseconds), convection is confined to a thin "turbulent" layer near the liquid surface. This cold layer is visible in the high-speed movies because of the shift in refractive index. The observations in this regime are qualitatively similar to those of Peterson *et al.* (1984), who studied the evaporation of R11 at much lower superheats ($\leq 5.7°C$). The cold layer that forms near the surface is convectively unstable, and over a period of several seconds, large-scale convection develops that carries warmer liquid to the surface. The mass transfer rate in the quiescent evaporation mode is about three orders of magnitude less than that associated with quasi-steady wave propagation.

---

4. By some combination of liquid motion and enhanced evaporation, the fragment is sometimes launched upward shortly after striking the surface, and then falls to strike the surface again.

5.4. Transition to Quasi-Steady Propagation.

In all cases it appears that processes qualitatively similar to those occurring in quasi-steady propagation are present from the time that explosive boiling has spread over the free surface. However, in the highest superheat cases for both liquids, the initial spatial scales (i.e., the leading-edge bubbles and bursts) are smaller and the initial rates (i.e., the wave speed and bursting frequency) are higher. The difference between the start-up and quasi-steady leading-edge structure can be appreciated by comparing Figure 5.3 with Figure 3.2 or 4.5a (R12), or Figure 5.4 with Figure 4.5c (R114). From Figure 4.9 (R12) it is seen that the peak wave speed, which occurs at about 3.3 ms, is roughly 7 times the average quasi-steady value. The temperature distribution near the free surface at times prior to the initiation of explosive boiling is affected by the fact that the pressure there is falling; however, the characteristic thickness of the thermal boundary layer is still of order $\sqrt{\kappa_{l0} t}$. The time interval between the arrival of the initial expansion wave at the free surface and the initiation of explosive boiling is sufficient that the thermal boundary layer is expected to achieve a thickness at least as great as the value associated with quasi-steady propagation. Hence, the higher initial wave speed would not appear to be explained by the idea that the liquid near the free surface at early times is hot compared to that at later times. A more plausible explanation would seem to be that the *superheat* of the entire liquid column, including the free surface region, is greatest initially, before the quasi-steady pressure is established. This suggestion is supported by the observation that the peak speed in Figure 4.9 occurs at a time (3.3 ms) when the liquid and exit pressures are close to their minimum values. Likewise, the average speed in Figure 4.9 is achieved at about the same time (i.e., between 5 and 10 ms) that average pressures are achieved. During the period in which the pressures and wave speed are adjusting toward their quasi-steady values, the appearance of the wavefront likewise evolves toward its quasi-steady appearance.

In contrast to the above behavior, the wave speed for R12, P_{res} = 1 bar does not peak during the start-up phase, but increases fairly monotonically to the quasi-steady condition (Figure 4.10). This is consistent with the fact that the wave amplitude, and thus the disparity between the start-up and quasi-steady liquid superheats, is very small in this case.[5] Moreover, comparing

Figure 5.5 with Figure 4.5b, the appearance of the starting wavefront is seen to be very similar to the quasi-steady wavefront in this case.

5. Recall (Table 4.1, Section 4.5.3) that the other run condition with a similarly low wave amplitude (R114, size 9 $\{P_{res}\}$ = 1/2 bar) is jump-started.

Chapter 6

Discussion of Wavefront Mechanisms

The previous three chapters have described new phenomena that appear to be essential to the explosive boiling process in evaporation waves. These mechanisms are found to be extremely complex; moreover, they are sufficiently rapid and fine-scale that they are not fully resolved in the present experiments. The purpose of this chapter is therefore to consider the implications of the combined observations presented in the previous chapters, in an attempt to provide as complete a picture of evaporation wave processes as possible given the available evidence. The primary questions that arose in the previous chapters are: What is the nature of the leading-edge bubble structures: Are they floating bubbles or open-ended perturbations? What are the mechanisms that produce explosive "bursts" of aerosol, and what is the relationship between bursts and the leading edge structures? If the leading edge structures are floating bubbles, then what is the source of nucleation? These questions are examined in the context of previous hypotheses. A qualitative process for evaporation wave propagation is then suggested, which takes into account both previous ideas and present observations.

6.1. General Considerations.

6.1.1. *Evaporation/Fragmentation Interaction.* On the most basic level, it is suggested that explosive boiling is caused by an interaction between evaporation and fragmentation, as illustrated in Figure 6.1. Evaporation from liquid/vapor interfaces induces forces on the liquid that can set it in motion. (The growth of a vapor bubble is one example.) If that motion leads to fragmentation of the liquid, the evaporating surface area and the evaporation rate are thereby increased. (Other factors being equal, the increase in evaporation rate is proportional to the increase in surface area.) Escalation to explosive behavior is expected if an unstable feedback arises whereby the increase in evaporation rate promotes further fragmentation, and vice versa.

6.1.2. *Lofting Criterion.* A given mass of adiabatically evaporating liquid becomes progressively colder as thermal energy is extracted from it as latent heat. When the Jakob number is less than one (as in the present experiments), the thermal energy available to produce

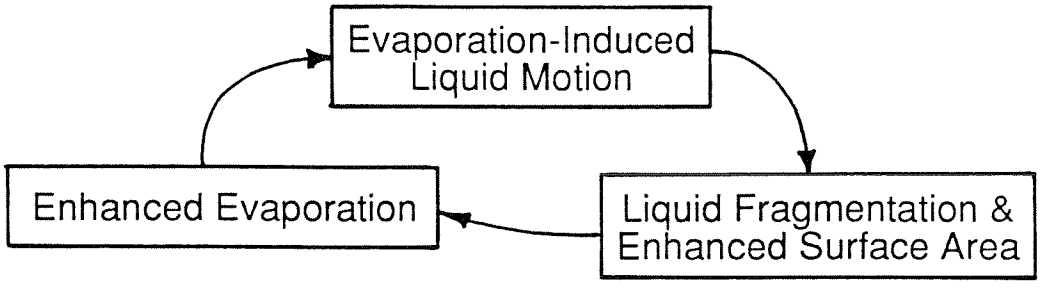

Figure 6.1: Generic "evaporation/fragmentation interaction."

evaporation is sufficient to evaporate only a portion of any given mass of liquid; i.e., a saturation condition is reached before the entire mass in question has evaporated (Section 1.2.2). The consequence in the present experiments is that liquid must be entrained by the evaporated vapor and carried away from the wavefront in order to achieve a sustained, quasi-steady wave. If fluid were not removed from the test cell in the liquid phase (for instance, if all droplets produced at the wavefront fell back to the leading edge), then the liquid column would become progressively colder and boiling would eventually cease.

In the present experiments it is observed that for all situations in which boiling occurs continuously over the entire liquid surface, liquid is also lofted. However, it would appear that for different liquids and/or container geometries, free-surface boiling can transiently occur in situations where lofting does not. In particular, Balaji and Mesler (1990) have studied free-surface boiling initiated in water and methyl alcohol, which was initiated by droplet impact on the free surface. Lofting did not occur; that is, fluid was not removed from the system in the liquid phase. The temperature of the superheated liquid pool fell continuously as boiling proceeded, reaching the saturation value in approximately 30 seconds. They described that "with water the temperature always fell to the saturation temperature before nucleate boiling ceased but with methanol the temperature fell only to about 10°C above saturation." Thus, free-

surface boiling can in some cases persist at low superheats and is not always explosive as it is in the present experiments.

6.2. Detailed Mechanisms.

In this section, specific mechanisms are considered by which the above generic evaporation/fragmentation interaction may be occurring in the present experiments. First, two differing explosive boiling hypotheses introduced by previous authors are discussed, and their relevance to the present experiments is considered in light of the observations presented in the previous three chapters. A qualitative process is then suggested, which includes aspects both of previous hypotheses and the present observations.

6.2.1. *Secondary Nucleation Hypothesis.* The term *secondary nucleation* has been used traditionally in the context of crystallization; it refers to the production of nuclei from the breakup of larger crystals (Garside *et al.*, 1979). On the basis of their experiments involving the boiling of thin films, Mesler and Mailen (1977) suggested that an analogous situation can occur in a boiling liquid; namely, that nucleation can occur as a result of the dynamics of the boiling process, besides at solid surfaces as is usually the case. Specifically, secondary nucleation requires that vapor be entrained a small distance beneath the liquid surface to form small bubbles. In order to form an active nucleation site, the entrained volume of vapor must be sufficiently large that the critical radius is exceeded. The primary question associated with the secondary nucleation hypothesis therefore concerns the mechanism of vapor entrainment.

Mesler (1988) has suggested a mechanism by which a secondary "chain nucleation" process may proceed in the case of free-surface boiling, which is illustrated in Figure 6.2. Consider a vapor bubble growing on the free surface of a pool of superheated liquid (top diagram, Figure 6.2). When the bubble ruptures, the film cap forming the top side of the bubble recedes. As it does so, it forms a toroidal rim due to surface tension; this in turn tends to form beads of liquid by essentially the same instability that leads to the breakup of a liquid jet. Mesler proposed that when the beads strike the liquid surface, they entrain vapor to form small bubbles that are carried a small distance (a few millimeters) below the free surface. The new bubbles then grow and rise to the free surface, break, and the cycle is repeated.

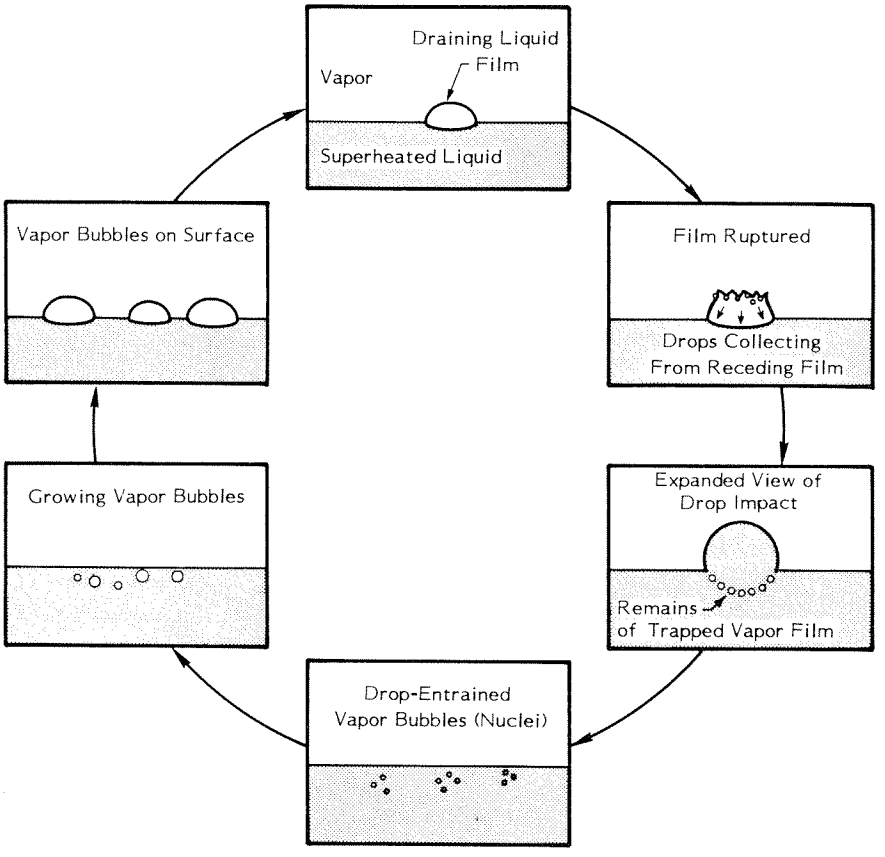

Figure 6.2: Mesler's Secondary Nucleation Hypothesis in the context of free-surface boiling (from Mesler, 1988).

6.2.1.1 Previous Experimental Evidence for Secondary Nucleation. The experimental basis for the secondary nucleation hypothesis in boiling is that in certain circumstances, a bubble at a free surface of a liquid pool is observed to generate small bubbles upon rupturing. MacIntyre (1972) noted that "under some conditions, the rupture of a large bubble will generate numerous small bubbles (diameter < 100 μm) at the periphery of the film cap, apparently when droplets or irregularities in the toroidal rim splash at the corner." MacIntyre also noted that the small bubbles are "frequently entrained in the downward jet and carried a centimeter or two below the surface." Bergman and Mesler (1981) studied the rupture of air bubbles at the free surface of a slightly superheated pool of water. They also noted that clusters of small bubbles were formed as the result of the rupture of the existing bubble, and that the cycle would tend to repeat itself. Herman and Mesler (1987) subsequently performed two sets of experiments to examine the

mechanisms of vapor entrainment by bursting bubbles in more detail. Two experiments were performed. In the first, a static floating bubble was created that was stablized by a surfactant. In this case it was seen that an irregular toroidal bubble was formed around the original circumference, which subsequently pinched off into individual bubbles. The mechanism for bubble formation appeared to be that the receding film was blown outward by the departing vapor, and subsequently rolled over and entrapped vapor. In the second set of experiments an air bubble was formed in a pool of deionized water and allowed to rise to the surface. Similar results were obtained as for the static bubbles containing a surfactant, but in this case the mechanism of bubble formation could not be observed.

In addition to their experiments of evaporation waves in vertical tubes, Grolmes and Fauske (1974) conducted experiments in a separate apparatus to study the onset of free-surface boiling. They observed that "a single surface bubble grew, shattered, and it appeared that drops from the shattered film caused bubbles to grow as they hit the liquid surface. The process repeated itself in rapid succession until the entire surface was erupting." As mentioned briefly in Section 6.1.2, Balaji and Mesler (1990) have measured the threshold of superheat necessary to sustain free-surface boiling in water and methyl alcohol. To accomplish this, they first heated the liquid in a smooth glass container. The container was then depressurized over a period of several seconds to superheat the liquid, during which time liquid drops were squirted at the surface of the liquid pool at the rate of about 3 to 4 drops/sec. The object was to determine the superheat at which the drops would trigger free-surface boiling. (Droplet addition was terminated upon initiation of boiling.) The threshold superheat temperatures so determined were 5.5±0.35°C and 14.4±0.40°C for water and methyl alcohol, respectively.

Apart from boiling studies, several experiments have used high-speed photography to observe single and/or multiple droplets striking a surface of the same type of liquid (which has virtually always been water). These have revealed that there are at least three mechanisms by which bubbles can be entrained into liquid by impacting drops. In the first mechanism, the drop upon impact creates a crater that throws a film of liquid up from its periphery, and the film then closes on itself. The final bubble is a relatively high Bond-number floating bubble (i.e., it is not entrained beneath the liquid surface), the radius of which is much larger than that of the impacting drop. This behavior was first observed by Worthington in 1894, and was subsequently seen by Franz (1959), and by Edgerton and Killian (1979).

In the second mechanism, the droplet upon impact forms a crater that collapses to eject a column of liquid that subsequently pinches off a "jet drop." The jet drop then falls to strike the surface, and in doing so forms a secondary crater that closes upon itself to form a bubble (Franz, 1959). In Franz's experiments the size of this bubble was close to that of the initial impinging liquid drop, and was completely entrained beneath the liquid surface. Hashimoto and Sudo (1980) described what appears to be essentially the same mechanism: "When a drop...impacts the free surface, a large crater is formed momentarily on the free surface. If another small drop...impacts the bottom of the crater just when the depth of the crater becomes maximum, a narrow but deep gas cavity is formed at the center of the crater. The upper part of the cavity is closed by the flow of the liquid around the first crater and immediately a spherical gas bubble is formed..." Hashimoto and Sudo were also able to adequately numerically model this process using a Marker-and-Cell method.

A third mechanism of bubble entrainment was recently observed by Pumphrey and Crum (1988). (See also Pumphrey *et al.*, 1989). Their discovery was motivated by previous observations that the frequency spectrum of noise produced by rainfall on a water surface exhibits sharp peaks between about 14 and 16 kHz. The source of the noise turns out to be entrained bubbles oscillating at their natural frequencies. The fact that the frequency peaks occur over a small region reflects the fact that this mechanism of bubble entrainment occurs over a quite limited range of conditions, which Pumphrey and Crum showed in their experiments. Their observations of this regime of bubble entrainment indicate that the crater caused by the impacting droplet becomes funnel-shaped as it collapses. The bubble is formed when the "stem" of the funnel pinches off. The resulting bubble is much smaller than the impacting droplet and is entrained beneath the liquid surface. Pumphrey and Crum observed that bubbles form consistently when this mechanism occurs; hence, they called it *regular entrainment.* They also observed that bubbles were sometimes entrained under conditions outside this range, but that the behavior was erratic and unpredictable. Hence, they called such behavior *irregular entrainment.* Irregular entrainment evidently includes the first two mechanisms, which by their nature can be seen to be more tenuous.

Oğuz and Prosperetti (1990) have developed a numerical model for droplet impact and have obtained excellent agreement with Pumphrey and Crum's observations. They have also expressed in dimensionless form the experimentally determined range of conditions for which

Pumphrey and Crum observed bubble entrainment in water. Moreover, they have succeeded in deducing the bounds of the range by relatively simple physical arguments. Oğuz and Prosperetti (1989) also predicted a fourth mechanism for bubble entrainment by impinging droplets; specifically, they calculated that for sufficient impact velocity a series of toroidal bubbles are formed shortly after the moment of initial contact, because the receding interface is not able to keep up with the impinging liquid.[1] This mode of bubble entrainment has evidently not been observed experimentally.

A mechanism has been observed by which bubbles are entrained into the liquid once they are formed. Blanchard and Woodcock (1957) have observed that a vortex ring was formed by the droplet impact, which carried the bubbles some distance below the liquid surface. Carroll and Mesler (1981), and Esmailizadeh and Mesler (1986) performed similar studies and arrived at basically the same conclusions.

6.2.1.2 Applicability to Present Experiments. Mesler's secondary nucleation hypothesis (Figure 6.2) is quite specific. For the purposes of the following discussion it is convenient to adopt a slightly more general definition of secondary nucleation, namely, "nucleation that occurs as a result of the dynamics of the boiling process". The discussion will proceed as follows: First, the evidence that nucleation of floating bubbles occurs at the wavefront leading edge is reviewed. Next, the likelihood that the source of nucleation is "secondary" in the above generalized sense is examined. Finally, Mesler's specific proposal for secondary nucleation is considered.

In considering whether nucleation occurs at the leading edge it should be emphasized that relatively few structures are not at least partially obscured by their neighbors and/or dark two-phase flow (cf. Sections 4.2.2.4 and 4.2.2.5). The following discussion must therefore refer to a minority of samples that are most fortuitously placed. Recall from Section 4.2.1.2 that bubbles surrounded completely by liquid (Figure 4.7a) are not observed; rather, the issue is whether the

1. In the 1989 study the initial contact area was infinitesimal, whereas in the 1990 study the initial contact area was defined to be finite.

leading-edge structures are floating bubbles (Figure 4.7b). In this scenario the wavefront leading edge would at any instant be composed of both floating bubbles and open perturbations that are the remains of ruptured bubbles. In some ways the leading edge would be expected to resemble a thin foam, but unlike a foam the wavefront is extremely dynamic.

New bubble structures are discrete in appearance from the time they can first be resolved and remain so as they grow. Full circular projections are not seen in profile; however, more than half-circular projections are observed in profile. Using water containing a surfactant, one can easily confirm that static floating bubbles with Bond numbers similar to that of the evaporation wave leading-edge bubble structures are very similar in appearance to the latter, and do not appear as complete circular outlines in profile either. When the view of the wavefront is from below (either obliquely or normally), distinct, full circular outlines can often be seen.

Bubble structures grow with the same time dependence as predicted by classical bubble-growth theory (i.e., $R \propto \sqrt{t}$), but at a slightly slower rate (Section 4.2.2.4). This would appear to be qualitatively consistent with the expected behavior of a relatively small-Bond-number floating bubble: The film side would contribute less evaporated vapor than the upstream side because the heat flux would be less (Figure 4.7b). In Section 4.2.2.5 it was observed that in instances where new structures do not form on the upstream surface of an existing structure, the latter will eventually stop growing and begin to recede; that is, its visible upstream surface begins to travel backward in the laboratory frame until it disappears behind other structures. The rupture of the bubble's film cap would explain this transition. (Cf. the classical spherical bubble in an infinite superheated liquid, which grows indefinitely.)

High-speed still photographs and certain high-speed movies indicate that there are small clusters and chains of bubbles in the two-phase flow that emanate from the wavefront region. These bubbles may be former leading-edge bubbles that survive the fragmentation process because they are small and hence relatively stable. (A means by which a floating bubble might make the transition to a flow bubble was suggested in Section 4.3.1.) Larger bubbles can be seen in the flow just after the wavefront reaches the bottom of the test cell (visible when using test cell #1). The same explanation may explain this behavior, except that the termination of the fragmentation process when the wavefront reaches the bottom of the test cell may then allow larger bubbles to survive.

Following wave breakdown at the absolute threshold, floating bubbles on the free surface become obvious (Section 4.4). The reasons are that, (1) no two-phase flow obscures their view, and (2), lacking fragmentation mechanisms, bubbles are able to grow to higher Bond numbers with large film caps. It appears likely that the floating bubbles clearly observed just subsequent to wave breakdown represent some fraction of those that nucleated just prior to breakdown.

Thus, there would appear to be substantial evidence that at least some of the leading-edge structures observed during quasi-steady propagation are in fact floating bubbles. Assuming this to be the case, the question of nucleation mechanisms is now examined. Since liquids generally contain potential nuclei (Section 1.2.1), it is first considered whether these provide a plausible source of nucleation. Equation 1.8b dictates how small a nucleus must be prior to depressurization in order to withstand a given superheat without exceeding the critical radius. No nucleation occurs *within* the liquid column in the present experiments, indicating that all nuclei there are stable. The question then becomes: Can a stable nucleus in the liquid bulk somehow be destabilized by the approaching wavefront and caused to grow? The primary effect of the approaching wavefront on a stable nucleus is to cool the liquid surrounding it. (The characteristic average thermal boundary layer thickness in the upstream liquid estimated by Equation 4.7 is somewhat greater than the critical diameter estimated by Equations 1.8.) In the neighborhood of the wavefront leading edge the superheat of the liquid surrounding a nucleus therefore decreases, while the surface tension of the liquid/vapor interface simultaneously increases. Both these effects stablize the nucleus; hence, there appears to be no theoretical expectation that preexisting nuclei (i.e., potential sites present within the liquid prior to depressurization) play a role in quasi-steady wave propagation. Moreover, if preexisting nuclei were driving the boiling process, one would expect the latter to be affected by the purity of the test liquid. Yet preliminary runs (in which the liquid was fed directly from the supply tank) behaved just like later runs (in which the liquid was distilled directly within the initially evacuated container).

Lacking a known mechanism for the activation of potential nuclei within the liquid, the case for secondary nucleation is now examined. The evidence for secondary nucleation in the present experiments is simply that 1) droplets striking a liquid surface have, under certain conditions, been observed to cause nucleation, and 2) many drops are generated in the bursting process, some of which undoubtedly strike the wavefront leading edge. The photographic

resolution is inadequate to resolve any such nucleation events; however, it must be considered that: (1) in certain runs with nucleation in the upstream liquid (Appendix C) a spray of droplets is observed to cause nucleation under essentially equivalent thermodynamic conditions and, (2) close examination of the high-speed movies suggests that material from a burst often impacts a portion of the leading edge, and that bubble structures follow a few frames later (e.g., Figure 4.12). High-speed movies also show that isolated bubble structures sometimes form in such a way that a discrete nucleation event by a stray droplet seems a likely possibility.

A few questions that arise in connection with secondary nucleation are now addressed. The first is, which if any of the previously observed modes of droplet-induced nucleation are likely to be occurring? Referring to the above discussion, the mechanism first identified by Worthington (1894) (in which a liquid film is thrown upward from the droplet-induced crater and subsequently closes on itself) is unlikely because the Bond number of the initially observed bubbles is too small. However, the mechanism described by Hashimoto and Sudo (1980) (in which a bubble is formed by the fortuitous impact of two or more droplets) would appear to be relevant here because of the large number of droplets produced in a burst. The mechanism identified by Pumphrey and Crum (1988) (in which a droplet-induced crater becomes funnel-shaped and pinches off at the bottom) must be appraised by considering whether the present experiments fall within the boundaries of the "regular entrainment" region found experimentally by Pumphrey and Crum. The dimensionless form of the region boundaries given by Oguz and Prosperetti (1990) is:

$$We \propto Fr^{\alpha}; \quad We \equiv \frac{\rho_l V_{dr}^2 d_{dr}}{\sigma}, \quad Fr \equiv \frac{V_{dr}^2}{g d_{dr}}, \quad \alpha = 0.179,\ 0.247 \qquad (6.1)$$

where We is the Weber number, Fr is the Froude number, and the values of α are taken from experimental data. In the present experiments the estimated approximate range of droplet Froude numbers $Fr = O(10^2 \rightarrow 10^4)$ encompasses most of the range of Froude numbers investigated by Pumphrey and Crum.[2] The estimated range of Weber numbers in the present

experiments $We = O(10^1 \rightarrow 10^3)$ is such that a substantial fraction of droplets that strike the wavefront leading edge would be expected to produce regular entrainment.

A second question that arises in connection with secondary nucleation is, how does the process begin since there is initially no source of droplets? Based on the observations of Chapter 5, it appears that preexisting nuclei at the liquid surface, which become active upon depressurization, are necessary in order to initiate the secondary nucleation process. The three observed start-up modes discussed in Section 5.2 can be explained on a superficial level by distinguishing between these two classes of nuclei, i.e., preexisting nuclei that initiate boiling, and secondary nuclei that sustain the boiling process. Which mode is observed then depends on the competition between two factors: the location and activation rate of preexisting nuclei, compared to propagation rate of the secondary nucleation process away from the initial sites. The difference between Mode 1 and Modes 2 and 3 is the location of the preexisting nuclei: in the former case at random spots on the free surface as well as at the glass/free-surface contact line; in the latter case only at the glass/free-surface contact line. The difference between Mode 2 and Mode 3 is in the rate at which preexisting nuclei become active. In Mode 2, the activation rate of preexisting nuclei around the glass/free-surface contact line is relatively great compared to the rate at which boiling spreads across the free surface, and conversely for Mode 3.

The locations of preexisting nuclei and the rates at which they become active evidently depends on both the magnitude and rate of depressurization. Moreover, they must also depend on unknown microscopic factors, such as what particulate impurities are present, the surface quality of the wall, and the way that the liquid wets the surface.[3] Nor can the rate at which explosive boiling spreads across a free surface currently be predicted since the detailed mechanisms are not understood. Hence it is currently not possible to predict which mode will

---

2. In calculating the Froude number for the droplets in the present experiments, the acceleration due to gravity g is replaced by the estimated characteristic acceleration associated with a burst.

3. The observation that nucleation occurs more readily at the glass/free-surface contact line than elsewhere on the free surface is perhaps to be expected. First, the free surface becomes cold when it begins to evaporate, which means that the wall is relatively warm. Therefore, heat is transferred to the liquid near the glass/free-surface contact line. Also, the meniscus at the wall may trap nuclei.

occur for new run conditions.

The extent to which the present observations are compatible with the specific mechanisms suggested by Mesler (1988) is now examined. Compared to the present experiments, Mesler's hypothesis and observations are most similar to the quiescent boiling regime that is observed near the self-start threshold before transition *to* explosive boiling (Section 5.3), and at the absolute threshold after transition *from* explosive boiling (Section 4.4). Recall from Section 5.3 that, near the self-start threshold, nucleation initiates at one or a few sites on the glass/free-surface contact line, or alternatively by a piece of falling diaphragm. In either case, bubbles at the free surface grow and break in the immediate vicinity of the initial nucleation site, forming a small cluster. At the absolute threshold the behavior is similar: Quiescent boiling persists for several hundred milliseconds after explosive boiling stops, and forms a froth (Run #: MPR 72, video supplement). Although the specific nucleation process is not resolved in the high-speed motion pictures, Mesler's proposal seems reasonable. In particular, in Mesler's experiments the Bond number appears to have typically been order one or greater (e.g., Figure 6.2). Likewise it is of order one in the present experiments during the initial quiescent boiling phase (which, recall, occurs for run conditions suitably close to the self-start threshold).

In an isolated incident, direct evidence that nucleation caused by receding liquid film can be important in the start-up process is observed in the present experiments: Recall the example (Section 5.3) in which a particularly large bubble formed in the initial quiescent bubbling stage. After the free surface had been quiescently evaporating for 350 ms, transition to explosive boiling occurred within 1.5 ms of the estimated time at which the receding film impacted the liquid surface (Run #: MPR 57, video supplement). However, in contrast to Figure 6.2, entrained bubbles are not observed beneath the liquid surface.[4]

---

4. One could adopt an alternative viewpoint here, namely that the droplets striking the liquid surface act to bring up warmer liquid below, thereby triggering an interfacial instability (to be discussed in the following section). It should be remembered, however, that for the same run conditions (and even earlier in the same run) pieces of diaphragm strike the surface and produce large craters, to no effect (cf. Section 5.3). The reader is referred in particular to MPR 61 of the video supplement.

Mesler's proposal (Figure 6.2) is less compatible with the present observations *after* transition to explosive boiling, because in the present experiments the Bond number of the leading-edge bubbles during quasi-steady propagation appears to be about an order of magnitude smaller than those observed by Mesler. This fact is important because, while his bubbles have large film caps, those inferred in the case of the present bubble structures would be very small. In particular, Kientzler (1954) has obtained high-speed motion pictures of the dynamics of a bursting sea-water bubble with a Bond number of 0.1, and did not report that new bubbles were entrained into the liquid in that case. It therefore seems doubtful that receding film is important in the present experiments.[5] More importantly, the observations of Chapter 4 indicate that in the present experiments the source of droplets are the explosive bursts of aerosol, which involve the fragmentation of many bubble structures. Because bursting appears to be an essential aspect of wave propagation, the present experiments do not support Mesler's view (1988) that the qualitative mechanisms illustrated in Figure 6.2 hold for high superheats but merely proceed at a greater rate.

Secondary nucleation ideas provide little insight as to the mechanism of bursts; however, in this scenario it is natural to suppose that bursts are composed of fragmented liquid previously residing in the interstitial liquid between floating bubbles (i.e. their film caps and mutual walls). A burst would therefore represent bubbles bursting in phase rather than individually, i.e., the material from previously shattered bubbles would act to rupture additional bubbles in a wavelike manner.

6.2.2. *Interfacial Instability Hypotheses.* The essence of interfacial instability hypotheses is that evaporation at a perturbed free surface can cause amplification of the perturbations. Several investigators have proposed mechanisms by which amplification may occur. The proposals of Miller (1973), Palmer and Maheshri (1981), Jacobs et al. (1984), and Prosperetti and Plesset (1984) relate to the interaction of the evaporative mass flux with the temperature

5. A second minor issue is that, because the superheat in the present experiments is substantial, the growth rate of nuclei evidently dominates any mechanism by which they would otherwise be entrained into the liquid pool (i.e., the droplet-formed vortex ring observed by Blanchard and Woodcock (1957) and by Carroll and Mesler (1981)).

distribution (i.e., thermal boundary layer thickness) in the liquid. The proposal of Shepherd and Sturtevant (1982) is an adaptation of the inertial instability proposed by Landau (1944) in connection with laminar flames and does not require variations in the thermal boundary layer thickness. Each of the above studies involves a linear instability analysis, which predicts a set of conditions under which a perturbation of a given wave number is expected to be amplified. Whichever specific mechanisms may occur (and they are by no means mutually exclusive) *explosive* boiling evidently requires that the instability grow into a nonlinear regime, in which the interface becomes sufficiently distorted that liquid droplets are stripped away. Such behavior would fall under the broad definition of an "evaporation/fragmentation interaction" given in Section 6.1.1.

6.2.2.1 Previous Experimental Evidence for Evaporative Interfacial Instabilities in Explosive Boiling. Those instability mechanisms alluded to above that explicitly involve temperature profiles in the liquid have not been compared with experiments, because there are evidently no relevant experiments in which the temperature profile has been measured. However, Shepherd and Sturtevant (1982) and Frost and Sturtevant (1986) have compared the Landau Instability Hypothesis with their experiments of exploding droplets (Section 1.3.2). These results are now discussed.

In the context of evaporation, the Landau instability is driven by the interaction between the mass flux and the shape of the distorted evaporating surface. Whether or not perturbations grow depends on the strength of the stabilizing factors present. Surface tension is always stabilizing because it acts to flatten regions of high curvature. Acceleration of the interface as a whole can be either stabilizing or destabilizing, depending on whether the sense of the acceleration is Rayleigh-Taylor stable or unstable.

Shepherd and Sturtevant (1982) applied Landau's analysis for a flame over a liquid and accounted for the acceleration of the interface as a whole, using bubble-growth theory. The result of the calculation was that the evaporating surface was absolutely stable at early (surface-tension dominated) and late (thermally dominated) stages of bubble growth, and unstable over a range of wave numbers during a period of time in between. Frost and Sturtevant (1986) used the same analysis, and obtained qualitatively the same results. The quantitative predictions of the linear theory were not directly verifiable from their photographs, because at the predicted times of instability the bubbles were too small. Rather, it was inferred

that the linear instability evolved into a nonlinear, saturated phase in which the perturbations became sufficiently large so as to strip droplets from the liquid/vapor interface, thereby producing the two-phase jet that was observed at later times.

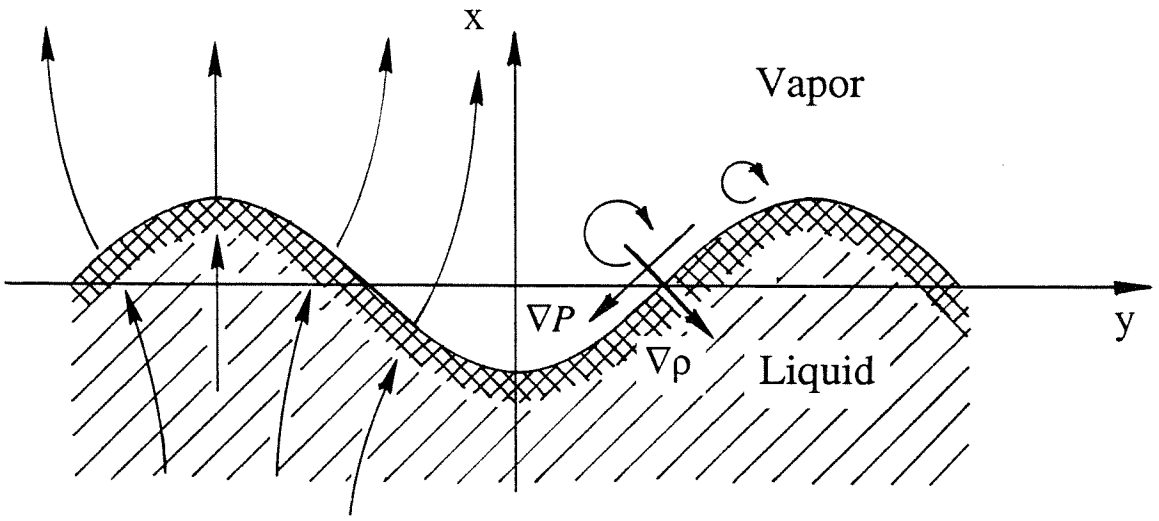

Figure 6.3: The Landau Instability Hypothesis, applied to an evaporating interface by Shepherd and Sturtevant (1982) and by Frost and Sturtevant (1986).

6.2.2.2 Applicability of the Landau Instability to the Present Experiments. The linear Landau instability calculations performed by Shepherd and Sturtevant (1982) and Frost and Sturtevant (1986) predict that the unstable wavelengths are quite small. For the example of ether at the superheat limit and atmospheric pressure, Frost and Sturtevant (1986) estimate that the unstable wavelengths range between 0.4 and 16 μm in their experiments. While no calculations exist for the postulated "saturated" Landau instability, Frost's photographs indicate that during explosive boiling the wavefront structure is also fine-scale, the largest perturbations being about 100 μm. (In Frost's best pictures of the wavefront, the 100 μm structures are reminiscent of the leading edge bubble-structures in the present experiments.) On the basis of these previous calculations and observations, the presence of fine-scale roughness on portions of the wavefront leading edge in the present experiments can be viewed as evidence for an interfacial instability acting in that region.[6] On the other hand, any tendency toward large

perturbations would have not been observed in the small-scale exploding drop experiments. Therefore one cannot rule out the possibility of larger-scale instability-induced perturbations in the present experiments on the basis of those experiments.

In Sections 4.2.1.1 and 4.2.2.3 it was noted that at any given instant, portions of the wavefront do appear rough. In the side view photographs, each portion of the leading-edge contour represents the upstream-most tip of the wavefront leading-edge surface for that particular lateral location. By considering many leading-edge *contour* samples from still photos and successive motion picture frames, one can surmise the typical structure of the leading-edge *surface*. (Because of their superior resolution, the still photographs are more useful than the high-speed movies in this capacity.) Smooth regions of the leading edge contour are relatively transparent to light; whereas, both rough regions of the leading edge and clouds of aerosol appear very dark due to light scattering. In general it is difficult to distinguish regions that are dark due to leading edge roughness from those that are dark due to aerosol. Darkness *at* the leading-edge contour, in combination with fine-scale leading-edge irregularities, are a good indication of surface roughness. In this manner it is observed that a small fraction of the leading-edge surface is rough at any given instant; most of the leading edge is composed of relatively large, smooth, bubble structures. The lower the superheat, the smoother the general appearance (Figure 4.5). These observations are also supported by the bottom views.

The dynamics associated with rough regions were discussed in Section 4.2.2.3. In particular, it was observed that rough regions are associated with surges in leading-edge velocity. It was also observed that any given region of roughness persists for only a few hundred microseconds, after which time smooth, larger bubble structures remain. If an interfacial instability acts at the leading edge, it therefore does so transiently (at least if roughness is an indication of its presence). It was also noted that in some cases droplets from a burst appear to splatter the leading-edge surface, and that these events appear to produce leading edge roughness. Perhaps such disturbances act to trigger a local interfacial instability exposing

---

6. An alternative that was previously suggested (Section 4.2.2.3) is that roughness can be caused by spray from a burst splattering a region of the wavefront leading edge (Section 4.2.2.3).

warmer liquid below. (Recall that the thermal boundary layer upstream of the leading edge is very thin (Sections 4.1.3, 4.2.2.4)).

In quasi-steady propagation individual bubble structures do not become rough at a critical size; rather, rough regions appear randomly. However there is one situation, namely, Mode 1 start-up, in which bubbles do tend to appear rough from about the diameter at which their surface features can be clearly distinguished from film grain (a few hundred microns). (Recall from Section 5.2 that in Mode 1 start-up—which is observed only for the case with the highest superheat, namely, R12 and zero bar reservoir pressure—nucleation initiates both at the glass/free-surface contact line and at random spots on the free surface.) The "rough" bubbles appear to be composed of smaller, smooth bubbles of approximately uniform size by the time they reach a size of order 1 mm. The behavior of these initial nucleation sites is similar to that reported by Shepherd and Sturtevant (1982) and Frost and Sturtevant (1986). It is probably not coincidental that this run condition has the highest superheat of the six run conditions, and that during the initial start-up phase the superheat is very close to its maximum value during the run (approximately 75°C). Bubbles observed in runs with lower superheats do not exhibit the same rough appearance (Figures 5.4 and 5.5).

In the interfacial instability scenario, bursts would be caused by droplets "torn" from the leading-edge surface. In this case aerosol would originate at the leading-edge surface and travel downstream. Is this an accurate view? The annular views (still photographs and motion pictures) provide the clearest picture. There are definitely instances in the annular movies and in the still photographs (Figure 4.6) in which fragmentation occurs in the region just downstream of the leading edge while the latter remains smooth. However, there are also situations where aerosol may be emanating from the leading-edge surface. The connection between bursts and an interfacial instability therefore remains uncertain.

6.2.3. *A Working Hypothesis for Evaporation Wave Propagation.* No existing hypothesis is alone adequate to explain the range of behavior observed in the present experiments. In particular, the tendency for fragmentation to occur in bursts was completely unexpected. However, previously expressed ideas (namely, secondary nucleation and interfacial instabilities) may both play a role. In this section a qualitative process for evaporation wave propagation is suggested based both upon the present observations and previous concepts discussed above. It cannot be yet be proven, but will hopefully provide useful ideas for further study.

Several situations in which explosive boiling has been observed have exhibited a common general sequence of events. Namely, the route to liquid fragmentation has been: pure liquid → bubbles in liquid → droplets in vapor. This general behavior was first reported by Friz (1965). Recall from Section 1.3.1 that Friz reported evaporation waves in which a bubbly superheated liquid was formed upon depressurization of heated water, and that the bubbly upstream liquid was fragmented into a spray through an "acceleration front."

Also recall the instances in the present experiments in which this pattern occurs: At conditions near the self-start threshold, explosive boiling begins when a cluster of bubbles, formed in an initial quiescent bubbling stage, explodes into aerosol (Section 5.3). The quasi-steady regime involves fragmentation of bubble structures, many of which are likely floating bubbles (Section 6.2.1). The two examples given in Appendix C also involve fragmentation of bubbles: In the "expulsion of a bubbly mixture" example, a coarse, bubbly mixture is fragmented and reaccelerated late in the run (Section C.1). In the "stream of rising bubbles" example, a fragmentation wave propagates through a bubbly superheated mixture (Section C.2).

Why would a conglomeration of bubbles in a superheated liquid be expected to be particularly explosive? One observation is that a liquid containing bubbles in relatively close proximity is mechanically unstable: it is in a state of relatively high surface energy. If in addition the superheat in the interstitial liquid between bubbles has not been completely expended in forming those bubbles, there is the potential for that interstitial liquid to be shattered, and the residual superheat to be quickly released. The suggestion is that once such a shattering process starts in a region, that fragmented mixture rapidly expands due to increased surface area and evaporation, and in turn shatters adjacent frangible liquid.[7] The shattering of individual bubbles, which occurs spontaneously in pure liquids because their lamellae are inherently unstable, provides a potential triggering mechanism. (For a static bubble, a lifetime greater than 10^{-2} sec usually indicates the presence of surface-active agents (MacIntyre, 1972).) This mechanism provides a possible qualitative explanation for the observed bursting

7. The manner in which interfacial instabilities might arise in such a situation is not understood, as previous workers have only considered simple geometries.

phenomenon.

The above suggestion is in some aspects similar to previous hypotheses for vapor explosions,[8] which basically proceed as follows: When the two liquid components initially mix, stable film boiling occurs so that the volatile liquid is temporally insulated from the hot liquid by a vapor blanket. If the situation is such that the two components are brought into intimate contact in some region, then rapid evaporation ensues in that region. A pressure wave is thereby generated that tends to disrupt and collapse the vapor blankets in its path, thereby causing the explosion to propagate. The first experimental visualization of such a process has recently been obtained by Frost *et al.* (1989). The similarity between vapor explosion hypotheses and the present hypothesis for a burst is that in both cases an expanding, fragmented, evaporating mixture sustains the rapid evaporation process by disrupting a superheated mixture in its path. The fundamental difference between the two processes is that in the case of a vapor explosion, the disruption involves mixing/heat-transfer between the components as well as fragmentation, and in the present case only fragmentation occurs.

In the context of the present experiments, it is suggested that the interstitial liquid between leading-edge bubbles provides the "fuel" for bursts. That bursts tend to propagate in the plane of the leading-edge bubble layer is compatible with such a view. Moreover, this framework provides an explanation for the inherent nonsteadiness of fragmentation: After a burst has just occurred in a certain region, there is evidently a delay time before interstitial liquid is "regenerated" by the nucleation and growth of new bubbles, so that it is once again susceptible to bursting. The observation that as the superheat decreases, the bursting frequency decreases while the scale of individual bursts increases also appears to fit: As the superheat decreases, it would be expected that the bubble layer must regenerate more fully for a burst to initiate. However, once initiated the greater degree of available interstitial liquid might allow more extensive propagation.

---

8. Board et al. (1975) first proposed that large-scale vapor explosions are analogous to chemical explosions. Since then several other authors—e.g. Sharon and Bankoff (1978, 1981), Scott and Berthoud (1978), Condiff (1982), Burger et al. (1986), and Fowles (1989)—have treated the problem in a like manner.

In Section 6.2.1.2 it was suggested that burst-generated droplets cause nucleation of floating bubbles at the wavefront leading edge. In this section it is suggested that interstitial liquid between bubbles leads to bursting under conditions of sufficient superheat. Thus, it is suggested that bubble nucleation and bursting play a necessarily interactive role, i.e., they enable one another (Figure 6.4). This being the case, the absence of either process would prevent wave propagation. If this view turns out to be correct, it may have important implications in explosive boiling processes in general.

Obviously, this discussion has drastically oversimplified the complex processes occurring in evaporation waves and, although it was not the intention of this research, far more new questions were raised than old ones answered. In particular, the comment made by Shepherd (1980) in the context of his exploding drop experiments seems equally appropriate a decade later: Rapid evaporation is still a much more complex subject than previously expected.

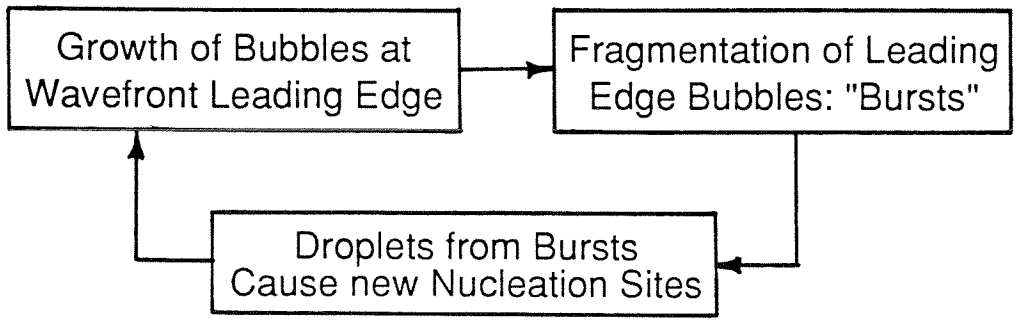

Figure 6.4: Suggested interaction between the leading-edge bubble layer and bursting.

Chapter 7

Jump Condition Model

In this chapter the evaporation wave is compared to its closest analog—a flame propagating in a premixed, combustible mixture, or "deflagration wave"—and is analyzed using the same concepts. The jump conditions for the conserved quantities—mass, momentum, and energy—are presented, and the ways in which previous authors have implemented them are discussed. It is shown that by taking advantage of simplifications that apply to evaporation waves in pure liquids[1] at relatively low, reduced pressures, the jump conditions can be reduced to a simple analytic expression in terms of readily measured and inferred quantities.

7.1. Analogy to a Premixed Flame.

An evaporation wave is analogous to a premixed flame in that the jump conditions for conserved quantities—mass, momentum, and energy—are the same. In both cases, the downstream flow is produced by dilatation of the fluid. In a premixed flame, dilatation is caused by chemical energy released as heat; in an evaporation wave, it is caused by thermal energy released through evaporation. The amount of energy released in a flame is typically of order 1000 times greater than that released in an evaporation wave. In both cases the wavefront propagates subsonically, at a negligible Mach number. In fact, typical wave speeds for premixed flames and evaporation waves in pure liquids are comparable; in both cases they are of order $0.1 \rightarrow 1$ m/s. In both cases the pressure decreases from upstream to downstream. For a premixed flame the pressure drop is often neglected; for an evaporation wave it must be considered.

---

1. Recall that in this context a "pure" liquid refers to one which has no bubbles (Section 1.3).

For both premixed flames and evaporation waves, the conservation equations provide insufficient information to determine the wave speed, given the initial and boundary conditions. An additional relationship must be specified that expresses the rate at which the driving process proceeds (Hayes, 1958). For premixed flames, it is observed that for a given temperature, pressure, and mixture of reactant gases there is a unique *burning velocity* in the direction normal to the local flame surface. For engineering purposes the burning velocity is usually measured; it can also be estimated theoretically. No analogous relation has been proposed for evaporation waves.

Despite general similarities, the physical processes that drive the two types of waves are different in detail. In a laminar flame, the burning velocity is controlled by diffusion of heat from the flame front to the upstream reactants, and by molecular diffusion of the various chemical species present. In the first approximation, a flame propagates because heat transferred from the reaction zone brings the reactants just ahead to the ignition temperature. (In practice, fluid-mechanical instabilities such as the Taylor-Markstein instability often lead to complex, nonsteady dynamical behavior reminiscent of that described in Section 4.2.) The dynamics of an evaporation wave are necessarily complex because it is driven by an interaction between liquid evaporation and fragmentation (Section 6.1).

7.2. Basic Assumptions.

Consider a one-dimensional evaporation wave in wave-fixed coordinates, as shown schematically in Figure 7.1. The upstream state (1) is assumed to be a pure, superheated liquid, and the downstream state (2) is assumed to be a two-phase mixture, consistent with the waves observed in this study. State (2) is taken sufficiently far downstream that the flow has reached an equilibrium, i.e., saturated condition. In the reference frame of Figure 7.1, the upstream liquid enters the stationary wavefront with speed $V_1 = V_w$, density ρ_1, pressure P_1, and specific enthalpy h_1, and leaves with the corresponding properties at state (2). The density and enthalpy at state (2) are mixture values, which are related to the individual phases by:

$$v_2 = (1 - \chi_2)v_{l2} + \chi_2 v_{v2} \tag{7.1a}$$

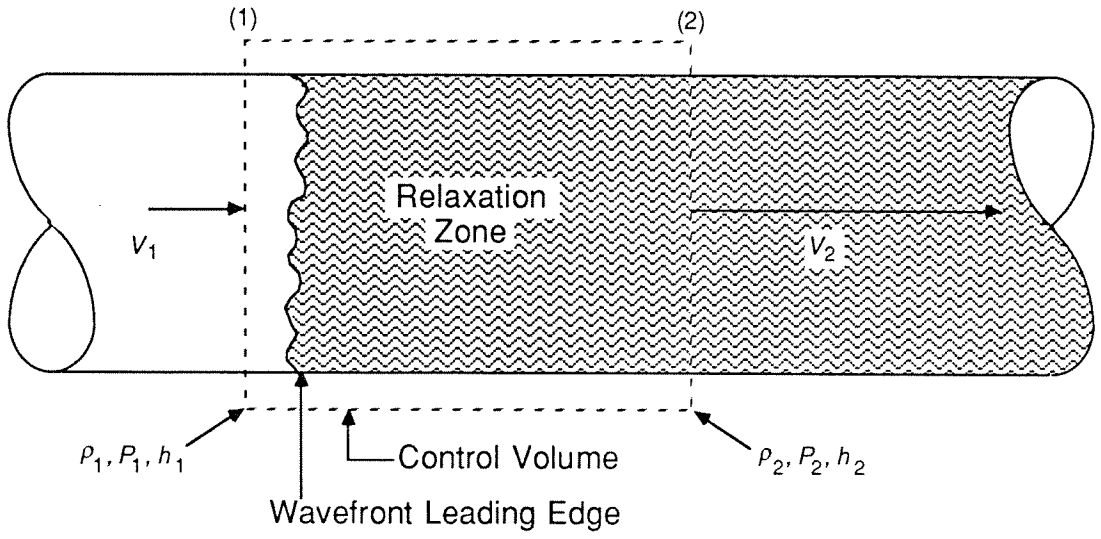

Figure 7.1: Schematic representation of an evaporation wave.

$$h_2 = (1 - \chi_2)h_{l2} + \chi_2 h_{v2} \tag{7.1b}$$

where χ_2 is the mass fraction of vapor, the subscript l refers to the liquid phase, and the subscript v refers to the vapor phase. Here, the density has been replaced by the specific volume v. The slip between the two phases is neglected, so that the downstream velocity V_2 pertains to the mixture. It is further assumed that the viscous pressure drop between the leading edge of the wavefront and the position of state (2) is small compared to that corresponding to the acceleration of the fluid caused by evaporation, that heat transfer from the test-cell wall is negligible, and that surface energy generation is negligible. Under these restrictions, the jump conditions for mass, momentum, and energy are:

$$\rho_1 V_1 = \rho_2 V_2 \tag{7.2a}$$

$$P_1 + \rho_1 V_1^2 = P_2 + \rho_2 V_2^2 \tag{7.2b}$$

$$h_1 + \frac{1}{2}V_1^2 = h_2 + \frac{1}{2}V_2^2 \tag{7.2c}$$

7.3. Rankine-Hugoniot Equation.

If the velocities V_1 and V_2 are eliminated, one obtains the Rankine-Hugoniot equation:

$$h_1 - h_2(P_2, v_2) = \frac{1}{2}(P_1 - P_2)(v_1 + v_2) \tag{7.3}$$

which specifies the locus of possible downstream states (2), given the upstream state (1). A generic Hugoniot curve applied to an evaporation wave, denoted by H, is shown in Figure 7.2.

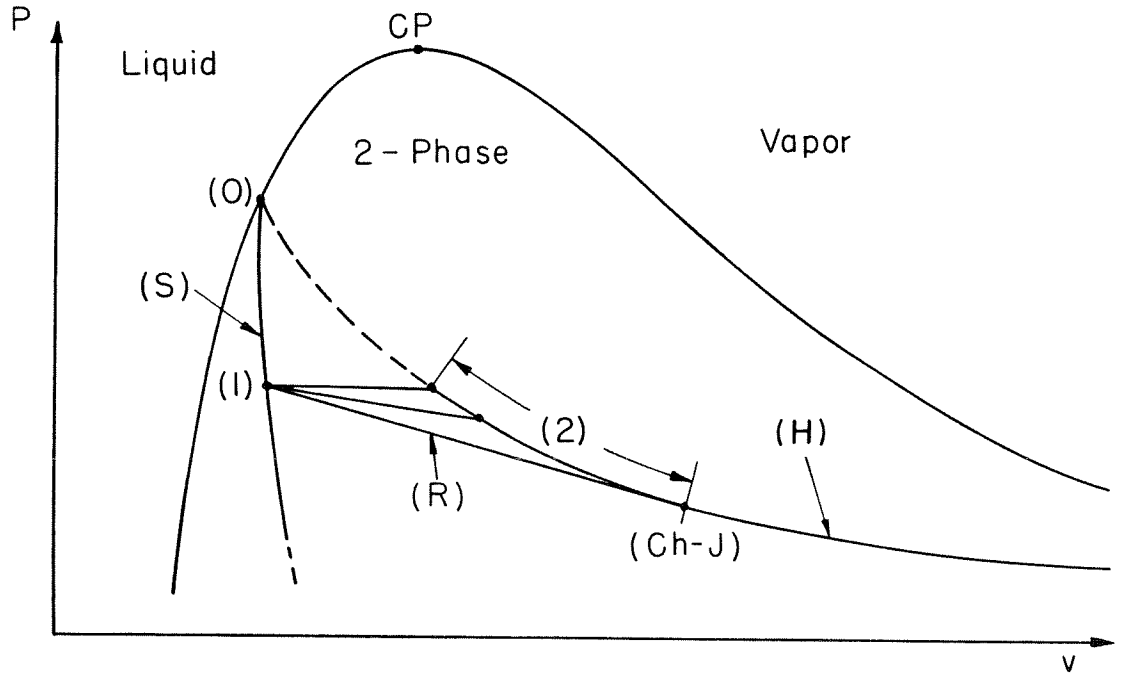

Figure 7.2: Generic Hugoniot curve for an evaporation wave.

As discussed in Section 4.1, the initial liquid state (0) lies on the saturation boundary. When the diaphragm is ruptured, the liquid pressure drops along the metastable isentrope (denoted by S) passing through state (0), to a value near the reservoir pressure. During the start-up phase it establishes state (1) at the somewhat higher pressure associated with quasi-steady propagation. Except for the phase diagram, the Hugoniot curve shown in Figure 7.2 is qualitatively the same as for combustion. The range of final states observed in the present study corresponds to a drop in pressure; i.e., $P_2 < P_1$. In combustion theory this family of solutions is called the *deflagration branch.*[2] The dashed region of the curve is nonphysical, because an increase in

pressure cannot increase the volume. (The equations express this fact by predicting an imaginary mass flux.) Lines connecting states (1) and (2) are called *Rayleigh lines* (denoted by R); the magnitude of their slopes are equal to the square of the mass flux through the wave. For each point (1) there is a unique point (2) for which the Rayleigh line has the maximum slope and hence the maximum wave speed. In combustion theory this condition is called the Chapman-Jouguet (Ch-J) point. At the Ch-J point V_2 is sonic; above the Ch-J point V_2 is subsonic (called a *weak deflagration*), and below the Ch-J point V_2 is supersonic (called a *strong deflagration*).

All evaporation waves that have been observed are weak deflagration-like waves. Strong deflagration-like evaporation waves cannot occur in a constant area test cell because of choking. Moreover, Chaves (1981) suggested on the basis of his rapid depressurization experiments that strong deflagration-like evaporation waves are not achieved even in a diverging tube, but that the minimum pressure at state (2) is dictated by the Ch-J condition. Frost *et al.* (1989) estimated sound speeds in the liquid-vapor mixtures downstream of the evaporation waves he observed in exploding droplets, and concluded that the Ch-J condition appeared to be satisfied. In the present experiments there is no significant distinction between a choked downstream condition and a Ch-J downstream condition because the wave speed is small compared to the two-phase flow speed; i.e., a sonic downstream condition, when it occurs, is essentially achieved simultaneously in the laboratory and wave-fixed coordinate systems (cf. Section 4.5.3).

7.4. Treatment by Previous Authors.

As mentioned in Section 1.3, other authors who have studied evaporation waves have used the jump conditions. Friz (1965) observed waves in bubbly liquids, and on the visual observations of many small bubbles in the bulk of the liquid, he assumed that the upstream

---

2. There is also a detonation-like branch of the Hugoniot curve, which corresponds to higher final pressures and lower specific volumes. This feasibility of such a phenomenon has been examined theoretically by several authors (see e.g., Fowles, 1989), but it has not been observed experimentally.

condition was an equilibrium mixture at the initial temperature. He neglected the effect of the bubbles on the upstream liquid density, which he took to be the initial value prior to depressurization. Friz assumed that the downstream mixture was in equilibrium at a lower pressure than the upstream value: either that of the reservoir (unchoked flow) or that consistent with a choked exit condition (which required an expression for the two-phase sound speed). The assumption that both the upstream and the downstream states are in thermodynamic equilibrium is somewhat idealistic, but has the advantage of completely specifying the problem so that a rate relation (i.e., an additional relation analogous to the flame speed) is unnecessary. Although his model is simple, Friz's predicted wave speeds agree with the observed values to within a factor of two over the entire range of his data.

Thompson *et al.* (1987) have collaborated in a series of experiments involving wavelike phase changes in substances of high specific heat; one of the experiments in the series is the thesis work of Chaves (1981, 1984). Chaves observed evaporation waves in bubbly liquids for initial conditions near the critical point. He was the first to recognize the analogy between an evaporation wave and a premixed flame and to use the graphical construction of Figure 7.2. Chaves assumed that nucleation in the upstream liquid had a negligible effect on its state, and treated the upstream liquid as if it were a single-phase, metastable liquid. His model was a numerical solution of the Hugoniot curve in which state (2) was taken as the Ch-J condition corresponding to a given (i.e., measured) upstream state (1). Chaves used equations of state in order to calculate the Hugoniot curve, thereby avoiding consideration of individual downstream phases and explicit expressions for the two-phase sound speed.

Shepherd *et al.* (1989) have developed a model that uses the same approach as Chaves', but which has been formulated to consider general deflagration solutions (i.e., not only Ch-J), including the possibility of complete evaporation of the downstream flow. Their model also uses the upstream state (1) as an input.

7.5. An Analytic Solution of the Jump Conditions.

In this section, a simple analytic solution of the conservation Equations 7.2 is obtained, which uses several approximations that are valid for evaporation waves in pure liquids at relatively low, reduced pressures. The formulation assumes a deflagration solution as is

illustrated in Figure 7.2, i.e., a superheated upstream liquid state (1) obtained by depressurization from an initially saturated liquid state (0), and an equilibrium mixture downstream state (2). The subscript "1" will refer to the properties of the nonequilibrium upstream liquid unless otherwise noted. The subscript "2" will refer to saturated properties evaluated at P_2. The first simplifying assumptions that can be made are:

$$\frac{\rho_{l2}}{\rho_{l1}} = O(1) \tag{7.4a}$$

$$\frac{\rho_{v2}}{\rho_{l2}} \ll 1 \quad \textit{Observed values}: \; O(10^{-3}) \tag{7.4b}$$

$$\left[\frac{V_1}{V_2}\right]^2 \ll 1 \quad \textit{Observed values}: \; O(10^{-4} \rightarrow 10^{-3}) \tag{7.4c}$$

Equation 7.4a can be applied fairly generally, whereas Equation 7.4b is valid for end states (2) with sufficiently small, reduced pressures. Equation 7.4c reflects the fact that the downstream *mixture* density is much less than the upstream liquid density (by Equation 7.2a). Physically, this condition is a consequence of Equation 7.4b and the fact that waves in pure liquid are observed to propagate only at Jakob numbers high enough to produce substantial evaporation.

Equations 7.2 are now combined (subject to the assumptions of Equations 7.4 and the mixture rules of Equations 7.1) and χ_2 and V_2 are eliminated. Also, the upstream liquid density ρ_{l1} and enthalpy h_{l1} are replaced by their initial values ρ_{l0} and h_{l0}, since in Section 4.1.1 it was shown that both of these properties are virtually unchanged by depressurization.[3] Three dimensionless parameters then arise:

3. This replacement does not change the form of the equations, but is convenient in assigning numerical values. In situations where this approximation is invalid, the metastable isentrope connecting states (0) and (1) must be calculated.

$$\beta \equiv \frac{\rho_{l0} V_w^{\,2}}{\Delta P_w} \; ; \; \Delta P_w \equiv P_1 - P_2, V_w = V_1 \tag{7.5a}$$

$$\hat{Ja}_2 \equiv \left[\frac{h_{l0} - h_{l2}}{L_2}\right] \frac{\rho_{l0}}{\rho_{v2}} = Ja_2 \left[\frac{\rho_{l0}}{\rho_{v2}}\right] \tag{7.5b}$$

$$\zeta_2 \equiv \frac{\Delta P_w}{2 \rho_{v2} L_2} \tag{7.5c}$$

where ΔP_w is the wave amplitude, L is the latent heat of evaporation, and Δh is the superheat enthalpy. The parameter β (taken as the dependent variable) expresses the relative importance of two independent measures of wave strength: the wave speed V_w and the wave amplitude ΔP_w. $\hat{Ja}_2$ is a modification of the Jakob number that was introduced in Section 1.2.2, which includes a liquid/vapor density ratio (see Equation 4.11).[4] ζ_2 is a dimensionless wave amplitude.

The resulting equation, expressed in terms of the above dimensionless quantities, is:

$$\beta\zeta_2 = \frac{1}{2}\left[\left(\frac{\rho_{l0}}{\rho_{l2}}\right)(\hat{Ja}_2 + 1) - 1 - 2\zeta_2\right] - \left\{\frac{1}{4}\left[\left(\frac{\rho_{l0}}{\rho_{l2}}\right)(\hat{Ja}_2 + 1) - 1 - 2\zeta_2\right]^2 - \zeta_2(\zeta_2 + 1)\right\}^{1/2} \tag{7.6}$$

An additional approximation can be made that leads to a substantial simplification of Equation 7.6, namely, that $\hat{Ja}_2 \gg \zeta_2$. In the present experiments, $\hat{Ja}_2 = O(10^2)$, whereas $\zeta_2 = O(10^{-3} \rightarrow 10^{-2})$. Using this fact and expanding the radical in a binomial series yields:

$$\beta = \frac{1 + \zeta_2}{\hat{Ja}_2} + \frac{(1 + \zeta_2)^2 \zeta_2}{\hat{Ja}_2^{\,3}} + \cdots \tag{7.7}$$

In view of the magnitudes of ζ_2 and $\hat{Ja}_2$, only the first term in the series need be considered.

4. In the literature, this grouping is often referred to simply as the Jakob number.

Moreover, in the present experiments $\zeta_2 \ll 1$, which leaves the simple result:

$$\beta \equiv \frac{\rho_{l0} V_w^2}{\Delta P_w} = \frac{1}{J\hat{a}_2} \tag{7.8}$$

Equation 7.8 dictates that as the modified Jakob number is increased, the wave speed becomes smaller compared to the wave amplitude. From the definition of β and the geometry of Figure 7.2, one can verify that β is single-valued along the Hugoniot curve (unlike the wave speed and the mass flux, which are double-valued).

Figure 7.3 shows Equation 7.8 compared to the data of the present study, as well as that of Grolmes and Fauske (1974). (The data of the present study is indicated by the solid shapes.) Grolmes and Fauske did not measure exit pressure, and in the cases they report, the reservoir was virtually evacuated. This means that their test cell was almost certainly choked, in which case the exit pressure was not the same as the reservoir pressure. For their data it is therefore assumed that the exit pressure is the average of the base and reservoir pressures. (This approximation is actually within 5% for the two choked cases in the present experiments.) Assuming different values for the exit pressure shifts their points approximately horizontally to the right; assuming higher values of exit pressure shifts their points up and to the left. Neither procedure gives substantially better agreement with the ideal curve than the values shown.

The data of the present experiments are in better agreement with the ideal curve. For both R12 and R114, the data corresponding to the intermediate $J\hat{a}_2$ agree best—to within experimental error of the theoretical curve. For both liquids, the deviation of the data corresponding to the lowest $J\hat{a}_2$ is significantly greater than that of the two intermediate points; however, the uncertainty in those cases is correspondingly higher because the wave amplitude for those cases is quite small. For both liquids the deviation of the data corresponding to the highest $J\hat{a}_2$ is the greatest relative to experimental error. In light of the relaxation lengths estimated in Section 4.3, it may be that the equilibrium assumption may not be satisfied at the test cell exit.

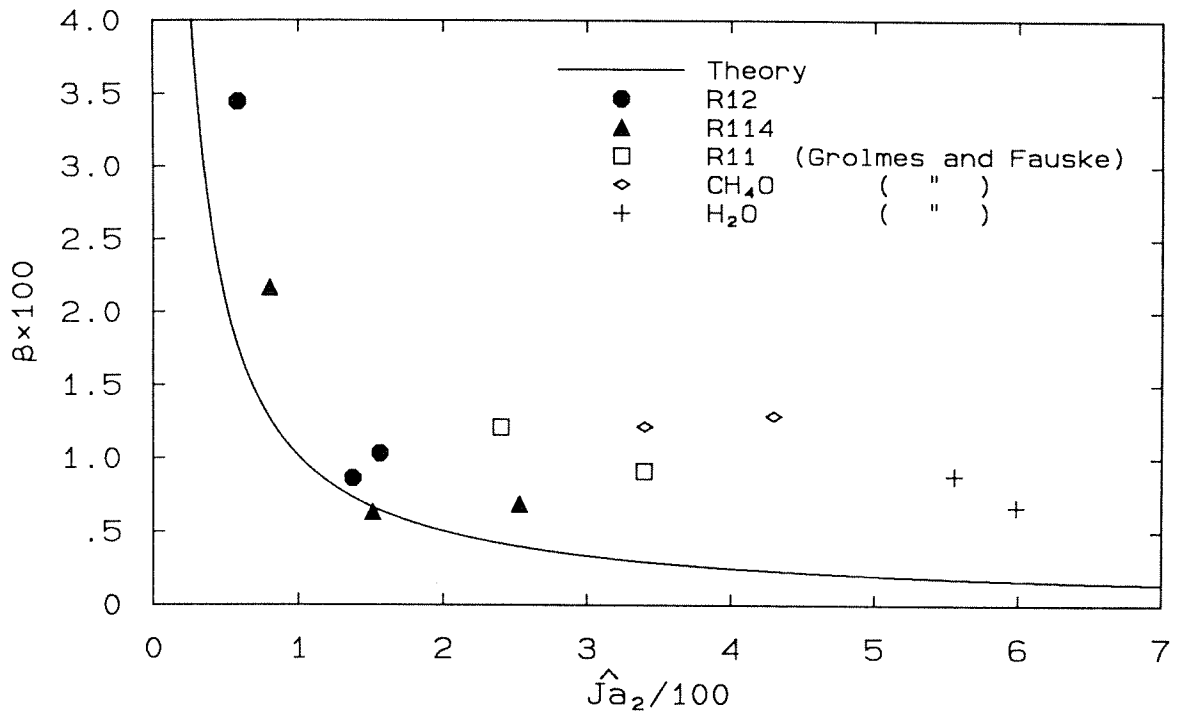

Figure 7.3: Ideal jump condition relation compared with experiments.

7.6. Analytic Expressions for Two-Phase Flow Properties.

By combining Equations 7.2a and 7.2b, the normalized exit velocity and normalized mixture density can be expressed in terms of β alone:

$$\frac{V_2}{V_w} = \frac{\beta + 1}{\beta} \approx \frac{1}{\beta} = \hat{Ja}_2 \tag{7.9a}$$

$$\frac{\rho_2}{\rho_{l1}} = \frac{\beta}{\beta + 1} \approx \beta = \frac{1}{\hat{Ja}_2} \tag{7.9b}$$

where the "≈" sign indicates the use of the approximation:

$$\beta \ll 1 \quad \textit{Observed values}: \; O(10^{-2}) \tag{7.10}$$

and $\hat{Ja}_2$ is substituted for β using Equation 7.8. By combining Equation 7.9b and the definition

of mixture density, the volume fraction of vapor α_2 can be expressed as:

$$\alpha_2 = 1 - \left[\frac{\rho_{l1}}{\rho_{l2}}\right]\beta \approx 1 \tag{7.11}$$

where "≈" indicates use of Equations 7.4a and 7.10. The predicted value of α_2 is therefore within about a percent of unity. Using Equations 7.11 and 7.4b, the mass fraction of vapor χ_2 can be expressed as:

$$\chi_2 = \left[\frac{\rho_{v2}}{\rho_{l2}}\right]\left[\frac{\frac{\rho_{l2}}{\rho_{l1}} - \beta}{\beta}\right] \approx \left[\frac{\rho_{v2}}{\rho_{l1}}\right]\frac{1}{\beta} = Ja_2\,; \quad Ja_2 \equiv \frac{h_{l0} - h_{l2}}{L_2} \tag{7.12}$$

where the "≈" indicates use of Equations 7.4a and 7.10, and again, $J\hat{a}_2$ is substituted for β using Equation 7.8. Note that the result $\chi_2 = Ja_2$ is a generalization of the result for the isobaric evaporation example of Section 1.2.2 (which, although the mechanisms of evaporation were not specified, can be taken to represent the hypothetical "zero strength" wave in which ΔP_w and V_w are zero). In the finite-strength case, Equation 7.12 dictates that the Jakob number must be based on the *downstream* pressure. Equation 7.12 predicts that χ_2 ranges from 0.22 to 0.35 for the present experiments. Thus, although the flow is almost entirely vapor by volume, it is mostly liquid by mass.

7.7. Comments on Model Closure.

The jump condition relations allow the wave speed and the flow properties to be determined given the upstream state and the downstream boundary condition. In the present experiments the appropriate downstream boundary conditions are:

$$P_2 = P_{res} \qquad (\textit{unchoked cases}) \tag{7.13a}$$

$$V_2 = a_2(P_2, \chi_2) \qquad (\textit{choked cases}) \tag{7.13b}$$

where a_2 is the sound speed of the downstream flow. In addition, it is known that the upstream pressure lies on the isentrope passing through the initial saturated liquid state. Consequently,

for a given initial liquid state (T_0, P_0) and reservoir pressure P_{res}, the wave speed and flow properties can be expressed as a function of a single unknown quantity, namely, the upstream pressure.

As mentioned in Section 7.1, an additional relationship is needed to close the equations. Such a relationship would be analogous to a flame speed in a premixed flame: It would express the rate at which the rapid evaporation processes occur. Equation 4.15—the expression for wave speed found in Section 4.2.2.7—is an attempt at such a relationship, but it is incomplete (it depends on measured quantities). Lacking a viable analytic solution, some effort was devoted to an empirical/dimensional approach without success. The search for a rate relation remains a challenge for future research.

Chapter 8

Summary and Conclusions

Evaporation waves have been experimentally studied by rapidly depressurizing two volatile liquids—Refrigerants 12 and 114. The study was motivated by the fact that the fundamental mechanisms of rapid evaporation in superheated liquids are poorly understood. Evaporation waves generated by rapid depressurization, and in particular waves in which nucleation within the liquid column is suppressed, provide the high degree of control necessary to study rapid evaporation processes effectively. High-speed motion pictures and spark-illuminated still photographs, in combination with fast-response pressure measurements, have revealed a variety of new phenomena.

When the diaphragm is ruptured to initiate the experiment, the liquid pressure drops within a few milliseconds virtually to the reservoir value. Provided that the liquid superheat produced by rapid evaporation is sufficiently high, the liquid free surface then erupts in explosive boiling, which is characterized by violent, fine-scale fragmentation of the superheated liquid and extremely rapid evaporation. The explosive boiling process proceeds as a "wavefront" into the liquid column, producing a high-speed, two-phase flow that travels upward into the low-pressure reservoir, emptying the test cell in a few hundred milliseconds. The mass fluxes generated by the evaporation wave are orders of magnitude greater than those associated with quiescent evaporation at the same thermodynamic conditions.

8.1. Quasi-Steady Propagation.

Within about 10 ms of explosive boiling initiation, the wave reaches a quasi-steady condition in which the average wave speed, two-phase flow speed, and base and exit pressures are constant. The flow can then be divided into three regions: 1) the upstream liquid region, 2) the wavefront region, and 3) the developed flow region.

8.1.1. *Upstream Liquid Region.* The density and enthalpy of the upstream liquid are virtually the same as the corresponding properties in the initial saturated liquid. Temporal fluctuations in the liquid's superheat (caused by pressure fluctuations) are negligible compared to the average superheat. Since nucleation within the liquid column is suppressed *entirely*, the upstream liquid is globally stagnant. Moreover, it is observed that the amount of convection in the upstream liquid induced by wavefront nonsteadiness is small. Heat absorption that is due to evaporation at the wavefront creates a cold thermal boundary layer in the upstream liquid. The quasi-steady nature of wavefront propagation implies that the average thickness of the layer does not increase with time, and calculations indicate that it is very thin compared to the characteristic structure of the wavefront. The expression for the average thermal boundary-layer thickness is shown to be the same as for a laminar flame.

8.1.2. *Wavefront Region.* The wavefront is defined as the order one-centimeter-thick region where most fragmentation, rapid evaporation, flow acceleration, and pressure drop occur. Although the average wave properties are constant, the mechanisms that generate the mean flow are observed to be inherently nonsteady. Nonsteadiness arises in the base pressure, in wavefront propagation, and in the liquid fragmentation processes.

Attention to photographic resolution and the use of several views have yielded new insight into the structure and dynamics of the explosive boiling process. Specifically, the leading edge of the wavefront is found to consist of a layer of bubbles, the lifetimes and maximum diameters of which are statistically distributed (the average values are of order 1 ms and 1 mm, respectively). The characteristic thickness of the leading-edge bubble layer is about 1 mm, i.e., about one bubble diameter. The growth rate of the leading-edge bubbles exhibits the same $\sqrt{t}$ time dependence as thermally limited bubbles in an infinite superheated liquid, but the growth rates are somewhat slower. The wavefront is globally convoluted, but the appearance of the bubble layer is fairly uniform over the entire leading edge. The walls play no noticeable role in quasi-steady explosive boiling.

One of the most important discoveries of these experiments is that the explosive nature of the evaporation waves arises through the violent and nonsteady breakup of the leading-edge bubbles in "bursts" of aerosol. Bursts are *not* associated with the rupture of single bubbles, but

are "large scale structures" associated with the fragmentation of many (hundreds of) bubbles. From the bottom views it is apparent that bursts are "fragmentation waves" that sweep randomly around the leading-edge bubble layer—i.e., they propagate in a direction normal to the direction of wavefront propagation. The rate of expansion and propagation of bursts is of the same order of magnitude as the speed of the developed two-phase flow, namely, 10 m/s.

Measurements of the "instantaneous" position of the wavefront upstream tip (from motion pictures) indicate that any given region of the wavefront tends to propagate in surges that are the same order of magnitude as the mean velocity. Observations of the wavefront coincident with the velocity surges indicate that the latter are generated by two mechanisms: 1) the nucleation of one or more new bubbles at the region of the leading edge in question, or 2) the generation of fine-scale "roughness," which gives way within a few hundred microseconds to smooth bubbles and/or surface perturbations. In many cases the cause of the roughness appears to be caused by aerosol from a burst striking the leading edge. In other cases the origin of roughness is unclear, raising the possibility of the action of interfacial instabilities suggested by previous authors.

The observations concerning bubble growth and the intermittent, surging nature of wavefront propagation were combined to arrive at an approximate, partial model for the average wave speed in terms of leading-edge bubbles. The model suggests that the wave speed is proportional to the square root of the thermal diffusivity, as is the flame speed for a laminar flame.

8.1.3. *Developed Flow Region.* Downstream of the wavefront region, the average speed and appearance of the flow are virtually constant. The flow is a highly nonuniform, two-phase spray containing streaklike structures. Its liquid phase is composed of drops (with a maximum diameter of about 100 μm), as well what appear to be clusters and chains of bubbles (with typical bubble diameters of a few hundred microns). Exit pressure measurements indicate that the flow chokes for sufficiently low reservoir pressure; at higher reservoir pressures the flow is unchoked. Estimates of the relaxation length for evaporating droplets suggest that evaporation still occurs downstream of the wavefront region, but that the test-cell length is the proper order of magnitude at which to expect the mixture to reach saturation at the test-cell exit. A thin

liquid layer begins climbing the wall upon wave initiation. Its speed is a few m/s—significantly slower than that of the two-phase flow through the center. The wall layer does not appear to affect the inner flow significantly, but does cause optical distortion of its image.

8.1.4. *Effect of Reservoir Pressure on Quasi-Steady Propagation.* The quasi-steady propagation mechanisms appear to be qualitatively the same for both liquids and all reservoir pressures tried. However, significant quantitative differences were noted. As the reservoir pressure is raised, the wavefront propagation and bursting process become more intermittent. The wave speed, wave amplitude, two-phase flow speed, and mass flux all decrease. For both liquids, the wave amplitude decreases in approximate proportion to the increase in reservoir pressure, so that the increase in *upstream* pressure (and therefore the decrease in the upstream liquid superheat) are small (about 10% or less). The wave speeds observed ranged from 0.21 $\rightarrow$ 0.63 m/s; the corresponding wave amplitudes ranged from 0.03 $\rightarrow$ 0.51 bar, the two-phase flow speeds ranged from 5 $\rightarrow$ 35 m/s, and the mass flux ranged from 471 $\rightarrow$ 837 kg $s^{-1}m^{-2}$.

8.2. Start-Up Behavior.

Three modes of wave initiation are observed depending on the liquid and reservoir pressure. In Mode 1 (which is observed only at the highest superheat, namely, R12, P_{res} = 0 bar), nucleation sites form at random spots on the liquid free surface and at the glass/free-surface contact line. Boiling spreads to the remaining surface within one motion picture frame (160 μs). In the highest superheat case for the less volatile liquid (R114), nucleation begins only at the glass/free-surface contact line, and spreads radially toward the center (Mode 2). In the lower superheated cases for both liquids, nucleation initiates at one or more sites on the glass/free-surface contact line (or in some cases on a bit of diaphragm that has struck the free surface), and propagates across the free surface (Mode 3). The third mode is sometimes observed for the condition R12, P_{res} = 0 bar as well.

Unlike quasi-steady propagation, the manner in which explosive boiling initiates appears to be sensitive to several extraneous factors, such as the depressurization rate, the liquid height, the cleanliness of the wall and liquid free surface, and the microscopic properties of the wall at the wall/free-surface contact line. Because the time scale of the start-up regime is very much less than that of the quasi-steady regime, the two are completely decoupled.

8.3. Thresholds.

8.3.1. *Self-Start Threshold.* For both liquids at the higher superheats, explosive boiling initiates a few milliseconds after diaphragm burst. This is essentially the same time scale in which depressurization occurs. However, if the reservoir pressure is raised above a certain approximate value, the onset of explosive boiling is delayed. During the delay period, relatively slow bubbling (initiated at one or more nucleation sites at the glass/free-surface contact line) occurs, and a cluster of bubbles forms in the vicinity of the initial site. The bubble cluster then explodes, indicating the transition to explosive boiling. As the reservoir pressure is increased slightly further, the delay period increases significantly, up to times of order 100 ms. The *self-start threshold* occurs when, for a given liquid temperature and reservoir pressure, transition to explosive boiling never occurs.

8.3.2. *Absolute Threshold.* The self-start threshold is not a threshold for *propagation*: Waves can propagate at somewhat lower superheats if started artificially. This was accomplished in Refrigerant 114 by "jump-starting" the wave using the more volatile Refrigerant 12. It is found that an *absolute threshold* exists when, for a given liquid, temperature, and reservoir pressure, a wave in R12 does not continue to propagate into the R114. As the absolute threshold is approached, bursting becomes increasingly sporadic, and the absolute threshold corresponds to the condition at which the bursting process breaks down completely. Observations near the absolute threshold confirm that bursting is a necessary aspect of wavefront propagation.

8.4. Mechanisms of Wave Propagation.

On a general level, it was inferred that explosive boiling is characterized by an interaction between evaporation-induced liquid motion (leading to liquid fragmentation and increased surface area) and enhanced evaporation caused by the surface area increase (which in turn causes more liquid fragmentation). The way in which the "evaporation/fragmentation" interaction is manifested was seen to be quite complicated in detail.

The two hypotheses suggested by previous authors— the secondary nucleation hypothesis (Mesler, 1988), and the interfacial instability hypothesis (e.g., Shepherd and Sturtevant,

1982)—were examined in the context of the present observations. Although both hypotheses may play a role, neither alone is found to be adequate to explain the full range of observed behavior (e.g., neither predicted bursting). The following tentative hypothesis was herein suggested regarding the qualitative nature of wave propagation: Nucleation of floating bubbles occurs at the wavefront leading edge, and bursting represents the phased fragmentation of those bubbles. It was suggested that the interstitial liquid between leading-edge bubbles is still superheated, so that when material from previously ruptured bubbles strikes and ruptures adjacent bubbles, the newly fragmented liquid rapidly expands driven by enhanced evaporation, in turn rupturing additional bubbles, and so on. This would explain the observed tendency for bursts to propagate transverse to the direction of wave propagation. (The way in which interfacial instabilities may enter in such a process is not understood.) It was further suggested that some fraction of the aerosol generated in bursts strikes the leading edge, and that some fraction of those striking droplets lead to nucleation of new bubbles. Thus in this scenario bursting and nucleation are interactive and are both equally necessary for wave propagation.

8.5. Jump Condition Model.

An evaporation wave is analogous to a premixed flame: In gasdynamic theory both are classified as "weak deflagration" waves. The evaporation wave was therefore modeled in a similar manner. It was shown that using several approximations valid for the type of evaporation waves studied, the conservation equations (jump conditions) can be reduced to a single, simple expression in terms of readily measured and inferred properties.

8.6. Suggestions for Future Work.

Evaporation wave experiments to the present date have revealed a variety of behavior, and it is not clear how to reconcile many of the differences that have arisen. More experiments, representing a wider variety of liquids, states and configurations, would be desirable in order to better characterize the possible range of behavior.

Despite the new observations offered by the present experiments, little is known about the detailed interaction between evaporation and fragmentation. The difficulty has been that experiments have not resolved the essential features of these fine-scale interactions; hence, numerical models—even greatly simplified ones—might provide useful insight.

The jump conditions for evaporation waves have now been treated by several authors, most of whom have also addressed the question of the downstream boundary conditions. However, an additional relationship is still needed to complete such models. This relation would evidently be analogous to the flame speed of a premixed flame, and would describe the rate at which rapid evaporation proceeds.

Appendix A

Guide to Video Supplement

The video supplement is a selection of several of the best high-speed movies obtained in this study. The video was transferred from the 16 mm camera negatives to a 3/4 inch "SP" encoded video master, via a Rank-Cintel machine.[1] Although the resolution of the video format is less than that of a 16 mm print, the fact that the "Rank" machine allows separate control of exposure and contrast is an important compensating factor. Please note:

1. The format is NTSC VHS (no sound).
2. It is important that the video be viewed in subdued lighting, and if possible on a studio monitor in the "underscan" mode.
3. Ordering information is provided at the end of this appendix.

A.1. Views.

Figure A.1 illustrates the four motion picture views used: 45° top oblique, side, 45° bottom oblique, and bottom. The prints in the figure illustrate the appearance of the test cell prior to depressurization. The camera is rotated 90° in order to frame the tube as efficiently as possible; hence, in the side and oblique views the tube appears horizontal. The liquid is on the left; the vapor is on the right. The side and oblique views appear light initially, because in these views the test cell is illuminated from behind, and the liquid and vapor are both transparent. The bottom view appears dark initially, because in this view the test cell is illuminated from the sides and the bottom. With the exception of the reflection from the diaphragm (which is the bright spot in the middle), very little light is scattered in the direction of the camera. The nominal liquid height is 7.00 cm in the side and bottom views. In the oblique bottom view the nominal liquid height is 7.75 cm, and in the oblique top view, it is 9.13 cm. In the oblique top view test cell #1 is used; in the other views, test cell #2 is used (Section 2.1.2). Note that only a portion of the test cell is photographed.

---

1. The transfer and editing were performed by Independent Producers Studio, Inc. 1741 N. Ivar Ave. Suite 109, Hollywood, CA 90028.

The "grey" scale in the side views is constructed of neutral density filters. The scale receives essentially the same illumination as the flow. By matching the grey level of a given part of the flow to the equivalent portion of the scale, the approximate degree of light extinction caused by the flow can be determined. The identification numbers are the common logarithm of the inverse transmittance of the filter. For example, the number "2" indicates that one hundredth of the light is transmitted. The ruler in the side views indicates centimeters (large divisions) and millimeters (small divisions). The numbers on the ruler indicate the height, in centimeters, from the bottom of the test cell.

When the run begins, the wave propagates from right to left ("down" in lab coordinates), and the flow travels from left to right ("up" in lab coordinates) In the bottom views, the wavefront approaches the observer. The reader is referred to Chapter 2 for more information about views and photographic methods.

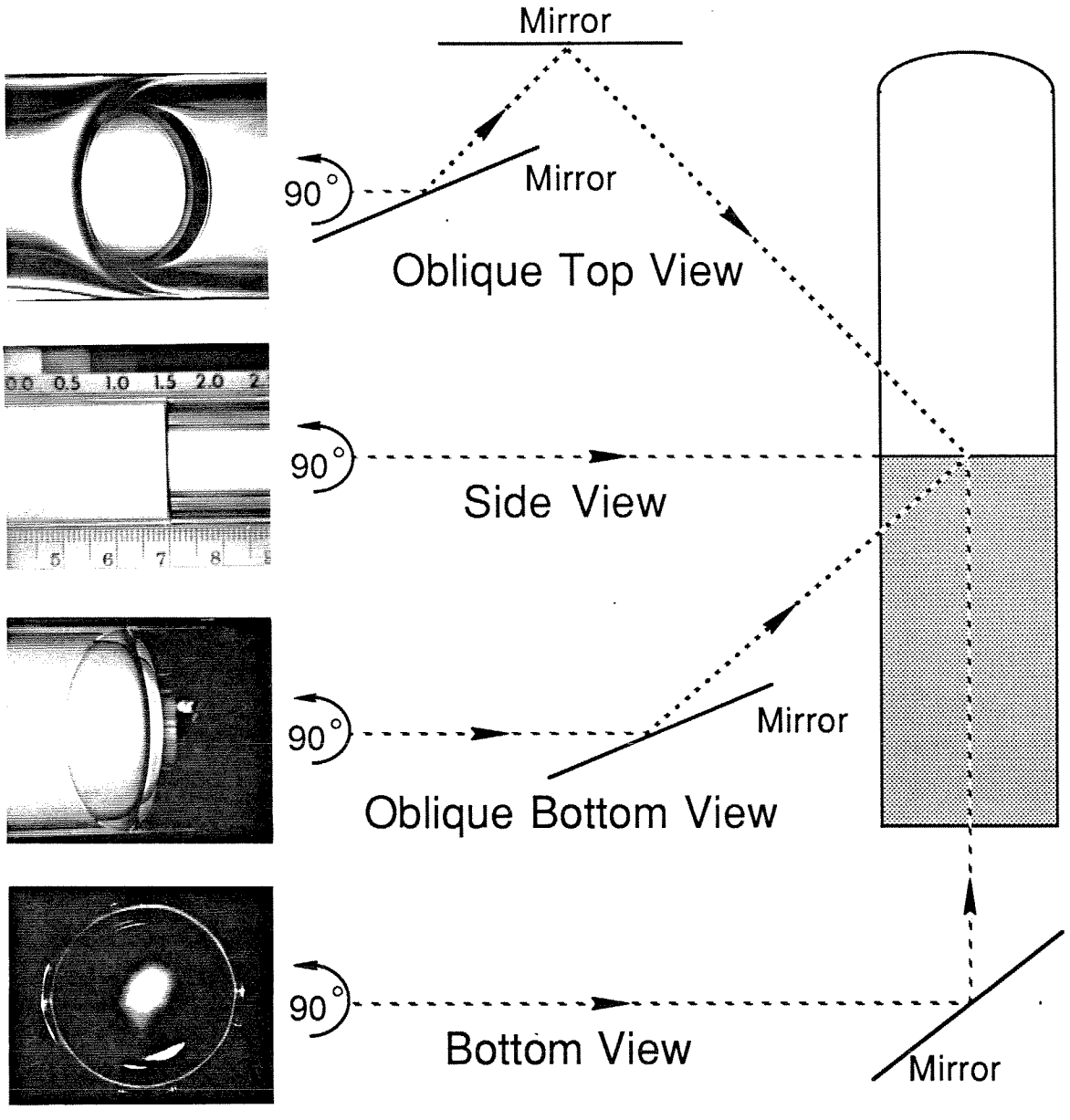

Figure A.1: The four motion picture views and their appearance in the video.

A.2. Program Guide.

In this section, the noteworthy features of each video entry are briefly described. The start-up process receives the most emphasis in this discussion only because the qualitative differences between runs occur primarily during this regime. The measured average wave properties corresponding to the side view runs appearing in the video are given in Table 4.1, and the corresponding pressure traces are given in Appendix B. (The condition R12, P_{res} = 1/2 bar is omitted from the video because its features are adequately represented in the other five run conditions.) The framing rate of the high-speed movie camera was set between 4000 and 6000 fr/sec depending on the expected run duration. Its *nominal* value for each run is indicated below, as well as in the video captions. The motion picture run (MPR) number of each video entry—which is indicated below—may be used for cross-reference to the text examples.

1. **Refrigerant 12 Experiments. Initial Temperature: 20°C, Initial Pressure: 5.69 bar.**

   1.1. **0 bar Reservoir Pressure.** This run condition has the highest superheat temperature (50.9°C), wave speed (0.63 m/s), and flow speed (35 m/s) of the six run conditions. The quasi-steady flow is choked for this condition, which limits the liquid superheat, the wave speed, and the two-phase flow speed (Section 4.5.3).

   Side view. Run number: MPR 25. Framing rate: 6000 fr/sec. Within 2 ms from the start of diaphragm rupture, the vapor above the liquid column condenses to form a fog. This is the expected behavior for a "normal" fluid upon adiabatic depressurization (Section 1.3.1). The fog appears very dark because it efficiently scatters incident light away from the camera. After fog formation and before the onset of explosive boiling, a contact surface rises from the liquid free surface, which separates the quasi-equilibrium "dry" vapor (which evaporates subsequent to depressurization), from the preexisting "wet" vapor (which condenses upon depressurization) (Section 5.1).

   Explosive boiling initiates within about 3 milliseconds of diaphragm rupture. (The manner in which it initiates is clear in the oblique and bottom views.) Within 10 ms of diaphragm rupture the quasi-steady regime is fully established, at which time the wave has forgotten the start-up process. As the wavefront propagates, it becomes convoluted on the scale of the test-cell diameter, indicating a lack of stabilizing forces (Section 4.2.2). The speed of the wavefront leading edge (which consists of a thin layer of bubbles) is constant when averaged over times greater than about 10 ms; however, its instantaneous rate of propagation is both spatially nonuniform and temporally nonsteady (Section 4.2.2). Fragmentation and acceleration of the fluid occur within several millimeters of the leading edge. This process is also spatially nonuniform and temporally nonsteady. Specifically, fragmentation tends to occur in

"bursts" of aerosol (Section 4.2.2).

The developed two-phase flow is a spatially nonuniform spray. It is composed of "streak-like structures," which are regions of relatively high liquid concentration. A slower (1 m/s) liquid layer on the wall is pulled up the wall by the faster flow through the center. The leading edge of this layer can be seen early in the run at the edges of the test cell (Section 4.3.1).

Oblique bottom view. Run number: MPR 44. Framing rate: 6000 fr/sec. This view illustrates Mode 1 start-up, in which nucleation occurs at random locations on the free surface and at the glass/free-surface contact line (Section 5.2). From this view it can be seen that the free surface remains very smooth between the arrival of the initial expansion wave and the onset of nucleation. Once nucleation begins, explosive boiling spreads to the remaining surface in a time of order 100 μs. The structure and dynamics of the wavefront and the liquid wall layer are accentuated in this view.

Bottom view. Run number: MPR 39. Framing rate: 6000 fr/sec. The rupture of the diaphragm can be seen in the reflected light pattern. After the diaphragm breaks fully (which takes slightly greater than 1 ms), the image is almost completely dark because virtually no light is scattered toward the camera. The image brightens as the fog forms (Section 5.1), at which time a mottled structure can be seen. This is believed to be associated with the contact surface rather than the liquid free surface, since, as noted in the above description of the oblique bottom view, the free surface remains smooth during this time.

In this run, start-up is primarily Mode 1; however, explosive boiling also propagates across a portion of the surface, so it is really a "mixed mode" (Section 5.2). In the bottom views, "bursts" appear as dark clouds that sweep through the leading-edge bubble layer (in a direction perpendicular to the direction of wave propagation) in a random fashion. Thus, they are essentially small "fragmentation waves" within the larger wavefront. The bottom views become dark when the wavefront goes below the level of the liquid jacket windows.

1.2. **1 bar Reservoir Pressure.** This condition is near the self-start threshold, and in such cases the transition to explosive boiling is delayed by times of order 10 ms. For this run condition, wave initiation follows a consistent pattern: Nucleation begins at one or more sites on the glass/free-surface contact line, then spreads to the immediate vicinity of the initial site(s) so that a cluster of bubbles is formed. The cluster "explodes," and boiling then rapidly propagates across the free surface and into the liquid column (Section 5.3).

When quasi-steady propagation is established, the appearance of the wave is qualitatively like that of the first (0 bar reservoir pressure) case. However, the

nonsteady processes of propagation and fragmentation tend to be both slower and more intermittent, and therefore easier to visualize (Section 4.2.2). For this run condition the liquid superheat temperature, wave speed, and flow speed are 48.8°C, 0.36 m/s, and 5 m/s, respectively. The quasi-steady flow is unchoked (Section 4.5.3).

Side view. Run number: MPR 31. Framing rate: 6000 fr/sec. As in the 0 bar reservoir pressure case, the initially saturated vapor condenses upon depressurization to form a fog. Since in this case explosive boiling is delayed, the fog cloud lingers for some time, and can be seen oscillating in response to reverberating pressure waves. Transition to explosive boiling occurs by Mode 3 (Section 5.2) in the manner described above.

Oblique bottom view. Run number: MPR 47. Framing rate: 5000 fr/sec. For this run condition, the delay to explosive boiling transition is generally sufficient that there is time for capillary waves to develop on the free surface. Their motion is clearly seen in this view and in the bottom view; they do not contribute to the onset of explosive boiling. Rather, transition to explosive boiling occurs by Mode 3 in the manner described above. For this condition, the boiling front sweeps across the surface at about 1 m/s.

Bottom view. Run number: MPR 43. Framing rate: 6000 fr/sec. This run provides another example of Mode 3 start-up near the self-start threshold. Note that in this view, the bubble cluster turns white upon explosive boiling initiation due to light scattering from the aerosol generated.

2. **Refrigerant 114 Experiments. Initial Temperature: 20°C, Initial Pressure: 1.83 bar.** The qualitative appearance of quasi-steady waves is essentially the same for R114 as for R12.

2.1. **0 bar Reservoir Pressure.** For this run condition, the liquid superheat temperature, the wave speed, and the flow speed are 36.2°C, 0.32 m/s, and 25 m/s, respectively. The quasi-steady flow is choked (Section 4.5.3).

Side view. Run number: MPR 55. Framing rate: 5000 fr/sec. The preexisting vapor does not condense upon depressurization because Refrigerant 114 is a "retrograde" fluid (Section 1.3.1). Consequently, the two-phase front that travels up the tube when explosive boiling initiates can be clearly seen in this view.

Oblique bottom view. Run number: MPR 60. Framing rate: 5000 fr/sec. This example shows a clear view of Mode 2 start-up, in which nucleation begins at many points on the glass/free-surface contact line and spreads radially inward (Section 5.2). The rate of propagation of the initial boiling front across the surface is about 10 m/s.

Bottom view. Run number: MPR 62. Framing rate: 6000 fr/sec. This run shows another example of Mode 2 start-up. Since there is no fog formation, the image in this view remains dark until boiling begins.

2.2. **1/3 bar Reservoir Pressure.** This condition is near the self-start threshold, which means that the transition to explosive boiling is delayed (cf. R12, P_{res} = 1 bar). The superheat is generally insufficient to produce bubble clusters at the glass/free-surface contact line that lead to explosive boiling for the case R12, P_{res} = 1 bar. However, additional help is provided by bits of diaphragm that fall into the test cell and strike the free surface. These play the same role as wall nucleation sites for R12, P_{res} = 1 bar, and transition to explosive boiling occurs in essentially the same manner. The liquid superheat temperature, wave speed, and two-phase flow speed for the quasi-steady propagation phase are 33.5°C, 0.27 m/s, and 15 m/s. The quasi-steady flow is unchoked (Section 4.5.3).

Side view. Run number: MPR 57. Framing rate: 5000 fr/sec. Since there is no fog formation and explosive boiling is delayed, there is no visual indication of when the diaphragm breaks. The delay in explosive boiling for this case is quite long (350 ms), and during most of this time the free surface remains quiescent. A cold, "turbulent" layer begins to form at the free surface, which is (barely) visible because of the shift in refractive index with temperature. The first action occurs when a bit of falling diaphragm strikes the free surface, creating a train of capillary waves. Upon hitting the surface, it is thrown a few centimeters back up into the vapor and out of the field of view. Later, three more bits of diaphragm can be seen falling. These strike the liquid and begin to sink. The event that leads to explosive boiling is the nucleation of a bubble on one of the diaphragm bits. This bubble grows to the point where its film cap extends about a centimeter above the liquid surface, and then breaks. A dramatic transition to explosive boiling occurs about 1.5 ms after the receding film strikes the free surface (Section 5.3).

Oblique top view. Run number: MPR 66. Framing rate: 5000 fr/sec. The top oblique view is only useful for R114 runs, because there is no fog formation. In this particular run, nucleation initiates at three sites on the glass/free-surface contact line. Quiescent bubbling spreads out from those sites to form a cluster of bubbles as was described above for the case R12, P_{res} = 1 bar. At about 6 ms, one of the bubble clusters dramatically explodes, driving aerosol upward and initiating the explosive boiling process (Section 5.3).

Oblique bottom view. Run number: MPR 61. Framing rate: 5000 fr/sec. In this run, start-up is aided by bits of falling diaphragm. The first bit that hits forms a crater in the liquid and generates a train of capillary waves. Shortly after these waves have died out, a second bit of diaphragm strikes the free surface, which this time results in

nucleation and transition to explosive boiling.

Bottom view. Run number: MPR 63. Framing rate: 5000 fr/sec. As in the previous example, it appears that quiescent bubbling is first initiated by a bit of diaphragm striking the free surface. Transition to explosive boiling occurs in the same manner.

2.3. **1/2 bar Reservoir Pressure.** This value of reservoir pressure corresponds to the absolute threshold, i.e., the absolute maximum pressure at which the wave can propagate in the given liquid at the given temperature (Section 4.4). At this condition the wave must be "jump-started" using the more volatile R12. R114 is filled to the 6.3 cm mark; R12 is then filled to the 9.5 cm mark. As the wave propagates from the R12 into the R114, the differences between the characteristics of wave propagation at a higher superheat and the lower superheat can be readily seen. Specifically, the wave speed decreases by a factor of 3, the flow speed decreases by a factor of 7, and the propagation and fragmentation processes become much more sporadic. The liquid superheat temperature, wave speed, and two-phase flow speed after propagation is established in pure R114 are 31.9°C, 0.21 m/s, and 5 m/s, respectively (Section 4.5.3). This value of wave speed is the slowest yet observed.

Side view. Run number: MPR 72. Framing rate: 4000 fr/sec. In this view, the R114 is dyed so that it appears slightly darker than the overlying R12. In this particular run the wave propagates 2.0 cm, at which point the wavefront processes break down. The breakdown of wave propagation is coincident with that of the bursting process. Some residual nucleation persists for several hundred milliseconds and, since fragmentation no longer occurs, these bubbles grow to form a froth. Eventually (long after the end of the movie), the liquid becomes sufficiently cold that all nucleation ceases.

Bottom view. Run number: MPR 74. Framing rate: 4000 fr/sec. In this run, wave initiation begins by Mode 2, which is anomalous for the condition R12, P_{res} = 1/2 bar (Section 5.2). The reason for the difference is believed to be the greater liquid height in this case. In this particular run, the wave does not breakdown in the R114, but continues until the container is emptied. One can tell approximately when the wavefront reaches the R114 because the sweeping motion of the bursts slows down (Section 4.2.2).

A.3. Ordering Information.

The video supplement may be obtained from:

Prof. Bradford Sturtevant
Mail Stop 301-46
California Institute of Technology
Pasadena, CA 91125

Please include a check for $15.00 payable to Prof. Sturtevant, to offset our distribution costs.

Appendix B

Base and Exit Pressure Traces for the Six Primary Run Conditions

This appendix presents examples of pressure traces from each of the six run conditions. The examples are taken from the same runs as appear in Table 4.1.[1] Figures B.1, B.3, B.5, B.6 and B.7 correspond to the side view motion picture runs in the video supplement. Each pressure trace is plotted both on a short time scale (to illustrate start-up features) and on a long time scale (to illustrate quasi-steady propagation features). The time origin corresponds to the time of oscilloscope trigger, which occurs within order 100 μs of the sharp drop in exit pressure.

1. An additional example of the near-threshold condition R12, P_{res} = 1 bar—in which a wave does not start—is also given (Figure B.4).

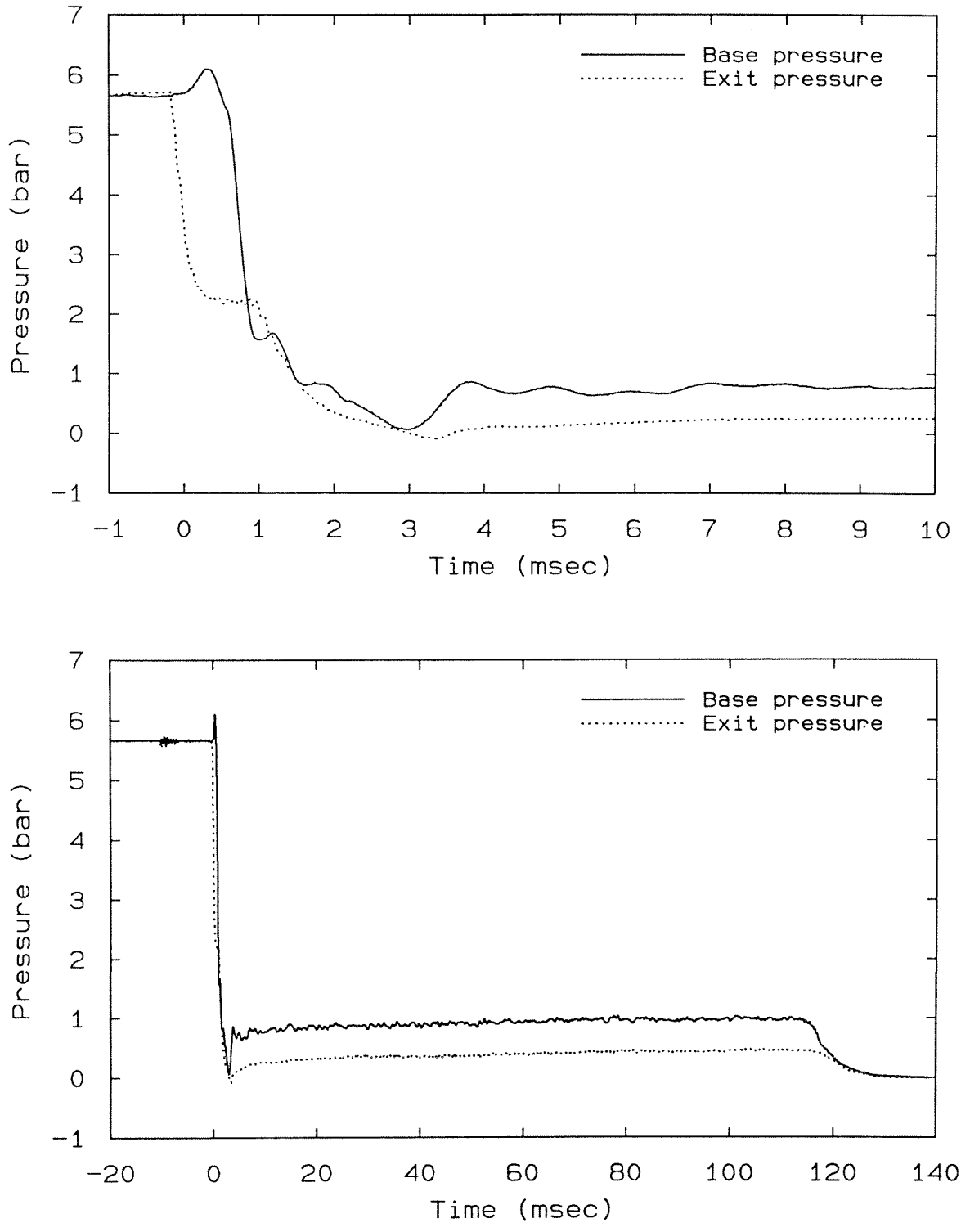

Figure B.1: Liquid: R12, T_0 = 20°C, P_{res} = 0 bar, Run #: MPR 25. Comments: choked exit during quasi-steady propagation phase.

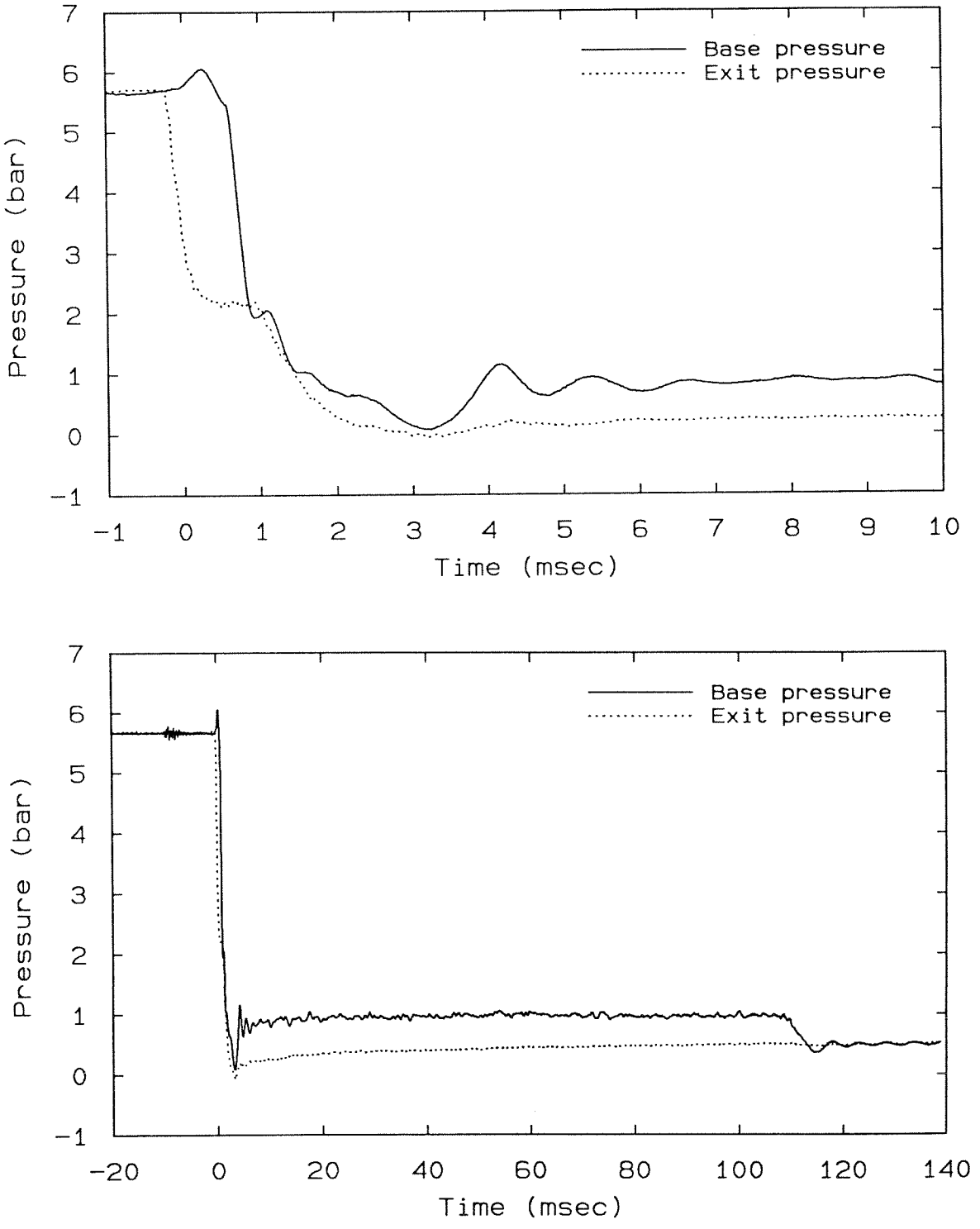

Figure B.2: Liquid: R12, T_0 = 20°C, P_{res} = 1/2 bar, Run #: MPR 26. Comments: unchoked exit during quasi-steady propagation phase.

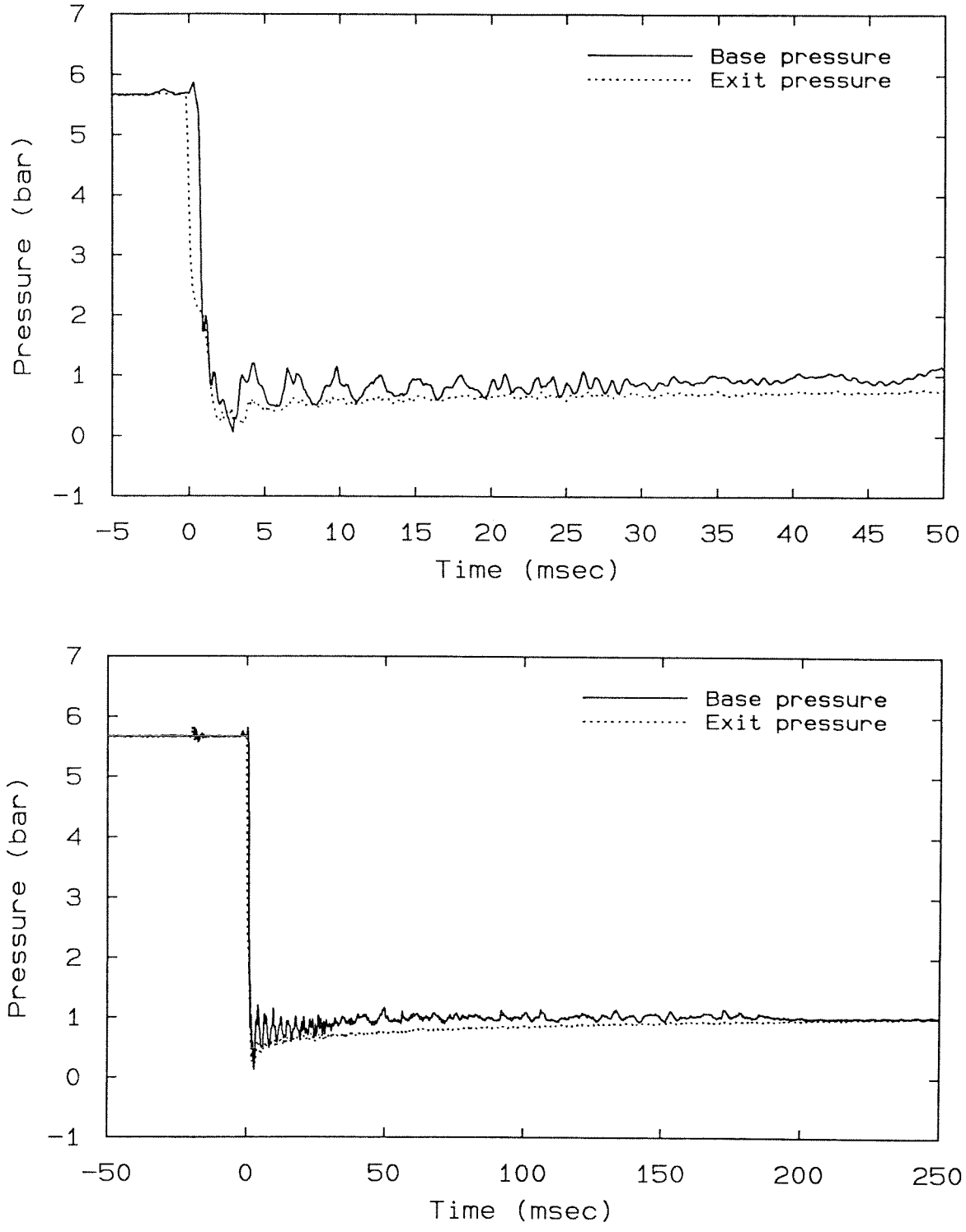

Figure B.3: Liquid: R12, T_0 = 20°C, P_{res} = 1 bar, Run #: MPR 31. Comments: unchoked exit during quasi-steady propagation phase; near self-start threshold; transition to explosive boiling occurs at about 25 ms.

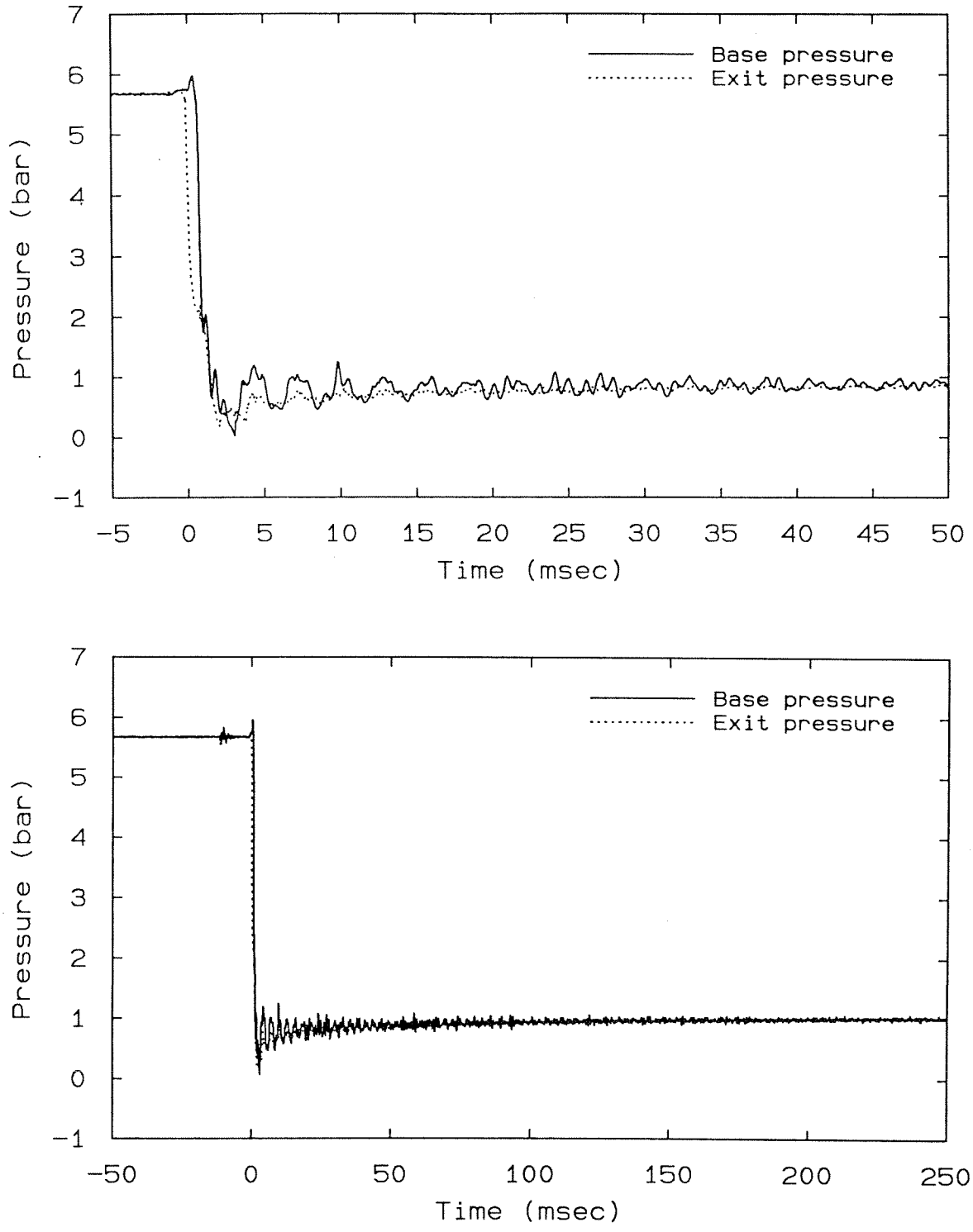

Figure B.4: Liquid: R12, T_0 = 20°C, P_{res} = 1 bar, Run #: MPR 30. Comments: near self-start threshold; transition to explosive boiling does not occur (cf. Figure B.3).

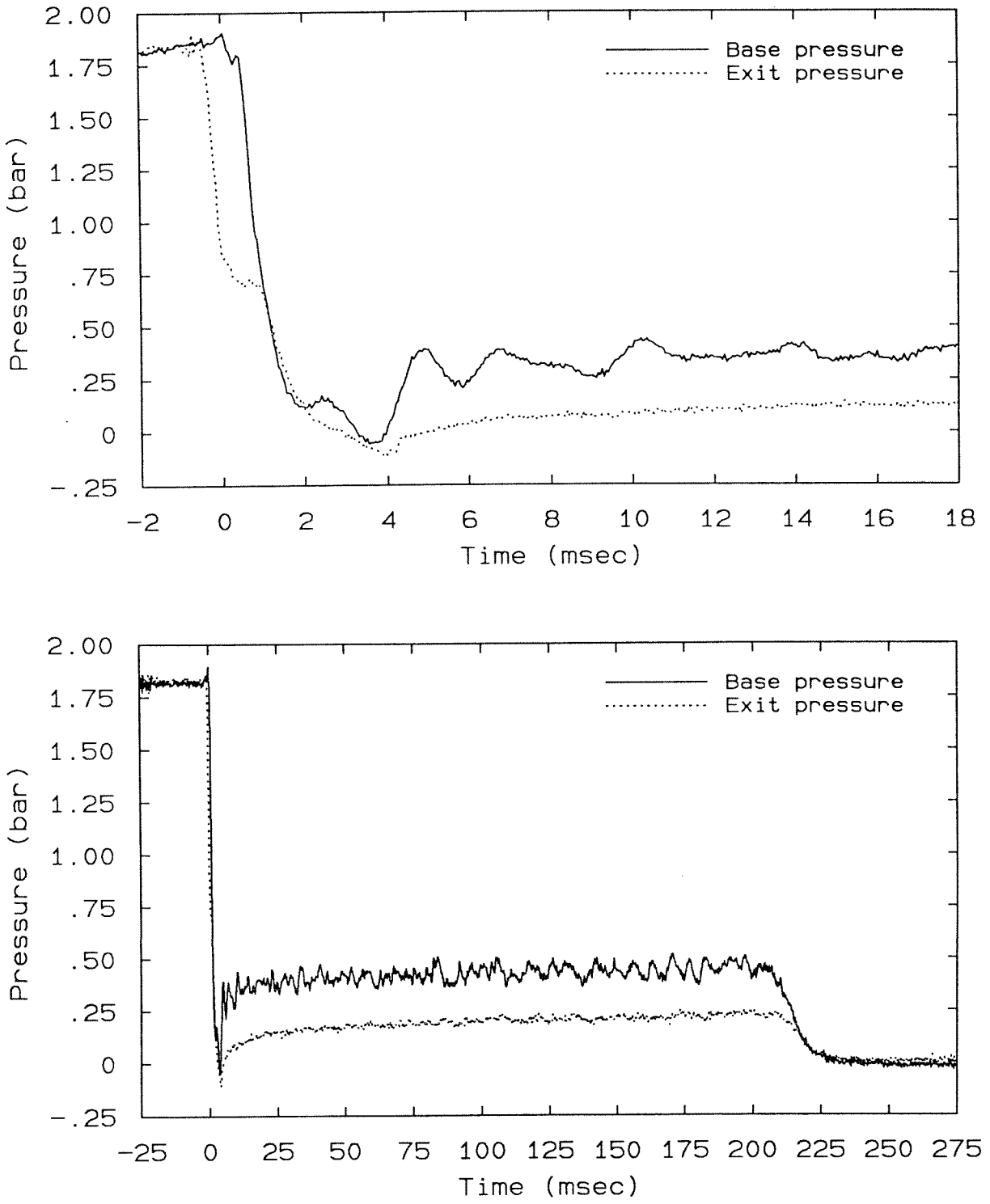

Figure B.5: Liquid: R114, T_0 = 20°C, P_{res} = 0 bar, Run #: MPR 55. Comments: choked exit during quasi-steady propagation phase.

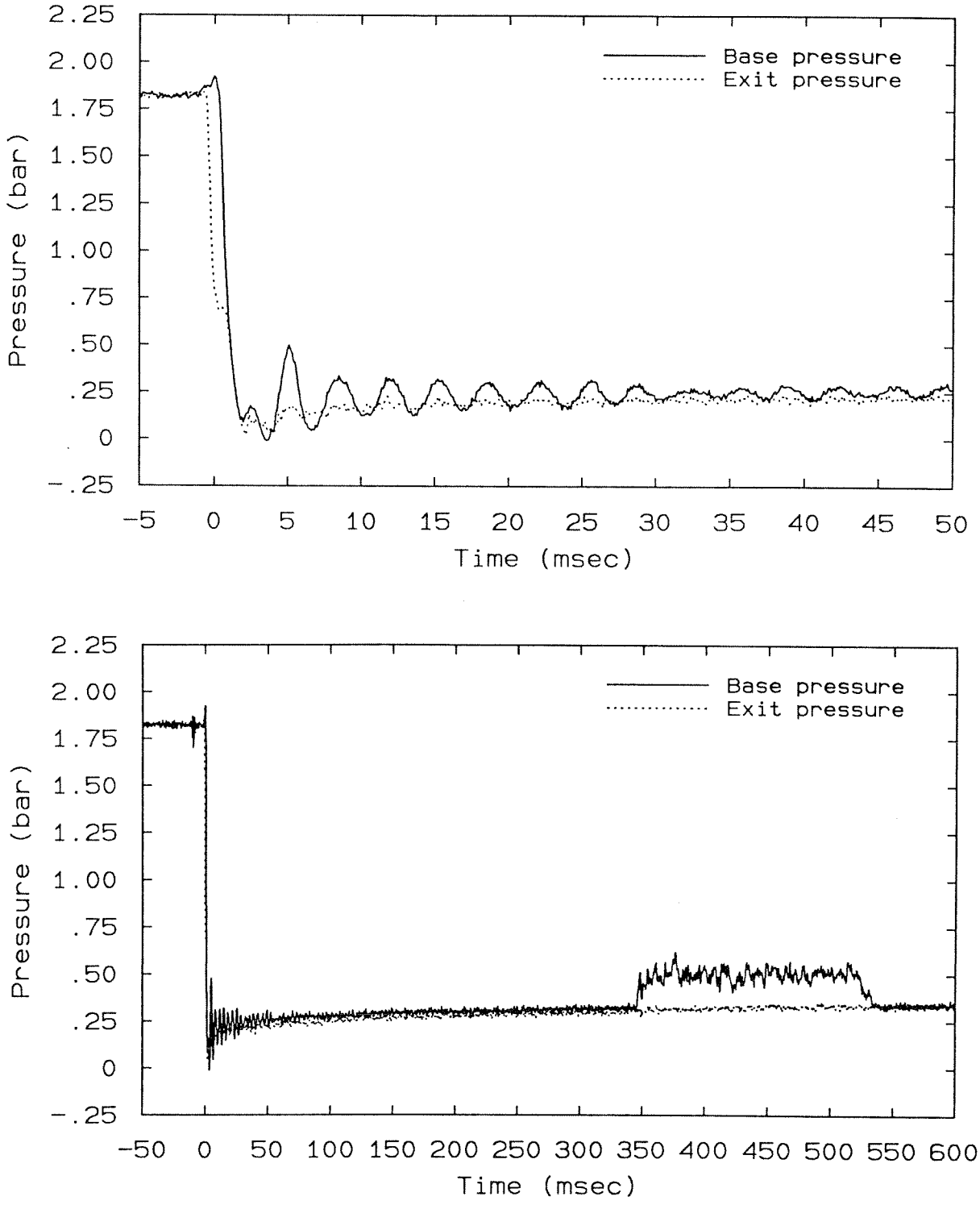

Figure B.6: Liquid: R114, T_0 = 20°C, P_{res} = 1/3 bar, Run #: MPR 57. Comments: unchoked exit during quasi-steady propagation phase; near self-start threshold; transition to explosive boiling occurs at about 350 ms.

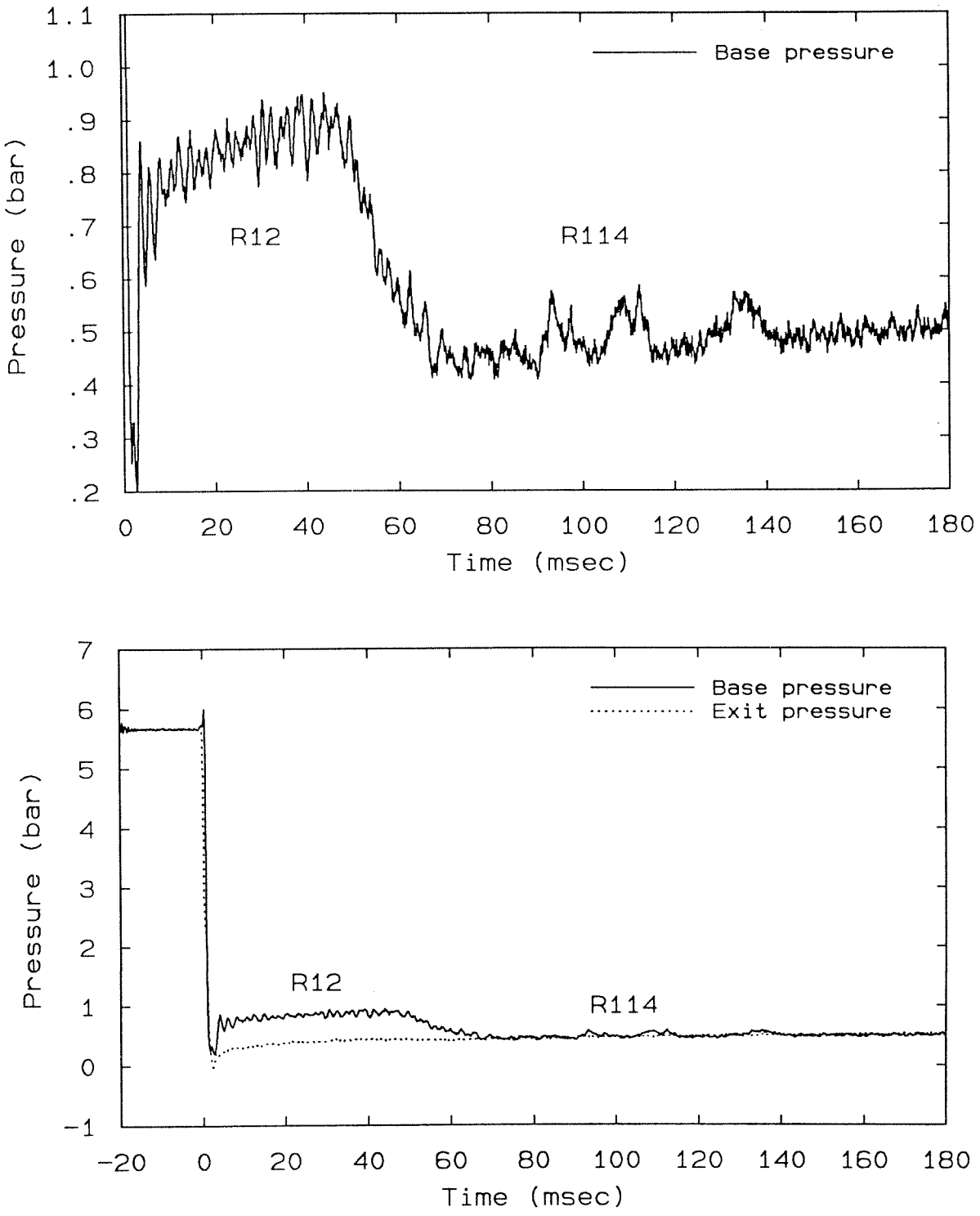

Figure B.7: Liquid: R114, T_0 = 20°C, P_{res} = 1/2 bar, Run #: MPR 72. Comments: near absolute threshold (jump-started with R12); exit is unchoked during R114 quasi-steady propagation phase; wave shuts off at 140 ms with liquid remaining.

Appendix C

Runs with Nucleation in the Upstream Liquid Column

Since the primary goal of the present experiments is to study evaporation waves in pure superheated liquids, nucleation in the liquid column is normally suppressed entirely. However, attempts to suppress nucleation are not always entirely successful, and in such cases the flow pattern is considerably different. Although they are of secondary interest in this study, these runs nevertheless exhibit new and interesting behavior.

C.1. Generation and Expulsion of a Bubbly Mixture.

When nucleation occurs within the liquid column in the present experiments, it generally does so only at the bottom of the test cell, due to some flaw(s) in the nucleation suppression layer (Section 2.4.1). Consequently, nucleation begins at only a few sites (cf. Friz, 1965, Thompson *et al.*, 1987). A typical sequence of events is shown in Figure C.1 for R12 at 20°C and 1.5 bar reservoir pressure. Upon depressurization, nucleation initiates at a few sites on the glass/free-surface contact line, as is characteristic of the higher reservoir pressures. Nucleation also initiates within the liquid column, which is then displaced upward by the growing bubbles. The upward motion of the free surface appears to stimulate nucleation, and a relatively mild transition to explosive boiling occurs at 70 ms (first photograph) even though the reservoir pressure is 1.5 times that of the self-start threshold value (Section 4.5.3).

The leading edge of the wavefront remains approximately fixed with respect to the test cell, evidently because nucleation sites at the wall persist once activated. In several other runs the portions of the wavefront leading edge away from the wall are pushed up by the rising liquid; this may occur to some extent in this example as well. Three large bubbles rise to meet the wavefront, whereupon an aerosol burst from the latter sprays the wall of one rising bubble and nucleates many smaller bubbles (evident from the intervening movie frames). Subsequently, a coarse, bubbly mixture is established throughout the tube. At about 140 ms, this mixture is further fragmented and accelerated to produce a flow with the same appearance as that of waves with pure upstream liquid. This process occurs fairly uniformly over the length of the tube.

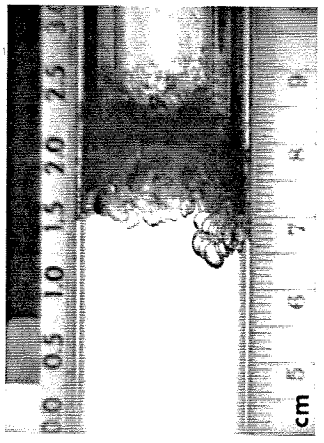

t = 70 ms

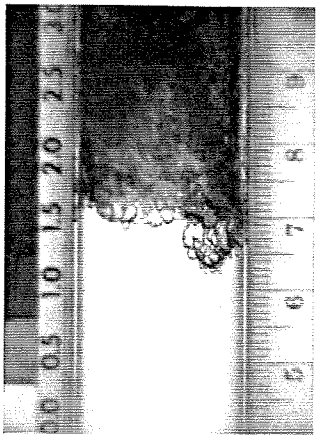

80 ms

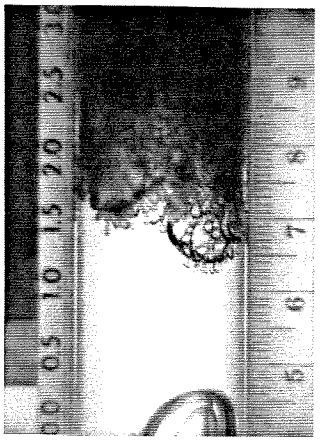

90 ms

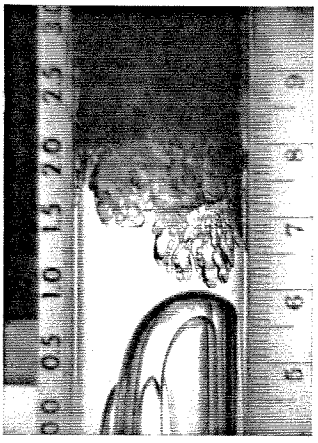

100 ms

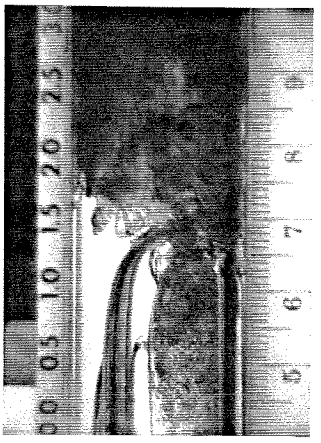

110 ms

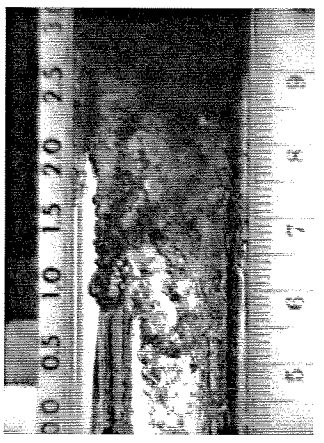

120 ms

130 ms

140 ms

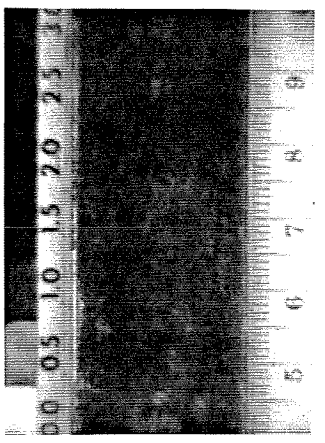

150 ms

Figure C.1: Sequence of motion pictures showing a typical run in which nucleation occurs within the liquid column. Liquid: R12, T_0 = 20°C, P_{res} = 1.5 bar, Test cell #: 2, Run #: MPR 29.

The base and exit pressure traces corresponding to Figure C.1 are shown in Figure C.2. Following the gentle transition to explosive boiling at about 70 ms, the base pressure builds up over a period of about 40 ms. Meanwhile, the exit pressure rises slightly above that of the reservoir value, suggesting that the flow chokes. Overall, the base and exit pressure traces have a more irregular appearance than those associated with evaporation waves because no quasi-steady condition is established (cf. Appendix B). The jump in base pressure at about 110 ms appears to be associated with the nucleation and growth of many new bubbles, which, as mentioned above, occurs when the rising bubbles meet the free surface. Fragmentation and acceleration of the residual mixture begin at about the same time as the exit pressure drops to the ambient value ($\approx$ 135 ms), suggesting that this phenomenon occurs as the result of the test-cell exit unchoking. At lower reservoir pressures the observations are similar, but the events are faster and more vigorous.

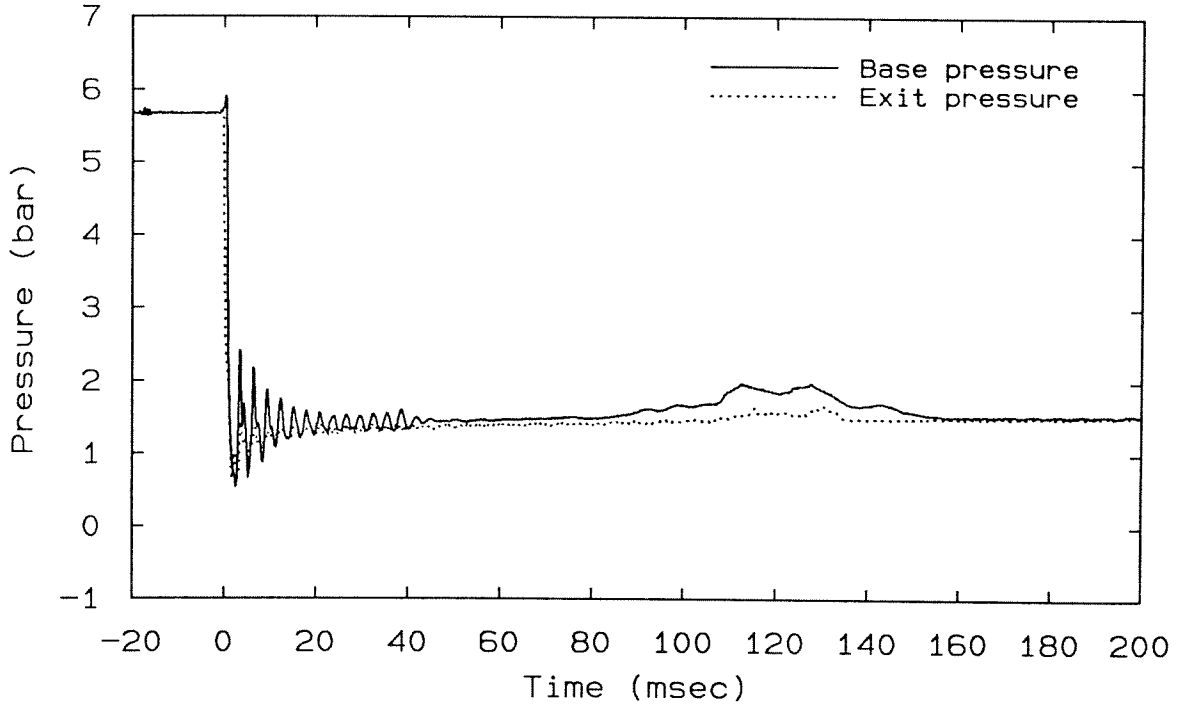

Figure C.2: Base and exit pressure traces corresponding to the run shown in the previous figure. Liquid: R12, T_0 = 20°C, P_{res} = 1.5 bar, Run #: MPR 29.

C.2. Evaporation Wave in a Column of Rising Bubbles.

This experiment is distinguished from other runs by a stream of bubbles rising to the surface prior to diaphragm rupture. The source of nucleation is a single site at the bottom of the test cell. This unusual initial condition was accidental, and the example that will be given is the only run of this type. It is a preliminary run, which accounts for a few departures from the later conventions.

The run in question is shown in Figure C.3. The liquid is R12 at 21.6°C, and P_{res} = 1 bar. When the diaphragm breaks, the liquid becomes superheated and the rising bubbles grow. In this particular run there is no liquid jacket, so the bubbles are magnified in the transverse direction. Between 2 and 3 ms, the bubble at the free surface becomes dark and rough, indicating the initiation of fine-scale fragmentation. The fragmentation process then propagates from bubble to bubble, and from the high-speed movies it appears that spray from each preceding bubble causes roughness and nucleation in the next. The speed of propagation is about 7.8 m/s—about an order of magnitude greater than that of an evaporation wave in a pure liquid under the same conditions. When the wave has propagated about half way into the container, fragmentation initiates virtually simultaneously in the remaining bubbles. This phenomenon appears to be initiated by the breakup of interstitial liquid between the remaining bubbles, which may in turn be caused by the pressure induced by the oncoming fragmentation wave. By 20 ms the flow clears substantially, and it can be seen that the former rising bubbles have become large voids, and many new bubbles have nucleated on their surfaces. Also of interest are the "finger-like" structures that originate at nucleation sites on the glass at the location of the initial glass/free-surface contact line. Because liquid is displaced upward, bubbles that nucleate at these fixed sites are swept upward to form a vapor wake. As in the example of Section C.1, the residual bubbly mixture in this example also experiences a fragmentation and acceleration phase at the end of the run.

The base pressure corresponding to Figure C.3 is shown in Figure C.4. The pressure initially falls to essentially the reservoir pressure (1 bar), but rises steeply as the fragmentation wave begins to propagate. The peak pressure is about 3 bar relative to the reservoir pressure, which is substantially greater than the rise seen in any of the other experiments. It occurs at about 6 ms, and appears to be associated with the most explosive phase, in which the bottom half of the vapor bubble column is fragmenting simultaneously.

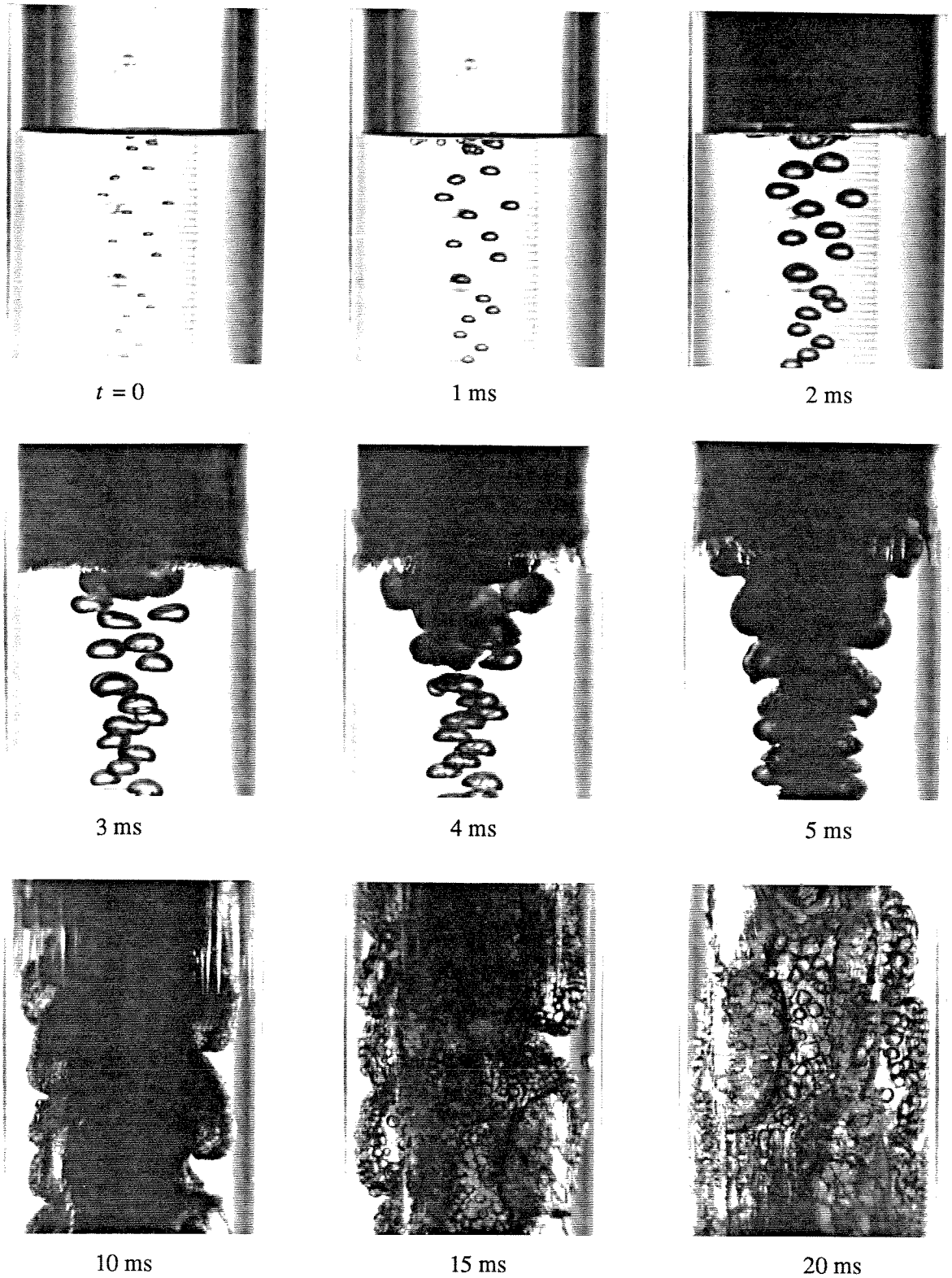

Figure C.3: Sequence of motion pictures showing an evaporation wave propagating into a column of rising bubbles. Liquid: R12, $T_0 = 21.6°C$, $P_{res} \simeq 1$ bar, Test cell #: 2, Run #: MPR 11.

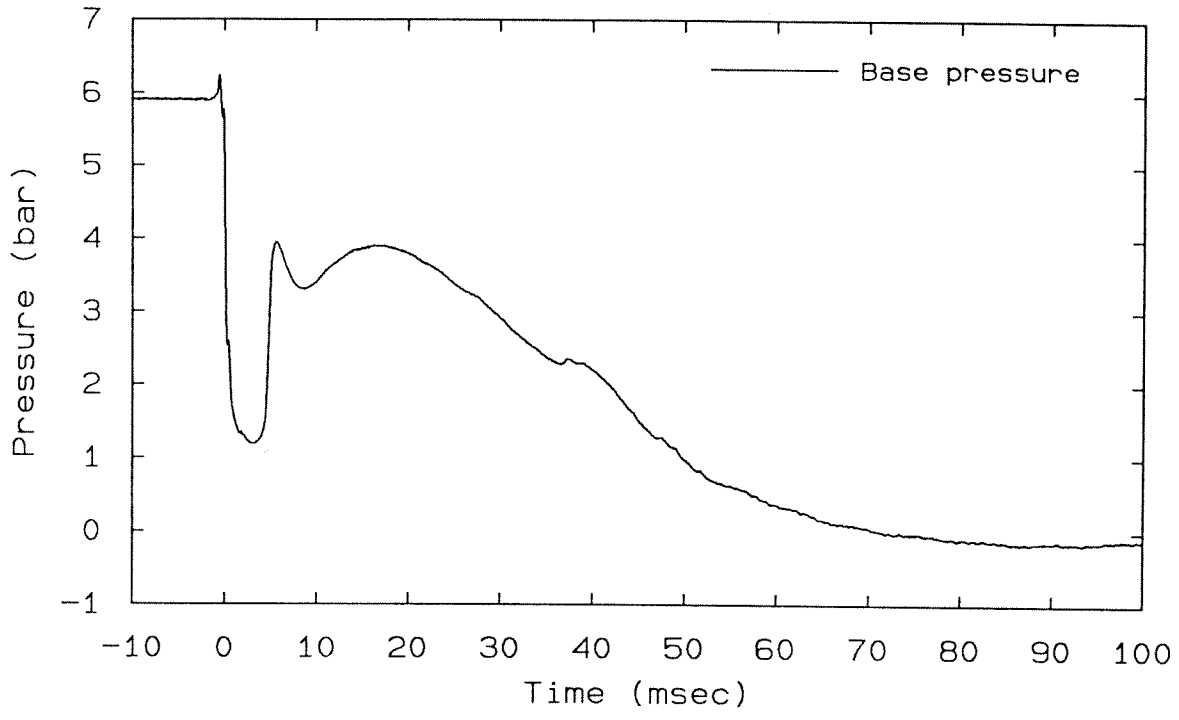

Figure C.4: Base pressure trace corresponding to run shown in the previous figure. Liquid: R12, T_0 = 20°C, $P_{res} \approx$ 1 bar, Run #: MPR 11.

References

ANILKUMAR, A.V. 1989 Experimental studies of high-speed dense dusty gases. Ph.D. Thesis, Caltech.

BALAJI, G.V & MESLER, R. 1990 Surface nucleate boiling, secondary nucleation and threshold superheat. *Proc. ASME Heat Trans. Conf.*, Seattle, WA.

BENNETT, F.D., KAHL, G.D. & WEDEMEYER, E.H. 1964 Resistance changes caused by vaporization waves in exploding wires. *Exploding Wires* (ed. W.G. Chace & H.K. Moore), vol. 3, pp. 65-88. Plenum Press.

BENNETT, F.D. 1965 Vaporization waves as a general property of high temperature matter. *Phys. Fluids*, vol. 8, no. 8, pp. 1425-1427.

BERGMAN, T. & MESLER, R. 1981 Formation of bubble nuclei in superheated water by bursting bubble. *AIChE J.*, vol. 27, no. 5, pp. 851-855.

BLANCHARD, D.C. & WOODCOCK, A.H. 1957 Bubble formation and modification in the sea and its meteorological significance. *Tellus*, vol. 9, no. 2, pp. 145-157.

BOARD, S.J., HALL, R.W. & HALL, R.S. 1975 Detonation of fuel coolant explosions. *Nature*, vol. 254, pp. 319-321.

BRENNEN, C. 1973 The dynamic behavior and compliance of a stream of cavitating bubbles. *J. Fluids Engineering, Transactions of the ASME*, vol. 95, series 1, no. 4.

BRELVI, S.W. & O'CONNELL, J.P. 1972 Corresponding states correlation for liquid compressibility and partial molal volumes of gases at infinite dilution in liquids. *AIChE J.*, vol. 18, pp. 1239-1243.

BÜRGER, M., CARACHALIOS, C., KIM, D.S., & UNGER, H. Theoretical investigations on the fragmentation of drops of melt with respect to the description of thermal detonations (vapor explosions) and their application in the code FRADEMO. *Commission of the European Communities*, report EUR 10660 EN.

CARROLL, K. & MESLER, R. 1981 Bubble entrainment by drop-formed vortex rings. *A.I.Ch.E.J.*, vol. 27, no. 5, pp. 851-855.

CHAVES, H. 1981 Verdampfungswellen in retrograden flüssigkeiten. Diplomarbeit, Georg-August-Universität, Göttingen.

CHAVES, H. 1984 Phasenübergänge und wellen bei der entspannung von fluiden hoher spezifischer wärme. Dissertation, Georg-August-Universität, Göttingen.

CONDIFF, D.W. 1982 Contributions concerning quasi-steady propagation of thermal detonations through dispersions of hot liquid fuel in cooler volatile liquid coolants. *Int. J. Heat Mass Transfer*, vol. 25, pp. 87-98.

DAILY, J.W. & JOHNSON, V.E. JR. 1956 Turbulence and boundary layer effects on cavitation inception from gas nuclei. *Trans. ASME* vol. 78, pp. 1695-1706.

DAS, P.K., BHAT, G.S. & ARAKERI, V.H. 1987 Investigations on the propagation of free surface boiling in a vertical superheated liquid column. *Int. J. Heat Mass Transfer*, vol. 30, no.

4, pp. 631-638.

DECKER, R. & DECKER, B. 1981 The eruptions of Mount St. Helens. *Scientific American*, vol. 244, no. 3, pp. 68-80.

EDGERTON, H.E & KILLIAN J.R. JR. 1979 *Moments of Vision.* MIT Press.

ESMAILIZADEH, L. & MESLER, R. 1986 Bubble entrainment with drops. *J. Colloid Interface Sci.*, vol. 110, no. 2, pp. 561-574.

FELLER, W. 1966 *An Introduction to Probability Theory and Its Applications.* Wiley.

FOWLES, G.R. 1989 Vapor detonations in superheated liquids. *Adiabatic Waves in Liquid-Vapor Systems* (ed. G.E.A. Meier & P.A. Thompson), pp. 407-416. Springer-Verlag.

FRANZ, G.J. 1959 Splashes as sources of sound in liquids. *J. Acoust. Soc. Am.* vol. 31, pp. 1080-1096.

FRIZ, G. 1965 Coolant ejection studies with analogy experiments. In *Proc. Conf. on Safety Fuels and Core Design in Large Fast Power Reactors*, ANL-7120, pp. 890-894.

FROST, D.L. 1985 Effects of ambient pressure on the instability of a liquid boiling explosively at the superheat limit. Ph.D. Thesis, Caltech.

FROST, D.L. 1987 Dynamics of explosive boiling of a droplet. *ASME/JSME Thermal Engineering Joint Conf.*, Hawaii.

FROST, D.L., CICCARELLI, G., & ZARAFONITIS, C. 1989 Propagation of a vapor explosion in a confined geometry. *Adiabatic Waves in Liquid-Vapor Systems* (ed. G.E.A. Meier & P.A. Thompson), pp. 417-426. Springer-Verlag.

FROST, D.L. & STURTEVANT, B. 1986 Effects of ambient pressure on the instability of a liquid boiling explosively at the superheat limit. *J. Heat Trans.*, vol. 108, pp. 418-424.

GARSIDE, J., RUSLI, I.T. & LARSON, M.A. 1979 Origin and size distribution of secondary nuclei. *A.I.Ch.E.J.*, vol. 25, no. 1, pp. 57-64.

GROLMES, M.A. & FAUSKE, H.K. 1970 Modeling of sodium expulsion with freon-11. *ASME Paper* no. 70-HT-24.

GROLMES, M.A. & FAUSKE, H.K. 1974 Axial propagation of free surface boiling into superheated liquids in vertical tubes. In *Proc. 5th Int. Heat Transfer Conf., Paper* B1.7, vol. 4, pp. 30-34. Japan.

HASHIMOTO, H. & SUDO, S. 1980 Surface disintegration and bubble formation in vertically vibrated liquid column. *A.I.A.A. J.*, vol. 18, no. 4, pp. 442-449.

HAYES, W.D. 1958 The basic theory of gasdynamic discontinuities. In *Fundamentals of Gasdynamics* (ed. H.W. Emmons), pp. 416-481. Princeton University Press.

HERMAN, J. & MESLER, R. 1987 Bubble entrainment from bursting bubbles. *J. Colloid & Interface Sci.*, vol. 117, no. 2, pp. 565-569.

JACOBS, J.W, CATTON, I., & PLESSET, M.S. 1984 The hydrodynamic stability of rapidly evaporating liquids with time dependent base states. *J. Fluids Eng.*, vol. 106, pp. 352-358.

KIENTZLER, C.F., ARONS, A.B., BLANCHARD, D.C. & WOODCOCK, A.H. 1954 Photographic investigation of the projection of droplets by bubbles bursting at a water surface. *Tellus*, vol. 6, no. 1, pp. 1-7.

KITCHENER, J.A. & COOPER, C.F. 1959 Current concepts in the theory of foaming. *Quart. Rev. London*, vol. 13, pp. 71-97.

KNAPP, R.T, DAILY, J.W. & HAMMITT, F.G. 1970 *Cavitation*. McGraw-Hill.

LANDAU, L.D. 1944 On the theory of slow combustion. *Acta Physicochimica U.R.S.S.*, vol. 19, no. 1, pp. 77-85.

LANDAU, L.D. & LIFSHITZ, E.M. 1969 *Statistical Physics*. Pergamon.

LE GONIDEC, ROUVILLOIS, SEMERIA, R., LIONS, N., ROBIN, M. & SIMON 1967 Experimental studies on sodium boiling. In *Proc. Int. Conf. on the Safety of Fast Reactors*, pp. IIb-3-1—IIb-3-22. Aix-en Provence, France.

MACINTYRE, F. 1972 Flow patterns in breaking bubbles. *J. Geophysical Research*, vol. 77, no. 27, pp. 5211-5228.

MALLARD, E. & LECHATELIER, H.L. 1883 *Ann. Mines*, vol. 4, p. 379.

MARSHALL, W.R. JR. 1954 Atomization and spray drying. *Chem. Eng. Prog. Monograph Series*, vol. 50, no. 2.

MESLER, R. 1988 Explosive boiling: a chain reaction involving secondary nucleation. *Proc. ASME National Heat Trans. Conf.* HTD-Vol. 96, vol. 2, pp. 487-491.

MESLER, R. & MAILEN, G. 1977 Nucleate boiling in thin liquid films. *A.I.Ch.E.J.*, vol. 23, no. 6, pp. 954-957.

MILLER, C.A. 1973 Stability of moving surfaces in fluid systems with heat and mass transport. II. Combined effects of transport and density difference between phases. *A.I.Ch.E. Journal*, vol. 19, no. 5, pp. 909-915.

NASON, J.R., WIERUM, F.A. & YANOSY, J.L 1983 Challenges in the development of the orbiter active thermal control subsystem. In *Proc. Space Shuttle Tech. Conf.*, CP 2342, Part 1, pp. 450-464. Johnson Space Center.

OGUZ, H.N. & PROSPERETTI, A. 1989 Surface-tension effects in the contact of liquid surfaces. *J. Fluid Mech.*, vol. 203, pp. 149-171.

OGUZ, H.N. & PROSPERETTI, A. 1990 Bubble entrainment by the impact of drops on liquid surfaces. *J. Fluid Mech.*, vol. 219, pp. 143-179.

PALMER, H.J. & MAHESHRI, J.C. 1981 Enhanced interfacial heat transfer by differential vapor recoil instabilities. *Int. J. Heat Mass Transfer*, vol. 4, pp. 117-123.

PETERSON, R.J., GREWAL, S.S. & EL-WAKIL, M.M. 1984 Investigations of liquid flashing and evaporation due to sudden depressurization. *Int. J. Heat Transfer*, vol. 2, pp. 301-309.

PROSPERETTI, A. & PLESSET, M.S. 1978 Vapour-bubble growth in a superheated liquid. *J. Fluid Mech.*, vol. 85, part 2, pp. 349-368.

PROSPERETTI, A. & PLESSET, M.S. 1984 The stability of an evaporating liquid surface. *Phys. Fluids*, vol. 27, no. 7, pp. 1590-1602

PUMPHREY, H.C. & CRUM, L.A. 1988 Acoustic emissions associated with drop impacts. In *Natural Mechanisms of Surface-Generated Noise in the Ocean* (ed. B.R. Kerman), pp. 463-483. Reidel.

PUMPHREY, H.C., CRUM, L.A. & BJORNO, L. 1989 Underwater sound produced by individual drop impacts and rainfall. *J. Acoust. Soc. Am.* vol. 85, pp. 1518-1526.

REID, R.C. 1976 Superheated liquids. *American Scientist*, vol. 64, pp. 146-156.

REID, R.C. 1983 Rapid phase transitions from liquid to vapor. *Adv. Chem. Eng.*, vol. 12, pp. 105-208.

REID, R.C., PRAUSNITZ, J.M. & SHERWOOD, T.K. 1977 *The Properties of Gases and Liquids*. McGraw-Hill.

REYNOLDS, W.C. 1979 *Thermodynamic properties in SI*. Dept. of Mech. Eng., Stanford Univ.

SCOTT, E. & BERTHOUD, G.J. 1978 Multiphase thermal detonation. *Topics in Two-Phase Heat Transfer and Flow* (ed. S.G. Bankoff), ASME.

SHARON, A. & BANKOFF, S.G. 1978 Propagation of shock waves in a fuel-coolant mixture. *Topics in Two-Phase Heat Transfer and Flow* (ed. S.G. Bankoff), ASME.

SHARON, A. & BANKOFF, S.G. 1981 On the existence of steady supercritical plane thermal explosions. *Int. J. Heat Mass Transfer*, vol. 24, pp. 1561-1572.

SHEPHERD, J.E. 1980 Dynamics of vapor explosions: rapid evaporation and instability of butane droplets exploding at the superheat limit. Ph.D. Thesis, Caltech.

SHEPHERD, J.E, McCAHAN, S. & CHO, J.H. 1989 Evaporation wave model for superheated liquids. *Adiabatic Waves in Liquid-Vapor Systems*, pp. 3-12. Springer-Verlag.

SHEPHERD, J.E. & STURTEVANT, B. 1982 Rapid evaporation at the superheat limit. *J. Fluid Mech.*, vol. 121, pp. 379-402.

SKRIPOV, V.P. 1974 *Metastable liquids*. Wiley.

SOLOMON, A.S.P., RUPPRECHT, S.D., CHEN, L.-D. & FAETH, G.M. 1982 Atomization and combustion properties of flashing injectors. In *Proc. AIAA 20th Aerospace Sci. Mtg.*, pp. 1-10. Orlando, FL.

STREETER, V.L. & WYLIE, E.B. 1981 *Fluid Mechanics*. McGraw-Hill.

STREHLOW, R.A. 1984 *Combustion Fundamentals*. McGraw-Hill.

TEPPER, W. 1983 Experimental investigation of the propagation of shock waves in bubbly liquid-vapour mixtures. *Proc. 14th Int. Symp. on Shock Tubes and Waves* (ed. R.D. Archer & B.E. Milton).

TERNER, E. 1962 Shock-tube experiments involving phase changes. *Ind. & Eng. Chem.: Process Design and Development*, vol. 1, no. 2, pp. 84-86.

THOMAS, W. JR. (ed.) 1973 *SPSE Handbook of Photographic Science and Engineering*. Wiley.

THOMPSON, P.A., CAROFANO, G.C. & KIM, Y.-G. 1986 Shock waves and phase changes in a large-heat-capacity fluid emerging from a tube. *J. Fluid Mech.*, vol. 166, pp. 57-92.

THOMPSON, P.A., CHAVES, H., MEIER, G.E.A., KIM, Y.-G. & SPECKMANN, H.-D. 1987 Wave splitting in a fluid of large heat capacity. *J. Fluid Mech.*, vol. 185, pp. 385-414.

TOBA, Y. 1959 Drop production by bursting of air bubbles on the sea surface (II) theoretical study on the shape of floating bubbles. *J. Oceanographical Society of Japan*, vol. 15, no. 3, pp. 1-10.

WALLIS, G.B. 1969 *One-Dimensional Two-Phase Flow*. McGraw-Hill.

WEGENER, P.P. 1969 Gasdynamics of expansion flows with condensation, and homogeneous nucleation of water vapor. *Nonequilibrium Flows*, (ed. P.P. Wegener), vol. 1, part 1, pp. 162-243. Marcel Dekker.

WHITHAM, G.B. 1974 *Linear and nonlinear waves*. Wiley.

WINTERS, W.S. & MERTE, H. JR. 1977 Measurement of sonic velocity in liquid Refrigerant 12. *J. Applied Phys.*, vol. 48, no. 8, pp. 3605-3606.

WINTERS, W.S. & MERTE, H. JR. 1979 Experiments and nonequilibrium analysis of pipe blowdown. *Nuc. Sci & Eng.*, vol. 69, pp. 411-429.

WORTHINGTON, A.M. 1894 The splash of a drop and allied phenomena. *Smithsonian Report*. (Reprinted with additions in 1963: *A Study of Splashes*. Macmillan.)